Enabling Technology and Proof-of-Principle Experiments for Strong Field Terahertz Spectroscopy

Inaugural dissertation
of the Faculty of Science,
University of Bern

presented by

David Rohrbach

from Rüeggisberg (BE)

Supervisor of the doctoral thesis:
Prof. Dr. T. Feurer

Institute of Applied Physics

Enabling Technology and Proof-of-Principle Experiments for Strong Field Terahertz Spectroscopy

Inaugural dissertation
of the Faculty of Science,
University of Bern

presented by

David Rohrbach

from Rüeggisberg (BE)

Supervisor of the doctoral thesis:
Prof. Dr. T. Feurer

Institute of Applied Physics

Accepted by the Faculty of Science.

Bern, March 30, 2023

The Dean
Prof. Dr. Marco Herwegh

Abstract

Electromagnetic radiation in the terahertz (THz) frequency range, from 0.1 THz to 10 THz, encompasses elementary excitations such as lattice vibrations in solids, rotational transitions in molecules, and the dynamics of free electrons. Recent breakthroughs in the generation of ultrafast high-field THz transients have not only enabled selective studies of such excitations, but also the creation of new transient states of matter, opening up a wide range of phenomena to be investigated in chemistry, biology, and materials science. Despite all advances, some experiments require electric or magnetic field strengths beyond what current THz sources can provide. Hence, field enhancement structures have attracted quite some attention. Additionally, control over the THz polarization state is often critical, especially when the symmetry of a particular excitation requires a very specific field direction.

In this thesis, we introduce novel concepts and structures to locally enhance the THz field beyond the corresponding values in free space, and demonstrate new technologies to manipulate the polarization state of broadband THz pulses. For experimental characterization, we use a THz time-domain spectrometer based on photoconductive antennas, a spatially resolved near-field electro-optical sampling setup with the capability to measure all three electric field components, and intense THz sources based on optical rectification in lithium niobate or OH1. We complement the experimental findings, unravel underlying principles, and optimize structures by means of numerical simulations.

This thesis begins with a demonstration of three-dimensional printing technology as a cost-effective and time-saving tool for fabricating THz wave- and phaseplates. We fabricate and demonstrate simple elements such as quarter- or half-waveplates, as well as more complex structures such as q-plates or spiral phaseplates for generating THz pulses carrying angular momentum. Next, we design field-enhancing sub-wavelength structures and use them for various applications, for example, to develop short-period undulators for future compact x-ray sources based on free electrons, or to study ultrafast mode switching in metamaterials based on field-induced carrier generation in semiconductors. We demonstrate THz Stark spectroscopy as a novel tool for time-resolved studies, allowing for the first time inferences about the static and dynamic electrochemical properties of molecular and, in particular, bio-molecular systems in their natural environment. Finally, we present an integrated THz waveguide platform featuring low loss, vacuum-like dispersion, and local field enhancement. Hence, it not only allows for reshaping-free propagation of single-cycle THz pulses, but also improves THz pump visible probe spectroscopy over an extended interaction length. We then use this platform to demonstrate THz-induced alignment of molecules in the gas phase to an extent that could not be achieved with conventional setups.

Contents

Chapter 1

Introduction

Electromagnetic radiation with frequencies between 0.1 THz and 10 THz lies in the so-called terahertz (THz) frequency range. This frequency range transitions to microwaves at lower frequencies, and to infrared radiation at higher frequencies. The THz range thus bridges the gap between conventional electronics and optics – that is, two frequency ranges that are popular in both basic research and commercial applications. However, the THz range itself has long been a challenge for researchers due to technical hurdles in generating and detecting THz frequencies. This even led to the term "THz gap", to designate this last unexplored region of the electromagnetic spectrum in the study of the interaction of electromagnetic fields with matter. It is only in the last few decades that THz science has developed rapidly and is now a very active and dynamic field with a variety of new applications in communication [1–4], nondestructive testing [5–8] or particle accelerators [9–11], to name a few. As indicated in Fig. 1.1, THz radiation encompasses elementary excitations such as lattice vibrations in solids, rotational and vibrational transitions of molecules, intraband transitions in semiconductors, molecular and collective electronic spin transitions, and the motions of free electrons. Therefore, the THz range is important for a variety of applications in chemistry, biology, and materials science.

Weak THz fields

Nowadays, tabletop femtosecond laser systems (i.e., with a pulse duration of about 100 fs) in the infrared and visible range can be used to generate and detect broadband THz radiation. For example, there are THz sources based on photoconductive antennas [12, 13] excited by femtosecond lasers with a high repetition rate on the order of 100 MHz. With the electro-optical scanning technique [14], the electric field of the generated THz pulses can be measured directly, so that not only the field amplitude but also the spectral phase can be detected. This is in stark contrast to optical spectroscopy, where usually only intensities are measured.

Relatively weak THz sources are used in THz time domain spectroscopy (THz-TDS) to measure linear optical material properties using a Fourier transform method [15, 16]. Linear THz-TDS is a powerful tool for characterizing material properties and the underlying fundamental processes. For example, rotational and vibrational transitions in gaseous or liquid molecular samples can be studied to identify chemical components such as amino acids, peptides, and explosives, which is particularly important for pharmaceutical or security applications. In condensed matter samples, THz-TDS can be used to study interband transitions in semiconductors, the dynamics of photocarrieres, or strongly correlated electron systems [15].

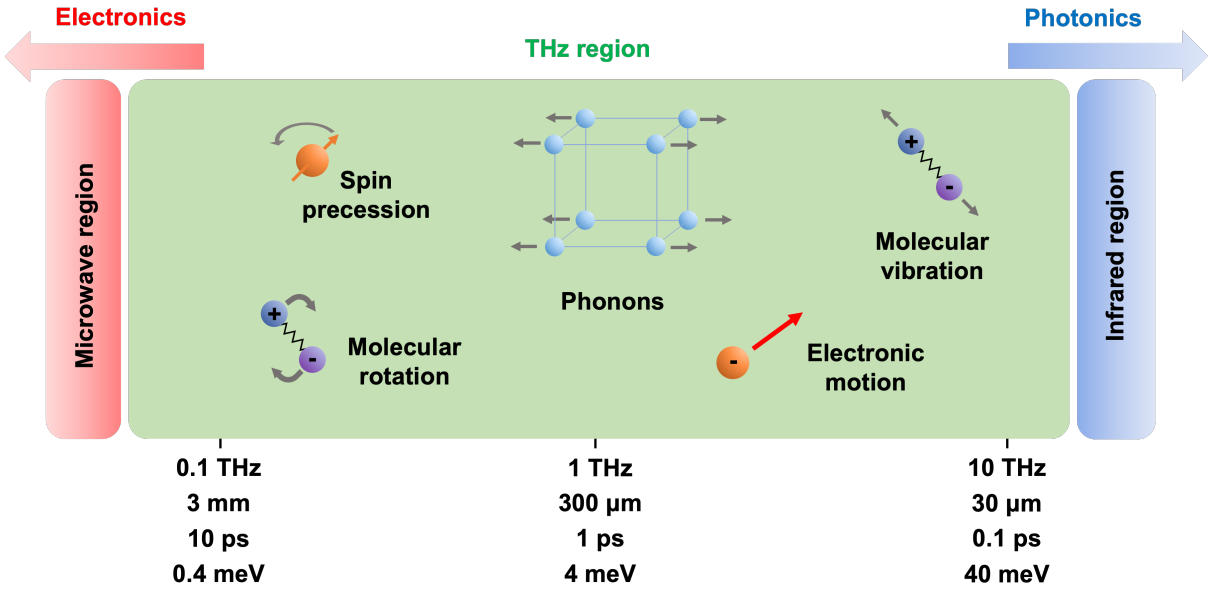

Figure 1.1: Overview of fundamental excitations in solids and molecular systems in the THz frequency range. The axis labels indicate the wavelength, oscillation period, and photon energy corresponding to the THz frequency.

Unlike THz sources and detectors, passive THz optical elements – such as mirrors, lenses, or waveguides – can be fabricated relatively easily. Since the THz free space wavelengths are on the order of 100 µm, the required accuracy for such elements can be achieved using conventional manufacturing methods such as CNC machining or three-dimensional printing.

Strong THz fields

With the advent of high power table-top femtosecond laser systems, strong THz sources became available which are based on optical rectification in nonlinear crystals such as lithium niobate ($LiNbO_3$), zinc telluride (ZnTe), or OH1 organic crystal [17]. Previously, intense THz sources were only found in large-scale facilities such as synchrotrons or free-electron lasers. In addition to improved availability, femtosecond laser systems also have the advantage that they can be used for time-resolved nonlinear spectroscopy on ultrashort time scales. Typically, these systems deliver THz single-cycle pulses at kHz repetition rates and peak electric field strengths ranging from 100 kV/cm to several MV/cm. The duration of a THz cycle is on the order of a picosecond, which is slower than typical electronic motions. Therefore, one can study the non-resonant distortion effect of the electronic potential leading to new dynamical states of matter.

Since the energy of the THz photons matches the energy of elementary excitations as shown in Fig. 1.1, it is possible to target a desired excitation. This allows controlled manipulation of processes as well as resonant manipulation of properties of matter, such as distortion of lattice structure, collective spin excitations, rotational/vibrational control in molecular systems, and charge carrier dynamics. For detailed information, there are several excellent reviews on the generation of high-field THz pulses and their application in spectroscopy [18–25].

Field enhancement structure

The study of nonlinear material properties is ultimately limited by the available THz field strength. Therefore, great efforts have been made to improve THz sources and THz focusing. In free space, focusing is limited by diffraction, but stronger THz fields can be generated in specially designed sub-wavelength structures that locally enhance the incident THz field. Similar sub-wavelength structures are also at the core of so-called meta-materials with unique optical properties not found in nature. In most cases, the enhancement occurs in micron or sub-micron insulating gaps between conductive elements such as dipole antennas (see reviews [26, 27]). Field enhancement of several orders of magnitude is found within nanometer-size regions, yielding field strengths so far exceeding 10 MV/cm in some cases [28, 29]. Waveguide-based field enhancement structures have also been demonstrated [30] and applied, for example, in particle acceleration [31].

Numerical simulations

The theory of light and electromagnetism is described by Maxwell's equations, known since the 19th century. However, even if we know the governing equation, we often cannot find analytical solutions to real-world problems where electromagnetic radiation interacts with various objects, such as the interaction of a THz pulse with a field enhancement structure. This is where numerical methods for solving the partial differential equations come into play. In the finite element method (FEM), for example, the space of the system under consideration is divided into thousands to millions – or even billions – of smaller and simpler elements called mesh cells. This corresponds to a large system of equations that models the entire problem. This system of equations can be solved using computers, with the available computer memory ultimately limiting the maximum number of mesh cells. Numerical simulations are nowadays usually performed using commercial software packages such as *CST Studio Suite* [32] and *COMSOL Multiphysics* [33].

Numerical simulations have two main strengths. First, quantities can be studied that cannot be directly measured experimentally. Therefore, simulations provide a better insight into the underlying microscopic mechanism. Second, simulations are a cost-effective and time-saving method to study versatile problems. Therefore, structures can be tested and optimized (e.g., in terms of field enhancement) prior to experimental implementation.

About this work

This cumulative thesis summarizes the technologies developed and the proof-of-principle experiments performed during my PhD at the Institute of Applied Physics at the University of Bern. In chapter 2 we start with the development of THz optics to control the polarization state and waveform, which is crucial for many strong THz-field applications such as nonlinear THz spectroscopy or for applications in free electron accelerators. As an example of such an application, a novel short-period undulator based on a THz-driven split ring resonator structure featuring field enhancement is discussed in chapter 3. Even higher field enhancement are demonstrated in chapter 4 considering ultrafast mode switching in metamaterials with nanometer-sized gaps. In chapter 5, we demonstrate a novel spectroscopy method for time-resolved THz Stark spectroscopy. To achieve higher field strengths in such nonlinear spectroscopy, we have developed

a versatile THz waveguide platform (chapter 6) and demonstrate its ability to take nonlinear spectroscopy to the next level (chapter 7).

In detail, this thesis is organized as follows.

- **Chapter** 2 (*published in Opt. Express **29** (17), 27160-27170 (2021)*)
  In many applications of intense THz pulses, control over the THz polarization and the wavefront is crucial. For example, radially polarized THz pulses are used to accelerate free electron bunches [10], or vortex beams carrying orbital angular momentum are used to study dichroism of antiferromagnetic resonances [34]. In this context, we demonstrated that various wave- and phase-plates can be manufactured by three-dimensional printing. We used numerical simulations for optimizing the structures, and we experimentally characterized their performance in detail by spatial characterization of all three electric field components. This work is of general interest for the THz community due to the cost-efficient and time-saving manufacturing technique for optical components with similar performance as commercial products.

  The entire work was carried out at the Institute of Applied Physics at the University of Bern. T. Feurer coordinated and supervised the project. The numerical simulations, waveplate manufacturing, and measurements were performed by D. Rohrbach. B. J. Kang and T. Feurer provided useful input for the measurements and the data analysis and assisted in writing the manuscript.

- **Chapter** 3 (*published in Phys. Rev. Accel. Beams **24**, 010703 (2021)*)
  One application of intense THz pulses is the manipulation of free electron bunches. In this work we propose a short period undulator based on the electromagnetic field pattern in a THz-driven split ring resonator structure. The resonator structure locally enhances the electric field, which in turn forces the electron bunches on an oscillatory trajectory. We developed an analytical model and compared different geometric configurations in detail using numerical simulations. This concept can be used as compact novel x-ray sources.

  This work is a collaboration between the Lawrence Berkeley National Laboratory (LBNL) in the Unites States, and the Institute of Applied Physics. T. Feurer coordinated and supervised the project. D. Rohrbach performed the numerical simulations. C. B. Schroeder and W. P. Leemans from LBNL helped with the simulation and the development of an analytical model. Z. Ollmann and M. Hayati assisted in writing the manuscript and with the data analysis.

- **Chapter** 4 (*published in Nano Lett. **22** (5), 2016-2022 (2022)*)
  Another application of intense THz pulses is ultrafast mode switching in metamaterials. Here, the electric field of a THz pulse is locally enhanced in nanometer-sized gaps of split-ring resonators and triggers nonlinear carrier generation in the semiconductor substrate. These additional carriers in turn change the resonance mode of the split-ring resonators. To get better insight into the observed nonlinear response, we developed coupled three-dimensional time-domain simulations for the electromagnetic fields and the carrier generation processes in the semiconductor substrate. Our results clarify which mechanisms of charge carrier generation prevail in different semiconductor materials and what their dynamical features are.

This work is a collaboration between the Laboratory for Micro- and Nanotechnology, the Paul Scherrer Institute (PSI) in Switzerland, and the Institute of Applied Physics. T. Feurer coordinated and supervised the project. The sample were manufactured and measured by F. D. J. Brunner, S. Bagiante, and H. Sigg. B. J. Kang evaluated the experimental data and D. Rohrbach carried out simulations that confirmed and extended the experimental results.

- **Chapter** 5 (*submitted*)
  In this chapter, we demonstrate that the electric field of intense single-cycle THz pulses induces a Stark shift in molecular samples and can therefore be used for ultrafast time-resolved Stark spectroscopy in liquids. THz Stark spectroscopy offers several advantages over conventional Stark spectroscopy, where the sample must be frozen in order to prevent poling effects.

  This work is a collaboration between Temple University (United States), the Chemistry and Biochemistry Department at the University of Bern (Switzerland), and the Institute of Applied Physics. T. Feurer coordinated and supervised the project. B. J. Kang, E. J. Rohwer, and D. Rohrbach performed THz Stark experiments, analyzed data and wrote the manuscript. S.-X. Liu, R. J. Stanley, S. Decurtins, E. Zyaee, A. Cannizzo and T. Feurer discussed and analyzed all results. M. Akbarimoosavi, E. J. Rohwer, S. E. Meckel and R. J. Stanley performed conventional Stark experiments and suggested ways to improve the analysis. G. Sorohhov, S. Decurtins, and S.-X. Liu prepared samples. A. Borgoo and M. Cascella performed DFT calculations.

- **Chapter** 6 (*submitted*)
  To further increase the available field strength in nonlinear THz Stark spectroscopy, we developed a broadband dispersion-free THz waveguide platform featuring field-enhancement. To ensure efficient coupling of free space single-cycle THz pulses, we present a judiciously designed horn antenna. Based on the robust waveguide platform, we demonstrate a compact power splitter and a THz-interferometer for waveform synthesis for potential applications in coherently controlled nonlinear interactions.

  The entire work was carried out at the Institute of Applied Physics at the University of Bern. D. Rohrbach and B. J. Kang performed the experiments and analyzed data. D. Rohrbach performed the numerical simulations. D. Rohrbach, B. J. Kang, E. Zyaee, and T. Feurer discussed all results and contributed to writing and reviewing of the final manuscript.

- **Chapter** 7 (*In preparation for submission*)
  To demonstrate the capabilities of our THz waveguide platform, we consider THz-induced alignment of gas molecules due to the interaction between their dipole moment and the THz electric field. Compared to the standard free space focusing of THz pulses, the THz waveguide approach increases the acquired signal in two ways: The electric field is locally enhanced and the interaction length is extended. We experimentally demonstrate a signal increase by more than an order of magnitude, allowing us to detect features that we could not measure otherwise.

  The entire work was carried out at the Institute of Applied Physics at the University of Bern. D. Rohrbach, H.-M. Frey, and B. J. Kang performed the experiments and analyzed

data. D. Rohrbach, H.-M. Frey, B. J. Kang, E. Zyaee, and T. Feurer discussed all results and contributed to writing and reviewing of the manuscript.

Additional work

During my PhD, I contributed to further projects and publications which are not within the scope of this thesis:

- K. Töpfer, A. Pasti, A. Das, S. M. Salehi, L. I. Vazquez-Salazar, D. Rohrbach, T. Feurer, P. Hamm, and M. Meuwly, *Structure, Organization and Heterogeneity of Water-Containing Deep Eutectic Solvents* in J. Am. Chem. Soc., (2022), DOI: `https://doi.org/10.1021/jacs.2c04169`.

  This work provides molecular-level insights in deep eutectic solvents using molecular dynamics simulations in combination with two complementary spectroscopic techniques – 2D infrared spectroscopy and standard linear THz spectroscopy.

- D. Rohrbach, C. B. Schroeder, A. Pizzi, R. Tarkeshian, M. Hayati, W. P. Leemans, and T. Feurer, *THz-driven surface plasmon undulator as a compact highly directional narrow band incoherent x-ray source* in PRAB **22**, 090702 (2019), DOI: `https://doi.org/10.1103/PhysRevAccelBeams.22.090702`

  In this work, we propose a short period undulator based on THz-driven surface plasmons in graphene, which features only minor field enhancement.

- Z. Ollmann, D. Rohrbach, B. J. Kang, M. Hayati, R. Tarkeshian, T. Feurer, H. W. Kim, I. H. Baek, K. Y. Oang, M. H. Kim, , Y. C. Kim, K.-H. Jang, and Y. U. Jeong, *THz streaking of relativistic electron bunches* (in preparation for submission)

  This work focuses on pulse duration and temporal jitter measurements of ultrashort electron bunches using a THz streak camera.

- B. J. Kang, M. A. Stucki, D. Rohrbach, H. Park, S. J. Hong, Y.-M. Bahk, and T. Feurer *Optical-induced nonlinear dynamics of complementary THz meta-surfaces on long-carrier lifetime semiconductor* (in preparation for submission)

  In this work, we investigate complementary THz meta-surfaces and characterize their nonlinear dynamics induced by optical pumping.

Acknowledgment

This work has been supported by the Swiss National Science Foundation (SNSF) under grant no. 200020-178812, no. 200021-204053, and the National Center of Competence in Research of Molecular Ultrafast Science and Technology (NCCR MUST).

Bibliography

[1] R. Piesiewicz, M. Jacob, M. Koch, J. Schoebel, and T. Kurner, "Performance Analysis of Future Multigigabit Wireless Communication Systems at THz Frequencies With Highly Directive Antennas in Realistic Indoor Environments", IEEE J. Sel. Top. Quantum Electron. **14**, 421–430 (2008), https://doi.org/10.1109/JSTQE.2007.910984.

[2] J. Federici and L. Moeller, "Review of terahertz and subterahertz wireless communications", J. Appl. Phys. **107**, 111101 (2010), https://doi.org/10.1063/1.3386413.

[3] T. Kleine-Ostmann and T. Nagatsuma, "A review on terahertz communications research", J. Infrared, Millimeter, Terahertz Waves **32**, 143–171 (2011), https://doi.org/10.1007/s10762-010-9758-1.

[4] Z. Chen, X. Ma, B. Zhang, Y. Zhang, Z. Niu, N. Kuang, W. Chen, L. Li, and S. Li, "A survey on terahertz communications", China Commun. **16**, 1–35 (2019), https://ieeexplore.ieee.org/document/8663550.

[5] I. Amenabar, F. Lopez, and A. Mendikute, "In introductory review to THz non-destructive testing of composite mater", J. Infrared, Millimeter, Terahertz Waves **34**, 152–169 (2013), https://doi.org/10.1007/s10762-012-9949-z.

[6] M. Neshat and N. P. Armitage, "Developments in THz Range Ellipsometry", J. Infrared, Millimeter, Terahertz Waves **34**, 682–708 (2013), https://doi.org/10.1007/s10762-013-9984-4.

[7] M. Naftaly, N. Vieweg, and A. Deninger, "Industrial Applications of Terahertz Sensing: State of Play", eng, Sensors **19**, 4203 (2019), https://pubmed.ncbi.nlm.nih.gov/31569789%20https://www.ncbi.nlm.nih.gov/pmc/articles/PMC6806174/.

[8] G. Tzydynzhapov, P. Gusikhin, V. Muravev, A. Dremin, Y. Nefyodov, and I. Kukushkin, "New Real-Time Sub-Terahertz Security Body Scanner", J. Infrared, Millimeter, Terahertz Waves **41**, 632–641 (2020), https://doi.org/10.1007/s10762-020-00683-5.

[9] J. Fabiańska, G. Kassier, and T. Feurer, "Split ring resonator based THz-driven electron streak camera featuring femtosecond resolution", Sci. Rep. **4**, 5645 (2014), https://doi.org/10.1038/srep05645.

[10] E. A. Nanni, W. R. Huang, K. H. Hong, K. Ravi, A. Fallahi, G. Moriena, R. J. D. Miller, and F. X. Kärtner, "Terahertz-driven linear electron acceleration", Nat. Commun. **6**, 8486 (2015), https://doi.org/10.1038/ncomms9486.

[11] D. Zhang, A. Fallahi, M. Hemmer, X. Wu, M. Fakhari, Y. Hua, H. Cankaya, A.-L. Calendron, L. E. Zapata, N. H. Matlis, and F. X. Kärtner, "Segmented terahertz electron accelerator and manipulator (STEAM)", Nat. Photonics **12**, 336–342 (2018), https://doi.org/10.1038/s41566-018-0138-z.

[12] P. R. Smith, D. H. Auston, and M. C. Nuss, "Subpicosecond photoconducting dipole antennas", IEEE J. Quantum Electron. **24**, 255–260 (1988), https://doi.org/10.1109/3.121.

[13] N. Katzenellenbogen and D. Grischkowsky, "Efficient generation of 380 fs pulses of THz radiation by ultrafast laser pulse excitation of a biased metal-semiconductor interface", Appl. Phys. Lett. **58**, 222–224 (1991), https://doi.org/10.1063/1.104695.

[14] J. A. Valdmanis, G. Mourou, and C. W. Gabel, "Picosecond electro-optic sampling system", Appl. Phys. Lett. **41**, 211–212 (1982), https://doi.org/10.1063/1.93485.

[15] S. G. Carter et al., *Terahertz Spectroscopy*, edited by S. L. Dexheimer, 1st ed. (CRC Press, Boca Raton, 2008), https://doi.org/10.1201/9781420007701.

[16] J. Neu and C. A. Schmuttenmaer, "Tutorial: An introduction to terahertz time domain spectroscopy (THz-TDS)", J. Appl. Phys. **124**, 10.1063/1.5047659 (2018), https://doi.org/10.1063/1.5047659.

[17] K.-L. Yeh, M. C. Hoffmann, J. Hebling, and K. A. Nelson, "Generation of 10 μJ ultrashort terahertz pulses by optical rectification", Appl. Phys. Lett. **90**, 171121 (2007), https://doi.org/10.1063/1.2734374.

[18] M. C. Hoffmann and J. A. Fülöp, "Intense ultrashort terahertz pulses: generation and applications", J. Phys. D. Appl. Phys. **44**, 83001 (2011), https://dx.doi.org/10.1088/0022-3727/44/8/083001.

[19] K. Tanaka, H. Hirori, and M. Nagai, "THz Nonlinear Spectroscopy of Solids", IEEE Trans. Terahertz Sci. Technol. **1**, 301–312 (2011), https://doi.org/10.1109/TTHZ.2011.2159535.

[20] M. Tonouchi, "Cutting-edge terahertz technology", Nat. Photonics **1**, 97–105 (2007), https://doi.org/10.1038/nphoton.2007.3.

[21] A. Pashkin, A. Sell, T. Kampfrath, and R. Huber, "Electric and magnetic terahertz nonlinearities resolved on the sub-cycle scale", New J. Phys. **15**, 65003 (2013), https://dx.doi.org/10.1088/1367-2630/15/6/065003.

[22] T. Kampfrath, K. Tanaka, and K. A. Nelson, "Resonant and nonresonant control over matter and light by intense terahertz transients", Nat. Photonics **7**, 680–690 (2013), https://doi.org/10.1038/nphoton.2013.184.

[23] R. Ulbricht, E. Hendry, J. Shan, T. F. Heinz, and M. Bonn, "Carrier dynamics in semiconductors studied with time-resolved terahertz spectroscopy", Rev. Mod. Phys. **83**, 543–586 (2011), https://link.aps.org/doi/10.1103/RevModPhys.83.543.

[24] H. Y. Hwang, S. Fleischer, N. C. Brandt, B. G. P. Jr., M. Liu, K. Fan, A. Sternbach, X. Zhang, R. D. Averitt, and K. A. Nelson, "A review of non-linear terahertz spectroscopy with ultrashort tabletop-laser pulses", J. Mod. Opt. **62**, 1447–1479 (2015), https://doi.org/10.1080/09500340.2014.918200.

[25] P. Salén, M. Basini, S. Bonetti, J. Hebling, M. Krasilnikov, A. Y. Nikitin, G. Shamuilov, Z. Tibai, V. Zhaunerchyk, and V. Goryashko, "Matter manipulation with extreme terahertz light: Progress in the enabling THz technology", Phys. Rep. **836-837**, 1–74 (2019), https://www.sciencedirect.com/science/article/pii/S0370157319302649.

[26] J.-H. Kang, D.-S. Kim, and M. Seo, "Terahertz wave interaction with metallic nanostructures", Nanophotonics **7**, 763–793 (2018), https://doi.org/10.1515/nanoph-2017-0093.

[27] Y.-M. Bahk, D. J. Park, and D.-S. Kim, "Terahertz field confinement and enhancement in various sub-wavelength structures", J. Appl. Phys. **126**, 120901 (2019), https://doi.org/10.1063/1.5110046.

[28] J.-Y. Kim, B. J. Kang, J. Park, Y.-M. Bahk, W. T. Kim, J. Rhie, H. Jeon, F. Rotermund, and D.-S. Kim, "Terahertz Quantum Plasmonics of Nanoslot Antennas in Nonlinear Regime", Nano Lett. **15**, 6683–6688 (2015), https://doi.org/10.1021/acs.nanolett.5b02505.

[29] B. J. Kang, D. Rohrbach, F. D. J. Brunner, S. Bagiante, H. Sigg, and T. Feurer, "Ultrafast and Low-Threshold THz Mode Switching of Two-Dimensional Nonlinear Metamaterials", Nano Lett. **22**, 2016–2022 (2022), https://doi.org/10.1021/acs.nanolett.1c04776.

[30] K. Iwaszczuk, A. Andryieuski, A. Lavrinenko, X.-C. Zhang, and P. U. Jepsen, "Terahertz field enhancement to the MV/cm regime in a tapered parallel plate waveguide", Opt. Express **20**, 8344–8355 (2012), http://opg.optica.org/oe/abstract.cfm?URI=oe-20-8-8344.

[31] M. A. K. Othman, M. C. Hoffmann, M. E. Kozina, X. J. Wang, R. K. Li, and E. A. Nanni, "Parallel-plate waveguides for terahertz-driven MeV electron bunch compression", Opt. Express **27**, 23791–23800 (2019), http://opg.optica.org/oe/abstract.cfm?URI=oe-27-17-23791.

[32] *CST – Computer Simulation Technology*, (2019) https://www.cst.com (visited on 06/08/2021).

[33] *COMSOL Multiphysics*, (2019) https://www.comsol.com (visited on 02/01/2019).

[34] A. A. Sirenko, P. Marsik, L. Bugnon, M. Soulier, C. Bernhard, T. N. Stanislavchuk, X. Xu, and S.-W. Cheong, "Total Angular Momentum Dichroism of the Terahertz Vortex Beams at the Antiferromagnetic Resonances", Phys. Rev. Lett. **126**, 157401 (2021), https://link.aps.org/doi/10.1103/PhysRevLett.126.157401.

Chapter 2

3D-printed THz wave- and phaseplates

David Rohrbach[1], Bong Joo Kang[1], and Thomas Feurer[1]

[1]Institute of Applied Physics, University of Bern, Sidlerstrasse 5, 3012 Bern, Switzerland

This work was published in Opt. Express **29** (17), 27160-27170 (2021)

Abstract
Three-dimensional printing based on fused deposition modeling has been shown to provide a cost-efficient and time-saving tool for fabricating a variety of THz optics for a frequency range < 0.2 THz. By using a broadband THz source, with a useful spectral range from 0.08 THz to 1.5 THz, we show that 3D-printed waveplates operate well up to 0.6 THz and have bandwidths similar to commercial products. Specifically, we investigate quarter- and half-waveplates, q-plates, and spiral phaseplates. We demonstrate a route to achieve broadband performance, so that 3D-printed waveplates can also be used with broadband, few-cycle THz pulses, for instance, in nonlinear THz spectroscopy or other THz high field applications.

2.1 Introduction

Recent progress in the development of THz systems led to a variety of new applications in communications [1–4], nondestructive testing [5–8] or particle accelerators [9–12], to name a few. For THz beam transport and beam manipulation, these systems need different passive THz optical elements, such as mirrors, lenses, beam splitters, waveguides, or waveplates. Beside conventional fabrication methods, such as cutting, milling, polishing, or etching, these elements can also be manufactured using a three-dimensional (3D) printer. Different 3D-printing technologies exist, but the most popular uses fused deposition modeling (FDM). This 3D-printing technique has several advantages: It is time- and cost-efficient, shows good reproducibility, and requires

no post-processing. Since the minimum feature size of most 3D-printers is around hundred microns, this fabrication method is best suited for the sub-THz range [13]. Printable materials are usually polymers with a THz refractive index around 1.5, which is favorably low for transmission type optical elements. In addition, a negligible absorption coefficient is essential and is provided, for instance, by polystyrene or by the cyclic olefin copolymer (COC) TOPAS [14, 15]. A variety of 3D-printed devices have already been demonstrated, e.g., THz lenses [14, 16], gratings [14, 16], waveguides [17], axicons [18], phaseplates [19, 20], half-waveplates [13] and q-plates [21]. A comprehensive review on different 3D-printed structures for THz applications is found in [15].

Most of these studies were performed in the frequency range between 0.1 THz to 0.2 THz and used continuous wave, narrowband THz sources. To the best of our knowledge, except for reference [20] pulsed broadband THz sources have never been used, for instance, to determine the useful bandwidth of 3D-printed THz waveplates. By using such a source, we characterize waveplates in a frequency range from 0.08 THz to 1.5 THz. We consider the most important waveplates for THz applications, namely quarter-waveplates (QWP), half-waveplates (HWP), q-plates and spiral phaseplates (SPP). We show that the operation frequency can be adjusted by a proper scaling of the design and we measure the useful bandwidth of all wave- and phaseplates. Finally, we outline a route toward achromatic waveplates, specifically we demonstrate a QWP design with a twice as large bandwidth compared to the standard QWP. This principle can be extended to other waveplates as well.

2.2 Experimental setup

The THz-pulses are generated by a photo-conductive antenna (PCA) gated by a bias voltage and exited by 780 nm, 100 fs laser-pulses at a repetition rate of 80 MHz. We mount a wire grid polarizer to define the THz polarization state to be linear horizontal. The source is imaged with two aspheric lenses with a focal length of 50 mm and 25 mm to the detection plane. In between the two lenses the THz beam has a diameter ($1/e^2$) of about 40 mm and is nearly collimated. Here, we mount the waveplate under investigation. The second lens focuses the modified THz beam and we use a near-field THz scanning microscope to characterize the electric field distribution at the focus as a function of time and transverse position. We cannot measure the electric field directly after the waveplate since the field strength there is too low. However, the measured electric field distribution in the focus is related to the field distribution after the waveplates by a two-dimensional Fourier transformation. Note that we also Fourier transformed the results of numerical simulations and analytical models before comparing them with the measured spatial distributions in the focal plane. The only caveat is that the second lens might modify the THz polarization due to the different Fresnel coefficients for the horizontal and vertical polarization component, but we calculated this effect to be less than 5%.

A detailed description of the near-field scanning unit is given in the supplemental document and in references [22, 23]. Briefly, the electric field of the THz pulse is measured through electro-optic sampling using ZnTe crystals. The spatial resolution is approximately 20 µm. The detection unit is mounted on a motorized x-, y- and z-stage, such that the electric field can be raster-scanned. By using either a $\langle 110 \rangle$-cut or a $\langle 100 \rangle$-cut ZnTe crystal we can measure the horizontal, vertical, and longitudinal components of the THz electric field as a function of transverse spatial position and cover a frequency range from 0.08 THz to 1.5 THz. Note that

due to imperfections of the coating and of the ZnTe-crystals, the detection efficiency varies for the different crystal orientations, and we estimate these variation to be smaller than 10 %. Based on the statistical analysis of multiple measurements we estimate the error in the measured phase to be of order 0.1 rad in the frequency range of interest. In the following we consider these amplitude and phase errors in the error propagation.

2.3 Wave- and phaseplate design and fabrication

In order to manufacture a birefringent metamaterial, out of which the waveplates were fabricated, we consider a one-dimensional array of alternating layers with a refractive index of n_1 and n_2 with a corresponding layer thickness of L_1 and L_2. The effective refractive indices n_e and n_o for an electric field polarization parallel and perpendicular to the layers are given by [24, 25]

$$n_e^2 = n_\parallel^2 + \frac{1}{3}\left[\frac{\Lambda}{\lambda}\pi\eta_1\eta_2(n_1^2 - n_2^2)\right]^2 \qquad n_o^2 = n_\perp^2 + \frac{1}{3}\left[\frac{\Lambda}{\lambda}\pi\eta_1\eta_2\left(n_1^{-2} - n_2^{-2}\right)n_\parallel n_\perp^3\right]^2, \tag{2.1}$$

where $\Lambda = L_1 + L_2$ is the period of the structure, λ is the free-space wavelength, and $\eta_1 = L_1/\Lambda$ and $\eta_2 = L_2/\Lambda$ are the filling factors of the individual components. We defined $n_\parallel^2 := \eta_1 n_1^2 + \eta_2 n_2^2$ and $n_\perp^2 := \left(\eta_1 n_1^{-2} + \eta_2 n_2^{-2}\right)^{-1}$. Equation (2.1) is only strictly valid for $\lambda > n_2\Lambda$ [26] assuming $n_2 > n_1$. In the limit of $\lambda \gg \Lambda$, the indices of refraction asymptotically approach $n_e \approx n_\parallel$ and $n_o \approx n_\perp$. For lower wavelengths, diffraction from the periodic one-dimensional grating structure degrades the performance of the waveplate.

Prior to fabrication, all waveplate designs were optimized by time-domain simulations performed with CST [27]. The simulation volume contained a single unit cell of the grating and we used periodic boundary conditions in transverse directions. The incident THz pulse was modeled as a plane wave and open boundary conditions were used in the propagation direction. With the help of the simulations the design parameters of all waveplates, i.e., grating period, height and filling factor, were optimized within the limitations of the printing process. Specifically, we fixed the wall thickness to a value determined by the nozzle of our 3D-printer. Then, we ran parametric sweeps for the period and the structure height and selected the best combination.

The wave- and phaseplates were fabricated using standard FDM technology with an *Ultimaker 2+* 3D-printer. We use commercially available COC-filaments, which have a measured refractive index of 1.53 and an absorption coefficient of less than 1 cm^{-1} for frequencies between 0.2 THz to 0.8 THz [14]. The waveplates are based on a grating-like alternating air ($n_1 = 1$) and filament ($n_2 = 1.53$) structure with the design parameters calculated from Eq. (2.1). All waveplates were printed in less than 12 hours using a nozzle diameter of 0.25 mm and a layer height of 0.1 mm. The nozzle temperature was set to 210 °C and the build plate temperature to 70 °C. All the waveplates have a 3 mm thick 3D-printed cylindrical support plate with a diameter of 50 mm. In order to minimize imperfections from 3D-printing we selected the wall thickness for all waveplates such that walls are printed as single lines from the extruder. Measurements revealed a wall thickness of (0.22 ± 0.02) mm, which is slightly smaller than the nozzle diameter. The error of 20 µm is due to thickness variations in the printing process. In order to minimize their influence we used, whenever possible, a filling factor well below 0.5. As a result the 3D-printed structure shows a birefringence of approximately 0.12, which is more than two

times higher than that of standard THz waveplates made out of quartz [28]. This is of special interest for the low THz frequency range, where standard waveplates tend to become rather bulky. From the frequency dependent birefringence $\Delta n(f)$ we calculate the structure height to $h = \frac{\delta}{2\pi}\frac{c}{f\Delta n(f)}$, where c is the speed of light in vacuum and δ is the target phase retardance at frequency f. Due to the minimum feature size and the accuracy of the FDM technology, the smallest useful period Λ is approximately 0.3 mm. As a result, the waveplates are limited to frequencies up to approximately 0.6 THz. Photographs of different 3D-printed wave- and phaseplates are shown in Fig. 2.1. Note that also much larger waveplates can be printed if needed. With our printer the maximum size is limited to 223×223 mm^2.

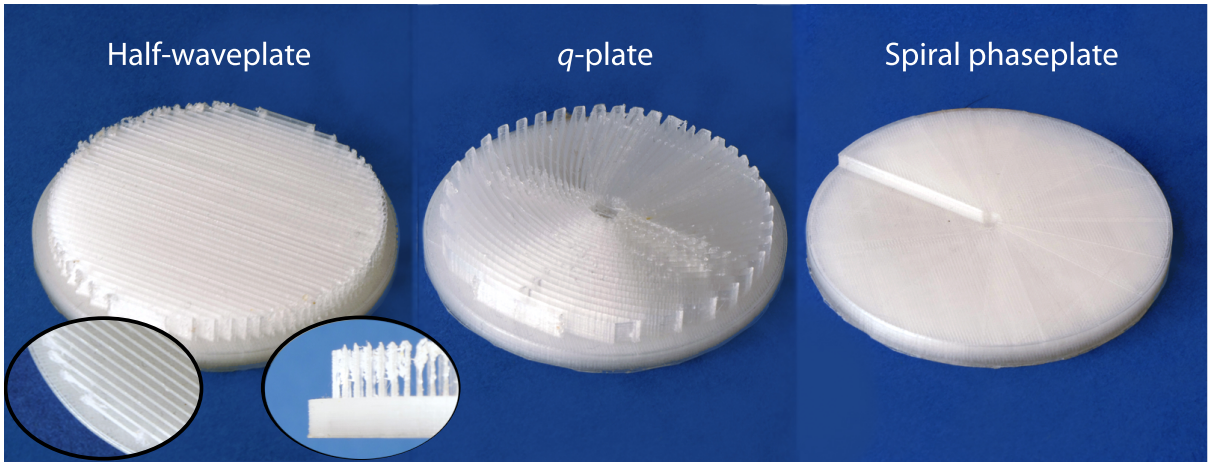

Figure 2.1: Photographs of a 3D-printed half-waveplate, q-plate, and spiral phaseplate. The two insets show a top- and side-view of the half-waveplate structure (Photographs are provided by Rhoda Berger).

First, we printed QWPs and HWPs with a design similar to the one proposed in reference [13], but scaled to the more than two times higher design frequency of 0.35 THz. The grating structure has a period of 0.7 mm and the grating height is 1.9 mm for a QWP and 3.8 mm for a HWP. To evaluate the influence of the grating period, we manufactured an additional HWP with a 1.1 mm period while keeping the grating height constant. Moreover, to demonstrate the tunability we fabricated a QWP and a HWP both with a higher design frequency of 0.5 THz. Here, the grating period was reduced to 0.4 mm and the grating height to 1.5 mm (QWP) and 3.0 mm (HWP). Next, we printed q-plates, which locally act as HWPs whereby the orientation of the fast axis changes as a function of azimuthal angle. For a q-plate with a topological charge of $q = 0.5$, the angle of the fast axis changes as $\alpha(\varphi) = 0.5\varphi + \alpha_0$, where φ is the azimuthal angle and α_0 is an offset corresponding to the plate orientation. The layout of the grating structure consists of a set of profile curves in the xy-plane each given by $y(x) = \pm\sqrt{y_0(y_0 + 2x)}$, where y_0 is the intercept of the considered curve with the y-axis. Note that the grating period and the filling factor change depending on the distance to the origin. The profile curves are chosen such that the grating period is 1.1 mm at a radius of 0.8 cm. Closer to the origin, the grating period is smaller, whereas further away it is larger. The grating height is fixed to 3.8 mm.

Spiral phaseplates, which change the orbital angular momentum of the THz beam, do not require a birefringent material, but a phase retardance that decreases or increases linearly with azimuthal angle. For a SPP with a topological charge of ± 1 at the design frequency f, the

step height h at an azimuthal angle of zero is given by [29, 30] $h = \frac{c}{\Delta n(f) f}$, where $\Delta n(f)$ is the frequency dependent refractive index difference between the plate material and its surroundings. As an example, we consider a topological charge of ± 1 at 0.3 THz, which corresponds to a step height of 1.9 mm. As demonstrated in [18] also higher topological charges can be achieved by using integer multiples of the step height h or multiple equidistant steps along the azimuthal angle. Ultimately, the step height is limited by the minimum 3D-printed layer thickness, which is typically as low as 60 µm.

2.4 Results

In this section, we analyze the performance of a QWP, HWP, q-plate, and SPP as a function of frequency, compare the results to an analytical model as well as numerical simulations, and extract the useful spectral bandwidth. Even though the setup allows to record data up to 1.5 THz, we show data only up to 0.6 THz, because the onset of diffraction above the critical frequency $f_c = c/\Lambda$ leads to meaningless results. In addition, diffraction losses are not properly captured by the CST simulations, because we use periodic boundary conditions. The analytical model is based on $4f$-imaging of a linearly polarized Maxwell-Gaussian beam [31, 32], where the polarization or the phase in the Fourier plane ($2f$) is modulated in accordance with an ideal wave- or phaseplate performance. A design frequency around 0.35 THz is a good compromise between the 3D-printer resolution and the spatial resolution of the THz near-field scanning setup. However, for one example, i.e. a QWP, we demonstrate that the design frequency can be adjusted by a scaling of the design parameters. Finally, we consider an achromatic QWP design based on a two layer structure.

2.4.1 Quarter-waveplate

Generally, a QWP produces an elliptical state of polarization with a left- or right-handed symmetry. To verify the proper functioning of the 3D-printed QWP, we measured the horizontal and the vertical polarization component for different waveplate rotation angles. In the following, a rotation angle of 0° corresponds to the fast axis pointing in $(1, 0, 0)$-direction.

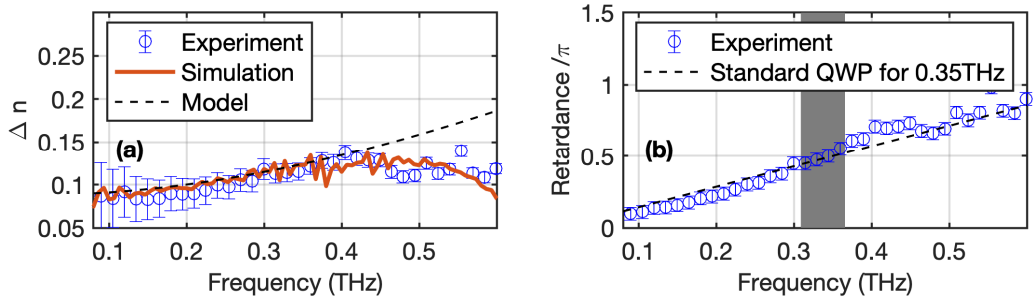

Figure 2.2: (a): Birefringence as function of frequency from experiments, simulations, and the analytic model. (b): Frequency dependent phase retardance normalized to π. The black dashed curve corresponds to a QWP with frequency-independent birefringence. The grey area indicates the frequency range within which the phase shift deviates less than 10 % from the nominal value of $\pi/2$.

Figure 2.2 (a) shows the birefringence as function of frequency. We compare the experimental results with CST-simulations as well as the analytic model based on Eq. (2.1). While the agreement between experiment and CST simulations is close to perfect for the entire frequency range, the analytical model starts deviating above 0.45 THz, where it is no longer valid since it neglects diffraction at the line structures. A key-parameter to characterize the performance of the QWP is the phase retardance between the fast and the slow axis. Figure 2.2 (b) shows the retardance normalized to π as function of frequency with the blue circles referring to the experimental results and the dashed curve corresponding to the analytic model assuming a standard QWP with a frequency independent birefringence. The grey region indicates the frequency range in which the retardance deviates less than $\pm 10\%$ from the ideal value of $\pi/2$. For the experimental results we find a bandwidth of approximately 60 GHz (i.e., a relative bandwidth of 17%), while the analytical model for a standard QWP predicts 70 GHz (i.e, a relative bandwidth of 20%). Thus, the bandwidth of the 3D-printed QWPs is similar to that of a standard commercial QWP. At the design frequency we found that approximately 80% of the incident power is transmitted and we attribute 9% of the losses to Fresnel reflections at the two interfaces and 11% to material absorption [14]. For comparison, the transmitted power for a standard waveplate made of quartz with $n = 2.1$ [28] is 76%.

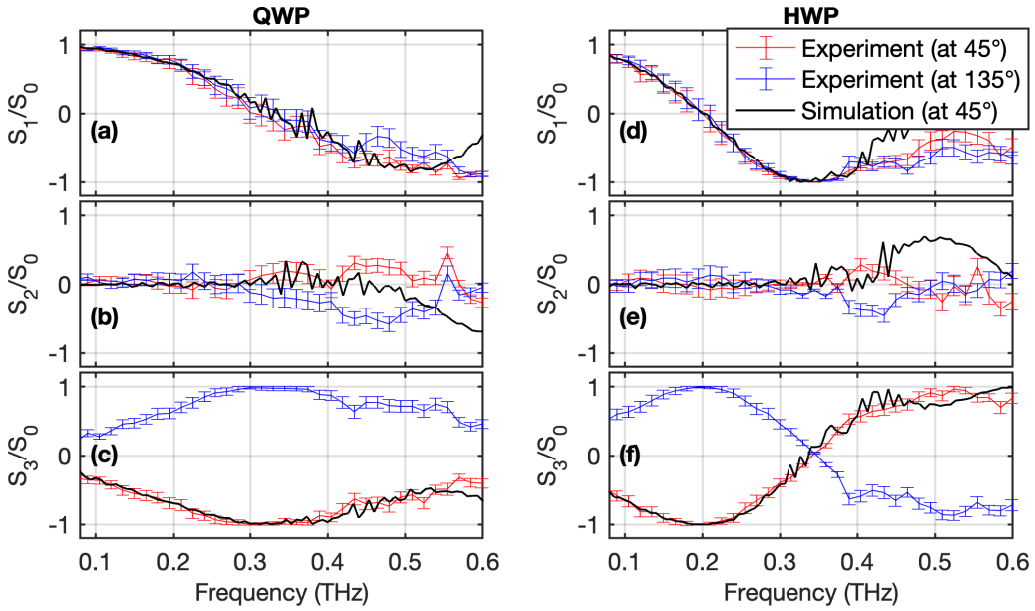

Figure 2.3: Normalized Stokes parameters of a QWP (left column) and a HWP (right column) as function of frequency for two different rotation angles of 45° and 135°. The black curves show the simulation results.

To study the frequency dependent waveplate performance it is useful to consider the Stokes parameters. Note that we can calculate the Stokes parameters from only two measurements, because we have access to the x- and y-component of the electric field. The normalized Stokes parameters are shown in Fig. 2.3 (a)-(c) where the solid black curves correspond to simulation results. We find excellent agreement between experiment and simulations. At the design frequency of 0.35 THz the normalized Stokes parameters of an ideal QWP are $S_1/S_0 = 0$,

$S_2/S_0 = 0$, and $S_3/S_0 = \pm 1$. For a QWP rotation angle of 45° the polarization is left-handed circular (using the source-convention) and we find $S_1/S_0 = -0.23 \pm 0.15$, $S_2/S_0 = 0.20 \pm 0.13$ and $S_3/S_0 = -0.95 \pm 0.04$. For a 135° rotation angle the polarization is right-handed circular with $S_1/S_0 = -0.10 \pm 0.16$, $S_2/S_0 = -0.19 \pm 0.14$ and $S_3/S_0 = 0.98 \pm 0.03$.

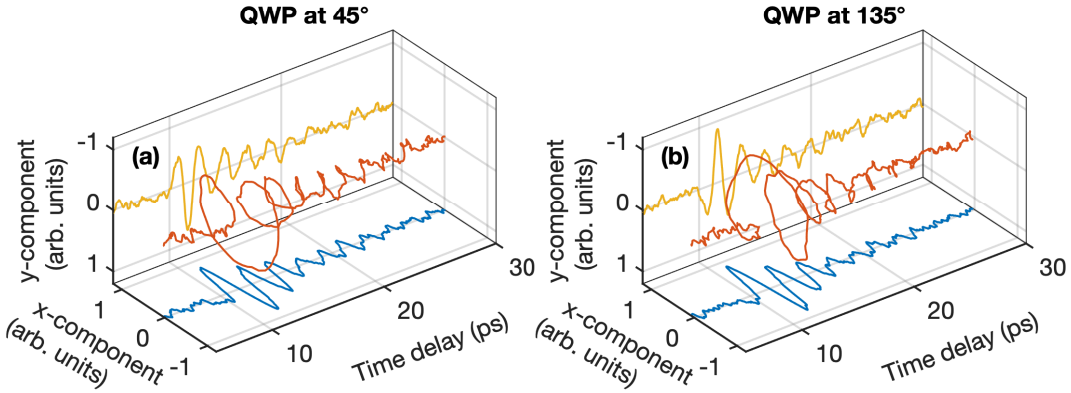

Figure 2.4: Electric field vector horizontal and vertical component of the transmitted signal through a band pass filter and the QWP optimized at 0.5 THz orientated at 45° (a) and at 135° (b).

To change the design frequency, we simply have to scale the design parameters, which we demonstrate by fabrication of a QWP for 0.5 THz. When we combine the waveplate with a bandpass filter also centered at 0.5 THz and with similar bandwidth, we expect perfect circularly polarized THz pulses. At 0.5 THz the filter transmits 80 % of the power and the bandwidth at $1/e^2$ is 0.15 THz. Figure 2.4 shows the measured horizontal and vertical component of the THz electric field for two different orientations of the QWP, namely at 45° (a) and at 135° (b). For better visualization, we applied a moving averaging with a 300 fs time window to the measured signals. While the horizontal components are identical for both orientations, the vertical components show a π phase-shift. As a result, the electric field vector as a function of time follows a left-handed or right-handed spiral, as indicated by the red curves. Hence, we can unambiguously distinguish between left (a) and right (b) circular polarization.

2.4.2 Half-waveplate

Next, we consider a HWP and Fig. 2.5 shows the relative power of the x- (a) and y-polarization (b) as a function of frequency and HWP rotation angle.

At rotation angles of 45° and 135° and for frequencies around 0.35 THz the horizontally polarized component (x) is minimal, whereas the vertical component (y) is maximal. At lower frequencies, the polarization remains predominantly horizontal, and at higher frequencies, diffraction losses at the HWP structure set in. These results indicate the correct functioning of the HWP with a phase retardance of π at the design frequency.

Figure 2.3 (d)-(f) show the normalized Stokes parameters as function of frequency for a HWP rotated to 45° and 135°. For comparison we show the simulated results for a rotation angle of 45° and we find excellent agreement between experimental results and simulations. Around the design frequency of 0.35 THz the polarization is rotated by 90° and the experimentally determined normalized Stokes parameters are $S_1/S_0 = -0.999 \pm 0.001$, $S_2/S_0 = 0.016 \pm 0.006$,

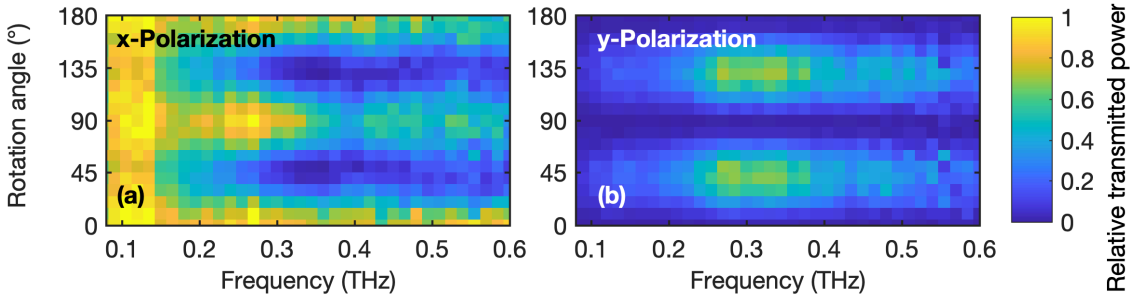

Figure 2.5: Relative transmitted power as function of frequency and rotation angle of the HWP for the horizontal (a) and vertical (b) polarization.

and $S_3/S_0 = 0.035 \pm 0.006$. Note that a HWP performs as a QWP around one half of its design frequency. Indeed, Fig. 2.3 (d)-(f) show normalized Stokes parameters indicative of a QWP around 0.2 THz. This frequency is larger than half of the design frequency, which is explained by the fact that the birefringence increases with frequencies, as shown in Fig. 2.2 (a). The influence of the grating period on the performance of the HWP is of special importance for the design of the q-plates, since they consists of a grating structure with a spatially varying grating period. Therefore, we increased the grating period of the HWP from 0.7 mm to 1.1 mm while keeping all other parameters fixed. For the larger period of 1.1 mm, diffraction losses start already at a frequency around 0.27 THz. Nevertheless, we find a normalized Stokes parameter $S_1/S_0 = -0.987 \pm 0.004$ at 0.3 THz, which indicates that the HWP performs as expected even if diffraction losses decrease the overall transmission.

2.4.3 q-plate

q-plates, depending on their rotation angle, convert an incident linear polarization into either a radial or an azimuthal polarization. If the symmetry axis of the waveplate is parallel (perpendicular) to the incident linear THz polarization, the beam is converted to a radially (azimuthally) polarized beam. To verify the proper functioning of the q-plate we measure, spatially resolved, all three electric field components. We scan an area of 3 mm-by-3 mm in the xy-plane in steps of 0.1 mm (i.e., 31-by-31 points).

Figure 2.6 shows the field distribution of the radial (a) and the azimuthal (b) polarization at a frequency of 0.325 THz. The color-coded amplitude of the transverse electric field is shown together with a vector field indicating the instantaneous direction. The amplitude shows the typical doughnut-shape spatial profile with a singularity at the origin. The three insets show the amplitude distribution of the horizontal, vertical, and longitudinal electric field components in the transverse plane. The horizontal and vertical field components exhibit the characteristic spatial distribution with two lobes, which are π-phase shifted. The asymmetry of the azimuthally polarized beam profile is most likely due to an unwanted tilt of the q-plate. In the supplemental document we present an analytic model assuming a perfect q-plate in a 4f-imaging system and we find good agreement of the resulting spatial polarization pattern with the experimental results. Moreover, for the radially polarized beam, we observe a strong longitudinal electric field component close to the beam center. A detailed description of the longitudinal field for a radial THz pulse can be found in [33]. For an azimuthal polarization, the longitudinal electric field is negligible, instead there is a strong longitudinal magnetic field

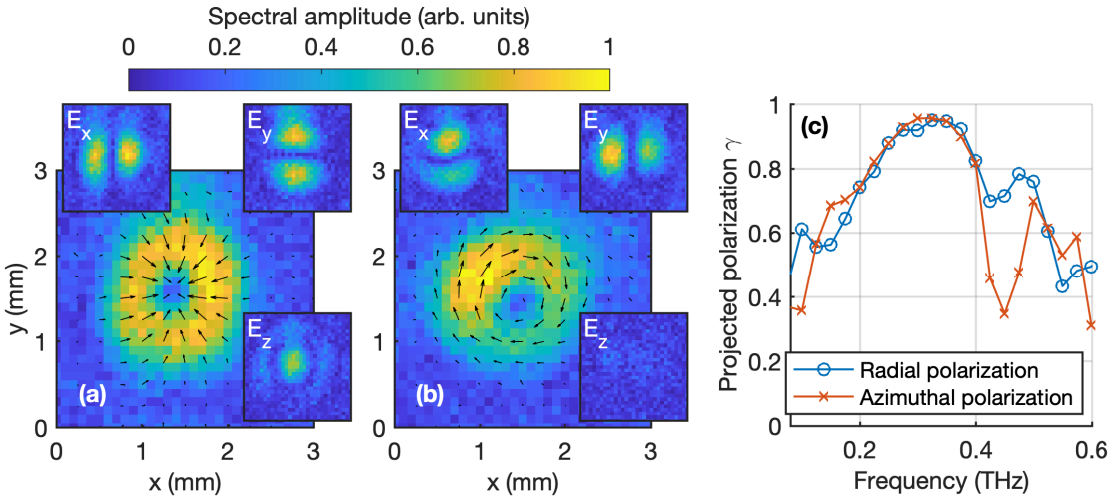

Figure 2.6: Measured radially (a) and azimuthally (b) polarized beams. The main figures show the color-coded amplitude distribution of the transverse electric field. The corresponding vector field $E_x\hat{\mathbf{x}}+E_y\hat{\mathbf{y}}$ is indicated by black arrows at an arbitrary overall phase (where $\hat{\mathbf{x}}$ and $\hat{\mathbf{y}}$ are unit vectors in x- and y-direction). The insets show the field distributions of the horizontal, vertical, and longitudinal electric field components. All plots are shown at a frequency of 0.325 THz and the same scaling is used for all the electric field components. (c): Normalized projected polarization for the radial and azimuthal polarization as function of frequency.

component (see supplemental document). To characterize the polarization state as a function of frequency, we project the measured transverse electric vector field distribution $\mathbf{E}(x_i, y_j, f)$ onto an ideal mode of the same polarization state

$$\gamma(f) = \sum_{i,j} \mathbf{E}(x_i, y_j, f) \cdot \mathbf{E}_0 \frac{\sqrt{2(x_i^2 + y_j^2)}}{w_0(f)} \exp\left[-\frac{x_i^2 + y_j^2}{w_0^2(f)}\right], \tag{2.2}$$

where the sum runs over all pixels and the amplitude of $\mathbf{E}_0$ is chosen such that a perfect radial or azimuthal polarized mode yields $\gamma(f) = 1$. The global phase of the electric field distribution $\mathbf{E}(x_i, y_j, f)$ is adjusted for a maximum $\gamma(f)$. The beam waist $w_0(f)$ is obtained from a fit to the measured amplitude distribution and we found $w_0(f) = 600\,\mu\text{m}\frac{0.325\,\text{THz}}{f}$ at the frequency f. Figure 2.6 (c) shows the projected polarization, γ, as function of frequency. A similar performance is found for both q-plate orientations, with the maximum projected polarization of 0.95 at 0.325 THz being close to the ideal value of 1. For frequencies between 0.275 THz and 0.375 THz we find a projected polarization larger than 0.9, which indicates that the q-plate works as intended in this frequency range. At lower and higher frequencies the projected polarization decreases rapidly.

2.4.4 Spiral phaseplate

SPPs are used to generate beams with angular momentum without affecting the state of polarization. Hence, the transmitted THz pulse remains horizontally polarized, but depending on the

spatial position the wavefront is retarded. We measured the horizontal electric field component in the transverse plane in an area of 3 mm-by-3 mm in steps of 0.1 mm (i.e., 31-by-31 points).

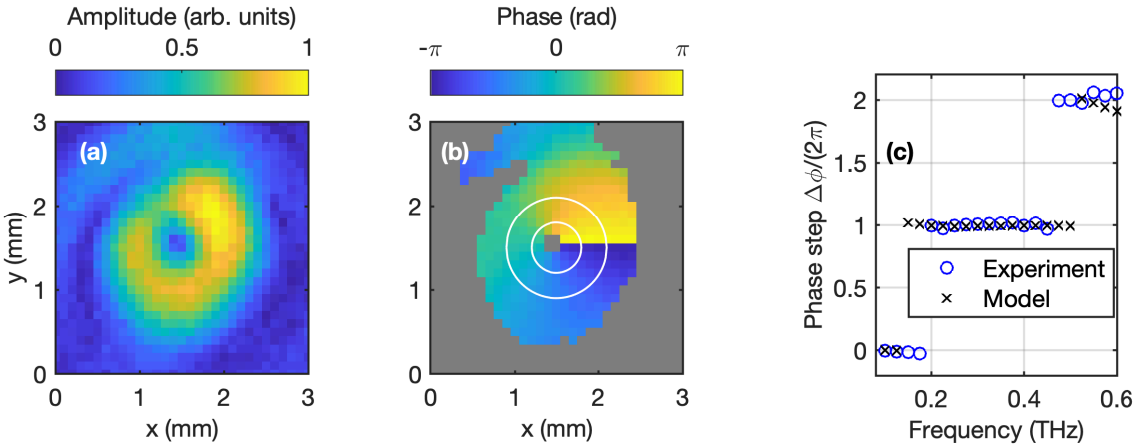

Figure 2.7: Amplitude distribution of the horizontal polarization (a) for a spiral phase plate with a topological charge of ±1 and the corresponding phase (b) for a frequency of 0.3 THz. For pixels with an amplitude of less than 30 % of the peak amplitude, the color-coded phase is greyed out. The white circles enclose the region used to extract the phase as a function of azimuthal angle. (c): Phase step height in units of 2π as function of frequency.

Figure 2.7 shows the amplitude of the horizontal field component at 0.3 THz (a) and the corresponding phase (b). The phase is shown only when the amplitude at the same pixel is larger that 30% of the maximum amplitude. The amplitude distribution shows a doughnut-shape spatial profile due to a singularity at the beam center. The color-coded phase distribution indicates that the phase retardance decreases linearly by 2π as function of the azimuthal angle around the beam center and exhibits a phase step $\Delta\phi$ at 0°. Due to the layer resolution of 0.1 mm, which is ten times smaller than the considered wavelength, no discrete phase steps are observed. Figure 2.7 (c) shows the phase step $\Delta\phi$ as function of frequency. The phase was averaged over the radial direction around the amplitude maximum, i.e., between $r = 0.3$ mm and 0.6 mm, as indicated by the two white circles in Fig. 2.7 (b). The phase step $\Delta\phi$ normalized to 2π corresponds to the topological charge. Note that $\Delta\phi$ has to be an integer multiple of 2π, because the unwrapped phase of electromagnetic fields must be continuous. For comparison, we used the same recipe to calculate the phase step from an analytical model. In both cases, we find discrete steps when plotting the phase step as function of frequency. When we use alternative recipes to extract the phase step, the overall picture remains the same, except the exact frequencies at which the topological charge changes are found to shift to somewhat lower or higher frequencies. On average, we find the first two steps at 0.15 THz and at 0.45 THz. These frequencies corresponds to 0.5 times and 1.5 times the design frequency, respectively. We also tested two different SPPs with a topological charge of ±2 at 0.3 THz and found similar performance.

2.4.5 Achromatic waveplates

For broadband THz applications, for instance using a femtosecond laser pumped $LiNbO_3$ source, the useful bandwidth of the waveplates presented above is not sufficiently broad. Hence, we aim at increasing the bandwidth by using an achromatic waveplate design. As an example, we discuss a QWP with an achromatic design consisting of two layers where the fast axis of the first layer is aligned with the slow axis of the second layer. Naturally, this design is motivated by commercially available achromatic waveplates. To optimize the performance, we tune the two grating heights as well as the two periods. Hence, we have a four dimensional parameter space, which allows us to optimize the structure for broadband performance. For optimization we use a genetic optimization algorithm (in Matlab) and minimize the cost function $\int \mathrm{d}f|\varphi(f) - \pi/2|$ for $f \in [0.23\,\mathrm{THz}, 0.4\,\mathrm{THz}]$, where $\varphi(f)$ is the phase retardance based on Eq. (2.1). We impose boundaries to the optimization: 1) The grating period is limited to the range between 300 µm and 675 µm, where the lower limit is due to the 3D-printer resolution and the upper limit is calculated from the onset of higher order diffraction, and to integer multiples of the accuracy of the 3D-printer, i.e., 12.5 µm. 2) The grating height is restricted to values lower than 10 mm, in order to be able to mount the achromatic QWP in a standard rotation mount, and to integer multiples of the minimum layer thickness, i.e., 100 µm. After successful optimization we find the following design parameters: The first grating period is 412.5 µm and has a height of 5.8 mm. The second grating has a grating period of 662.5 µm and a height of 3.5 mm. Between the two layers we include a 1 mm thick spacer layer for mechanical support of the second layer. Note that the achromatic structure was printed as a single part.

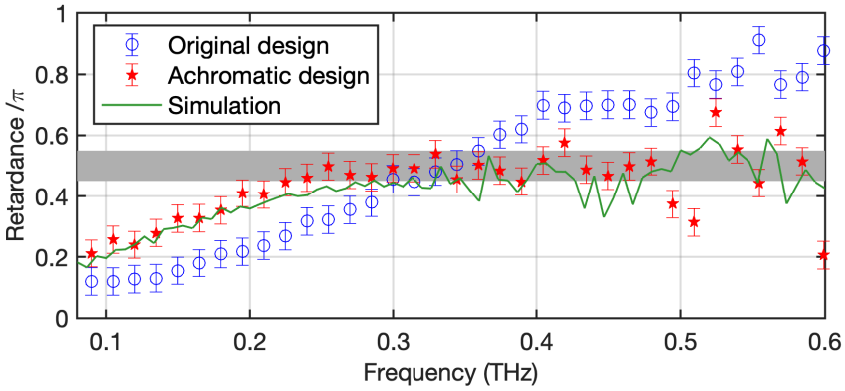

Figure 2.8: Measured retardance as function of frequency for the original one layer QWP and for the optimized achromatic design. The blue circles corresponds to the results already shown in Fig. 2.2 (b) and the green curve corresponds to the simulation of the achromatic design. The grey area indicates a 10 % deviation from the ideal retardance of $\pi/2$.

Figure 2.8 compares the retardance of the single layer QWP with the optimized achromatic design. The grey area indicates a 10% deviation from the ideal retardance of $\pi/2$. The experimental data are in good agreement with the double layer simulation results. The bandwidth of the achromatic design is more than two times larger than that of the single layer design. Diffraction losses limit the useful frequency range up to approximately 0.5 THz. We would like to stress that the bandwidth can be even further increased by using more than two layers and that the same design principles can be applied to HWPs and q-plates.

2.5 Conclusions

We experimentally evaluated 3D-printed QWP, HWP, q-plate, and SPP for broadband THz applications and compared the results to finite element simulations. We demonstrated that 3D-printed wave- and phaseplates, using fused deposition modeling, are not limited to a frequency range < 0.2 THz, as indicated by previous publications. By using a broadband THz source with a useful spectral range from 0.08 THz to 1.5 THz we showed that 3D-printed waveplates perform as expected up to about 0.6 THz. We found that all waveplates have bandwidths similar to commercial products and we demonstrated a route to achieve broadband performance, so that 3D-printed waveplates can also be used in combination with few-cycle THz pulses. Our results demonstrate that 3D-printing is a cost-efficient and time-saving fabrication method for a variety of narrow- and broadband wave- and phaseplates.

2.6 Supplemental document

2.6.1 Experimental setup

A schematic of the setup is shown in Fig. 2.9. The THz pulse generation and detection is based on a femtosecond erbium fiber laser (*Femto Fiber Pro* by *Toptica*), which provides pulses with a duration of less than 100 fs, a repetition rate of 80 MHz, and an average output power of 130 mW at around 780 nm. The laser output is split with one part being sent to the emitter and the other to the electro-optic detector. The ratio can be adjusted by a half waveplate. Pulses sent to the emitter are attenuated to 40 mW in order to prevent damage of the GaAs photo-conductive antenna (PCA) and are focused by a 10 mm focal length lens. For a lock-in detection scheme, the bias voltage of the PCA is modulated with 800 kHz. Specifically, the 2.4 V reference signal from the lock-in amplifier (*HF2LI* from *Zurich Instruments*) is amplified to 120 V by a power amplifier (*Falco Systems*). The THz pulses are imaged by four off-axis parabolic mirrors enclosed in a dry-air box to an intermediate image plane. Even though the PCA is orientated to produce horizontally polarized THz pulses, we use an additional wire grid polarizer in order to better define the polarization direction. An additional 4f, lens-based imaging system (aspheric lenses with $f_1 = 50$ mm and $f_2 = 25$ mm, each with a diameter of two inches) is used to incorporate the wave- and phaseplates and to direct the modified THz pulses to the electro-optic detection unit.

The average power of the probe pulses is approximately 4 mW, which is ultimately limited by the damage threshold of the ZnTe detection crystal. They can be delayed with respect to the pulses sent to the PCA by a motorized linear stage (*LMS-80* from *Micos*) with a maximum travel range of 120 mm. We measure the horizontal and the vertical components of the THz signal with a $\langle 110 \rangle$-cut and the longitudinal component with a $\langle 100 \rangle$-cut ZnTe crystal. The 100 µm thick ZnTe crystals are mounted on a 2.5 mm thick c-cut sapphire substrate to avoid the appearance of Fabry-Perot replica within the measurement window. The probe beam is focused to a spot size of about 20 µm by a lens with a focal length of approximately 10 mm. It is reflected by the dielectric coating on the front side of the crystals and co-propagates with the THz-pulse on its way back through the crystal. The reflected pulses are directed to a standard electro-optic detection unit consisting of a quarter-waveplate, a polarizing beam splitter, and a balanced photo-detector pair (*Thorlabs*). The sampling crystal is mounted on motorized x-, y- and z-stages and allows us to measure all three electric field components within a defined

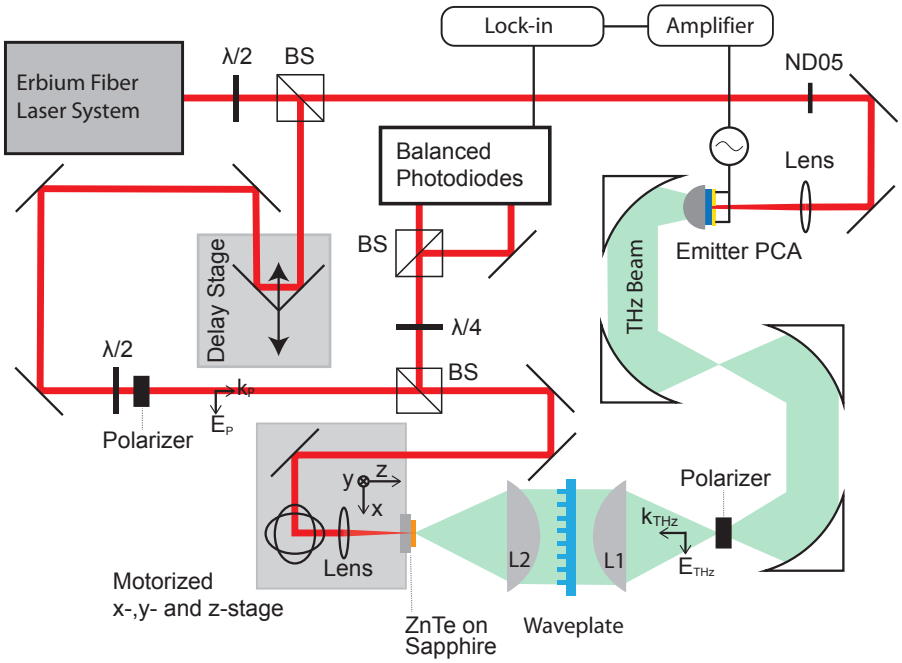

Figure 2.9: Schematic of the setup (top view): THz pulses are generated by a PCA and detected in a ZnTe electro-optic sampling crystal. The THz-pulses are horizontally polarized and transported to the detector by four off-axis parabolic mirrors and two THz lenses (L1 and L2). The detector is mounted on motorized x-, y- and z-stages.

volume around the focal position with a spatial resolution of 20 µm. Each time delay scan covers a range between 5 mm to 10 mm corresponding to a time window between 33 ps and 67 ps, with a resolution of 33.4 fs.

2.6.2 Polarization sensitive detection

Both ZnTe crystals were rotated by 360 degrees while recording the electro-optic signal. For the ⟨110⟩-cut ZnTe crystal the intensity difference ΔI measured by the balance photo detector as a function of the rotation angle is given by [34]

$$\Delta I(\alpha, \phi) = I_p \frac{\omega n^3 E_{THz} r_{41} L}{2c} \left(\cos\alpha \sin 2\phi + 2 \sin\alpha \cos 2\phi\right), \tag{2.3}$$

with the probe intensity I_p, the crystal thickness L, the speed of light in vacuum c, the carrier frequency of the probe pulse ω, the electric field strength of the THz pulse E_{THz}, the unperturbed refractive index n, and the relevant electro-optic tensor element r_{41}. The angle between the polarization direction of the THz beam and the (001)-crystal axis is α and the angle between the polarization direction of the probe beam and the (001)-crystal axis is ϕ. For the x-polarized air-reference THz pulse we have $\alpha = \phi - \pi/2$. Similarly, we find for the ⟨100⟩-cut ZnTe crystal

$$\Delta I(\phi) = I_p \frac{\omega n^3 E_{THz} r_{41} L}{c} \sin 2\phi. \tag{2.4}$$

Note that equations (2.3) and (2.4) indicate that the maximum detection efficiency for the horizontal, vertical, and longitudinal field components is the same.

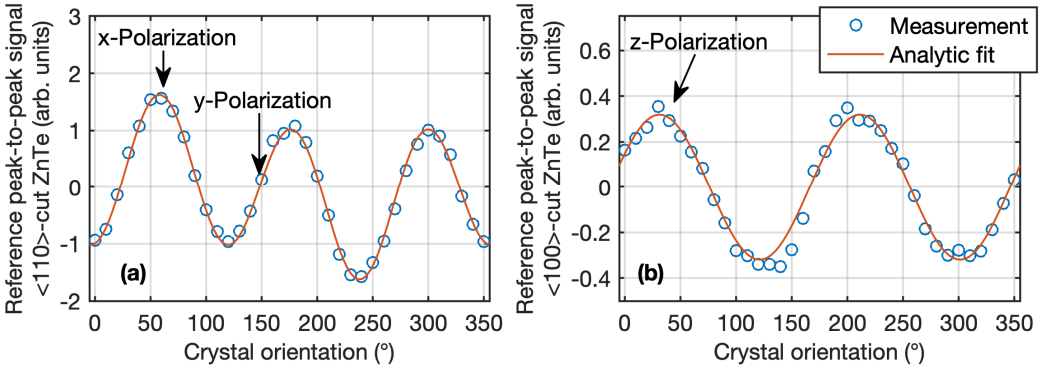

Figure 2.10: Measured signal as a function of rotation angle for a ⟨110⟩-cut (a) and a ⟨100⟩-cut (b) ZnTe crystal. The solid curves represent fits based on Eqs. (2.3) and (2.4). The arrows indicate the crystal orientations, which we used to measure the x-, y- and z-component of the THz electric field.

Figure 2.10 shows the measured signal as function of rotation angle for a ⟨110⟩-cut (a) and a ⟨100⟩-cut (b) ZnTe crystal. The sign convention of the peak-to-peak signal is as follows: When the signal minimum is at an earlier time-delay than the signal maximum we use a positive sign - otherwise the sign is set to be negative. The solid curves correspond to a fit to Eqs. (2.3) and (2.4). From this fit we find that x-polarized THz electric field component must be measured at 58°, while the y-polarized component is measured at 148°. Furthermore, the THz polarization in z-direction is to be measured at 32°. These angles are used for all following measurements.

2.6.3 Field pattern of the reference beam

The THz beam without any wave- or phaseplate was fully characterized for reference. Figure 2.11 (a) shows the corresponding measurement results, i.e., the amplitude of the transverse electric field and the three polarization components in a plane perpendicular to the propagation direction at an arbitrary frequency of 0.325 THz. While the horizontal component clearly dominates, we also find a nonzero longitudinal component. Specifically, the longitudinal component shows two lobes, which are π-phase shifted with respect to each other. For comparison, Fig. 2.11 (b) shows the analytical field components of a Maxwell-Gauss beam as described in [31, 32] for a frequency of 0.325 THz and a beam waist of 600 µm. Except for the ring structure around the main central part of the beam, which is a result of the finite size optics in the imaging system and/or imperfections of the PCA, we find good agreement between the measurement and analytical model, specifically the shape of the longitudinal component is well reproduced.

2.6.4 Details on the different wave- and phaseplate measurements

QWP and HWP for 0.5 THz

Figure 2.12 shows the measured Stokes parameters for a QWP (left) and a HWP (right) for a design frequency of 0.5 THz. We find good agreement between experiment and simulations,

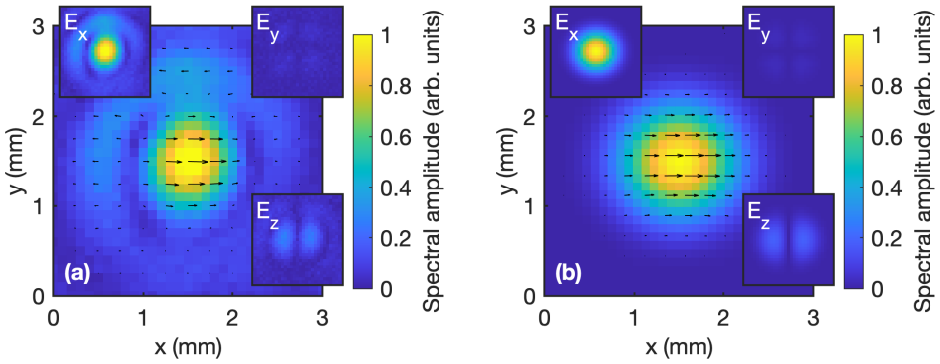

Figure 2.11: Experimental measurement (a) and analytical model (b) of the reference beam. The main figures show the color-coded amplitude distribution in the transverse plane. The corresponding vector field is indicated by black arrows at an arbitrary overall phase. The insets show the spectral amplitudes of the horizontal, vertical, and longitudinal field components. All plots are shown at a frequency of 0.325 THz and use the same scaling.

specifically around the design frequency. For these measurements we did not use a bandpass filter. But for reference, we also included the transmission curve of the bandpass filter in Fig. 2.12 (b) and (e) which was used for the results presented in the main text in Fig. 2.4.

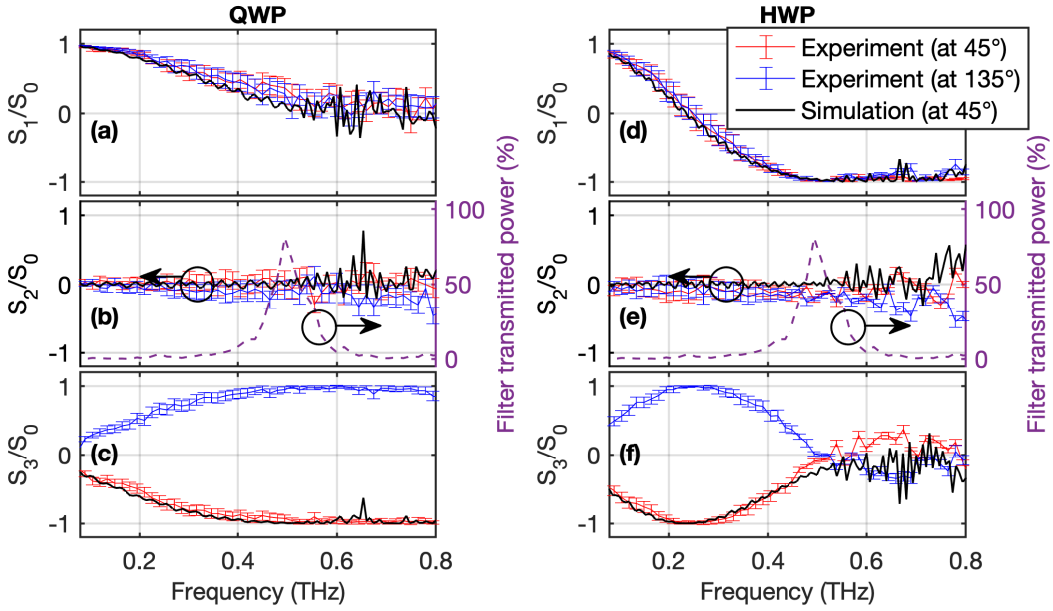

Figure 2.12: Measured and simulated Stokes parameters for a QWP and a HWP designed for a frequency of 0.5 THz. The transmitted power of the bandpass filter is included in (b) and (e).

Analytical model for *q*-plates

The analytical model is based on the Maxwell-Gauss beam already introduced above. Since the *q*-plate is placed at the back focal plane of the second lens in the 4f imaging setup, the

transverse electric field distribution in the detection plane is calculated via a two-dimensional Fourier transformation. At the Fourier-plane the beam is modulated by a transfer matrix M, such that

$$\begin{pmatrix} E_{x,out}(r,\varphi,\omega) \\ E_{y,out}(r,\varphi,\omega) \end{pmatrix} = M(r,\varphi,\omega) \begin{pmatrix} E_{x,in}(r,\varphi,\omega) \\ E_{y,in}(r,\varphi,\omega) \end{pmatrix}. \tag{2.5}$$

The z-component of the electric field is calculated from the third Maxwell equation, $\boldsymbol{\nabla}\cdot\mathbf{E} = 0$, to $E_z = \frac{c}{2\pi i f_0}(\partial_x E_x + \partial_y E_y)$. Note that at the design frequency the q-plate acts locally as a HWP with an axis orientation of $\varphi/2$, where φ is the polar angle. This corresponds to a transfer matrix

$$M = \begin{pmatrix} i\cos\varphi & i\sin\varphi \\ i\sin\varphi & -i\cos\varphi \end{pmatrix} \tag{2.6}$$

for generating radial polarization and

$$M = \begin{pmatrix} -i\sin\varphi & i\cos\varphi \\ i\cos\varphi & i\sin\varphi \end{pmatrix} \tag{2.7}$$

for generating azimuthal polarization. Figure 2.13 shows the results of the analytic model for a radial (a) and an azimuthal (b) polarization. While the main frame shows a false color image of the amplitude of the transverse electric field, the three insets show the amplitudes of the three polarization components. When going from radial to azimuthal polarization the x- and y-electric field components are interchanged. Somewhat more striking is the difference in the longitudinal component. While the radially polarized beam possesses a strong longitudinal electric field component, this is absent in the azimuthally polarized mode.

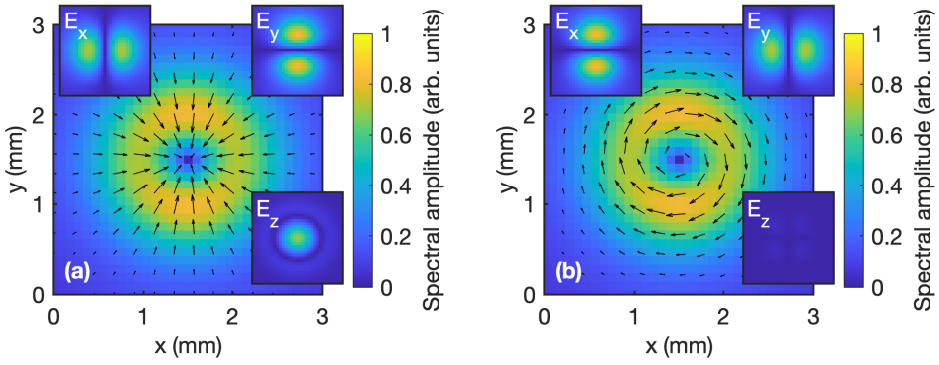

Figure 2.13: Beam at the focus based on an analytic model at 0.325 THz using a Maxwell-Gauss beam and assuming a 4f-imaging system with perfect performance of the q-plate for generating radial (a) and azimuthal (b) polarization.

From the measurement of all three electric field components, we can calculate the magnetic flux based on

$$\boldsymbol{\nabla} \times \mathbf{E}(\mathbf{r},\omega) = -\mathrm{i}\omega\mathbf{B}(\mathbf{r},\omega). \tag{2.8}$$

We assume $\partial_z E_x = -\mathrm{i}k_0 E_x$ and $\partial_z E_y = -\mathrm{i}k_0 E_y$, which is justified since we measure at the focus where the longitudinal variation of the electric field is mainly determined by the wave vector k_0. Figure 2.14 shows the calculated x-, y-, and z-components of the magnetic

flux at 0.325 THz for the radial polarization (top row) and azimuthal polarization (bottom row). Note that the spatial amplitude distribution of the magnetic field components of the radial polarization is similar to the amplitude distribution of the electric field components of the azimuthal polarization (and vice versa). Especially, the azimuthal polarization shows a strong magnetic component in the longitudinal direction, which explains the absence of the longitudinal electric field component in Fig. 2.13.

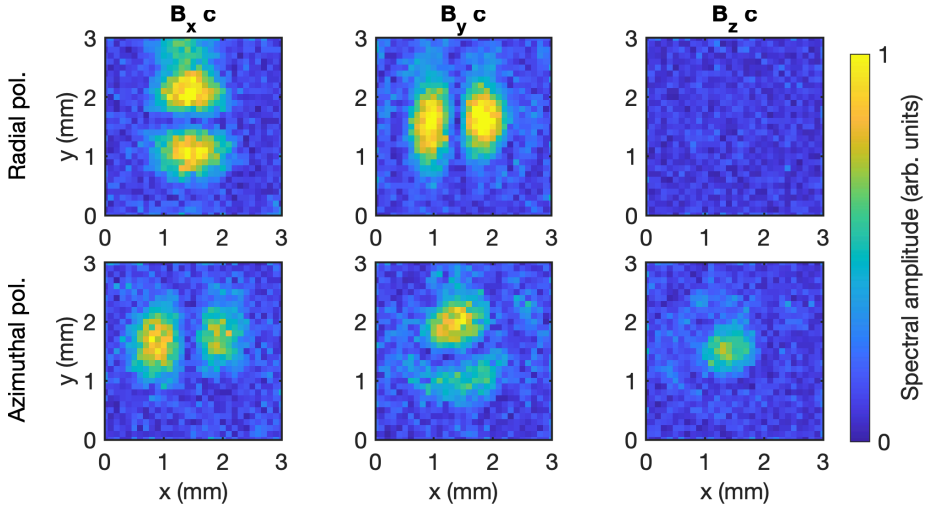

Figure 2.14: Calculated magnetic flux components based on the measured electric field components in the focal plane at a frequency of 0.325 THz. Top: radial polarization and bottom: azimuthal polarization. All three components are multiplied by c and the same scaling factor as for the electric fields is used.

Spiral phaseplate

For completeness, we show the electric field amplitude as well as the amplitudes of the three electric field components for a THz beam which passed through a spiral phaseplate. Figure 2.15 (a) shows the measured and (b) the analytical results and we find good agreement. As expected, the horizontal component is dominant as a spiral phaseplate does not affect the state of polarization. The black arrows indicate the instantaneous electric field direction at an arbitrary overall phase, and reveal that there are two spatially separated contributions which are π-phase shifted and spiral around the center. Here, the analytical model at the design frequency is based on the transfer matrix

$$M = \begin{pmatrix} \mathrm{e}^{i\varphi} & 0 \\ 0 & \mathrm{e}^{i\varphi} \end{pmatrix}, \tag{2.9}$$

where φ is the polar angle. Hence, the matrix M describes a linearly increasing phase with a total phase shift of 2π after one revolution.

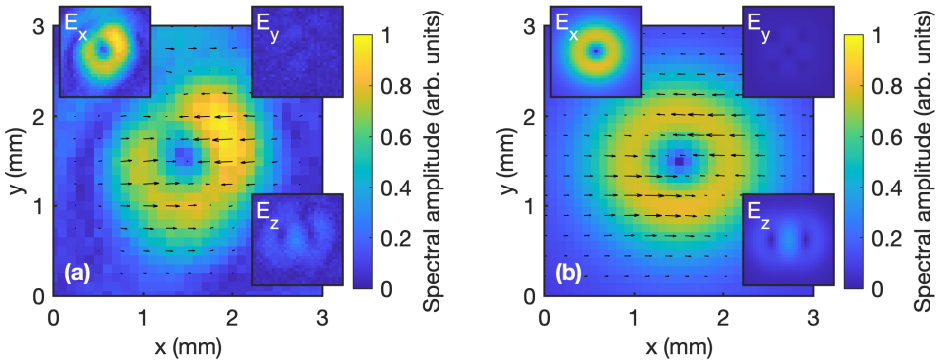

Figure 2.15: Experimental (a) and analytic model (b) of a beam with angular momentum. The main figures show the color-coded amplitude distribution of the transverse electric field. The corresponding vector field is indicated by black arrows at an arbitrary overall phase. The insets show the spectral amplitudes of the horizontal, vertical, and longitudinal electric field components for a frequency of 0.3 THz and the same scaling is used for all electric field components.

Bibliography

[1] R. Piesiewicz, M. Jacob, M. Koch, J. Schoebel, and T. Kurner, "Performance Analysis of Future Multigigabit Wireless Communication Systems at THz Frequencies With Highly Directive Antennas in Realistic Indoor Environments", IEEE J. Sel. Top. Quantum Electron. **14**, 421–430 (2008), https://doi.org/10.1109/JSTQE.2007.910984.

[2] J. Federici and L. Moeller, "Review of terahertz and subterahertz wireless communications", J. Appl. Phys. **107**, 111101 (2010), https://doi.org/10.1063/1.3386413.

[3] T. Kleine-Ostmann and T. Nagatsuma, "A review on terahertz communications research", J. Infrared, Millimeter, Terahertz Waves **32**, 143–171 (2011), https://doi.org/10.1007/s10762-010-9758-1.

[4] Z. Chen, X. Ma, B. Zhang, Y. Zhang, Z. Niu, N. Kuang, W. Chen, L. Li, and S. Li, "A survey on terahertz communications", China Commun. **16**, 1–35 (2019), https://ieeexplore.ieee.org/document/8663550.

[5] I. Amenabar, F. Lopez, and A. Mendikute, "In introductory review to THz non-destructive testing of composite mater", J. Infrared, Millimeter, Terahertz Waves **34**, 152–169 (2013), https://doi.org/10.1007/s10762-012-9949-z.

[6] M. Neshat and N. P. Armitage, "Developments in THz Range Ellipsometry", J. Infrared, Millimeter, Terahertz Waves **34**, 682–708 (2013), https://doi.org/10.1007/s10762-013-9984-4.

[7] M. Naftaly, N. Vieweg, and A. Deninger, "Industrial Applications of Terahertz Sensing: State of Play", eng, Sensors **19**, 4203 (2019), https://pubmed.ncbi.nlm.nih.gov/31569789%20https://www.ncbi.nlm.nih.gov/pmc/articles/PMC6806174/.

[8] G. Tzydynzhapov, P. Gusikhin, V. Muravev, A. Dremin, Y. Nefyodov, and I. Kukushkin, "New Real-Time Sub-Terahertz Security Body Scanner", J. Infrared, Millimeter, Terahertz Waves **41**, 632–641 (2020), https://doi.org/10.1007/s10762-020-00683-5.

[9] J. Fabiańska, G. Kassier, and T. Feurer, "Split ring resonator based THz-driven electron streak camera featuring femtosecond resolution", Sci. Rep. **4**, 5645 (2014), https://doi.org/10.1038/srep05645.

[10] E. A. Nanni, W. R. Huang, K. H. Hong, K. Ravi, A. Fallahi, G. Moriena, R. J. D. Miller, and F. X. Kärtner, "Terahertz-driven linear electron acceleration", Nat. Commun. **6**, 8486 (2015), https://doi.org/10.1038/ncomms9486.

[11] D. Zhang, A. Fallahi, M. Hemmer, X. Wu, M. Fakhari, Y. Hua, H. Cankaya, A.-L. Calendron, L. E. Zapata, N. H. Matlis, and F. X. Kärtner, "Segmented terahertz electron accelerator and manipulator (STEAM)", Nat. Photonics **12**, 336–342 (2018), https://doi.org/10.1038/s41566-018-0138-z.

[12] D. Rohrbach, Z. Ollmann, M. Hayati, C. B. Schroeder, W. P. Leemans, and T. Feurer, "THz-driven split ring resonator undulator", Phys. Rev. Accel. Beams **24**, 010703 (2021), https://doi.org/10.1103/PhysRevAccelBeams.24.010703.

[13] X.-P. Dong, J.-R. Cheng, F. Fan, S.-T. Xu, X.-H. Wang, and S.-J. Chang, "Wideband sub-THz half-wave plate using 3D-printed low-index metagratings with superwavelength lattice", Opt. Express **27**, 202–211 (2019), https://doi.org/10.1364/oe.27.000202.

[14] S. F. Busch, M. Weidenbach, J. C. Balzer, and M. Koch, "THz Optics 3D Printed with TOPAS", J. Infrared, Millimeter, Terahertz Waves **37**, 303–307 (2016), https://doi.org/10.1007/s10762-015-0236-7.

[15] E. Castro-Camus, M. Koch, and A. I. Hernandez-Serrano, "Additive manufacture of photonic components for the terahertz band", J. Appl. Phys. **127**, 210901 (2020), https://doi.org/10.1063/1.5140270.

[16] A. D. Squires, E. Constable, and R. A. Lewis, "3D Printed Terahertz Diffraction Gratings And Lenses", J. Infrared, Millimeter, Terahertz Waves **36**, 72–80 (2015), https://doi.org/10.1007/s10762-014-0122-8.

[17] M. Weidenbach, D. Jahn, A. Rehn, S. F. Busch, F. Beltrán-Mejía, J. C. Balzer, and M. Koch, "3D printed dielectric rectangular waveguides, splitters and couplers for 120 GHz", Opt. Express **24**, 28968–28976 (2016), https://doi.org/10.1364/oe.24.028968.

[18] X. Wei, C. Liu, L. Niu, Z. Zhang, K. Wang, Z. Yang, and J. Liu, "Generation of arbitrary order Bessel beams via 3D printed axicons at the terahertz frequency range", Appl. Opt. **54**, 10641–10649 (2015), https://doi.org/10.1364/ao.54.010641.

[19] J. Gospodaric, A. Kuzmenko, A. Pimenov, C. Huber, D. Suess, S. Rotter, and A. Pimenov, "3D-printed phase waveplates for THz beam shaping", Appl. Phys. Lett. **112**, 221104 (2018), http://dx.doi.org/10.1063/1.5027179.

[20] A. A. Sirenko, P. Marsik, L. Bugnon, M. Soulier, C. Bernhard, T. N. Stanislavchuk, X. Xu, and S.-W. Cheong, "Total Angular Momentum Dichroism of the Terahertz Vortex Beams at the Antiferromagnetic Resonances", Phys. Rev. Lett. **126**, 157401 (2021), https://link.aps.org/doi/10.1103/PhysRevLett.126.157401.

[21] A. I. Hernandez-Serrano, E. Castro-Camus, and D. Lopez-Mago, "q-plate for the Generation of Terahertz Cylindrical Vector Beams Fabricated by 3D Printing", J. Infrared, Millimeter, Terahertz Waves **38**, 938–944 (2017), https://doi.org/10.1007/s10762-017-0396-8.

[22] A. Bitzer, H. Merbold, A. Thoman, T. Feurer, H. Helm, and M. Walther, "Terahertz near-field imaging of electric and magnetic resonances of a planar metamaterial", Opt. Express **17**, 3826–3834 (2009), http://www.opticsexpress.org/abstract.cfm?URI=oe-17-5-3826.

[23] S. Bagiante, F. Enderli, J. Fabiańska, H. Sigg, and T. Feurer, "Giant electric field enhancement in split ring resonators featuring nanometer-sized gaps", Sci. Rep. **5**, 8051 (2015), https://doi.org/10.1038/srep08051.

[24] M. Scheller, C. Jördens, and M. Koch, "Terahertz form birefringence", Opt. Express **18**, 10137–10142 (2010), https://doi.org/10.1364/oe.18.010137.

[25] B. Zhang and Y. Gong, "Achromatic terahertz quarter waveplate based on silicon grating", Opt. Express **23**, 14897–14902 (2015), https://doi.org/10.1364/oe.23.014897.

[26] P. Lalanne and M. Hutley, *Artificial media optical properties - subwavelength scale* (Marcel Dekker, 2003), pp. 62–71, https://www.researchgate.net/publication/239767043_Artificial_Media_Optical_Properties-Subwavelength_Scale.

[27] *CST – Computer Simulation Technology*, (2019) https://www.cst.com (visited on 06/08/2021).

[28] J.-B. Masson and G. Gallot, "Terahertz achromatic quarter-wave plate", Opt. Lett. **31**, 265–267 (2006), https://doi.org/10.1364/ol.31.000265.

[29] M. W. Beijersbergen, R. P. Coerwinkel, M. Kristensen, and J. P. Woerdman, "Helical-wavefront laser beams produced with a spiral phaseplate", Opt. Commun. **112**, 321–327 (1994), https://doi.org/10.1016/0030-4018(94)90638-6.

[30] K. Miyamoto, K. Suizu, T. Akiba, and T. Omatsu, "Direct observation of the topological charge of a terahertz vortex beam generated by a Tsurupica spiral phase plate", Appl. Phys. Lett. **104**, 261104 (2014), http://dx.doi.org/10.1063/1.4886407.

[31] L. W. Davis, "Theory of electromagnetic beams", Phys. Rev. A **19**, 1177–1179 (1979), https://link.aps.org/doi/10.1103/PhysRevA.19.1177.

[32] J. P. Barton and D. R. Alexander, "Fifth-order corrected electromagnetic field components for a fundamental Gaussian beam", J. Appl. Phys. **66**, 2800–2802 (1989), https://doi.org/10.1063/1.344207.

[33] M. J. Cliffe, A. Rodak, D. M. Graham, and S. P. Jamison, "Generation of longitudinally polarized terahertz pulses with field amplitudes exceeding 2 kV/cm", Appl. Phys. Lett. **105**, 191112 (2014), https://doi.org/10.1063/1.4901904.

[34] P. C. M. Planken, H.-K. Nienhuys, H. J. Bakker, and T. Wenckebach, "Measurement and calculation of the orientation dependence of terahertz pulse detection in ZnTe", J. Opt. Soc. Am. B **18**, 313–317 (2001), https://doi.org/10.1364/josab.18.000313.

Chapter 3

THz-driven split ring resonator undulator

David Rohrbach[1], Zoltan Ollmann[1], Mozhgan Hayati[1], Carl B. Schroeder[2], Wim P. Leemans[3], and Thomas Feurer[1]

[1]Institute of Applied Physics, University of Bern, Sidlerstrasse 5, 3012 Bern, Switzerland
[2]Lawrence Berkeley National Laboratory, Berkeley 94720, CA, USA
[3]Deutsches Elektronen-Synchrotron (DESY), 22607 Hamburg, Germany

This work was published in Phys. Rev. Accel. Beams **24**, 010703 (2021)

Abstract
We propose a short period undulator based on the electromagnetic field pattern in a THz-driven split ring resonator structure. An analytical model is developed that allows to assess the key performance parameters of the undulator and to estimate the emitted radiation spectrum. Different geometric configurations are compared in detail using numerical simulations. A 100 MeV electron bunch with 5 pC charge is shown to emit narrow band 83 eV photon pulses with a peak brightness of approximately 10^{19} photons/(s mrad^2 mm^2 0.1% BW) when passing through the 100 mm long undulator with a 1 mm period.

3.1 Introduction

Undulators are generally composed of a periodic, alternating array of normal- or superconducting electromagnets, permanent magnets or hybrid magnets [1–3]. Relativistic electron bunches propagating through an undulator are forced on an oscillatory orbit, which leads to emission of intense narrow band radiation pulses [4]. The emission can range from THz to hard x-ray photon energies and is determined by electron kinetic energy and undulator period. Typical undulator periods are tens of millimeters, magnetic field strengths range from about one Tesla

to more than ten Tesla for superconducting magnets, and undulators in free electron lasers can be tens to hundreds of meters in length [5, 6].

Decreasing the undulator period is generally beneficial, because less electron energy is required to produce a given photon energy. Likewise, the emitted photon energy would increase for a given electron energy. In addition, smaller scale undulators in combination with miniaturized accelerators are suitable for the development of compact future light sources. Such advanced accelerators are for example based on laser wakefields in plasma [7] or laser-driven dielectric structures [8]. In the past, several efforts to reduce the periodicity of static magnetic field patterns have been made and values as low as 15 mm [9–12] were achieved. Further reduction down to about 100 µm was realized with laser micro-machined permanent magnets [13] or electromagnets [14]. The peak magnetic field in these devices was still as high as 0.7 T [15]. Usually, a shorter undulator period also requires a smaller undulator gap, which is ultimately limited by the transverse beam size, the radiation opening angle and the generated wakefields.

The undulator performance is mostly determined by the undulator parameter K which scales linearly with field strength and is proportional to the undulator period. Because optimal performance is achieved for an undulator parameter on the order of unity [4], a smaller undulator period would require a larger magnetic field. For example, a reduction of the undulator period to 1 mm already requires a magnetic field strength around 10 T. To the best of our knowledge, such field strength cannot be obtained by today's micro-machined electromagnets. A conceptually different approach for a short period undulator uses oscillating electromagnetic fields, for example, in laser irradiated dielectric gratings [16], laser-driven undulators [17], microwave undulators [18], plasma wave undulators [19–21] or surface plasmon polariton (SPP) undulators [22–24].

Here, we propose a THz-driven undulator with a period of approximately 1 mm. It consists of an array of split ring resonators (SRRs) which locally enhance the THz driver field [25]. Similar structures have recently been used for electron deflection in streaking experiments [26–28]. Generally, the THz frequency range is of interest for electron bunch manipulations because the wavelength is well matched to the typical electron bunch size of several tens of microns. In comparison to THz-driven SPP undulators [24], SRR based undulators benefit from an order of magnitude larger field enhancement. In addition, wakefield effects are substantially reduced and the proposed undulator structure requires only one THz driver pulse (TDP).

A schematic of the proposed THz-driven SRR undulator is shown in Fig. 3.1. It is composed of C-shaped SRRs, which are known to feature considerable field enhancement. In principle, other sub-wavelength structures with different resonance characteristics or field enhancement properties may be used [27, 28]. Resonance frequency and field enhancement are mainly determined by geometry, namely by gap height g, gap width w and hole radius R (see Fig. 3.1 for the definition of the parameters). The TDP is linearly polarized along the y-direction and propagates in positive x-direction. It couples to the fundamental resonance of the SRR and leads to a locally enhanced electric field inside the gap. This field is relatively homogeneous and predominantly polarized in y-direction.

The electron bunches propagate through the SRR gaps in positive z-direction, as indicated by the green dashed curve, and interact with the electromagnetic fields. Due to the strong field enhancement, the electron dynamics is predominantly determined by the y-component of the in-gap electric field rather than any of the other electric or magnetic field components. By adjusting the SRR distance d to half of the free space resonance wavelength, the electrons are periodically deflected in $\pm y$-direction. Therefore, the optimal undulator period is directly linked

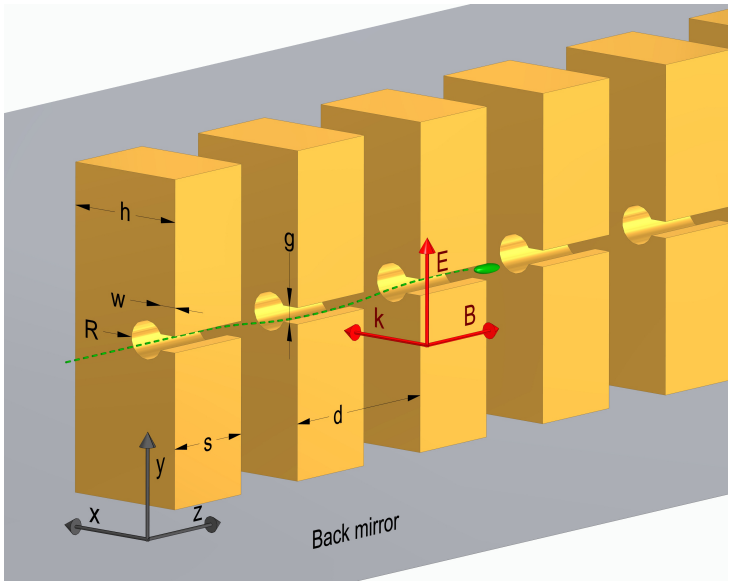

Figure 3.1: Schematic of the THz-driven undulator: The electric field of the TDP (shown by red arrows) is enhanced inside the gap of the C-shaped SRRs. An electron bunch (green) propagating in positive z-direction, as indicated by the green dashed curve, is periodically deflected in $\pm y$-direction and as a result emits linearly polarized radiation.

to the resonance frequency of the SRR. The electron deflection pattern is further influenced by the filling factor $F := s/d$ of the SRR array. Note that for $F = 1$ the individual SRRs merge into a slotted tube. Here, we consider relativistic electron energies, which are of particular interest because of small radiation opening angles and lower wake field instabilities.

3.2 Case study

In this section we present a case study of the SRR undulator concept with experimentally viable parameters. First, we define the undulator geometry and calculate the resonance condition as well as the electromagnetic fields via finite element simulations. Based on the simulations we derive an approximate analytic undulator model, which predicts the K-parameter and the emitted photon energies. Next, we study the dynamics of a single electron in a weak undulator field. Specifically, we study the emission spectrum as a function of the electron injection time relative to the TDP, initial transverse position, undulator periodicity and undulator filling factor. We conclude with electron bunch simulations, i.e., we simulate wakefields which allows us to specify upper limits for the bunch charge, we investigate the effect of stronger electromagnetic fields of the TDP and we study photon emission for two different (100 MeV and 1 GeV) electron beam energies.

3.2.1 Geometry

The SRR gap height g and width w are set to 50 µm, which is a good compromise to accommodate electron bunches with transverse sizes on the order of tens of microns while resulting in a close to homogeneous in-gap field distribution in x- and y-direction. The gap is at

$x \in [-25\,\mu\text{m}, 25\,\mu\text{m}]$ and $y \in [-25\,\mu\text{m}, 25\,\mu\text{m}]$. The hole radius R is tuned for a resonance frequency of approximately 270 GHz, which corresponds to an undulator period of $2d = 1.1$ mm. The distance h is chosen such that the in-gap electric field at the resonance frequency is enhanced by the TDP reflected from the back mirror. The undulator length is arbitrarily set to $L = 100$ mm, but in practice is linked to the available THz source [29] as one has to maintain the desired electromagnetic field strength over the entire undulator length. We estimate the required THz energy, assuming a focal spot size of 100 mm by 1 mm, a pulse duration of 5 ps and a peak electric field strength of 10 MV/m, to approximately 70 µJ TDP energy, which is experimentally achievable with different types of THz sources [29–31]. Table 3.1 summarizes all the relevant dimensions of the SRR undulator.

Table 3.1: SRR undulator dimensions (see also Fig. 3.1 for the definition of parameters).

Parameter	Symbol	Value
Gap height	g	50 µm
Gap width	w	50 µm
Hole radius	R	60 µm
SRR thickness	s	50 µm – 555 µm
SRR distance	d	555 µm
Filling factor	F	0.09 – 1
Distance to wall	h	390 µm
Undulator length	L	100 mm

3.2.2 Undulator fields

The spatial and temporal electric and magnetic field distributions of the SRR resonators were simulated with the finite-element software COMSOL [32]. The simulations were performed in three dimensions with periodic boundary conditions in z-direction and scattering boundary conditions in x- and y-directions. The permittivity of the SRR and the back mirror material was described by a Drude-model with a plasma frequency of 2.2 PHz and a damping rate of 6.4 THz (these parameter values have only minor influence on the field maps). The TDP was modeled by a plane wave. First, we performed frequency domain simulations to identify resonance, field enhancement and spatial distribution of the electric and magnetic fields at resonance. Then, we performed time-dependent simulations to determine the time dependence of the electric and magnetic fields when excited with a realistic TDP. For further simulations of the electron dynamics all six field maps at resonance were exported for a discrete grid with a maximum spacing of 2 µm, 1 µm and 5 µm in x-, y- and z-direction, respectively.

The simulations show that the in-gap resonance electric field is dominated by the enhanced y-component with negligible E_x and E_z contributions. The magnetic field is mostly in z-direction and concentrated in the circular SRR hole but decays into the gap region. The frequency dependent electric field enhancement was calculated as the volume average of E_y inside the SRR gap normalized to the electric field strength of the TDP.

Figure 3.2 (a) shows the y-component of the electric field at resonance as a function of longitudinal position through the center of four SRR gaps (i.e., at $x = y = 0\,\mu\text{m}$) and normalized to the electric field strength of the incident TDP. The thickness s was arbitrarily set to 300 µm. The inset shows the electric field amplitude E_y at the gap center versus x and y. Close to the

center, it is rather homogeneous with some inhomogeneities at the edges of the gap. Figure 3.2 (b) shows the Fourier decomposition of $E_y(z)$ at a fixed time, with a harmonic spectrum typical of the longitudinal, almost square electric field distribution.

Figure 3.2 (c) shows a realistic TDP (red dash-dotted curve) and the excited in-gap y-component of the electric field (blue solid curve). The in-gap field oscillates for times longer that the impulsive excitation because the resonance linewidth is narrower than the excitation spectrum, as indicated in Fig. 3.2 (d).

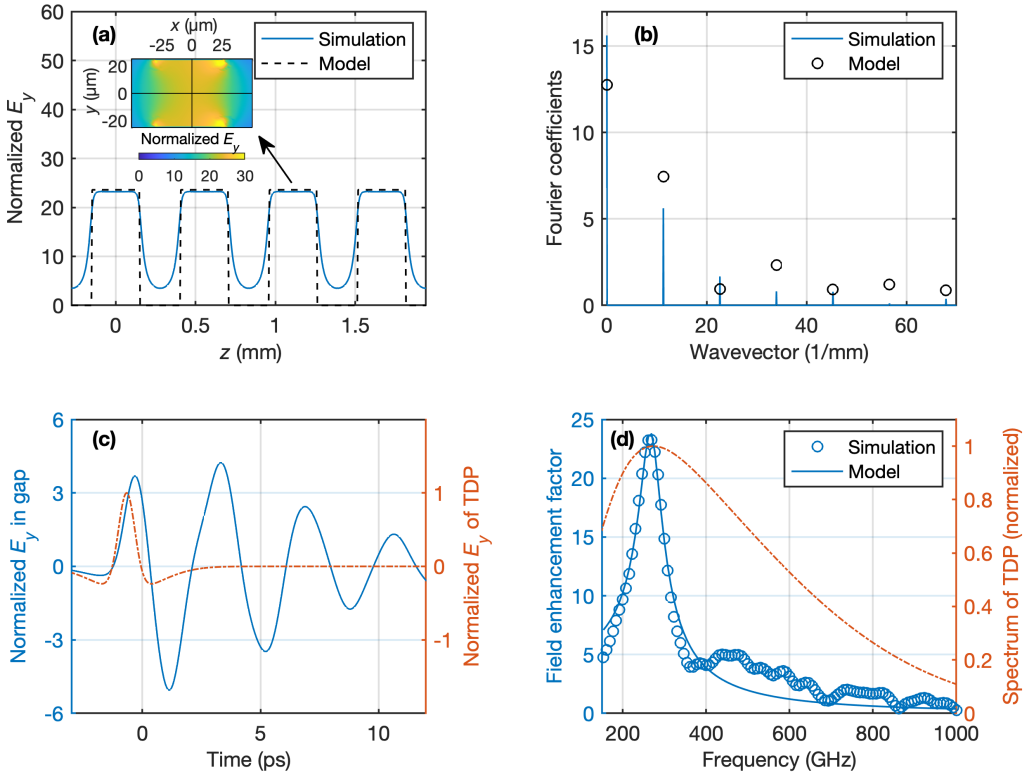

Figure 3.2: (a) Simulated y-component of the electric field at the middle of the SRR gap as a function of the longitudinal position. The field is normalized to the electric field strength of the TDP and the time is fixed for the maximum field strength. The SRR thickness s is 300 µm and distance d is 555 µm. The black dashed curve corresponds to the assumption used in the analytic model Eq. (3.5). The inset shows the y-component of the electric field in a xy-slice at the longitudinal position of the gap middle. (b) Fourier spectrum of the longitudinally varying electric field together with the Fourier components from the analytic model Eq. (3.6). (c) Simulated time-dependent field inside the SRR gap exited by a specific TDP. (d) Spectrum of the TDP and the frequency dependent enhancement factor. The solid curve corresponds to a fit based on Eq. (3.2).

Figure 3.3 shows the absolute value of the in-gap field enhancement factor as a function of frequency and filling factor. This figure shows that the resonance frequency of approximately 270 GHz is independent of the filling factor F. For the considered SRR thickness, which exceeds

the skin depth, the full width at half maximum (FWHM) decreases from 190 GHz to 70 GHz for larger filling factors. Therefore, a realistic single-cycle TDP spectrum is broader than the resonance curve. The highest field enhancement of 29 is found for the structure with the smallest filling factor and can be attributed to the maximal field concentration and contribution from the reflected pulse.

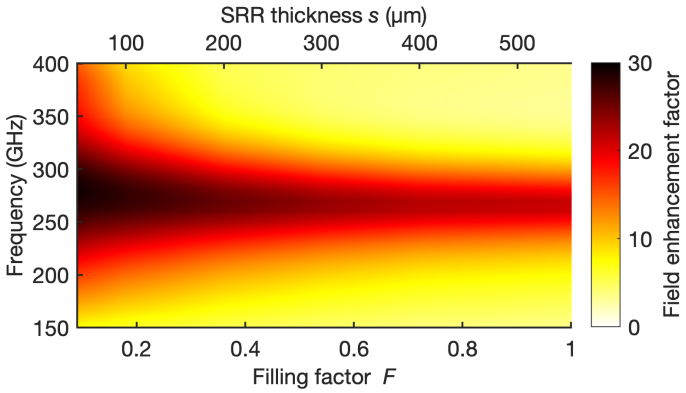

Figure 3.3: Color-coded field enhancement $|\eta(\omega)|$ as a function of frequency and filling factor for a SRR array with a fixed distance of $d = 555\,\mu\text{m}$.

3.2.3 Approximate analytic model

Here we derive an analytic model to estimate the undulator performance. In particular, we solve the Lorentz equation of motion for a single electron moving through the periodic deflection fields, and determine the K-parameter and the wavelength of the emitted radiation. The TDP spectrum $E_d(\omega)$ and the time varying electric field inside the SRR gap $E_{gap}(t)$ are related via

$$E_{gap}(t) = \text{Re}\left\{\frac{1}{2\pi}\int_{-\infty}^{\infty} E_d(\omega)\eta(\omega)\text{e}^{\text{i}\omega t}d\omega\right\}, \tag{3.1}$$

where $\eta(\omega)$ is the frequency dependent complex field enhancement factor. Figure 3.2 (d) shows that $\eta(\omega)$ can be well approximated by a Lorentz curve

$$\eta(\omega) = \frac{\eta_0}{\omega_0^2 - \omega^2 + \text{i}\zeta\omega}, \tag{3.2}$$

where $f_0 = \frac{\omega_0}{2\pi}$ is the resonance frequency and ζ is the damping factor. The parameter η_0 determines the maximum field enhancement factor. In order to have oscillations the resonator must not be overdamped, which implies an upper limit of the damping factor. Since the TDP spectrum is much broader than the resonance curve, we can assume the TDP spectrum to be approximately constant in the frequency range of significant field enhancement. Therefore, at a time Δt after excitation with the TDP we find

$$E_{gap}(\Delta t) \approx \frac{2|E_d(\omega_0)|\eta_0\text{e}^{-\zeta\Delta t/2}}{\sqrt{4\omega_0^2 - \zeta^2}}\sin\left(\frac{\Delta t}{2}\sqrt{4\omega_0^2 - \zeta^2}\right). \tag{3.3}$$

For small damping factors and at times close to the excitation (i.e., $\zeta \ll \omega_0$ and $\zeta\Delta t \ll 1$) the electric field inside the gap can be approximated by

$$E_{gap}(t) \approx E_0 \sin(\omega_0 t + \varphi_0), \tag{3.4}$$

where φ_0 is an arbitrary phase and $E_0 := E_{THz}|\eta(\omega_0)|$ with $E_{THz} := |E_d(\omega_0)|\zeta$. Note that damping can also be neglected if a TDP with a tilted pulse front is employed. The tilt should be matched to the electron velocity [33–35]. Employing the Fourier decomposition of the z-dependent electric field we find

$$E_y(z,t) = E_0 \sin(\omega_0 t + \varphi_0) \sum_{n=-\infty}^{\infty} A_n \cos\frac{2\pi n z}{d}, \tag{3.5}$$

with the Fourier amplitudes of the harmonics A_n. In case we approximate the longitudinal field distribution by a square function, as shown in Fig. 3.2 (a), the Fourier amplitudes can be estimated to

$$A_n := \begin{cases} F, & n = 0 \\ \frac{1}{\pi n} \sin \pi n F, & n \neq 0 \end{cases}. \tag{3.6}$$

For solving the equation of motion of a single electron, we assume $z(t) = \beta_{z0} ct$, where β_{z0} is the initial electron velocity in z-direction normalized to the speed of light in vacuum c. We further assume zero initial velocity in x- and y-direction and find

$$\begin{aligned} \gamma(t) &= \left[1 + \left(\gamma_0 \beta_{z0}\right)^2 + \Big(\sum_{n=-\infty}^{\infty} K_n \cos\psi_n\Big)^2\right]^{1/2} \\ \beta_z(t) &= \frac{\gamma_0}{\gamma(t)} \beta_{z0} \\ \beta_y(t) &= \frac{1}{\gamma(t)} \sum_{n=-\infty}^{\infty} K_n \cos\psi_n \end{aligned} \tag{3.7}$$

where γ_0 is the initial Lorentz factor,

$$K_n := \frac{e E_0 d A_n}{cm(d\omega_0 + 2\pi n c \beta_{z0})}, \tag{3.8}$$

and $\psi_n := (\omega_0 + \frac{2\pi c \beta_{z0} n}{d})t + \varphi_0$ for $n \in \mathbb{Z}$, where m is the electron rest mass and e the elementary charge. The assumption $z(t) = \beta_{z0} ct$ breaks down in the limit of large K_n-values, but it allows to find analytic expressions for relevant radiation properties. Note that K_0 is proportional to the filling factor, because $A_0 \approx F$. For example, we find an undulator parameter of $K_0 \approx 0.07$ for a resonance frequency of 270 GHz, a filling factor of $F = 0.2$ and $E_0 = 1$ GV/m. By increasing the filling factor up to $F = 1$ the undulator parameter increases to $K_0 \approx 0.35$.

Based on the slippage condition, the emitted photon frequencies in the lab frame are given by

$$\omega_{r,n} = \frac{|\omega_0 + 2\pi \beta_{z0} c n/d|}{1 - \beta_{z0} \cos\theta} \tag{3.9}$$

where θ is the emission angle with respect to the z-axis. The best undulator performance is expected for a structure with $2\pi c/\omega_0 = \lambda_0 = 2d$, since the electric field inside the gap changes

sign each time the bunch travels from one resonator to the next and yields an oscillatory motion with a period of $2d$. The on-axis photon frequencies are $2\gamma^2 c k_n$, with $k_n := |k_0(2n+1)|$ and $k_0 := \omega_0/c$, that is, the emission spectra consist of multiple odd higher harmonics.

The relative bandwidth of the emission mainly depends on the number of undulator periods and the relative energy spread of the electrons. The natural bandwidth of an undulator can be estimated by considering the Fourier transform limit of the radiation cycles [36]. At the resonance frequency f_0, the electrons oscillate $N_{u,n} = Lk_n/(2\pi)$ times (where L is the total undulator length) resulting in a relative bandwidth

$$\frac{\Delta\omega_{r,n}}{\omega_{r,n}} = \sqrt{(0.886/N_{u,n})^2 + (2\Delta E/E)^2}, \tag{3.10}$$

where $\Delta\omega_{r,n}$ is the FWHM of the on-axis spectral intensity and $\Delta E = 2\sqrt{2\ln 2}\,\sigma_E$ is the FWHM of the initial energy spread of the electrons (assuming a Gaussian energy distribution with standard deviation σ_E). Furthermore, the radiation is confined in a narrow emission cone with an opening angle of $\theta \approx 1/\gamma$ [4].

3.2.4 Single electron dynamics

In this section we consider a single electron with an initial energy of 100 MeV for the calculation of the electron trajectories and the emitted radiation spectra. The electron trajectories were calculated with VDSR (*Virtual Detector for Synchrotron Radiation*) [37] based on the three dimensional field maps from the frequency-domain COMSOL simulation. From the trajectories the intensity of the emitted radiation per frequency interval and per solid angle in the far field is calculated [38]

$$\frac{\mathrm{d}^2 I}{\mathrm{d}\omega \mathrm{d}\Omega} = \frac{e^2}{16\pi^3 \varepsilon_0 c}\left| \int_{-\infty}^{\infty} \frac{\hat{\mathbf{n}}_r \times \left[\left(\hat{\mathbf{n}}_r - \boldsymbol{\beta}\right) \times \dot{\boldsymbol{\beta}}\right]}{\left(1 - \hat{\mathbf{n}}_r \boldsymbol{\beta}\right)^2} \exp\left(i\omega\left(t - \frac{\hat{\mathbf{n}}_r \mathbf{r}}{c}\right)\right) \mathrm{d}t \right|^2 \tag{3.11}$$

where $\hat{\mathbf{n}}_r$ is a unit vector pointing in the observation direction. From the simulated on-axis spectra we estimate the radiation peak brightness using the peak intensity (in units of photons/(sr 0.1%BW)) divided by the bunch duration $2\sigma_z/c$ and the bunch cross section area $\pi\sigma_r^2$.

The SRR thickness is set to $s = 100\,\mu\mathrm{m}$ and the incident peak THz electric field is $E_{THz} = 1$ MV/m. Note that for high undulator field strengths the net deflection can be as large as the gap size and the electron may collide with the SRRs.

A consequence of time dependent undulator fields is that the time delay between the TDP and the electron injection into the structure is crucial. The exact injection time determines the overall deflection in y-direction as well as the emitted radiation intensity. Note that the deflection in x-direction is negligible irrespective of injection time. Figure 3.4 shows the y-deflection at the end of the undulator and emitted peak intensity versus time delay between TDP and electron injection.

An electron injected at zero time delay, or at an integer multiple of half the oscillation period, reaches the SRR gap when the field strength is at its maximum resulting the highest peak intensity. Note that this corresponds to $\varphi_0 = \pi/2$ in Eq. (3.4). If the electron has no initial momentum in y-direction, a net deflection arises which is determined by the first momentum

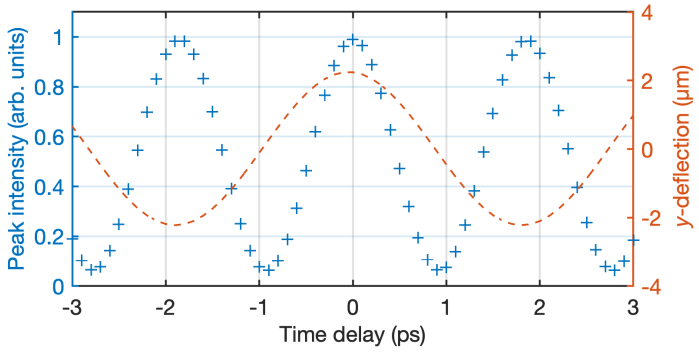

Figure 3.4: Simulated on-axis peak intensity and total deflection in y-direction as a function of time delay between electron injection and TDP.

kick at the undulator entrance. As a consequence, the emission cone bends away from the z-axis. If the time delay is adjusted such that the electron passes the gap when the deflection field has a zero-crossing, the net deflection is zero but also the peak intensity is minimal. To avoid a net deflection while maintaining the time delay for maximum emitted intensity we propose to compensate the deflection with a matched initial momentum in y-direction. For the simulation parameters used here, we found that an initial normalized y-momentum of 0.004 can balance the net deflection at zero time delay. In the following the initial y-momentum is always adjusted for zero net deflection. Such initial y-momentum can be achieved with a standard undulator end design, here for example with the first SRR having only half the thickness s or a larger width w for reducing the deflection field strength at the undulator entrance [4].

The emitted radiation spectra can be tuned by adjusting the SRR distance d and the filling factor F. Figure 3.5 summarizes the simulated on-axis radiation spectra for different parameters. Note that all structures have the same resonance frequency of 270 GHz. The gray dashed curves show the predicted photon energies based on Eq. (3.9) for the corresponding harmonics n. In Fig. 3.5 (a) we show the spectra for different filling factors F but for a fixed distance of 555 µm. Because the distance is matched to the resonance frequency each emission peak has contributions from two Fourier components A_n as indicated by the corresponding values of n. For increasing F we found an increased emission intensity at the photon frequency $\omega_{r,0}$ (which corresponds to 86.4 eV). This is explained by the increased interaction time between the electric field and the electrons. For increasing F, the higher order harmonics diminish, as it is expected based on the corresponding Fourier coefficients A_n. In the limit of a slotted tube, i.e., $F = 1$, no harmonics are generated, which is in agreement with $A_n = 0$ for $n \neq 0$. For small filling factors, multiple emission lines occur at odd higher harmonics.

On the other hand, in Fig. 3.5 (b), we fixed the SRR thickness to 100 µm but changed the distance between resonators. Again we find good agreement between simulated emission peaks and analytic model. The highest emission intensity is obtained when the distance is matched to the resonance frequency ($d = 555$ µm) or when the SRRs are closely spaced such that the structure approaches a slotted tube. Likewise, the photon energy of the higher order harmonics can be tuned over a wide range by adjusting the SRR distance. Also here, the resulting emission intensities are governed by the Fourier coefficients A_n.

Any inhomogeneity of the undulator fields in the gap area could potentially effect the undulator performance. Therefore we compare the radiation spectra for different initial x-positions

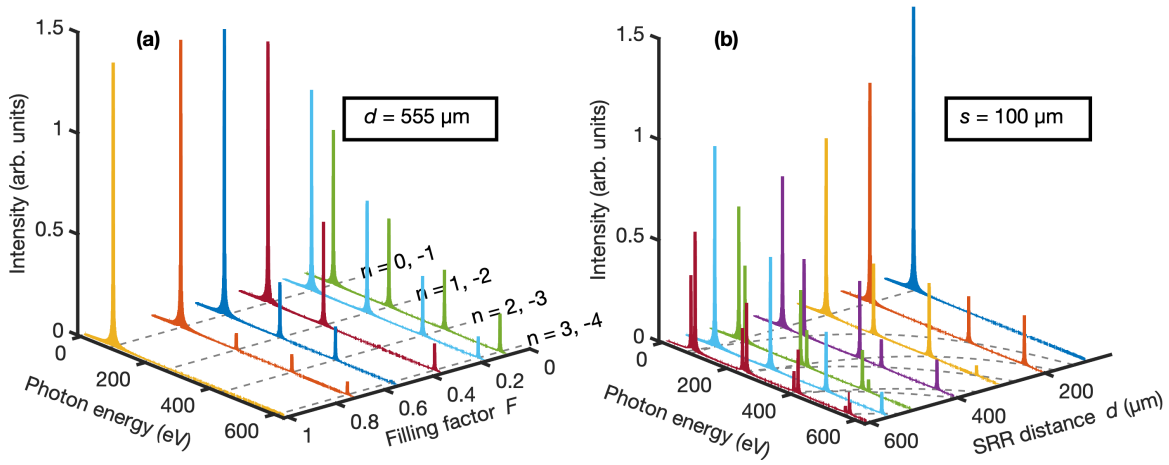

Figure 3.5: Simulated on-axis spectra and the predicted photon energies based on the analytic model (gray dashed curves) for different filling factors (a) and distances (b). Geometries for six different filling factors (a) and for seven different SRR distances (b) were considered.

x_0 as shown in Fig. 3.6. While the emitted photon energy is unchanged, the intensity decreases when the electron travels off-axis. Note that the intensity is still more than 60% of the on-axis intensity even if the electron travels alongside the SRR gap. Since the deflection field is not entirely symmetric in x-direction, the emission intensities for $x_0 = -30\,\mu\text{m}$ and $x_0 = 30\,\mu\text{m}$ are slightly different. The analytic model in Eq. (3.9) predicts a photon energy of 86.4 eV (shown as black dashed line), which is in agreement with the simulation results.

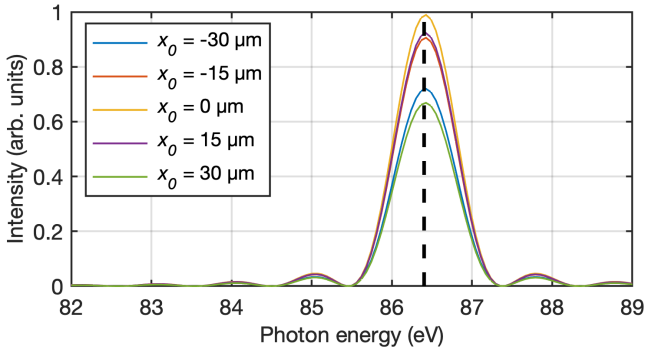

Figure 3.6: Simulated on-axis spectra for different initial x-positions.

3.2.5 Electron bunch dynamics

In the following, we discuss the dynamics of an electron bunch, rather than a single particle, interacting with the undulator fields. A undulator structure with $s = 300\,\mu\text{m}$ and $d = 555\,\mu\text{m}$ is considered, but similar results are obtained for different filling factors. The kinetic energy of the bunch was fixed to 100 MeV and we assumed a relative energy spread of 1%, as provided by today's accelerators [39]. The total bunch charge is 5 pC with a Gaussian distribution

and standard deviations $\sigma_r = 5\,\mu m$ and $\sigma_z = 20\,\mu m$ in transverse and longitudinal direction. Table 3.2 summarizes the electron bunch parameters. For simplicity, we set the emittance to zero, that is, the electrons have no initial momentum spread in the x- and y-direction. If required, the maximum allowed emittance can be estimated by setting the maximum transverse bunch size equal to the gap size and by using a beta function determined by the undulator length L. As a result, the geometric emittance must be much smaller than $g^2/(4L) = 6.3\,\text{nm rad}$ which corresponds to a normalized emittance of $1.2\,\mu m\,\text{rad}$.

Table 3.2: Electron bunch parameters considered in the numerical simulations.

Parameter	Symbol	Value
Kinetic energy	E	100 MeV
Relative energy spread	σ_E/E	1%
Bunch charge	Q	5 pC
Transverse size	σ_r	$5\,\mu m$
Longitudinal size	σ_z	$20\,\mu m$

The electron bunch will generate its own wakefield when propagating through the SRR structure. In the worst case this undesirable wakefield can lead to substantial beam degradation. Therefore the wakefield limits the total allowed bunch charge and/or the minimum beam energy. Figure 3.7 shows the simulated on-axis longitudinal wake potential, which generally leads to an energy loss of the electrons and therefore to an increasing energy spread. We simulated wakefields with the finite-element software CST [40], where the electron bunch was approximated by a line current with a longitudinal Gaussian distribution with standard deviation σ_z. Ideally, the integration of the wakefields is performed over the whole structure length, which was not feasible due to long computation times. Therefore, just a fraction of the structure was considered and the wake potential per SRR was calculated (i.e., the simulated wake potential divided by the number of SRRs used in the simulation). The number of considered SRRs was increased until convergence is reached, which is usually 5 SRRs.

The wakefield is zero at the head of the bunch and increases toward the tail. Because the slotted tube structure has no longitudinal corrugation, its wake potential is much smaller. For better visualization the wake potential of this structure is multiplied by a factor of 30 as indicated in the legend. For the other two structures we found a wake potential per SRR with a maximum amplitude of approximately 600 V/pC. Therefore, the maximum energy loss in a 100 mm long undulator which consists of 180 SRRs would be 110 keV/pC. For a beam energy of 100 MeV one would be limited to bunch charges smaller than approximately 5 pC, if one claims an energy loss of less than 1%. Note that for the slotted tube structure and the same beam energy, the bunch charge can reach 300 pC while the wakefield induced energy loss is still less than 1%.

The radiation spectra generated by an electron bunch was calculated by incoherently adding all spectra of the 1000 macro-particles, which were used for representing the bunch. Figure 3.8 shows the simulated on-axis spectra for different THz electric field strength E_{THz}. Recall that increasing the THz field strength should improve the undulator performance since the undulator parameter K approaches unity, and also the peak intensity is proportional to E_{THz}^2. The relative bandwidth of 5% is in good agreement with the theoretical bandwidth Eq. (3.10). For a classical undulator the relative bandwidth is typically around 0.7% [41]. In order to achieve a similar

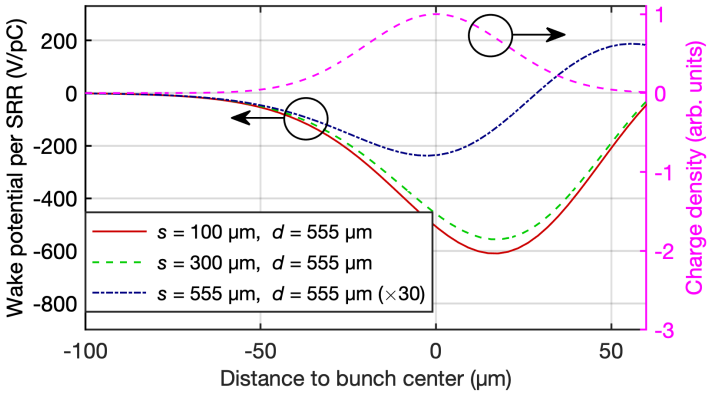

Figure 3.7: Simulated on-axis wake potential per SRR normalized to the bunch charge as a function of distance to the bunch center (negative values refer to positions at the bunch front). For better visualization, the wake potential for a structure with $s = d = 555\,\mu\text{m}$ is multiplied by a factor of 30. The longitudinal bunch charge density with $\sigma_z = 20\,\mu\text{m}$ is shown as pink dashed curve.

value for the SRR undulator, the energy spread must be reduced to 0.1% and the undulator length must be increased to 200 mm. For the highest THz field strengths, before the wiggling motion becomes similar to the gap size, we observe a red shift of the emitted spectra, which is a consequence of the decreased average velocity in z-direction. For $E_{THz} = 40$ MV/m (which corresponds to an electric field strength of approximately 900 MV/m inside the gap) we find a peak intensity of 10^9 photons/(sr 0.1% BW) which corresponds to peak brightness of 10^{19} photons/(s mrad^2 mm^2 0.1% BW). The electric field strength is ultimately limited by the breakdown threshold of the SRR material. To the best of our knowledge, there is no measurement of the gold breakdown threshold in the THz range. However, based on experiment with nano-gap SRRs, we can confirm that the breakdown threshold exceeds 8 GV/m.

Due to wakefield instabilities the kinetic energy of 100 MeV should be regarded as a lower limit. However, we may increase the kinetic energy to the operation regime of recently commissioned XFELs of several GeV. An increase in kinetic energy causes the emitted photon energy to grow as γ^2 and the emission opening angle to shrink as $1/\gamma$. As an example we consider a beam energy of 1 GeV and a TDP peak electric field of $E_{THz} = 40$ MV/m while all the other parameters remain as summarized in Tab. 3.2. The emitted photon energy increases to 8.2 keV with a peak brightness of 10^{21} photons/(s mrad^2 mm^2 0.1% BW). Therefore, depending on the electron energy the undulator can operate from the UV to the hard x-ray range.

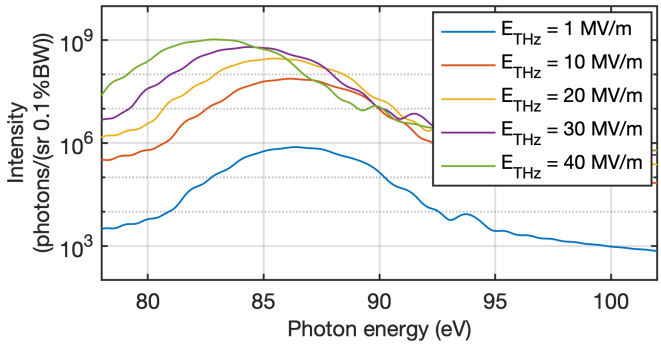

Figure 3.8: On-axis spectra for bunches with 100 MeV energy, 5 pC charge, 1% relative energy spread and for different THz electric field strength.

3.3 Conclusions

A new type of short period undulator is proposed, which is based on a SRR array structure driven by a THz pulse. Undulator periods around 1 mm with a deflection electric field strength of 1 GV/m are experimentally achievable. The corresponding undulator parameter K is approximately 0.3 and could be further increased towards unity depending on the available THz source. Due to its compact size the whole undulator structure could be directly installed in the vacuum beam tube. Propagating a 100 MeV electron bunch with 5 pC charge through a 100 mm long undulator driven by a state-of-the-art THz source was shown to emit 83 eV photons with a peak brightness of 10^{19} photons/(s mrad^2 mm^2 0.1% BW). For a 1 GeV bunch, the photon energy increases to 8.2 keV with a peak brightness of 10^{21} photons/(s mrad^2 mm^2 0.1% BW). Also higher order harmonic emission occurs whose intensity can be tuned by varying the filling factor or the SRR distance. Hence, the undulator can also act as a frequency comb. In comparison with the previously proposed SPP based THz undulator [24], the new concept benefits from a higher field enhancement and also reduces wakefield effects. Therefore it is a promising candidate for a low cost and compact radiation source, which produces directional, linearly polarized and narrow band radiation pulses in the UV to x-ray range. By combining the proposed undulator with a miniaturized advanced accelerator, a table top x-ray source is within reach. Such a source could find application in radiotherapy, ultrafast x-ray diffraction experiments or time-resolved x-ray spectroscopy.

Investigating alternative resonator structures could further improve the undulator performance. In general, structures with an increased gap area, a higher field enhancement or a shorter undulator period would be beneficial. A larger gap area would reduce the restrictions on the electron beam emittance, while an additional increase in field enhancement would further lower the demand on the TDP. A smaller periodicity would miniaturize the device even more and would reduce the kinetic energy requirement for producing a fixed photon energy.

Bibliography

[1] C. Pellegrini, A. Marinelli, and S. Reiche, "The physics of x-ray free-electron lasers", Rev. Mod. Phys. **88**, 15006 (2016), https://link.aps.org/doi/10.1103/RevModPhys.88.015006.

[2] J. M. Madey, "Stimulated emission of bremsstrahlung in a periodic magnetic field", J. Appl. Phys. **42**, 1906–1913 (1971), https://doi.org/10.1063/1.1660466.

[3] D. A. G. Deacon, L. R. Elias, J. M. J. Madey, G. J. Ramian, H. A. Schwettman, and T. I. Smith, "First Operation of a Free-Electron Laser", Phys. Rev. Lett. **38**, 892–894 (1977), https://link.aps.org/doi/10.1103/PhysRevLett.38.892.

[4] J. A. Clarke, *The Science and Technology of Undulators and Wigglers* (Oxford University Press, 2004), https://doi.org/10.1093/acprof:oso/9780198508557.001.0001.

[5] V. (Paul Scherrer Institute (PSI), *SwissFEL - Conceptual design report*, tech. rep. (Switzerland, 2010), p. 132, https://inis.iaea.org/search/search.aspx?orig_q=RN:42006326.

[6] *LCLS Parameters*, https://portal.slac.stanford.edu/sites/lclscore_public/Accelerator_Physics_Published_Documents/LCLS-parameters-3-22-17.pdf.

[7] E. Esarey, C. B. Schroeder, and W. P. Leemans, "Physics of laser-driven plasma-based electron accelerators", Rev. Mod. Phys. **81**, 1229–1285 (2009), https://link.aps.org/doi/10.1103/RevModPhys.81.1229.

[8] R. J. England et al., "Dielectric laser accelerators", Rev. Mod. Phys. **86**, 1337–1389 (2014), https://link.aps.org/doi/10.1103/RevModPhys.86.1337.

[9] J.-C. Huang, H. Kitamura, C.-K. Yang, C.-H. Chang, C.-H. Chang, and C.-S. Hwang, "Challenges of in-vacuum and cryogenic permanent magnet undulator technologies", Phys. Rev. Accel. Beams **20**, 64801 (2017), https://link.aps.org/doi/10.1103/PhysRevAccelBeams.20.064801.

[10] H. Hsieh, S. Krinsky, A. Luccio, C. Pellegrini, and A. Van Steenbergen, "Wiggler, undulator and free electron laser radiation sources development at the national synchrotron light source", Nucl. Instruments Methods Phys. Res. **208**, 79–90 (1983), http://www.sciencedirect.com/science/article/pii/0167508783911067.

[11] W. Gudat, J. Pflüger, J. Chatzipetros, and W. Peatman, "An undulator/multipole wiggler for the BESSY storage ring", Nucl. Instrum. Methods Phys. Res., Sect. A 246, 50 **246**, 50–53 (1986), https://www.sciencedirect.com/science/article/pii/0168900286900434?via%3Dihub.

[12] S. Yamamoto, T. Shioya, M. Hara, H. Kitamura, X. W. Zhang, T. Mochizuki, H. Sugiyama, and M. Ando, "Construction of an in-vacuum type undulator for production of undulator x rays in the 5–25 keV region", Rev. Sci. Instrum. **63**, 400–403 (1992), https://doi.org/10.1063/1.1142768.

[13] B. A. Peterson, O. D. Oniku, W. C. Patterson, D. Le Roy, A. Garraud, F. Herrault, N. M. Dempsey, D. P. Arnold, and M. G. Allen, "Technology Development for Short-period Magnetic Undulators", Phys. Procedia **52**, 36–45 (2014), http://www.sciencedirect.com/science/article/pii/S1875389214000182.

[14] J. Harrison, A. Joshi, Y. Hwang, O. Paydar, J. Lake, P. Musumeci, and R. N. Candler, "Surface-micromachined Electromagnets for 100μm-scale Undulators and Focusing Optics", Phys. Procedia **52**, 19–26 (2014), http://www.sciencedirect.com/science/article/pii/S1875389214000169.

[15] J. Harrison, A. Joshi, J. Lake, R. Candler, and P. Musumeci, "Surface-micromachined magnetic undulator with period length between 10μm and 1 mm for advanced light sources", Phys. Rev. ST Accel. Beams **15**, 70703 (2012), https://link.aps.org/doi/10.1103/PhysRevSTAB.15.070703.

[16] T. Plettner and R. L. Byer, "Proposed dielectric-based microstructure laser-driven undulator", Phys. Rev. ST Accel. Beams **11**, 30704 (2008), https://link.aps.org/doi/10.1103/PhysRevSTAB.11.030704.

[17] F. Toufexis, T. Tang, and S. G. Tantawi, "A 200 μm-PERIOD LASER-DRIVEN UNDULATOR", Proc. 36th Int. Free. Laser Conf., 131–136 (2014), https://accelconf.web.cern.ch/FEL2014/papers/mop047.pdf.

[18] S. Tantawi, M. Shumail, J. Neilson, G. Bowden, C. Chang, E. Hemsing, and M. Dunning, "Experimental Demonstration of a Tunable Microwave Undulator", Phys. Rev. Lett. **112**, 164802 (2014), https://link.aps.org/doi/10.1103/PhysRevLett.112.164802.

[19] S. Corde and K. T. Phuoc, "Plasma wave undulator for laser-accelerated electrons", Phys. Plasmas **18**, 033111 (2011), https://aip.scitation.org/doi/10.1063/1.3569827.

[20] R. L. Williams, C. E. Clayton, C. Joshi, and T. C. Katsouleas, "Studies of classical radiation emission from plasma wave undulators", IEEE Trans. Plasma Sci. **21**, 156–166 (1993), https://doi.org/10.1109/27.221115.

[21] S. G. Rykovanov, C. B. Schroeder, E. Esarey, C. G. R. Geddes, and W. P. Leemans, "Plasma Undulator Based on Laser Excitation of Wakefields in a Plasma Channel", Phys. Rev. Lett. **114**, 145003 (2015), https://link.aps.org/doi/10.1103/PhysRevLett.114.145003.

[22] L. J. Wong, I. Kaminer, O. Ilic, J. D. Joannopoulos, and M. Soljac̆ić, "Towards graphene plasmon-based free-electron infrared to X-ray sources", Nat. Photonics **10**, 46 EP – (2015), https://doi.org/10.1038/nphoton.2015.223.

[23] G. Rosolen, L. J. Wong, N. Rivera, B. Maes, M. Soljac̆ić, and I. Kaminer, "Metasurface-based multi-harmonic free-electron light source", Light. Appl. **7**, 64 (2018), https://doi.org/10.1038/s41377-018-0065-2.

[24] D. Rohrbach, C. B. Schroeder, A. Pizzi, R. Tarkeshian, M. Hayati, W. P. Leemans, and T. Feurer, "THz-driven surface plasmon undulator as a compact highly directional narrow band incoherent x-ray source", Phys. Rev. Accel. Beams **22**, 90702 (2019), https://link.aps.org/doi/10.1103/PhysRevAccelBeams.22.090702.

[25] J.-H. Kang, D.-S. Kim, and M. Seo, "Terahertz wave interaction with metallic nanostructures", Nanophotonics **7**, 763–793 (2018), https://doi.org/10.1515/nanoph-2017-0093.

[26] I. H. Baek, H. W. Kim, Y. C. Kim, M. Kim, S. J. Park, K. Y. Oang, K. Jang, K. Lee, Y. U. Jeong, N. Vinokurov, and T. Feurer, "Terahertz activities at KAERI ultrafast electron diffraction facility", in 2018 43rd int. conf. infrared, millimeter, terahertz waves (2018), pp. 1–2, https://doi.org/10.1109/IRMMW-THz.2018.8510096.

[27] D. Zhang, A. Fallahi, M. Hemmer, X. Wu, M. Fakhari, Y. Hua, H. Cankaya, A.-L. Calendron, L. E. Zapata, N. H. Matlis, and F. X. Kärtner, "Segmented terahertz electron accelerator and manipulator (STEAM)", Nat. Photonics **12**, 336–342 (2018), https://doi.org/10.1038/s41566-018-0138-z.

[28] X. L. Shen, E. C. Snively, J. G. Navarro, D. Cesar, and P. Musumeci, "A THz driven split-ring resonator based ultrafast relativistic electron streak camera", AIP Adv. **9**, 85209 (2019), https://doi.org/10.1063/1.5080374.

[29] J. A. Fülöp, S. Tzortzakis, and T. Kampfrath, "Laser-Driven Strong-Field Terahertz Sources", Adv. Opt. Mater. **8**, 1–25 (2020), https://doi.org/10.1002/adom.201900681.

[30] F. Ahr, S. W. Jolly, N. H. Matlis, S. Carbajo, T. Kroh, K. Ravi, D. N. Schimpf, J. Schulte, H. Ishizuki, T. Taira, A. R. Maier, and F. X. Kärtner, "Narrowband terahertz generation with chirped-and-delayed laser pulses in periodically poled lithium niobate", Opt. Lett. **42**, 2118–2121 (2017), http://ol.osa.org/abstract.cfm?URI=ol-42-11-2118.

[31] L. Wang, A. Fallahi, K. Ravi, and F. Kärtner, "High efficiency terahertz generation in a multi-stage system", Opt. Express **26**, 29744 (2018), https://doi.org/10.1364/oe.26.029744.

[32] *COMSOL Multiphysics*, (2019) https://www.comsol.com (visited on 02/01/2019).

[33] T. Feurer, J. C. Vaughan, and K. A. Nelson, "Spatiotemporal Coherent Control of Lattice Vibrational Waves", Science (80-.). **299**, 374 (2003), http://science.sciencemag.org/content/299/5605/374.abstract.

[34] S. Akturk, X. Gu, E. Zeek, and R. Trebino, "Pulse-front tilt caused by spatial and temporal chirp", Opt. Express **12**, 4399–4410 (2004), http://www.opticsexpress.org/abstract.cfm?URI=oe-12-19-4399.

[35] L. J. Wong and I. Kaminer, "Ultrashort Tilted-Pulse-Front Pulses and Nonparaxial Tilted-Phase-Front Beams", ACS Photonics **4**, 2257–2264 (2017), https://doi.org/10.1021/acsphotonics.7b00464.

[36] P. Schmüser, M. Dohlus, J. Rossbach, and C. Behrens, *Free-Electron Lasers in the Ultraviolet and X-Ray Regime* (Springer International Publishing, Cham, Heidelberg, New York, Dordrecht, London, 2014), https://link.springer.com/book/10.1007%2F978-3-319-04081-3.

[37] M. Chen, E. Esarey, C. G. R. Geddes, C. B. Schroeder, G. R. Plateau, S. S. Bulanov, S. Rykovanov, and W. P. Leemans, "Modeling classical and quantum radiation from laser-plasma accelerators", Phys. Rev. ST Accel. Beams **16**, 030701 (2013), https://journals.aps.org/prab/abstract/10.1103/PhysRevSTAB.16.030701.

[38] J. D. Jackson, *Classical electrodynamics*, 3rd ed. (Wiley, New York, 1999), http://cdsweb.cern.ch/record/490457.

[39] *Sparc Parameters*, (2019) https://www.lnf.infn.it/acceleratori/sparc/parameters.html.

[40] *CST – Computer Simulation Technology*, (2019) https://www.cst.com (visited on 06/08/2021).

[41] *Undulators at SLS*, (2020) https://www.psi.ch/de/insertion-devices/sls (visited on 12/01/2020).

Chapter 4

Ultrafast and Low-Threshold THz Mode Switching of Two-Dimensional Nonlinear Metamaterials

Bong Joo Kang[1], David Rohrbach[1], Fabian D. J. Brunner[1], Salvatore Bagiante[1,2], Hans Sigg[2], and Thomas Feurer[1]

[1]Institute of Applied Physics, University of Bern, Sidlerstrasse 5, 3012 Bern, Switzerland
[2]Laboratory for Micro- and Nanotechnology, Paul Scherrer Institute, 5232 Villigen, Switzerland

This work was published in Nano Lett. **22** (5), 2016-2022 (2022)

Abstract

Judiciously designed two-dimensional THz metamaterials consisting of resonant metallic structures embedded in a dielectric environment locally enhance the electromagnetic field of an incident THz pulse to values sufficiently high to cause nonlinear responses of the environment. In semiconductors, the response is attributed to carrier generation via intervalley scattering, impact ionization, or interband tunneling and can affect the resonant behavior of the metallic structure, which results, for instance, in mode switching. However, details of mode switching, especially time scales, are still debated. By using metallic split-ring resonators with nm-sized gaps on intrinsic semiconductors with different bandgaps we identify the most relevant carrier generation processes. In addition, by combining nonlinear THz time-domain spectroscopy with simulations, we establish the fastest time constant for mode switching to around hundred femtoseconds. Our results not only elucidate dominant carrier generation mechanisms and dynamics, but also pave the route towards optically driven modulators with THz bandwidth.

4.1 Main article

Since a few decades, researchers have devised strategies to tailor the linear response of passive metamaterials [1, 2]. More recently, these concepts were extended towards nonlinear responses, aiming for tunable or active functionality [3, 4]. A promising approach is to incorporate nonlinear materials, such as semiconductors, liquid crystals, or phase-transition materials, either as environmental or as constituent components [5–7]. These materials change their electric or magnetic susceptibility under the influence of intense fields, and hence modify the response of the metamaterial [8–10]. For instance, resonant responses change their quality factor, disappear entirely, or a new set of resonances appears, often at different frequencies [11, 12]. The latter is referred to as mode switching.

At terahertz (THz) wavelengths, the metallic structures containing nanometer size features, such as tips or gaps, exhibit strongly enhanced local near-fields [13–15]. Hence, even for relatively low incident THz fields, they can drive a nonlinear response. As a consequence, progress in metamaterial research [16, 17] alongside recent advances in THz sources has led to a variety of nonlinear THz metamaterials [18, 19]. For instance, two-dimensional metal structures on semiconductors have shown nonlinear responses, which originate from nonlinear transport phenomena, such as intervalley scattering (IVS) [20–22], impact ionization (IMI) [22–25], or interband Zener tunneling (ZT) [11, 26]. Understandably, these phenomena are relevant for the performance of semiconductor-based optoelectronic devices, such as efficient photovoltaic nano-cells [27, 28], electroluminescent emitters [29, 30], or highly sensitive photon detectors [31, 32]. Several of those studies have demonstrated nonlinear mode switching, but even though the physics underlying the field-induced semiconductor response was tentatively assigned to specific carrier generation mechanisms, a detailed picture is still under debate. Moreover, the dynamics of mode switching has never been investigated.

Here, we aim to shed further light on carrier generation at THz frequencies in nanometer size volumes and its dynamics, especially with regards to mode switching of a two-dimensional metamaterial. We fabricated arrays of metallic split-ring resonators (SRR) on intrinsic semiconductor substrates with different band gaps. In addition, the SRRs contained a nm-size gap of different widths to control the electric near-field distribution within the gap. In all SRRs the gap electric field is orders of magnitude higher than the incident electric field, so that mode switching can be induced even at moderate incident THz energies. By using different band gap substrates and different gap widths, we are able to distinguish between different carrier generation mechanisms. Additionally, by combining THz time-domain spectroscopy with numerical simulations, we establish the electric field-dependent time scales for mode switching, and demonstrate that a metamaterial can switch modes within 120 fs.

A cartoon of the concept is shown in Figure 4.1a. A nearly single-cycle THz pulse impulsively excites all SRR resonance frequencies within the excitation spectrum and causes the charge distribution on the SRR to oscillate along the metallic structure. As a result of the periodic charge accumulation across the gap, the electric near-field inside the gap is significantly enhanced. Once it exceeds a material-specific critical electric field, carrier generation and multiplication in the semiconductor substrate beneath the gap set in and as soon as the conductivity there exceeds a certain threshold mode switching occurs. All samples were illuminated from the metal structure side and the polarization of the incident electric field was parallel to the SRR side containing the gap. The transmitted time-dependent THz field is composed of the incident

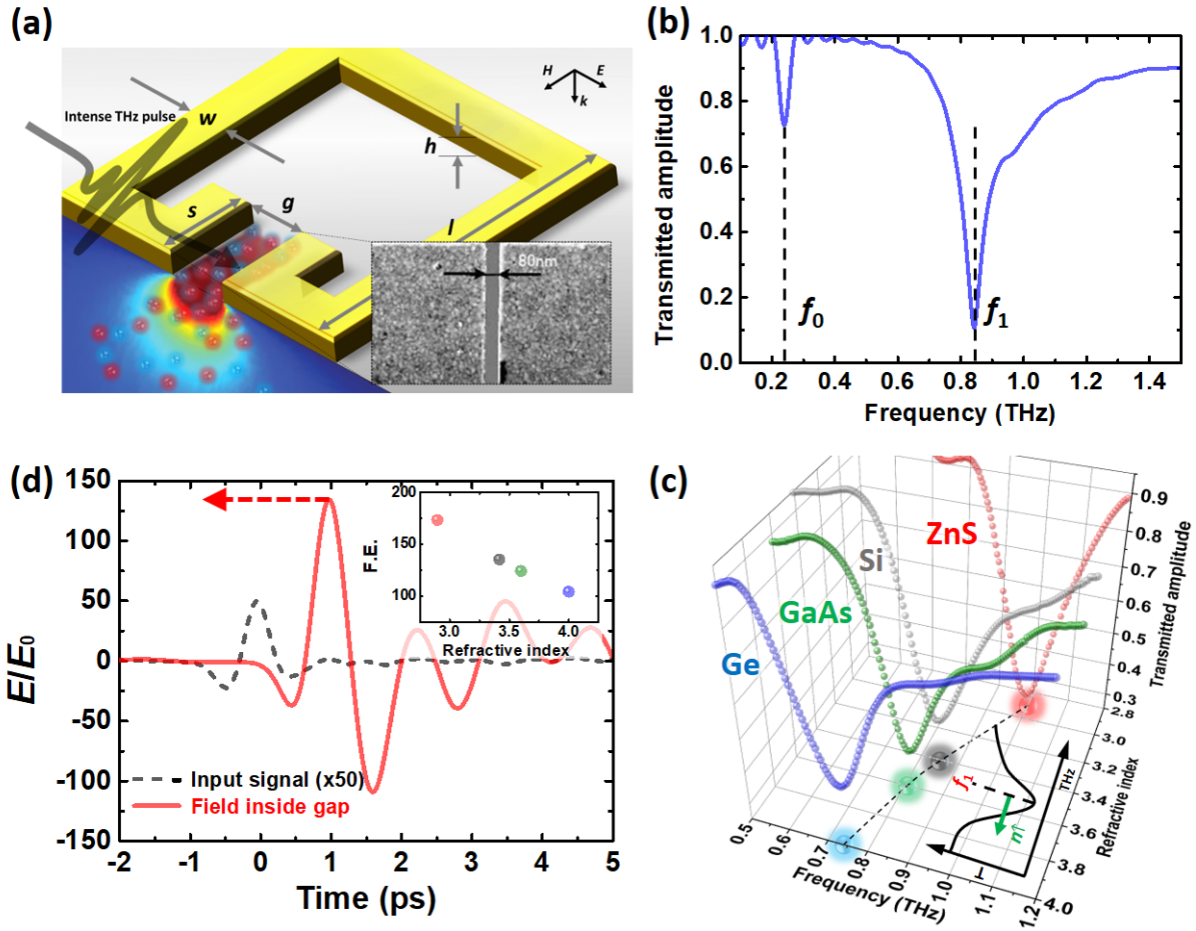

Figure 4.1: Experimental concept and linear properties. (a) The unit cell of the two-dimensional metamaterial consists of a single metallic SRR, here featuring a 80 nm wide gap (inset), on different band gap semiconductors. The illustration defines the geometry of the SRR with all relevant dimensions and the (E, H, k) triad of the incident THz field. (b) Simulated linear transmission spectrum of SRRs on Si. (c) Measured linear transmission spectra around the main resonance for different band gap semiconductor substrates, i.e. Ge, GaAs, Si, and ZnS. (d) Measured incident THz electric field (dashed black curve) and simulated gap electric field for SRRs on Si (solid red curve). The peak electric field enhancement (F.E.), as defined in the figure by the red arrow, depends on the refractive index of the substrate as shown in the inset.

field and the field radiated out from the SRR. Hence, we can observe the linear and nonlinear response of the SRR and analyze the dynamics of mode switching.

The unit cell of the two-dimensional metamaterial consists of a single SRR as shown in Figure 4.1a with $l = 51\,\mu\text{m}$, $w = 5\,\mu\text{m}$, $s = 10\,\mu\text{m}$, $h = 60\,\text{nm}$. We consider two different gap widths g, in the following referring as "small" ($g = 80\,\text{nm}$) and "large" ($g = 200\,\text{nm}$ to $g = 240\,\text{nm}$). The lattice constant is $p = 102\,\mu\text{m}$ in both lateral directions and the total size is 2 mm by 2 mm. The lattice constant was selected such that no lattice modes are excited within the considered frequency range [33]. The SRRs were fabricated by electron-beam lithography (supplemental document: The fabrication details) on high-resistivity semiconductor

substrates to suppress possible intraband processes, such as IVS, at low electric field strength [34]. Specifically, we used Germanium (Ge, $n = 4$, $E_g = 0.67$ eV, indirect bandgap), Silicon (Si, n = 3.42, $E_g = 1.12$ eV, indirect bandgap), Gallium Arsenide (GaAs, n = 3.6, $E_g = 1.43$ eV, direct bandgap), and cubic Zinc Sulfide (ZnS, n = 2.9, $E_g = 3.7$ eV, direct bandgap), where n is the refractive index at THz frequencies and E_g is the band gap energy. After fabrication, the geometry was confirmed via scanning electron microscopy and a zoom to the gap area is shown in the inset of Figure 4.1a.

Figure 4.1b shows the simulated linear transmission spectrum of SRRs on silicon at low incident THz fields in the spectral range between 0.1 THz and 1.5 THz (supplemental document: Nonlinear THz time-domain spectroscopy setup). We identify two resonances (f_0 and f_1) and hereafter we focus on the stronger resonance at around $f_1 = 0.85\,\mathrm{THz}$, which overlaps with the maximum of our THz source spectrum. The measured transmitted amplitude for the different substrates is shown in Figure 4.1c. The resonance frequency f_1 changes from 1 THz to 0.7 THz as the refractive index of the substrate increases from 2.9 to 4 (see also Figure 4.7b), which is explained by a suitable equivalent circuit model [35]. While the resonance frequencies match well with simulations, the measured width is somewhat broader due to the limited resolution of the time-domain THz spectroscopy setup.

The simulations also yield the electric field enhancement in the gap. For instance, Figure 4.1d shows the measured incident THz electric field together with the simulated electric field in the middle of the gap, 20 nm beneath the substrate surface. The peak electric field is enhanced by more than 100 times, with the exact value depending on the substrate material, as shown in the inset of Figure 4.1d. With increasing refractive index the peak electric field enhancement decreases from 173 (ZnS) to 104 (Ge) (supplemental document: Temporal electric field enhancement). Moreover, the electric field shows an oscillating tail due to the SRR resonance.

If the enhanced electric field in the gap exceeds a certain material-dependent threshold, it provokes carrier generation in the substrate beneath the gap. Therefore, the carrier concentration and the conductivity in this volume increase. Figure 4.2a shows the simulated transmission spectra for low and high gap conductivities. Below a few hundred S/m, THz pulses couple to two distinct modes at $f_0 = 0.25\,\mathrm{THz}$ (dipole-like mode) and $f_1 = 0.85\,\mathrm{THz}$ (quadrupole-like mode). Above 3×10^4 S/m, only one mode at $f_2 = 0.75$ THz (dipole-like mode) is electrically exited with an in-plane THz polarization. Figure 4.2b shows the simulated apparent frequency shift $\Delta f/f_1 := (f_c - f_1)/f_1$ for conductivities between 10 S/m and 10^6 S/m. For intermediate conductivities (above 2000 S/m to 3×10^4 S/m) both modes (f_1 and f_2) are exited, and the superposition of the two modes has an apparent transmission minimum at f_c.

To better understand the carrier generation process, we performed time-domain simulations incorporating temporally and spatially resolved IMI [36, 37] and ZT [11, 38] (see supplemental document: Simulation details). The two processes are sketched in Figure 4.2c. In IMI, the enhanced gap electric field accelerates conduction band electrons to kinetic energies high enough to create additional carriers via collisions, resulting in a relaxed conduction band electron and an additional electron-hole pair near the band extrema [19]. On the other hand, in ZT, a strong electric field bends the bands so much that electrons tunnel from valence to conduction band. Since ZT is a momentum-conserving process, it occurs between equal wave vector states and is therefore relevant across direct band gaps [26]. While IMI cascades on femtosecond timescales, ZT is instantaneous. Both processes result in substantial carrier multiplication and a transient increase of the conductivity [39]. The critical electric fields for both processes are on the order

of 10 MV/cm (i.e., 1 V/nm), which we easily exceed given a maximum incident THz electric field strength of 300 kV/cm combined with a hundredfold field enhancement. We neglect IVS for all substrates because the associated change in effective mass would be too small to explain the required changes in conductivity. Figure 4.2d shows the carrier density after the THz pulse has interacted with the sample as a function of the gap electric field strength E_{gap}. While IMI dominates the carrier generation in Si, ZT is the main source of carriers in GaAs. In Ge, just above the critical electric field IMI as well as ZT contribute to carrier generation, however, at higher electric fields IMI becomes dominant.

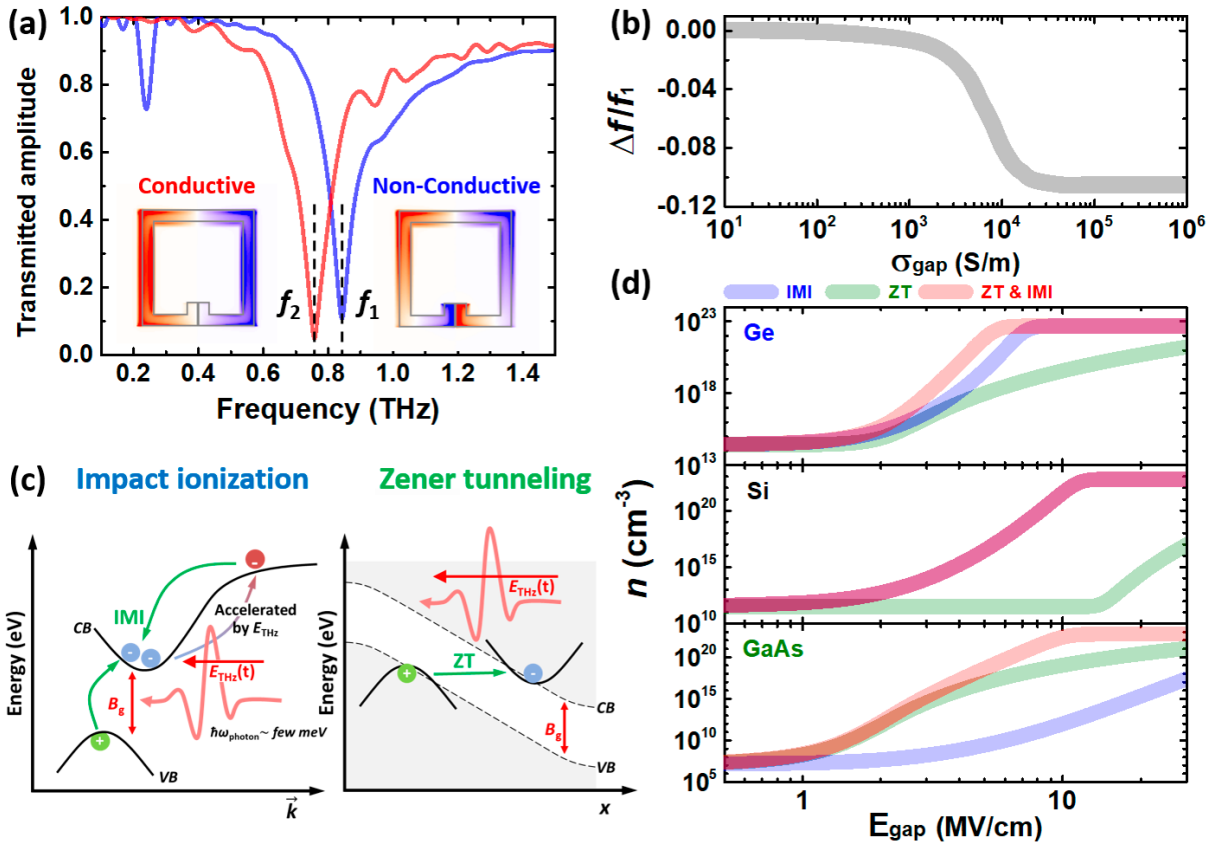

Figure 4.2: Numerical simulations. (a) Transmission spectrum of SRRs on Si for a low (< 100 S/m) and a high (> 30'000 S/m) substrate conductivity underneath the gap σ_{gap}. The insets show the charge distribution for the two modes with resonance frequencies at f_1 and f_2. (b) Apparent frequency shift as a function of the substrate conductivity underneath the gap. (c) Sketch of THz-induced IMI and ZT. (d) IMI- (blue) and ZT-induced (green) plus the total carrier concentration (red) as a function of gap electric field strength after the THz pulse has interacted with the metamaterial.

We first analyze the electric field-dependent transmission spectra up to a maximum incident electric field of 300 kV/cm (supplemental document: Experimental results). Figure 4.3a shows a false-color plot of the transmitted amplitude versus incident electric field Einc and frequency for SRRs with a small gap on Si. Up to about 30 kV/cm, we observe the low conductivity mode. Above 30 kV/cm, the apparent frequency shift starts until complete mode switching occurs for

field strengths higher than 150 kV/cm. Even before the apparent frequency shift sets in, the Q-factor decreases. It drops to about one half of its low electric field value before increasing again to its initial value, when mode switching is completed. A similar behavior was reported in reference [40].

For comparison, the simulated transmission spectra are shown in Figure 4.3b. The simulations take into account that individual SRRs in the array experience a spatially varying incident electric field due to the Gauss-shaped beam profile of the THz beam (supplemental document: Spatial averaging effect). We note that the electric field dependence of the mode switching is well reproduced.

Figure 4.3c shows the measured and the simulated apparent frequency shift, $\Delta f/f_1$, as a function of the gap electric field strength for the four different substrates. Generally, we find excellent agreement between measurements and simulations. From the apparent frequency shift we determine the critical electric field, E_c, which we define as the electric field that causes $\Delta f/f_1 = -0.01$. Tentatively, lower band gap substrates exhibit a lower critical electric field and also complete mode switching at lower electric fields. The critical electric fields at THz frequencies are very similar to those reported in the literature (see inset of Figure 4.3c) [37, 41, 42]. The results confirm that in Si the dominant carrier generation mechanism is IMI, while in GaAs it is ZT. In Ge ZT accounts for approximately 10% of the total carrier concentration at the critical electric field. Hence, the measurements confirm that ZT may seed IMI close to the critical electric field, but is overtaken by IMI with increasing electric fields [43]. In ZnS it is difficult to distinguish between IMI and ZT because the maximum incident electric field is too low to induce complete mode switching.

Further evidence as to which mechanism dominates the generation of free carriers comes from analyzing the mode switching for different gap widths. Figure 4.3d compares the measured and simulated frequency f_c as a function of the gap electric field for SRR structures featuring a small and large gap and we find good agreement. The larger gap reduces the total length of the SRR, which results in a higher f_1 irrespective of substrate. In addition, the larger gap exhibits a smaller electric field enhancement factor of order 38 to 54, resulting in a smaller gap electric field strengths for a given incident field strength. (supplemental document: Apparent frequency shift for different gap widths). While the overall trend of the mode switching is very similar for both gap widths, the critical electric fields are distinctly different. For GaAs the critical electric field seems to be independent of gap width, which would indeed be consistent with Zener tunneling. Conversely, Ge as well as Si show a lower critical electric field for the larger gap, which is explained by the dead space effect of IMI: When low-energy carriers enter the high electric field region, they have to traverse a certain distance (dead space) before they acquire sufficient energy for impact ionization [44]. This effect is usually observed in avalanche devices or PIN diodes with a sub-µm gap and it becomes significant as the interaction length decreases [45, 46].

To investigate whether the type of metal has an influence on the electric field dependence of the mode switching, we fabricated SRR structures from Aluminum (supplemental document: Influence of different metals). The experimental results indicate that mode switching as well as critical electric field do not depend on the type of metal, which allows us to rule out, for instance, carrier injection through a Schottky barrier [47].

Finally, we investigate the dynamics of mode switching by analyzing the transmitted time-dependent THz electric field. Exemplary, we focus on gold SRRs on intrinsic silicon where IMI dominates the carrier generation, but similar results are found for the other substrates

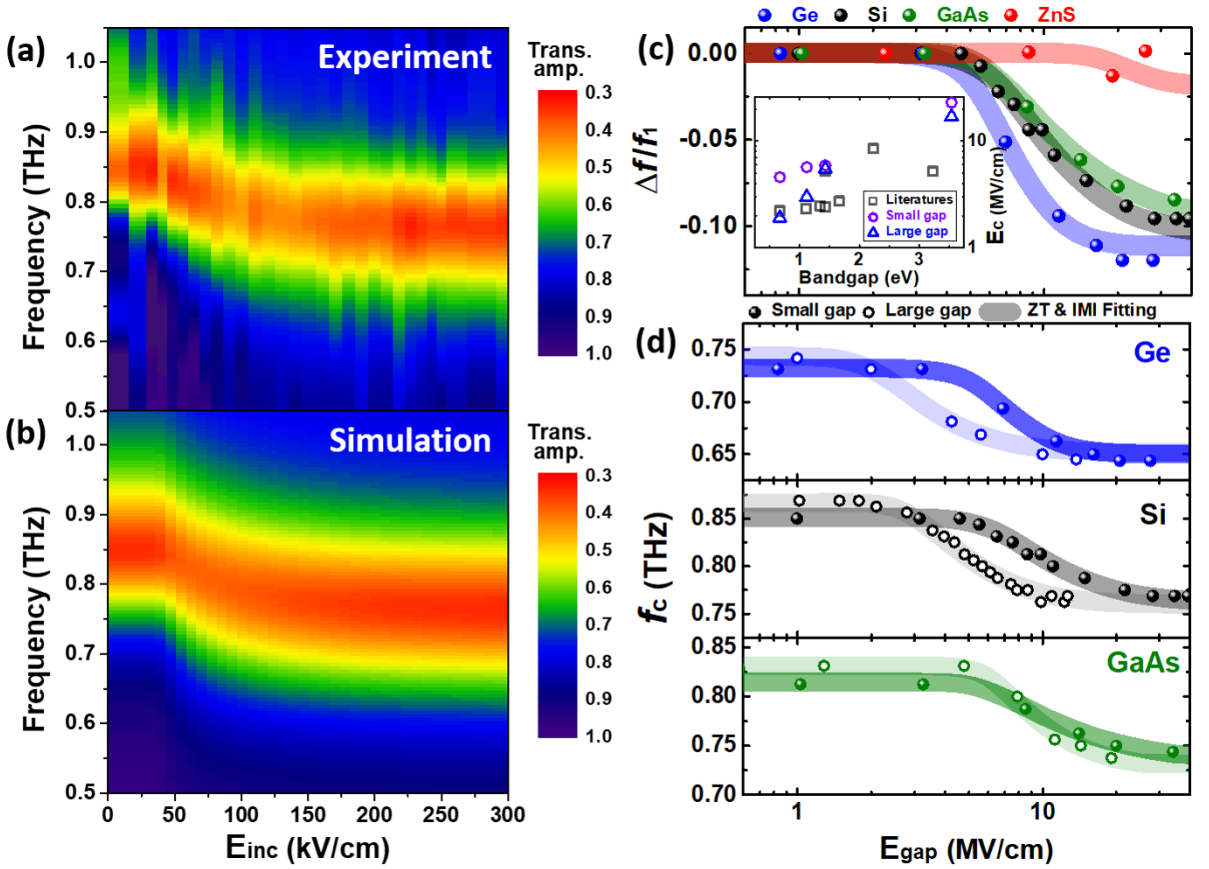

Figure 4.3: Mode switching for different band gap substrates and different gap widths. Two-dimensional false-color plot of the (a) measured and (b) simulated THz transmission spectra of Si based metamaterials versus peak electric field strength of the incident THz pulse and frequency. (c) Apparent frequency shift as a function of the electric field in the gap for different substrates (circles: experimental results; solid curves: simulation results). The inset compares measured and reported critical electric fields of IMI as a function of band gap. The purple circles and blue triangles indicate experimental results for small and large gaps, respectively, whereas the black open squares show literature values for electrons. (d) Measured (circles) and simulated (solid curves) frequency f_c for small (filled circles) and large gaps (open circles) as a function of the electric field in the gap.

as well. It is important to note that the transmitted THz far-field contains radiation that has interacted with the metamaterial but also with the bare substrate. In order to isolate the metamaterial contribution, we subtract the normalized incident THz electric field from the transmitted electric field (supplemental document: Time-domain analysis) [26]. Figure 4.4a (top) shows the resulting THz electric field as a function of time and incident peak electric field strength. Below 30 kV/cm the oscillatory signal is consistent with the low-field mode of the SRR. Above 30 kV/cm the oscillation period abruptly increases and the time of mode switching moves closer toward time zero as the peak electric field strength increases. In other words, the higher the peak electric field strength the earlier the SRR switches modes. Due to the Gaussian beam profile of the incident THz beam, not all SRRs switch at the same time and the transition

is somewhat washed out. Above approximately 150 kV/cm mode switching occurs during the time the resonator is loaded and we only observe the high conductivity mode.

Preliminary simulations, which are based on a volume-average gap electric field et cetera, provide a first glimpse on the carrier dynamics in the Si substrate beneath the gap area. Figure 4.4b, from top to bottom, shows the normalized gap electric field, the impact ionization coefficient, the accumulated carrier density, the gap conductivity, and the corresponding frequency f_c as a function of time for a low and a high peak electric field strength. Generally, the highest carrier generation rate in IMI is close to the extrema of the vector potential where kinetic energy reaches its maximum. However, when the system is heavily damped, the carrier generation tends to follow the electric field [48]. Hence, the carrier concentration and the conductivity increase in steps and, in turn, influence the subsequent THz-metamaterial interaction. As the carrier concentration increases, field screening by the newly generated carriers reduces the electric field enhancement, consequently, acting as a negative feedback to the IMI process. Screening as well as the density of states limits the maximum carrier concentration. The apparent frequency shift is more or less the mirror image of the transient conductivity and mode switching occurs when the conductivity exceeds a critical value. The two examples shown in Figure 4.4b indicate that a sufficiently high peak electric field induces a more or less instantaneous mode switching, whereas for a lower peak electric field it may take up to a few picoseconds before the conductivity reaches a value high enough to cause mode switching (supplemental document: Evolution of mode switching dynamics).

More refined simulations, taking into account the spatial variation of the gap electric field and of all derived quantities (most importantly conductivity), show a very similar picture. The simulated transmitted THz electric field as a function of time and incident peak electric field strength is depicted in Figure 4.4a (bottom) and we find excellent agreement with the experimental results. From experiments as well as simulations we establish the minimum build-up time of mode switching for the highest applied THz electric field to around 120 fs, which is shorter than one half THz cycle ($\sim$300 fs). Hence, mode switching is completed during the main cycle of the incident THz pulse, and consequently, the time evolution of the incident THz pulse should be affected by the sudden change in carrier concentration. Specifically, we expect the THz pulse to self-shorten due to the sudden onset of carrier absorption [49]. Figure 4.15 shows a false-color plot of the measured as well as simulated temporal electric field of the transmitted THz pulse as a function of time and peak electric field strengths. As expected, experiments as well as simulations indicate that the transmitted THz pulse self-shortens as the peak electric field strength increases.

In conclusion, we investigated the THz nonlinear response of two-dimensional metamaterials consisting of resonant metallic structures deposited on different high-resistivity semiconductors. The metallic split-ring resonators contain a nanometer size gap featuring a local enhancement of the electric near-field. This serves to lower the threshold above which a nonlinear response is observed and allows for studying carrier generation mechanisms in nanometer size volumes at THz frequencies. In essence, we found that carrier generation in the different semiconductors and the associated critical electric fields are consistent with those found, for instance, in standard semiconductor devices. While impact ionization dominates in Ge and Si, Zener tunneling is the main source of carrier generation in GaAs. The newly generated carriers short circuit the gap of the split-ring resonator and force it to oscillate at a different frequency. By investigating this mode switching dynamics in detail, we found that it can happen within a few hundred femtoseconds. These findings make such two-dimensional metamaterials an interesting platform

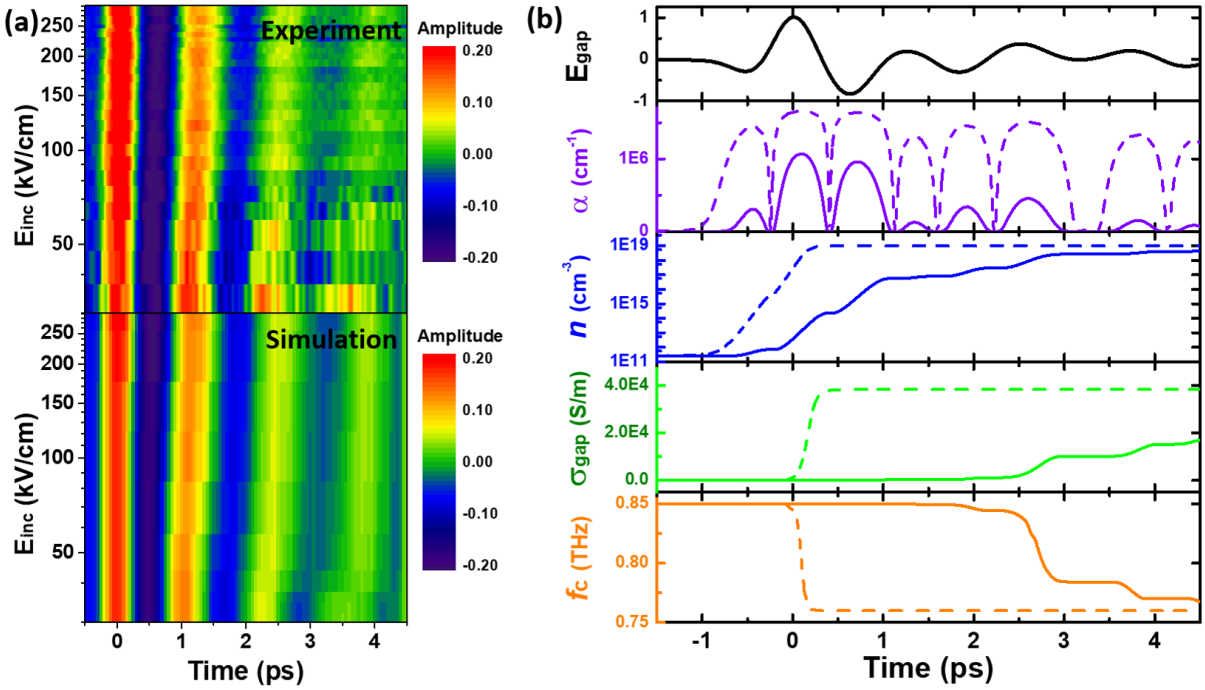

Figure 4.4: Time-domain analysis of the THz-induced mode switching dynamics in Si. (a) False-color plot of the transmitted minus incident THz signal as a function of time and incident electric field strength. Top panel: experiment; bottom panel: simulation. The dashed white lines are a guide to the eye. (b) Detailed time-domain simulations, from top to bottom: normalized THz electric field in the gap (black), IMI coefficient (purple), carrier density (blue), gap conductivity (green), and corresponding frequency f_c (orange) for a low electric field (solid curves) and a strong electric field (dashed curves).

for single-photon detection, nonlinear devices operating at ultrahigh speeds, or fundamental research on 2D materials, liquids, or magnetic materials. Further, the observed nonlinear mode switching can be made reversible, for instance, by using a substrate with an ultrashort carrier lifetime [50] or functional nano-structures that can extract carriers, paving the way toward ultrafast modulators.

4.2 Supplemental document

4.2.1 Details on the fabrication procedure for split-ring resonators

To fabricate arrays of SRRs featuring a nm-sized gap with extended internal capacitive faces, we applied electron-beam lithography, evaporation of metal, and a lift-off procedure to high-resistivity semiconductors (see Figure 4.5). In detail, the first step is the deposition of a double layer of photoresist (PR) by spin coating (positive PR1 and positive PR2). Then the SRR pattern is directly written into the photoresist using electron-beam lithography. After removing the resist affected by the e-beam, a small undercut remains since the bottom layer is more sensitive to e-beam radiation. In a third step, a thin adhesion layer of chromium and the respective metal are deposited on top of the sample by evaporation. Finally, the remaining resist

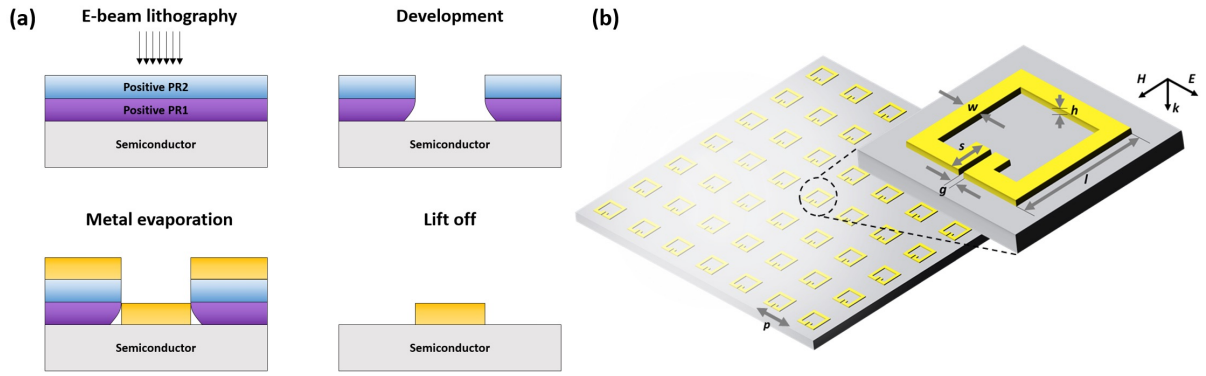

Figure 4.5: (a) Schematic of the fabrication procedure for THz SRR. (b) Geometry of a single SRR, the SRR array, and the (E, H, k) triad of the incident THz field with all relevant dimensions.

together with the mfetal is removed by the lift-off technique. The resulting sample consists, for instance, of a 60-nm-thick Au layer with a 2-nm-thick Cr adhesion layer on a silicon substrate. The relevant dimensions of the SRR structure are depicted in Figure 4.5b (length of the split ring $l = 51\,\mu\text{m}$, width $w = 5\,\mu\text{m}$, extended length of capacitive faces $s = 10\,\mu\text{m}$, thickness of metal $h = 60\,\text{nm}$, gap width $g = 80\,\text{nm}$ and $\sim 200\text{nm}$, and period of SRRs $p = 102\,\mu\text{m}$). The total area covered by SRRs was 2 mm by 2 mm. All samples were characterized by scanning electron microscopy.

4.2.2 Nonlinear THz time-domain spectroscopy setup

The nonlinear THz spectroscopy system to measure the THz field- and the time-dependent nonlinear response of the samples is shown in Figure 4.6. The pump source for THz wave generation was an optical parametric amplifier system (HE-TOPAS, Light Conversion) emitting 100-fs pulses at a wavelength of 1300 nm and pumped by a 1-kHz Ti:sapphire regenerative amplifier system (Legend Elite Duo, Coherent; $\lambda = 800$ nm, 90 fs pulse duration, 8 W average power). The intense THz pulses were generated by collinear optical rectification with wavefront control in a 0.54-mm-thick nonlinear organic crystal OH1 [51], which has a huge nonlinear coefficient near 1300 nm. The THz source was imaged to the sample position by a combination of two 90-degree off-axis parabolic mirror with focal lengths of 9 inches and 2 inches, resulting a 4.5:1 imaging ratio. The time-dependent THz electric field was recorded by electro-optic sampling using a 0.3-mm-thick $\langle 110 \rangle$ GaP crystal attached to a 3-mm-thick $\langle 100 \rangle$ GaP crystal and a 90 fs scanning probe beam at 800 nm. The corresponding THz spectra were obtained by fast Fourier transformation of the time traces. To determine the THz electric field strength, we, in addition, measured the THz pulse energy and the THz spatial profile at the sample position. The maximum electric field strength was found to be around 300 kV/cm and the corresponding THz spectral amplitude shows a center frequency of 0.85 THz with a bandwidth of 1.1 THz (FWHM) and an almost constant electric field strengths between 0.7 and 1 THz where the samples have their resonance frequencies. We used two pairs of wire-grid polarizers before and after the sample to attenuate the THz electric field at the sample position while keeping it constant at the electro-optic sampling crystal.

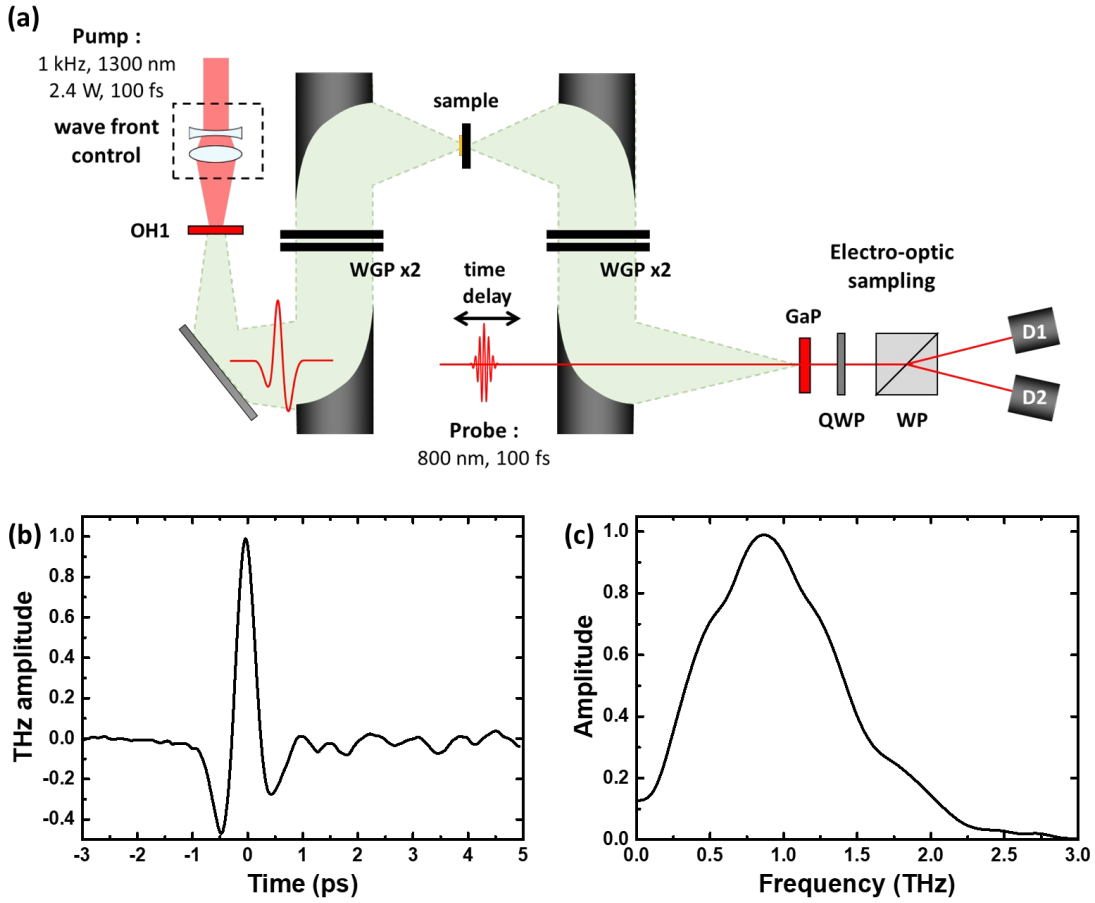

Figure 4.6: (a) Nonlinear THz spectroscopy system based on an OH1 organic crystal with wave front control. (b) Normalized time trace of the THz electric field $E_{THz}(t)$ generated in OH1 and (c) the corresponding normalized THz spectral amplitude $E_{THz}(f)$.

4.2.3 Resonant features and temporal electric field enhancement

Figure 4.7a shows the simulated transmission spectra for two identical SRR arrays with a non-conductive and a conductive substrate below the gap. The lowest resonance frequency f_0 around 0.2-0.3 THz exhibits a small oscillator strength and is entirely quenched for non-zero conductivities. The next higher frequency mode at f_1 shows a much larger oscillator strength and switches to a lower frequency mode at f_2 for non-zero conductivities but the oscillator strength and linewidth remain almost unaffected. The geometry of the SRRs was selected such that the second resonance coincides with the maximum spectral intensity of the incident THz pulses. The different false-color plots show the normalized amplitude of the electric field component normal to the surface and 5 µm above the surface for frequencies indicated by arrows. The normal electric field component is proportional to the spatial distribution of the carrier density in the SRR and indicates a charge accumulation across the gap at the second resonance for a non-conductive substrate and a very symmetric charge distribution for the conductive case, which essentially results from a short-circuited gap. Figure 4.7b compares the simulated (CST Studio Suite) to the measured normalized transmission for different substrates

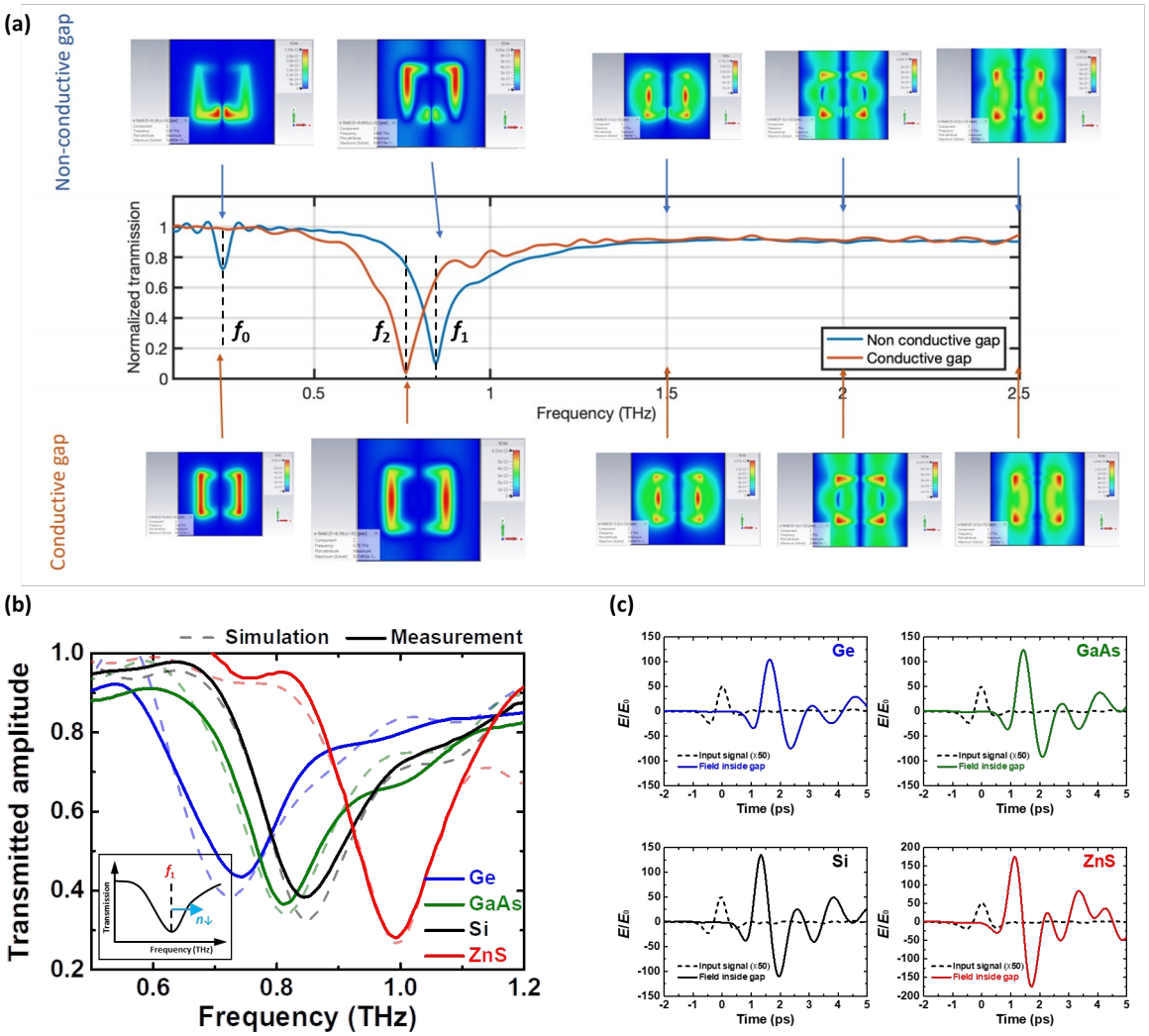

Figure 4.7: (a) Simulated transmission spectra for two identical SRR arrays with a non-conductive and a conductive substrate below the gap. The two-dimensional color maps show the normalized amplitude of the electric field normal to the substrate 5 µm above the surface at frequencies indicated by arrows. (b) Zoom around the resonance frequency f_1 comparing measured (solid curves) and simulated (dashed curves) transmission for four different substrate materials (blue: Ge; green: GaAs; black: Si; red: ZnS). (c) Measured incident THz electric field (dashed black curves) and simulated gap electric fields indicating the electric field enhancement for the different substrate materials.

around the second resonance f_1 and we generally find very good agreement. Next, we use the measured incident THz electric field as an input for the simulations to determine the gap electric field (20 nm beneath the substrate surface) for a non-conductive substrate below the gap, as shown in Figure 4.7c. We find that the electric field enhancement decreases for increasing refractive index of the substrate, which can be explained by the modal expansion based on the perfect electric conductor (PEC) model, $|\frac{E_{gap}}{E_0}| \sim \frac{n_{sub}+1}{2} \frac{\lambda}{\frac{\epsilon_{sub}}{\epsilon_0}\pi h}$ where ϵ_{sub} is the relative

permittivity of the considered substrate, n_{sub} is the refractive index of the substrate, and h is the gold thickness [52, 53]. We also observed that the gap field oscillation frequency increases with the refractive index of the substrate in accordance with Figure 4.7b. Moreover, the reduced resonance amplitude as shown in Figure 4.7b is explained by the decrease of the remaining gap electric field when the refractive index of the surrounding medium increases [54].

4.2.4 Simulation of time-dependent carrier generation

Impact ionization

To simulate the electric field-dependent impact ionization, we adopted the Okuto-Crowell model [37]. In this model the carrier generation rate is given by

$$\frac{\mathrm{d}n}{\mathrm{d}t} = n v_{sat} \alpha_n \left| \frac{n_0 - n}{n_0} \right| \tag{4.1}$$

with

$$\alpha_n = A_n \exp\left(- \left(\frac{B_n}{|E|} \right)^{C_n} \right) \tag{4.2}$$

$|E|$ is the applied electric field strength in the substrate and $v_{sat} = \sqrt{\frac{E_{op}}{2 m_{cc} m_0}}$ is the saturation velocity, where E_{op} is the optical phonon energy, m_{cc} is the effective mass of conduction band electron, and m_0 is the electron mass. All parameters used are listed in Table 4.1.

Correction factors between 1 and 2 are used to match the threshold electric field strength with the measured values for the different materials. The substrate conductivity is given by $\sigma = \frac{e^2 n}{m_{cc} m_0} \frac{\gamma}{\omega_0^2 + \gamma^2}$ where ω_0 is the resonance frequency and $\gamma = 1/\tau$ is the damping constant. Note that carrier multiplication can be saturated by Pauli blocking considering the limited density of states in the conduction band. It's also worth noting that the calculated IMI coefficients are higher than those reported from DC measurements [44], because the applied THz electric field strengths can be higher than the dielectric DC breakdown voltage without causing any damage [55] The IMI rate is still below Okuto limit and also below previously reported values in the silicon with an initial carrier density of 1.5×10^{10} [25, 37]. Figure 4.8 compares the impact ionization rates for the different substrate materials as a function of the inverse of the applied electric field.

Interband Zener tunneling

Figure 4.9 compares the interband tunneling rates for the four different substrate materials as a function of the electric field as calculated from Kane's model [11, 38]

$$r_{ZT} = \frac{e^2 |E|^2 (m_r^* m_0)^{1/2}}{18 \pi \hbar^2 E_g^{1/2}} \exp\left(\frac{-\pi (m_r^* m_0)^{1/2} E_g^{3/2}}{2 \hbar e |E|} \right) \tag{4.3}$$

where $|E|$ is the applied electric field, E_g is the bandgap energy, and m_r^* is the reduced effective mass.

4.2.5 Summary of model parameters

Table 4.1 summarizes all parameters used in the two carrier generation models.

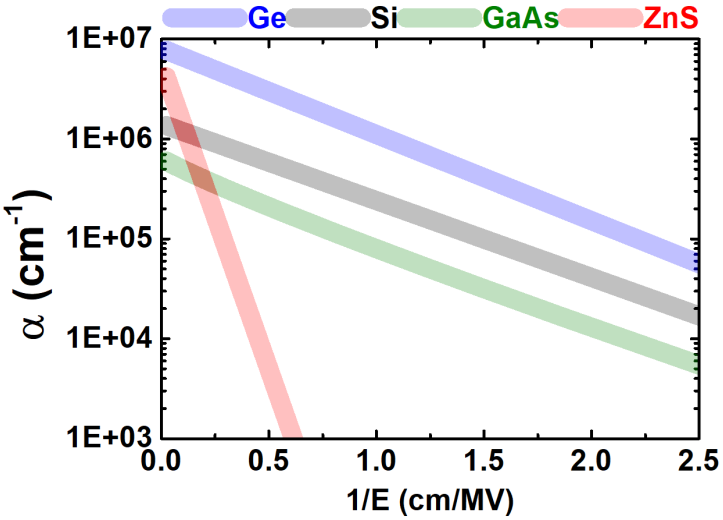

Figure 4.8: Impact ionization rate for different materials (Ge: blue; Si: gray; GaAs: green; ZnS: red) as a function of the inverse applied electric field.

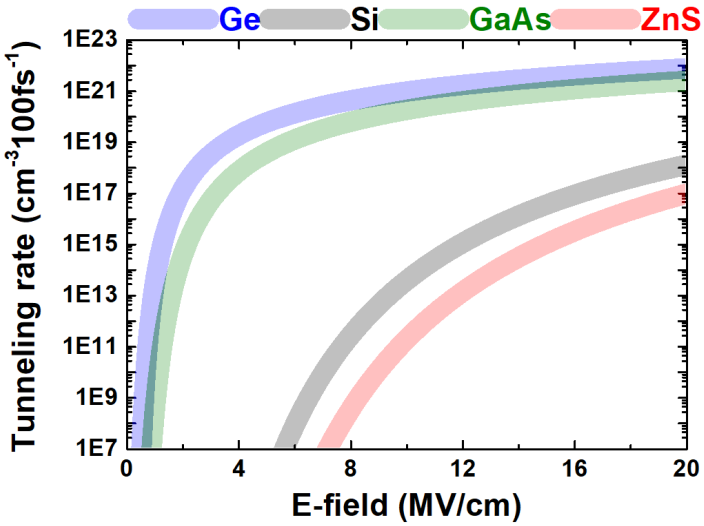

Figure 4.9: Interband tunneling rate for different substrate materials (Ge: blue; Si: gray; GaAs: green; ZnS: red) as a function of the electric field.

4.2.6 Detailed comparison between experimental and simulation results of SRRs on different semiconductor substrates

Figure 4.10 summarizes experimental as well as simulation results on the electric field dependence of the mode switching process for all four different semiconductor substrates, i.e. (a) Germanium (Ge, n = 4, E_g = 0.67 eV, indirect bandgap), (b) Silicon (Si, n = 3.42, E_g = 1.12 eV, indirect bandgap), (c) Gallium Arsenide (GaAs, n = 3.6, E_g = 1.43 eV, direct bandgap), and (d) Cubic Zinc Sulfide (zincblende, β-ZnS, n = 2.9, E_g = 3.7 eV, direct bandgap). The top left plots compare the measured with the simulated frequencies f_c and we find excellent

Table 4.1: Simulation parameters for the different semiconductor substrates [38, 48, 56–61]

Parameter	**Ge substrate**	**Si substrate**	**GaAs substrate**	**ZnS substrate**
Small gap	80 nm	80 nm	80 nm	80 nm
Large gap	200 nm	230 nm	200 nm	240 nm
F.E. (Small gap)	104	135	124	173
F.E. (Large gap)	38	44	45	54
A_n	8.04×10^6 cm^{-1}	7.03×10^5 cm^{-1}	6.39×10^5 cm^{-1}	5.9×10^6 cm^{-1}
B_n	$\frac{1.4 \times 10^6 \text{ V/cm}}{\sqrt{2(1+(\omega_0\tau)^2)}}$	$\frac{1.23 \times 10^6 \text{ V/cm}}{\sqrt{2(1+(\omega_0\tau)^2)}}$	$\frac{1.6 \times 10^6 \text{ V/cm}}{\sqrt{2(1+(\omega_0\tau)^2)}}$	$\frac{9.6 \times 10^6 \text{ V/cm}}{\sqrt{2(1+(\omega_0\tau)^2)}}$
C_n	1	1	0.9	1
Initial carrier density n_{ini}	2.4×10^{14} cm^{-3}	2.5×10^{11} cm^{-3}	1×10^7cm^{-3}	1×10^{10} cm^{-3}
Mean free path mfp	3.6 nm	4.8 nm	3.3 nm	3.2 nm
Relaxation time $\tau = \frac{mfp}{v_{sat}}$	17.83 fs	36.55 fs	19.42 fs	45 fs
Density of states in conduction band	3×10^{25} m^{-3}	3×10^{25} m^{-3}	4.4×10^{23} m^{-3}	1×10^{25} m^{-3}
Number of atoms n_0	4.42×10^{28} m^{-3}	5×10^{28} m^{-3}	4.42×10^{28} m^{-3}	2.5×10^{28} m^{-3}
Optical phonon energy E_{op}	0.019 eV	0.051 eV	0.022 eV	0.033 eV
Effective mass of conduction band electron m_{cc}	0.12	0.26	0.067	0.28
Reduced effective mass m_r^*	0.058	0.25	0.037	0.28
E_g (indirect)	0.66 eV	1.12 eV		
E_g (direct)	0.8 eV	3.4 eV	1.42 eV	3.7 eV

agreement for all substrates. In addition, the simulations reproduce the intermediate increase of the transmission amplitude reasonably well (top right). Note that an increase in transmission corresponds to a decrease in resonance amplitude. The reduction in amplitude or Q-factor at intermediate electric fields relates to the mode switching after the resonator has started to oscillate. This change in resonance frequency during the exponentially decaying oscillation causes a broadening and a decrease of the resonance amplitude. For sufficiently high electric fields, the mode switches before the resonator is fully loaded and the Q-factor is restored to its initial value (note that both resonances have very similar Q-factors). For the substrate with the largest bandgap, i.e. ZnS, we observe a decrease of the Q-factor, but no discernible mode switching, up to the highest electric fields applied (300 kV/cm). Even though the electric field enhancement for ZnS is the largest, the larger bandgap greatly reduces the carrier generation rate leading to a conductivity, even for the maximum incident THz electric field, which is too low to cause a detectable mode switching. Based on our simulation, considering IMI as the sole source of

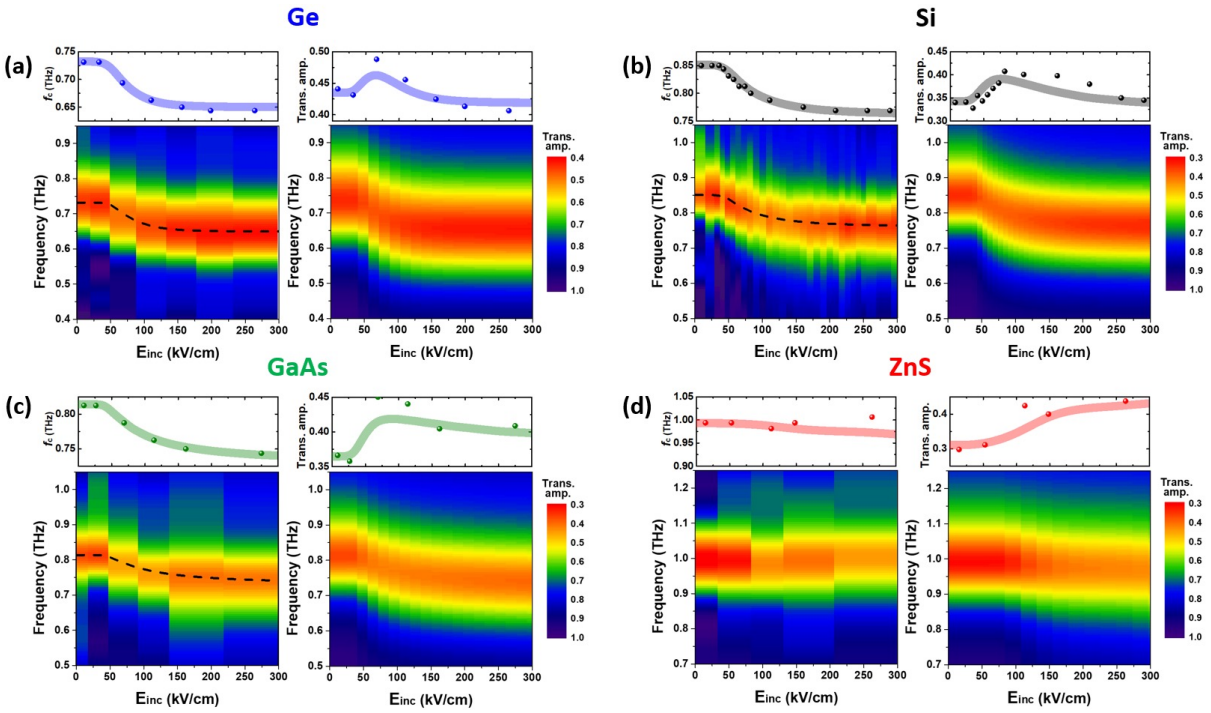

Figure 4.10: For all four substrate materials, i.e. Ge (a), Si (b), GaAs (c), and ZnS (d), we show the frequency f_c (top left), the transmitted amplitude (top right), and false-color plots of the measured (bottom left) and the simulated (bottom right) transmission spectra as a function of the incident electric field. The two plots at the top show experimental (filled circles) as well as simulation results (shaded curves).

carriers, ionization should should set in for electric field strengths in excess of 200 kV/cm, resulting in apparent resonance shift. However, impact ionization might be suppressed or in competition with inter-valley scattering because of ZnS's large bandgap ($\sim$ 3.7 eV), which is much larger than the inter-valley energy difference ($\sim$ 1.3 eV for $\Gamma \Longleftrightarrow X$ and $\sim$ 1.4 eV for $\Gamma \Longleftrightarrow L$) [62–64]. As a consequence, when electrons are accelerated to an energy of $\sim$ 1.3 eV, IMI starts to compete with scattering from the Γ valley to the X or L valley [65]. Inter-valley scattering leads to an increase in effective mass and a pronounced reduction of carrier mobility, thus resulting in a damping of the plasmonic resonance, thereby reducing the Q-factor [20]. Hence, it can be speculated that the competition between IMI and IVS hinders an increase in conductivity shifting the critical electric field beyond 200 kV/cm [66].

4.2.7 Spatial averaging over THz beam profile

In the electromagnetic (EM) simulations with CST Studio Suite we use a spatially uniform (plane wave) pulsed THz excitation and a single SRR with periodic boundary conditions in the two dimensions perpendicular to the wavevector of the incident THz pulse. Hence, all SRRs experience the same electric field strength. Conversely, in the experiment the THz pulses have a spatial beam profile, which is, to a good approximation, Gauss-shaped with a diameter of approximately 0.7 mm (compared to the sample area of 2×2 mm^2 containing 21 by 21 SRRs).

Hence, individual SRRs experience different electric field strengths depending on their relative position with respect to the spatial profile of the THz pulses. When the THz electric field strength exceeds a certain threshold only the SRRs close to the center of the THz beam start to experience a noticeable carrier generation. With a further increase of the THz electric field, more and more SRRs start to undergo mode switching. Consequently, the measured global response is a superposition of SRRs experiencing a spatially dependent apparent frequency shift. We consider this effect in the simulations by modeling the spatial dependence of the THz electric field $E(x, y)$ with a Gaussian beam profile:

$$E(x, y) = E_{peak} \mathrm{e}^{-\left(\frac{p(x,y)}{\omega_0}\right)^2} \tag{4.4}$$

where E_{peak} is the peak electric field, $p(x, y)$ describes the position of each unit cell (SRR), and ω_0 is the beam waist. Each SRR in the array of 21×21 SRRs is included in the simulations and is subject to an electric field given by its spatial position.

4.2.8 Apparent frequency shift for different gap widths

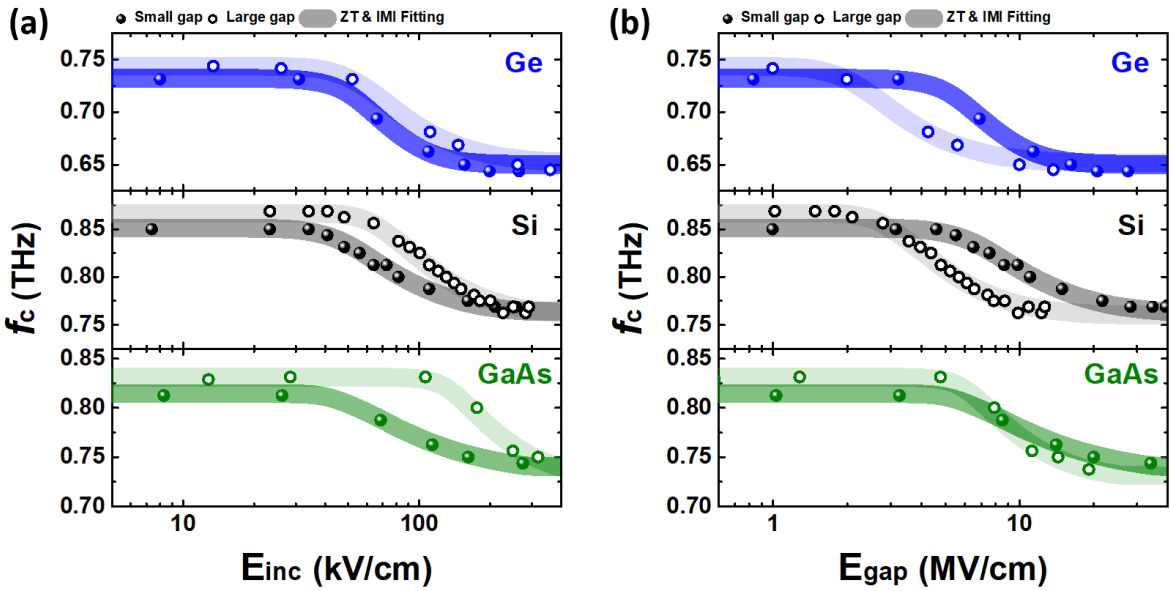

Figure 4.11: Measured (circles) and simulated (solid curves) frequency f_c for small (filled circles) and large gaps (open circles) as a function of (a) incident THz electric field strength and (b) gap electric field strength.

Figure 4.11 compares the measured and simulated frequency f_c as a function of (a) incident THz electric field strength and (b) gap electric field strength for SRR structures featuring a small and large gap. We find a smaller critical "incident" electric field strength for smaller gaps in all semiconductors. The carriers in smaller gaps are accelerated more rapidly to reach the energy required to induce impact ionization at the same incident electric field. The picture changes when we plot the apparent frequency shift versus gap electric field strength because a larger gap has a smaller electric field enhancement factor. Now we find smaller critical electric fields for the larger gap in the case of Ge and Si, and similar critical electric fields for GaAs.

This is explained by the dead space effect of IMI, which is not found in GaAs, where carrier generation is dominated by ZT.

4.2.9 Influence of different metals and gap geometry

In order to establish the role of the metal in mode switching, we fabricated identical SRR arrays from gold and aluminum. In addition, we changed the geometry of the gap to find out whether this influences the observed behavior.

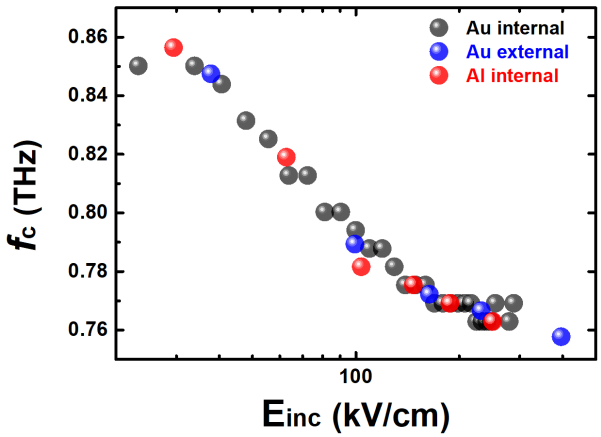

Figure 4.12: Frequency f_c as a function of incident THz electric field strength for SRRs made from different metals, i.e. gold and aluminum, and with different gap geometries.

Figure 4.12 shows the frequency f_c of SRRs fabricated with gold or aluminum and with two different gap geometries as a function of incident THz electric field strength. In one geometry, the extended gap was pointing toward the center of the SRR (internal) and in the other geometry away from the SRR (external). In all three cases, we find the identical electric field dependence, strongly suggesting that carrier injection through the metal-semiconductor interface as well as gap geometry have a negligible effect on the mode switching behavior of the SRRs.

4.2.10 Time-domain analysis

The transmitted THz signal is composed of two parts, the transmitted incident pulse and the polarization emitted from the driven SRR array. In order to better visualize the SRR response, we subtract a time-dependent reference signal (measured for the substrate alone) from the time-dependent sample signal (see Figure 4.13 and for details also Ref [26]), $E_{em}(t) = \frac{E_{sam}(t) - E_{ref}(t)}{E_{ref,peak}}$ where $E_{em}(t)$ is the polarization emitted from the SRR array, $E_{sam}(t)$ is the THz signal transmitted through the sample, $E_{ref}(t)$ is the THz signal transmitted through the substrate only, and $E_{ref,peak}$ is the peak electric field strength of $E_{ref}(t)$. This procedure allows separating the resonator response from the 'background' for the different THz electric field strengths. Note that the sample is very thin (60 nm), hence we neglect the delay (∼0.2 fs) introduced by the sample.

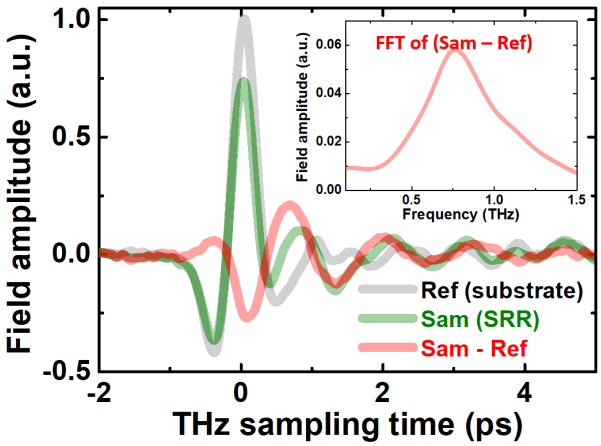

Figure 4.13: Normalized time-dependent THz electric field of pulses passing through the substrate only (grey, reference) and sample (green). The red curve labeled 'Sam-Ref' shows the difference between the time-dependent THz signal transmitted through the sample (green) and the reference (grey). The inset shows the corresponding spectrum.

4.2.11 Evolution of mode switching dynamics

Exemplary, we simulated the electric field-dependent carrier dynamics for an SRR array on a silicon substrate, where only IMI is of relevance, with the aim to extract the build-up time of mode switching. We define the build-up time as the time it takes for the conductivity to increase from σ_1 to σ_2, where σ_1 (σ_2) is the conductivity at which the apparent frequency has shifted by 10% (90%) of its asymptotic high electric field value (100%), as shown in Figure 4.14a and 4.14b. While 10% of the apparent frequency shift is found at a conductivity of approximately 1800 S/m, 90% of the shift corresponds to a conductivity of 15500 S/m. Figure 4.14c shows the times t_1 and t_2 at which the conductivity reachs σ_1 and σ_2, respectively, as a function of the incident THz electric field strength. The build-up time, i.e. $t_2 - t_1$, decreases from 2 ps to 120 fs within the range of electric fields simulated. It goes without saying that the build-up time depends on the selection of the conductivities σ_1 and σ_2, hence, we show the build-up time also for 1% to 99%, 5% to 95%, 10% to 90%, and 20% to 80% in Figure 4.14d. Irrespective of the definition of the build-up time, carrier multiplication by IMI causes mode switching within a few hundreds of femtoseconds, which is less than one period of the driving THz field.

4.2.12 THz pulse self-shortening

Since mode switching is, at least for above threshold electric fields, completed within the duration of the incident THz pulse, the time evolution of the transmitted incident THz pulse (the part not interacting with the SRRs) should be affected by the sudden change in carrier concentration. For instance, we might expect a spectral blue shift due to a varying temporal phase associated with the increasing carrier density, or a self-shortening of the temporal amplitude, due to a sudden onset of carrier-induced THz absorption. To shed more light on this aspect, we show a false-color plot of the leading and the trailing edges of the main THz peak transmitted through an SRR array on a silicon substrate, see Figure 4.15. Indeed experiments as well as simulations show a slight self-shortening for the highest electric fields applied. Moreover, we

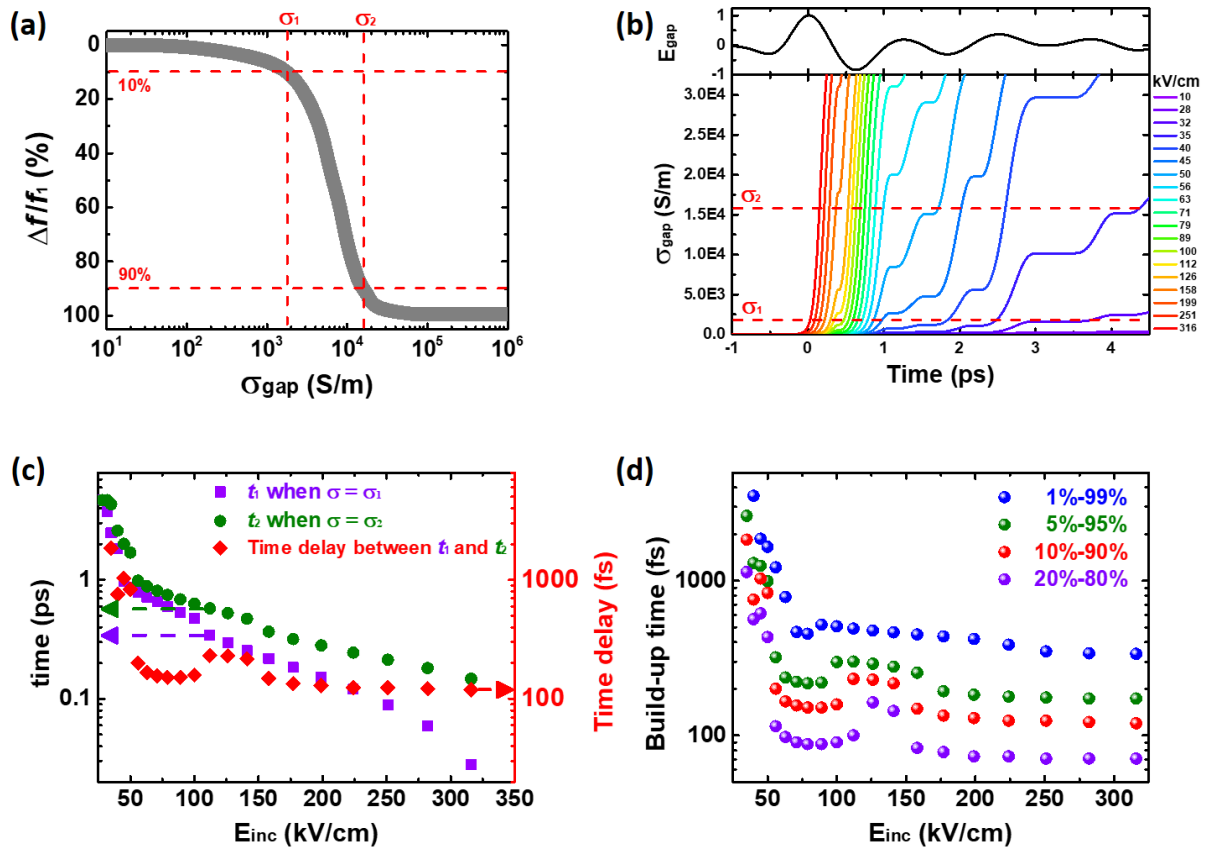

Figure 4.14: Simulated apparent frequency shift rescaled to range of 0 to 100% as a function of the substrate conductivity underneath the gap. The dashed red lines indicate a 10% and 90% apparent frequency shift and the corresponding conductivities σ_1 and σ_2. (b) Simulated time-dependent conductivity for different THz gap electric fields. For comparison we show the normalized THz gap electric field. (c) The purple squares and the green circles indicate the times t_1 and t_2 at which the conductivity reaches σ_1 and σ_2, respectively, as a function of incident THz electric field strength. The red diamonds show the build-up time $(t_2 - t_1)$. (d) Build-up time as a function of incident THz electric field strength for different threshold pairs, i.e. 1%-99%, 5%-95%, 10%-90%, and 20%-80%.

find the self-shortening to coincide with the broadening of the first half cycle in Figure 4.4a, which in turn, suggests that IMI is the dominant carrier generation mechanism.

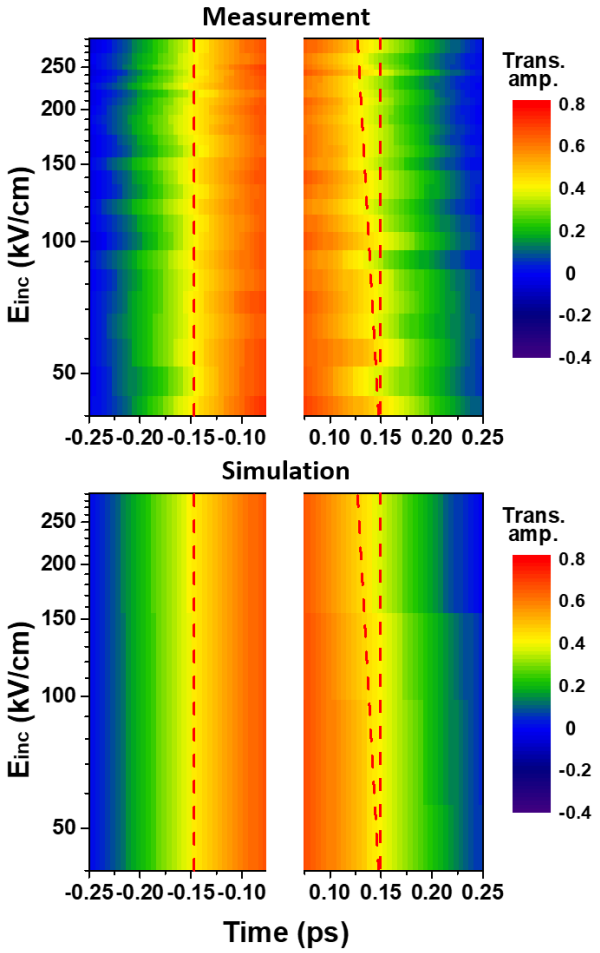

Figure 4.15: The false-color plot of the leading and trailing edges of the main peak of the transmitted THz signal as a function of time and incident electric field strength. Top panel: experiment; bottom panel: simulation. The dashed lines are a guide for the eyes to emphasize the pulse self-shortening effect.

Bibliography

[1] D. R. Smith, J. B. Pendry, and M. C. K. Wiltshire, "Metamaterials and Negative Refractive Index", Science (80-.). **305**, 788–792 (2004), https://doi.org/10.1126/science.1096796.

[2] M. Choi, S. H. Lee, Y. Kim, S. B. Kang, J. Shin, M. H. Kwak, K.-Y. Kang, Y.-H. Lee, N. Park, and B. Min, "A terahertz metamaterial with unnaturally high refractive index", Nature **470**, 369–373 (2011), https://doi.org/10.1038/nature09776.

[3] O. Hess, J. B. Pendry, S. A. Maier, R. F. Oulton, J. M. Hamm, and K. L. Tsakmakidis, "Active nanoplasmonic metamaterials", Nat. Mater. **11**, 573–584 (2012), https://doi.org/10.1038/nmat3356.

[4] S. Lee, S. Baek, T.-T. Kim, H. Cho, S. Lee, J.-H. Kang, and B. Min, "Metamaterials for Enhanced Optical Responses and their Application to Active Control of Terahertz Waves", Adv. Mater. **32**, 2000250 (2020), https://doi.org/10.1002/adma.202000250.

[5] N. I. Zheludev and Y. S. Kivshar, "From metamaterials to metadevices", Nat. Mater. **11**, 917–924 (2012), https://doi.org/10.1038/nmat3431.

[6] I. Staude and J. Schilling, "Metamaterial-inspired silicon nanophotonics", Nat. Photonics **11**, 274–284 (2017), https://doi.org/10.1038/nphoton.2017.39.

[7] M. Liu, H. Y. Hwang, H. Tao, A. C. Strikwerda, K. Fan, G. R. Keiser, A. J. Sternbach, K. G. West, S. Kittiwatanakul, J. Lu, S. A. Wolf, F. G. Omenetto, X. Zhang, K. A. Nelson, and R. D. Averitt, "Terahertz-field-induced insulator-to-metal transition in vanadium dioxide metamaterial", Nature **487**, 345–348 (2012), https://doi.org/10.1038/nature11231.

[8] M. Fleischhauer, A. Imamoglu, and J. P. Marangos, "Electromagnetically induced transparency: Optics in coherent media", Rev. Mod. Phys. **77**, 633–673 (2005), https://link.aps.org/doi/10.1103/RevModPhys.77.633.

[9] K. Lee, J. Park, B. J. Kang, W. T. Kim, H.-D. Kim, S. Baek, K. J. Ahn, B. Min, and F. Rotermund, "Electrically Controllable Terahertz Second-Harmonic Generation in GaAs", Adv. Opt. Mater. **8**, 2000359 (2020), https://doi.org/10.1002/adom.202000359.

[10] H. Merbold, A. Bitzer, and T. Feurer, "Second harmonic generation based on strong field enhancement in nanostructured THz materials", Opt. Express **19**, 7262–7273 (2011), https://opg.optica.org/oe/abstract.cfm?URI=oe-19-8-7262.

[11] C. Lange, T. Maag, M. Hohenleutner, S. Baierl, O. Schubert, E. R. J. Edwards, D. Bougeard, G. Woltersdorf, and R. Huber, "Extremely Nonperturbative Nonlinearities in GaAs Driven by Atomically Strong Terahertz Fields in Gold Metamaterials", Phys. Rev. Lett. **113**, 227401 (2014), https://link.aps.org/doi/10.1103/PhysRevLett.113.227401.

[12] T. Dong et al., "Nonlinear THz-Nano Metasurfaces", Adv. Funct. Mater. **31**, 2100463 (2021), https://doi.org/10.1002/adfm.202100463.

[13] J.-H. Kang, D.-S. Kim, and M. Seo, "Terahertz wave interaction with metallic nanostructures", Nanophotonics **7**, 763–793 (2018), https://doi.org/10.1515/nanoph-2017-0093.

[14] M. A. Seo, H. R. Park, S. M. Koo, D. J. Park, J. H. Kang, O. K. Suwal, S. S. Choi, P. C. M. Planken, G. S. Park, N. K. Park, Q. H. Park, and D. S. Kim, "Terahertz field enhancement by a metallic nano slit operating beyond the skin-depth limit", Nat. Photonics **3**, 152–156 (2009), https://doi.org/10.1038/nphoton.2009.22.

[15] S. Koo, M. S. Kumar, J. Shin, D. Kim, and N. Park, "Extraordinary Magnetic Field Enhancement with Metallic Nanowire: Role of Surface Impedance in Babinet's Principle for Sub-Skin-Depth Regime", Phys. Rev. Lett. **103**, 263901 (2009), https://link.aps.org/doi/10.1103/PhysRevLett.103.263901.

[16] H. Tao, W. J. Padilla, X. Zhang, and R. D. Averitt, "Recent Progress in Electromagnetic Metamaterial Devices for Terahertz Applications", IEEE J. Sel. Top. Quantum Electron. **17**, 92–101 (2011), https://doi.org/10.1109/JSTQE.2010.2047847.

[17] G. Li, S. Zhang, and T. Zentgraf, "Nonlinear photonic metasurfaces", Nat. Rev. Mater. **2**, 17010 (2017), https://doi.org/10.1038/natrevmats.2017.10.

[18] H. A. Hafez, X. Chai, A. Ibrahim, S. Mondal, D. Férachou, X. Ropagnol, and T. Ozaki, "Intense terahertz radiation and their applications", J. Opt. **18**, 093004 (2016), https://doi.org/10.1088/2040-8978/18/9/093004.

[19] T. Kampfrath, K. Tanaka, and K. A. Nelson, "Resonant and nonresonant control over matter and light by intense terahertz transients", Nat. Photonics **7**, 680–690 (2013), https://doi.org/10.1038/nphoton.2013.184.

[20] H. R. Seren, J. Zhang, G. R. Keiser, S. J. Maddox, X. Zhao, K. Fan, S. R. Bank, X. Zhang, and R. D. Averitt, "Nonlinear terahertz devices utilizing semiconducting plasmonic metamaterials", Light Sci. Appl. **5**, e16078–e16078 (2016), https://doi.org/10.1038/lsa.2016.78.

[21] P. Gaal, K. Reimann, M. Woerner, T. Elsaesser, R. Hey, and K. H. Ploog, "Nonlinear Terahertz Response of n-Type GaAs", Phys. Rev. Lett. **96**, 187402 (2006), https://link.aps.org/doi/10.1103/PhysRevLett.96.187402.

[22] K. Fan, H. Y. Hwang, M. Liu, A. C. Strikwerda, A. Sternbach, J. Zhang, X. Zhao, X. Zhang, K. A. Nelson, and R. D. Averitt, "Nonlinear Terahertz Metamaterials via Field-Enhanced Carrier Dynamics in GaAs", Phys. Rev. Lett. **110**, 217404 (2013), https://link.aps.org/doi/10.1103/PhysRevLett.110.217404.

[23] J. C. Cao, "Interband Impact Ionization and Nonlinear Absorption of Terahertz Radiation in Semiconductor Heterostructures", Phys. Rev. Lett. **91**, 237401 (2003), https://link.aps.org/doi/10.1103/PhysRevLett.91.237401.

[24] A. T. Tarekegne, K. Iwaszczuk, M. Zalkovskij, A. C. Strikwerda, and P. U. Jepsen, "Impact ionization in high resistivity silicon induced by an intense terahertz field enhanced by an antenna array", New J. Phys. **17**, 43002 (2015), https://dx.doi.org/10.1088/1367-2630/17/4/043002.

[25] A. T. Tarekegne, H. Hirori, K. Tanaka, K. Iwaszczuk, and P. U. Jepsen, "Impact ionization dynamics in silicon by MV/cm THz fields", New J. Phys. **19**, 123018 (2017), https://dx.doi.org/10.1088/1367-2630/aa936b.

[26] W. Kuehn, P. Gaal, K. Reimann, M. Woerner, T. Elsaesser, and R. Hey, "Terahertz-induced interband tunneling of electrons in GaAs", Phys. Rev. B **82**, 75204 (2010), https://link.aps.org/doi/10.1103/PhysRevB.82.075204.

[27] R. D. Schaller and V. I. Klimov, "High Efficiency Carrier Multiplication in PbSe Nanocrystals: Implications for Solar Energy Conversion", Phys. Rev. Lett. **92**, 186601 (2004), https://link.aps.org/doi/10.1103/PhysRevLett.92.186601.

[28] R. Rana, L. Balaghi, I. Fotev, H. Schneider, M. Helm, E. Dimakis, and A. Pashkin, "Nonlinear Charge Transport in InGaAs Nanowires at Terahertz Frequencies", Nano Lett. **20**, 3225–3231 (2020), https://doi.org/10.1021/acs.nanolett.9b05328.

[29] J. A. Misewich, R. Martel, P. Avouris, J. C. Tsang, S. Heinze, and J. Tersoff, "Electrically Induced Optical Emission from a Carbon Nanotube FET", Science (80-.). **300**, 783–786 (2003), https://doi.org/10.1126/science.1081294.

[30] Y. Zhao, V. Wang, D.-H. Lien, and A. Javey, "A generic electroluminescent device for emission from infrared to ultraviolet wavelengths", Nat. Electron. **3**, 612–621 (2020), https://doi.org/10.1038/s41928-020-0459-z.

[31] R. H. Hadfield, "Single-photon detectors for optical quantum information applications", Nat. Photonics **3**, 696–705 (2009), https://doi.org/10.1038/nphoton.2009.230.

[32] P. M. Echternach, B. J. Pepper, T. Reck, and C. M. Bradford, "Single photon detection of 1.5 THz radiation with the quantum capacitance detector", Nat. Astron. **2**, 90–97 (2018), https://doi.org/10.1038/s41550-017-0294-y.

[33] S. Linden, F. B. P. Niesler, J. Förstner, Y. Grynko, T. Meier, and M. Wegener, "Collective Effects in Second-Harmonic Generation from Split-Ring-Resonator Arrays", Phys. Rev. Lett. **109**, 15502 (2012), https://link.aps.org/doi/10.1103/PhysRevLett.109.015502.

[34] I.-C. Ho and X.-C. Zhang, "Driving intervalley scattering and impact ionization in InAs with intense terahertz pulses", Appl. Phys. Lett. **98**, 241908 (2011), https://doi.org/10.1063/1.3600791.

[35] O. Sydoruk, E. Tatartschuk, E. Shamonina, and L. Solymar, "Analytical formulation for the resonant frequency of split rings", J. Appl. Phys. **105**, 14903 (2009), https://doi.org/10.1063/1.3056052.

[36] A. G. Chynoweth, "Ionization Rates for Electrons and Holes in Silicon", Phys. Rev. **109**, 1537–1540 (1958), https://link.aps.org/doi/10.1103/PhysRev.109.1537.

[37] Y. Okuto and C. R. Crowell, "Energy-Conservation Considerations in the Characterization of Impact Ionization in Semiconductors", Phys. Rev. B **6**, 3076–3081 (1972), https://link.aps.org/doi/10.1103/PhysRevB.6.3076.

[38] E. O. Kane, "Zener tunneling in semiconductors", J. Phys. Chem. Solids **12**, 181–188 (1960), https://www.sciencedirect.com/science/article/pii/0022369760900354.

[39] M. C. Hoffmann, J. Hebling, H. Y. Hwang, K.-L. Yeh, and K. A. Nelson, "Impact ionization in InSb probed by terahertz pump—terahertz probe spectroscopy", Phys. Rev. B **79**, 161201 (2009), https://link.aps.org/doi/10.1103/PhysRevB.79.161201.

[40] H.-T. Chen, J. F. O'Hara, A. K. Azad, A. J. Taylor, R. D. Averitt, D. B. Shrekenhamer, and W. J. Padilla, "Experimental demonstration of frequency-agile terahertz metamaterials", Nat. Photonics **2**, 295–298 (2008), https://doi.org/10.1038/nphoton.2008.52.

[41] M. A. Saleh, M. M. Hayat, P. P. Sotirelis, A. L. Holmes, J. C. Campbell, B. E. Saleh, and M. C. Teich, "Impact-ionization and noise characteristics of thin III-V avalanche photodiodes", IEEE Trans. Electron Devices **48**, 2722–2731 (2001), https://doi.org/10.1109/16.974696.

[42] Y. Zhao, H. Niwa, and T. Kimoto, "Impact ionization coefficients of 4H-SiC in a wide temperature range", Jpn. J. Appl. Phys. **58**, 18001 (2019), https://dx.doi.org/10.7567/1347-4065/aae985.

[43] P. Rodin, U. Ebert, W. Hundsdorfer, and I. Grekhov, "Tunneling-assisted impact ionization fronts in semiconductors", J. Appl. Phys. **92**, 958–964 (2002), https://doi.org/10.1063/1.1486258.

[44] J. S. Cheong, M. M. Hayat, X. Zhou, and J. P. R. David, "Relating the Experimental Ionization Coefficients in Semiconductors to the Nonlocal Ionization Coefficients", IEEE Trans. Electron Devices **62**, 1946–1952 (2015), https://doi.org/10.1109/TED.2015.2422789.

[45] D. S. Ong, K. F. Li, G. J. Rees, J. P. R. David, and P. N. Robson, "A simple model to determine multiplication and noise in avalanche photodiodes", J. Appl. Phys. **83**, 3426–3428 (1998), https://doi.org/10.1063/1.367111.

[46] M. A. Saleh, M. M. Hayat, B. E. A. Saleh, and M. C. Teich, "Dead-space-based theory correctly predicts excess noise factor for thin GaAs and AlGaAs avalanche photodiodes", IEEE Trans. Electron Devices **47**, 625–633 (2000), https://doi.org/10.1109/16.824739.

[47] Y. Chen, Z. Wang, S. Chen, H. Ren, L. Wang, G. Zhang, Y. Lu, J. Jiang, C. Zou, and Y. Luo, "Non-catalytic hydrogenation of VO2 in acid solution", Nat. Commun. **9**, 818 (2018), https://doi.org/10.1038/s41467-018-03292-y.

[48] H. Hirori, K. Shinokita, M. Shirai, S. Tani, Y. Kadoya, and K. Tanaka, "Extraordinary carrier multiplication gated by a picosecond electric field pulse", Nat. Commun. **2**, 594 (2011), https://doi.org/10.1038/ncomms1598.

[49] D. Turchinovich, J. M. Hvam, and M. C. Hoffmann, "Self-phase modulation of a single-cycle terahertz pulse by nonlinear free-carrier response in a semiconductor", Phys. Rev. B **85**, 201304 (2012), https://link.aps.org/doi/10.1103/PhysRevB.85.201304.

[50] A. T. Tarekegne, K. J. Kaltenecker, P. Klarskov, K. Iwaszczuk, W. Lu, H. Ou, K. Norrman, and P. U. Jepsen, "Subcycle Nonlinear Response of Doped 4H Silicon Carbide Revealed by Two-Dimensional Terahertz Spectroscopy", ACS Photonics **7**, 221–231 (2020), https://doi.org/10.1021/acsphotonics.9b01462.

[51] M. Shalaby and C. P. Hauri, "Demonstration of a low-frequency three-dimensional terahertz bullet with extreme brightness", Nat. Commun. **6**, 5976 (2015), https://doi.org/10.1038/ncomms6976.

[52] Y.-M. Bahk, S. Han, J. Rhie, J. Park, H. Jeon, N. Park, and D.-S. Kim, "Ultimate terahertz field enhancement of single nanoslits", Phys. Rev. B **95**, 75424 (2017), https://link.aps.org/doi/10.1103/PhysRevB.95.075424.

[53] F. J. Garcia-Vidal, L. Martin-Moreno, T. W. Ebbesen, and L. Kuipers, "Light passing through subwavelength apertures", Rev. Mod. Phys. **82**, 729–787 (2010), https://link.aps.org/doi/10.1103/RevModPhys.82.729.

[54] L. Sabri, Q. Huang, J.-N. Liu, and B. T. Cunningham, "Design of anapole mode electromagnetic field enhancement structures for biosensing applications", Opt. Express **27**, 7196–7212 (2019), https://opg.optica.org/oe/abstract.cfm?URI=oe-27-5-7196.

[55] D. Zhang, A. Fallahi, M. Hemmer, X. Wu, M. Fakhari, Y. Hua, H. Cankaya, A.-L. Calendron, L. E. Zapata, N. H. Matlis, and F. X. Kärtner, "Segmented terahertz electron accelerator and manipulator (STEAM)", Nat. Photonics **12**, 336–342 (2018), https://doi.org/10.1038/s41566-018-0138-z.

[56] S. M. Sze and K. K. Ng, *Physics of Semiconductor Devices*, Vol. 3 (John Wiley & Sons, 2006), https://doi.org/10.1002/0470068329.

[57] *New Semiconductor Materials Home Page*, (2022) http://matprop.ru (visited on 11/23/2022).

[58] *THE SEMICONDUCTORS-INFORMATION WEB-SITE*, https://www.semiconductors.co.uk (visited on 11/23/2022).

[59] P. D'Amico, A. Calzolari, A. Ruini, and A. Catellani, "New energy with ZnS: novel applications for a standard transparent compound", Sci. Rep. **7**, 16805 (2017), https://doi.org/10.1038/s41598-017-17156-w.

[60] M. E. Elta and G. I. Haddad, "Mixed tunneling and avalanche mechanisms in p-n junctions and their effects on microwave transit-time devices", IEEE Trans. Electron Devices **25**, 694–702 (1978), https://doi.org/10.1109/T-ED.1978.19156.

[61] A. C. Seabaugh and Q. Zhang, "Low-Voltage Tunnel Transistors for Beyond CMOS Logic", Proc. IEEE **98**, 2095–2110 (2010), https://doi.org/10.1109/JPROC.2010.2070470.

[62] B. Khamala, L. Franklin, Y. Malozovsky, A. Stewart, H. Saleem, and D. Bagayoko, "Calculated electronic, transport, and bulk properties of zinc-blende zinc sulphide (zb-ZnS)", Comput. Condens. Matter **6**, 18–23 (2016), https://www.sciencedirect.com/science/article/pii/S2352214315300204.

[63] W. Luo, S. Ismail-Beigi, M. L. Cohen, and S. G. Louie, "Quasiparticle band structure of ZnS and ZnSe", Phys. Rev. B **66**, 195215 (2002), https://link.aps.org/doi/10.1103/PhysRevB.66.195215.

[64] E. Schreiber and H.-J. Fitting, "Ballistic electrons in GaAs and ZnS", J. Electron Spectros. Relat. Phenomena **131-132**, 87–98 (2003), https://www.sciencedirect.com/science/article/pii/S0368204803001087.

[65] H. Zhao, Y. Wang, Z. Xu, and X. Xu, "Intervalley Transfer of Electrons in ZnS-Type Thin Film Electroluminescent Devices", Acta Phys. Pol. A **96**, 475–482 (1999), http://przyrbwn.icm.edu.pl/APP/PDF/96/a096z3p17.pdf.

[66] X. Zhao, J. Zhang, K. Fan, G. Duan, G. D. Metcalfe, M. Wraback, X. Zhang, and R. D. Averitt, "Nonlinear terahertz metamaterial perfect absorbers using GaAs [Invited]", Photonics Res. **4**, A16–A21 (2016), https://opg.optica.org/prj/abstract.cfm?URI=prj-4-3-A16.

Chapter 5

Time-resolved THz Stark spectroscopy

Bong Joo Kang[1], Egmont J. Rohwer[1], David Rohrbach[1], Maryam Akbarimoosavi[1], Zoltan Ollmann[1], Elnaz Zyaee[1], Steven E. Meckel[2], Raymond F. Pauszek III[3], Gleb Sorohhov[4], Alex Borgoo[5], Michele Cascella[5], Andrea Cannizzo[1], Silvio Decurtins[4], Robert J. Stanley[2], Shi-Xia Liu[4], and Thomas Feurer[1]

[1]Institute of Applied Physics, University of Bern, Sidlerstrasse 5, 3012 Bern, Switzerland
[2]Department of Chemistry, Temple University, Philadelphia 19122, Pennsylvania, United States
[3]Department of Integrative Structural & Computational Biology, The Scripps Research Institute, La Jolla 92037, California, United States
[4]Department of Chemistry, Biochemistry and Pharmaceutical Sciences, University of Bern, 3012 Bern, Switzerland
[5]Department of Chemistry and Hylleraas Centre for Quantum Molecular Sciences, University of Oslo, Oslo N-0315, Norway

This work has been submitted.

Abstract
We introduce THz Stark spectroscopy by using intense single-cycle terahertz pulses as the electric field source and monitoring the induced spectral response of an isotropic molecular ensemble with a coincident femtosecond supercontinuum pulse. THz Stark spectroscopy offers several advantages over conventional Stark spectroscopy and opens previously inaccessible perspectives. Most importantly, THz pulses oscillate faster than typical molecular rotations and consequently eliminate the requirement to freeze the samples to prevent poling effects. Hence, THz Stark spectroscopy allows for time-resolved studies at arbitrary temperatures, specifically ambient conditions more relevant to physiological or operative conditions. Moreover, dynamical field effects, e.g., higher order Stark contributions or hysteresis effects (non-Markovian behavior), can be studied on the time scales of molecular vibrations or rotations. We demonstrate THz Stark spectroscopy for two judiciously selected molecular systems and compare the results to conventional Stark spectroscopy and first principle calculations.

5.1 Introduction

Stark spectroscopy is an invaluable tool to reveal information about physicochemical properties of molecules [1–9]. Sufficiently strong electric fields modify absorption spectra of isotropic ensembles of molecules if ground and excited state energy eigenvalues of the respective optical transition shift in energy due to the interaction with the applied electric field. In most cases, the interaction can be treated as a perturbation and expanded in a power series of the electric field. To first order, Stark spectroscopy reveals information on the electric dipoles, and to second order, on the induced dipoles, i.e. on the polarizabilities, of the two states. The former is referred to as the linear Stark effect (Fig. 5.1a), the latter is called the quadratic Stark effect (Fig. 5.1b). It is important to note that only a nonzero difference between ground and excited state dipole or polarizability results in a modified absorption spectrum, and consequently, only those differences can be extracted from a measurement. While a change in dipole moment, for instance, reflects the degree of charge separation or charge transfer associated with the transition, a change in polarizability describes the sensitivity of a transition to an external electric field [2]. These effects are also known as electro-chromism [5] and a corresponding measurement gives insight in, for instance, photo-induced electron or charge transfer [10–14], nonlinear material properties [2, 4, 8, 15], biological organization and energy tuning [16–21], or solvato-chromism. Also, vibrational Stark spectroscopy of CO or CN ligands has developed into an important tool to measure in situ electric field strength in various chemical environments [22].

Conventional Stark spectroscopy uses low frequency (kHz) electric fields, which oscillate much slower than typical rotation times of molecules in solution. Hence, molecules must be immobilized in order to avoid alignment of their dipoles along the applied electric field, otherwise this poling effect would result in an overwhelming increase of the overall absorption and obscure any Stark signatures. Typically, this is achieved by freezing the solvent, which limits the range of solvents that can be used since these need to form optical glasses to avoid scattering of probe light. Moreover, freezing prevents molecules to be characterized in their natural, liquid or physiological environment. Finally, the sample geometry, with the electrodes on the front- and backside of the sample cuvette, leads to a non-optimal geometry with the angle between the polarization of the Stark field and the probe being far from the ideal value of 0 deg (typically 50 to 60 deg) [23].

Here, we demonstrate that increasing the frequency of the oscillating electric field to the terahertz (THz) regime removes all of the above mentioned constraints and disadvantages of conventional Stark spectroscopy. Since a number of years it became possible to generate phase stable single- or few-cycle THz pulses with sufficiently strong electric fields (up to or even exceeding 10^6 V/m) to induce measurable Stark shifts as well as femtosecond supercontinuum (fs-SC) probe pulses to time-resolve those transient Stark signatures [24, 25]. A schematic of the experimental realization is shown in Fig. 5.1c. Scanning the time delay between probe pulse and the THz waveform allows for the measurement of Stark signatures for positive or negative electric fields and from zero field up to the peak field strength of the THz pulse (see supplemental document: Experimental setup). At THz frequencies the electric field oscillates faster than typical molecular rotation times, hence for the first time, time-resolved Stark spectroscopy of molecules is performed without freezing the sample. Consequently, virtually any solvent can be used and molecules can be studied in their natural chemical or biological environment. Moreover, a wider temperature range becomes accessible, especially temperatures above the freezing point

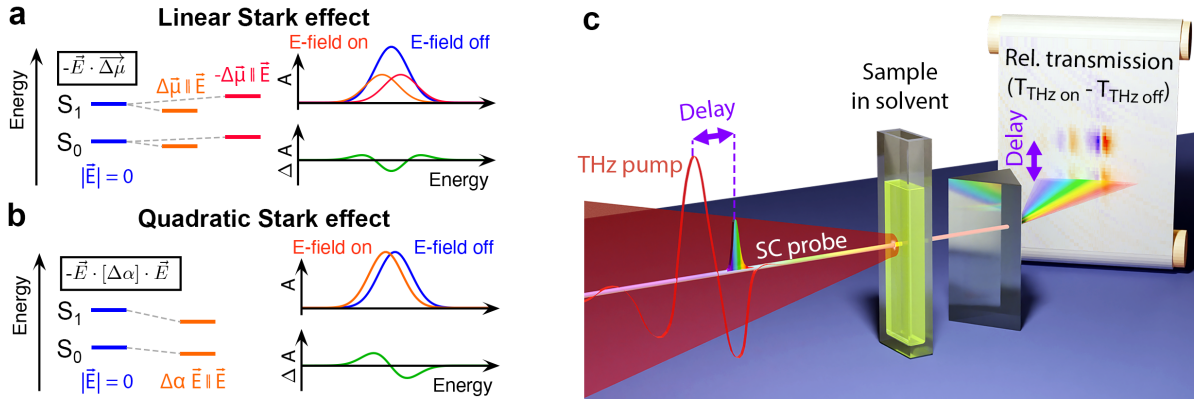

Figure 5.1: Electric field induced Stark effect and experimental concept. Electric field induced Stark shift due to a difference in ground- and excited state dipole (**a**), i.e. linear Stark effect, and polarizability (**b**), i.e. quadratic Stark effect. For an isotropic distribution of molecules the ground state absorption band versus energy $A(E)$ broadens in the case of the linear Stark effect with the difference signal $\Delta A(E)$ resembling the second order derivative of the absorption band. In the case of the quadratic Stark effect the ground state absorption band shifts resulting in a difference signal $\Delta A(E)$ that is proportional to the first order derivative of absorption band. **c** Schematic representation of the experimental setup. The femtosecond supercontinuum probe pulse is scanned in time across the collinear single-cycle THz pulses and its spectrum is recorded by a spectrometer.

of the solvent but also room temperature or higher. The THz frequency of the field source also entails a higher dielectric breakdown allowing for electric field strengths, which were impossible to attain previously [26–28]. At such field strengths, for instance, transition polarizability or hyper-polarizability may play a more important role, particularly for weakly allowed transitions. Such higher-order electric field effects may require a new theoretical concept, especially when the applied electric field can no longer be treated as a perturbation to the system's Hamiltonian or when magnetic effects need to be considered. THz Stark spectroscopy offers additional minor advantages, i.e., the sample thickness can be substantially increased and is limited only by absorption or velocity matching between the THz and the probe pulse. Additionally, arbitrary angles between the electric field vector and the probe polarization can be used and the absence of electrodes avoids potential redox chemistry in the pristine sample.

For the present THz Stark spectroscopic study, we selected two molecules and for comparison we performed quantum chemical calculations as well as conventional Stark spectroscopy. One molecule consists of a strong electron donor tetrathiafulvalene and an electron acceptor benzothiadiazole, showing an energetically low-lying intramolecular charge transfer state with a substantial change in dipole moment. The other is an anthanthrene derivative tetrasubstituted with silyl-protected acetylene groups to extend its π-conjugation, leading to an intense and sharp absorption band with a large change in polarizability.

5.2 Results and discussion

5.2.1 Dynamics of the Stark signature

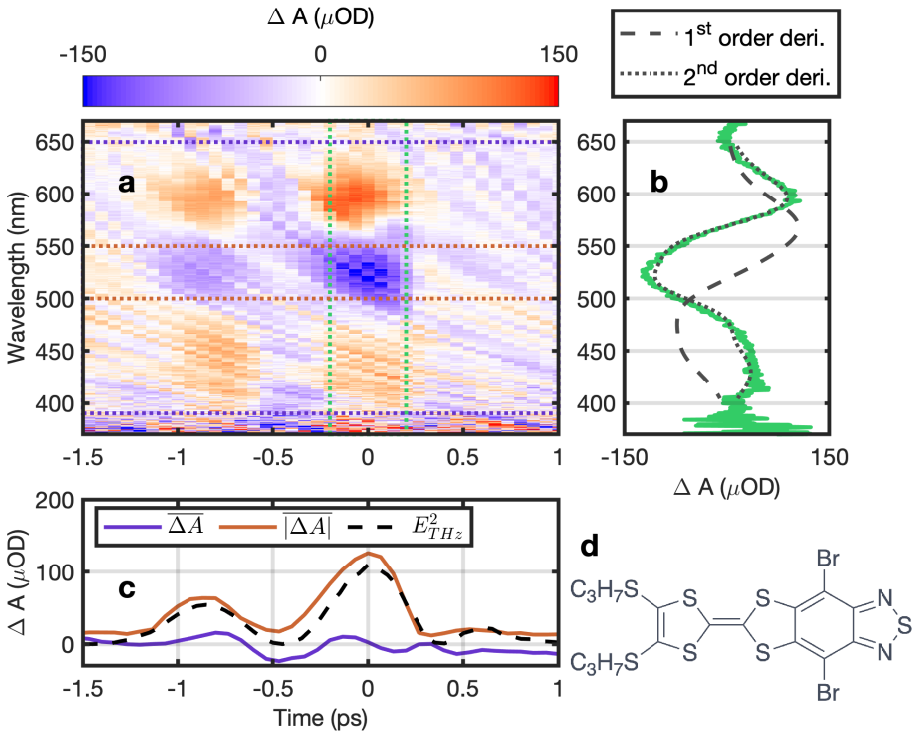

Figure 5.2: THz Stark signal of TTF-BTD with parallel orientation. **a** False-color plot of the measured change in absorption spectrum as a function of time delay between THz and probe pulse and wavelength. **b** Time-averaged (between the two green dotted lines) change in absorption versus wavelength (green solid curve) compared to the scaled first (black dashed curve) and second order derivative (black dotted curve) of the ground state absorption spectrum. **c** Spectral average of the change in absorption between the purple dotted (purple curve) and red dotted lines (red curve) in **a**. The red curve is compared to the scaled square of the measured THz electric field E^2_{THz} (black dashed curve). **d** Chemical structure of TTF-BTD.

We first discuss the experimental results of a molecule with a pronounced intramolecular charge-transfer (ICT) character, namely an annulated electron donor-acceptor compound. Thereby, tetrathiafulvalene (TTF) acts as a strong donor and benzothiadiazole (BTD) equally as an acceptor within the compact and planar dyad [29, 30]. The bromine functionalization of BTD increases its acceptor strength and the propyl chains on TTF act as solubilizing groups (Figure 5.2d) (see supplemental document: Synthesis and preparation). Figure 5.2a shows the color-coded THz-induced change in absorption $\Delta A(\tau, \lambda)$ in TTF-BTD versus time delay τ and wavelength λ for parallel polarization orientation between probe pulse and THz waveform (corresponding results for a perpendicular orientation are provided in the supplemental document: Additional THz Stark spectroscopy results). The color scale indicates the difference in absorption in units of optical density (OD). The two-dimensional distribution reveals both temporal

and spectral characteristics of the THz field-induced Stark shift. Time zero is set arbitrarily to the maximum change in absorption $\Delta A_{\max}$. The two peaks of the single-cycle THz pulse are well resolved with zero signal at the zero-crossing of the THz electric field. The measured spectra around the peaks of the THz field indicate a spectral broadening of the rather broad $S_0 - S_1$ absorption band between 390 nm to 650 nm, which is not unusual for ICT transitions.

Calculating the margin along the delay axis between the two green dotted vertical lines results in the average Stark signal versus wavelength (green curve in Fig. 5.2b). Comparing the measured signal to the scaled first- and second-order derivative of the ground state absorption curve reveals that the Stark signature is dominated by a first order Stark contribution (black dotted curve) revealing a linear Stark effect caused by a change in dipole moment between ground and excited state. Additionally, we calculate two margins along the wavelength axis, first between the purple dotted horizontal lines resulting in the purple curve in (Fig. 5.2c), and second between the the two red dotted horizontal lines yielding the red curve in (Fig. 5.2c). The margin over the entire transition (purple curve) versus time delay is essentially zero confirming that no alignment of molecules to the applied THz field occurs. The residual small signal is most likely due to an imperfect correction of the group velocity dispersion in the fs-SC (see supplemental document: Group velocity dispersion correction) as well as a noise level of 20 μOD due to fs-SC fluctuations. These findings constitute an important result as they demonstrate that THz Stark spectroscopy can be applied to molecules in solution without the need to freeze the solvent. The red curve, averaged over one of the peaks in the Stark spectrum, indicates that the instantaneous Stark signal scales as the square of the THz field which is in agreement with Liptay's derivation of the linear and the quadratic Stark effect of an ensemble of molecules with isotropic orientation.

The second molecule, anthanthrene [31], is a π-conjugated organic molecule of interest due to its semiconducting properties and potential applications in light emitting diodes or solar cells. The structure of anthanthrene is shown in Fig. 5.3d. It constitutes an interesting building block for organic electronics and Stark spectroscopy has the potential to reveal some of its relevant physicochemical properties. The transient Stark signal of the $S_0 - S_1$ transition of anthanthrene in toluene is shown in Fig. 5.3. The polarization between probe pulse and the THz waveform was parallel and the corresponding results for perpendicular polarization are provided in the supplemental document: Additional THz Stark spectroscopy results. The electronic transition shows a well separated vibrational progression, hence all vibrational bands are treated as one transition within our detection window. Margins are calculated following the same recipe as outlined above. A comparison of the time averaged Stark signature (Fig. 5.3b green curve) with the scaled first- (black dashed curve) and second-order derivative (black dotted curve) of the ground state absorption reveals a mostly quadratic Stark effect related to a difference in polarizability of ground and excited state. It also suggests that ground and excited state dipoles are, very likely based on symmetry arguments, negligible or similar in value. The two margins along the wavelength axis shown in Fig. 5.3c (purple and red curves) confirm that poling effects can be excluded, hence the sample maintains an isotropic distribution throughout, confirming again that the THz field oscillation is faster than any molecular rotation time.

That is, both molecules show a pronounced instantaneous Stark signature, which is well-matched to either the first- or the second-order derivative of the ground state absorption band, suggesting a dominant quadratic or linear Stark effect, respectively. In both cases, the Stark signal is proportional to the square of the THz electric field in agreement with Liptay formalism (see

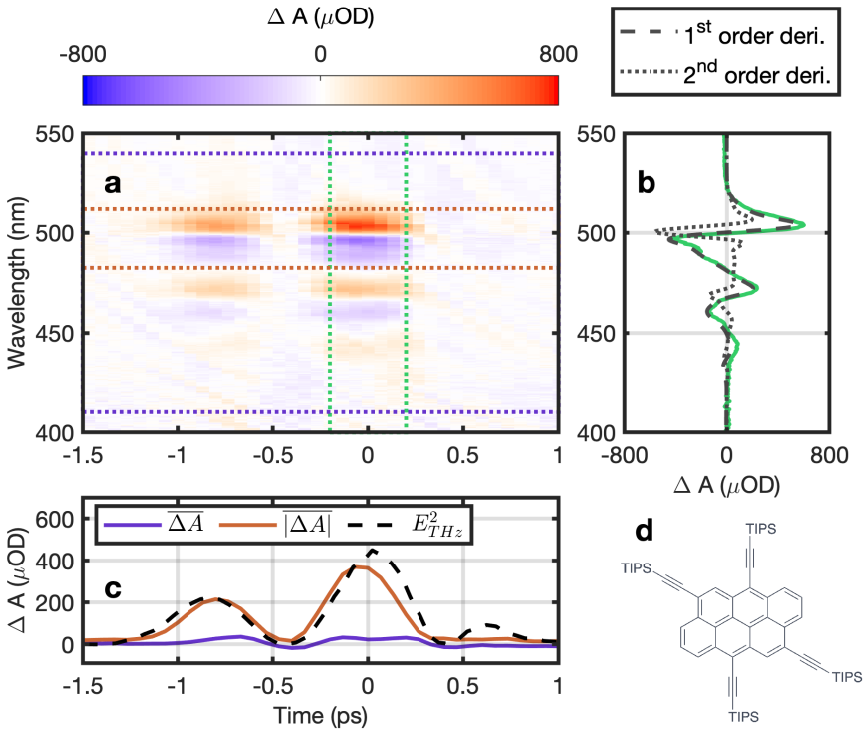

Figure 5.3: THz Stark signal of anthanthrene with parallel orientation. **a** False-color plot of the measured change in absorption spectrum as a function of time delay between THz and probe pulse and wavelength. **b** Time-averaged (between the two green dotted lines) change in absorption versus wavelength (green solid curve) compared to the scaled first (black dashed curve) and second order derivative (black dotted curve) of the ground state absorption spectrum. **c** Spectral average of the change in absorption between the purple dotted (purple curve) and red dotted lines (red curve) in **a**. The red curve is compared to the scaled square of the measured THz electric field E^2_{THz} (black dashed curve). **d** Chemical structure of anthanthrene.

supplemental document: Liptay analysis) tracing the few-picosecond single-cycle THz waveform and we identify no measurable hysteresis or memory effect.

5.2.2 Comparison between conventional and THz Stark spectroscopy

For both molecules the Stark spectra for parallel and perpendicular polarization between probe pulse and THz waveform are fitted simultaneously and analyzed using the formalism outlined by Liptay [5, 32] to extract relevant molecular parameters, such as differences in dipole moment or polarizability. We compare the results to those obtained from conventional Stark spectroscopy (see supplemental document: Conventional Stark spectroscopy) and those calculated from Density Functional Theory (DFT). DFT also provides molecular orbitals and associated energies for further discussion of results, specifically the charge redistribution associated with an excitation (see supplemental document: Density Functional Theory calculations). Recall that conventional Stark spectroscopy is done at 77 K, that is well below the freezing temperature of toluene, whereas THz Stark spectroscopy can be performed in principle at any temperature, but

here is done at room temperature. To account for different optical path lengths, sample concentrations or electric field strength in the two measurement techniques, we compare the change in molar attenuation coefficient $\Delta\epsilon$ scaled to 1 MV/cm rather than the change in absorption.

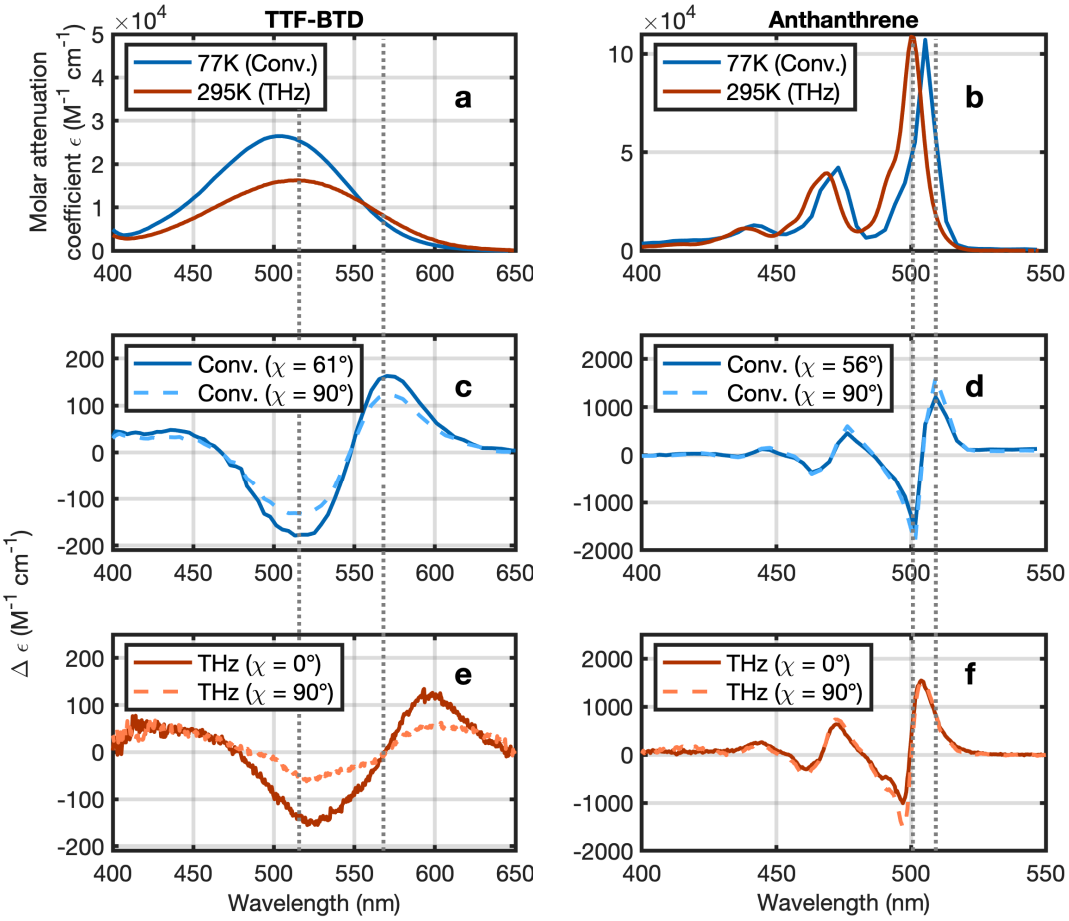

Figure 5.4: Comparison of conventional and THz Stark spectroscopy. **a,b** Low temperature (77 K) and room temperature (295 K) absorption spectra of (a) TTF-BTD and (b) anthanthrene. **c,d** Conventional Stark spectra measured at 77 K for two values of the angle χ between the polarization of the THz and the probe pulses. **e,f** THz Stark spectra recorded at room temperature for parallel and perpendicular orientation of THz and probe polarization. For direct comparison the y-scale is in units of $\Delta\epsilon$ scaled to an electric field of 1 MV/cm. The grey dotted vertical lines are guides to the eye and help to visualize the shift of the spectra at the different temperatures.

The ground state absorption spectra of TTF-BTD and anthanthrene in toluene are shown in Fig. 5.4a and b for 77 K (blue curves) and room temperature (red curves). The DFT calculations suggest that TTF-BTD exhibits a broad absorption band due to a substantial ICT in the excited state. Anthanthrene, on the other hand, exhibits relatively narrow absorption features with an evident vibronic progression and DFT calculations mainly suggest a change in polarizability.

When decreasing the temperature from 300 K to 77 K toluene is known to increase its effective polarity due to an increase in density [33]. While in TTF-BTD this results in a blue-shift of the absorption peak from 514 nm to 505 nm due to the solvent's instantaneous electronic polarizability [34], in anthanthrene this leads to a increased stabilization of the energy levels and an associated red-shift of the lowest vibronic mode of the $S_0 - S_1$ HOMO - LUMO transition from 500 nm to 505 nm. Irrespective of molecule, thermal broadening of the absorption features is evident for increasing temperatures. Both effects illustrate the importance of fitting Stark spectra with ground state absorption spectra recorded at the same temperature.

Figure 5.4c and d show the change in molar attenuation coefficient $\Delta\epsilon$ scaled to 1 MV/cm for TTF-BTD and anthanthrene as measured by conventional Stark spectroscopy for a relative orientation between probe pulse and THz waveform polarization of 56 deg/61 deg (blue solid curve) and 90 deg (blue dashed curve). Note, that angles smaller than 56 deg are difficult to realize due to above mentioned geometrical constraints. The corresponding results of the THz Stark spectroscopy are shown in Fig. 5.4e and f. THz results were averaged over a 467 fs time window around the larger peak of the THz pulse. Unlike conventional Stark spectroscopy, the THz variant has no geometrical constraints and allows for angles down to 0 deg, which helps to improve the dynamic range of measurement as well as the accuracy of the Liptay analysis. Except for the temperature related blue- or red-shift and the different minimal angle, the Stark signatures of both methodologies are in excellent agreement with each other. The peak change in molar attenuation coefficient for TTF-BTD is slightly lower in the THz measurement due to the thermal broadening of the absorption spectrum at room temperature.

5.2.3 Relevant molecular parameters

A more rigorous comparison becomes available after analyzing the spectra in Fig. 5.4 following the Liptay protocol. It reveals the change in dipole moment, $\Delta\mu$, the angle between the change in dipole moment and the transition dipole moment m, ζ, the average change in polarizability, $\mathrm{Tr}(\Delta\alpha)$, and the change in polarizability parallel to the transition dipole moment m, $m\ \Delta\alpha\ m$. The latter consistently showed large fitting errors and is not reported here. Table 5.1 summarizes these molecular parameters calculated from DFT as well as measured and extracted via the Liptay analysis of both Stark spectroscopy methodologies.

Table 5.1: Comparison of relevant molecular parameters as calculated via DFT or measured by conventional and THz Stark spectroscopy.

Parameter	DFT	Conventional Stark	THz Stark
TTF-BTD: tetrathiafulvalene-benzothiadiazole			
$\Delta\mu$ (D)	16.2	14.7 ± 0.1	15.3 ± 1.8
ζ (°)	≈ 0	24.8 ± 0.2	18.7 ± 1.1
anthanthrene: 4,6,10,12-tetrakis(triisopropylsilylethynyl)anthanthrene			
$\mathrm{Tr}(\Delta\alpha)$ (Å^3)	457	363 ± 20	296 ± 70

The agreement within the error bars in all molecular parameters extracted from the two Stark spectroscopy modalities is remarkable and confirms that both techniques deliver results which are in quantitative agreement with each other. The biggest source of error comes from the uncertainty of the electric field applied to the sample (see supplemental document: Char-

acterization of THz pulses). Furthermore, the experimental results are in reasonable agreement with DFT calculations given the fact that the solvent environment can only be treated approximately if at all. Including the solvent effect in the DFT calculations for TTF-BTD leads to marginal modifications to the molecular geometry as compared to the gas phase and details can be found in reference [32]. The mismatch in measured and calculated angle ζ most likely is due to these structural modifications, but may be also a result of temperature affecting electrostatic interactions and molecular geometry [32, 35]. For the anthanthrene, the DFT calculations were performed at 0 K and without solvent effects, nevertheless, the experimental results agree very well with the DFT calculations. Hence, neither the low polarity of the solvent nor the increased temperature seem to drastically affect the dipole moment or the electronic polarizability of the molecule.

5.3 Conclusion

In conclusion, we have demonstrated that THz Stark spectroscopy indeed reveals the same physicochemical properties of molecules as conventional Stark spectroscopy, but at the same time opens hitherto inaccessible opportunities, because it is not subjected to the same limitations that apply to conventional Stark spectroscopy. Geometrical constraints are removed allowing for arbitrary angles between probe pulse and THz waveform polarization, no electrodes are required, which helps to avoid potential redox chemistry in the pristine sample, and the much higher frequency of THz waveforms allows for higher electric field strengths before the threshold for dielectric breakdown is reached. Most importantly however, THz Stark spectroscopy removes the need to immobilize the molecular ensemble by freezing the solvent. Hence, molecules or bio-molecules can now be studied in their natural environment and at relevant temperatures. Our findings are based on measurements of two molecules relevant in the context of molecular electronics.

In principle, THz Stark spectroscopy will allow to observe transient or non-equilibrium electronic properties of molecules with sub-100 fs resolution. Consequently, THz Stark spectroscopy can be used to study molecular ensembles at conditions not accessible to conventional Stark spectroscopy, for instance, within a much increased range of temperatures or in different non-polar or polar solvents, even those that do not form transparent glasses at low temperatures. Today's high-field THz sources generate field strengths in excess of 1 MV/cm so that higher-order Stark contributions may become observable, such as non-Markovian responses (hysteresis effects) originating from electron-phonon couplings. Higher order Stark contributions are impossible to access via conventional Stark spectroscopy but are relevant to model electron dynamics induced by external or local fields (e.g. charge and electron transfer) or to refine quantum chemistry codes. Moreover, the intrinsic time resolution of around 100 fs facilitates studies on the time-dependent physicochemical properties of a molecule during its photo-cycle, specifically it allows for Stark spectroscopy of excited states.

Methods: THz Stark spectrometer

The THz Stark spectrometer was designed to record the change in absorption $\Delta A(\tau, \lambda) = A_{\text{THz on}}(\tau, \lambda) - A_{\text{THz off}}(\tau, \lambda)$ as a function of time delay between the THz waveform and the probe pulse τ and of wavelength λ. The recorded Stark maps $\Delta A(\tau, \lambda)$ were subsequently corrected for the fs-SC group velocity dispersion (see supplemental document: Group velocity

dispersion correction) and the background resulting from the pure solvent (see supplemental document: Background measurements). The analysis of the Stark spectra, here at maximum electric field, $\Delta A(\lambda)$, was outlined in reference [5]. After having identified the Stark-active transitions, the Stark spectra were subsequently analyzed with the Liptay formalism, which links the molar absorption $\Delta\epsilon(\bar{\nu})$ as a function of wavenumber to the ground state absorption spectrum $\epsilon(\bar{\nu})$. The model assumes a fixed angle between electric field and probe polarization and an isotropic distribution of transition dipole moments, which is achieved by freezing the sample in conventional Stark spectroscopy. The ground-state absorption spectra and two Stark spectra for different probe polarizations were fitted simultaneously with a weighted sum of the zeroth, first, and second order derivative of the ground state absorption spectrum.

$$\Delta\epsilon(\bar{\nu}) = f_l^2|\mathbf{E}|^2 \left\{ a\epsilon(\bar{\nu}) + b\frac{\mathrm{d}}{\mathrm{d}\bar{\nu}}\left(\frac{\epsilon(\bar{\nu})}{\bar{\nu}}\right) + c\frac{\mathrm{d}^2}{\mathrm{d}\bar{\nu}^2}\left(\frac{\epsilon(\bar{\nu})}{\bar{\nu}}\right)\right\}. \tag{5.1}$$

From the fit parameters a, b, and c we extracted the trace of the polarizability tensor, its projection along the transition dipole moment, the angle between the applied electric field and the probe polarization, the change in dipole moment, and the angle between the change in dipole moment and the transition dipole moment. An important ingredient to the fit is the THz electric field strength $|\mathbf{E}|$ in the sample at which the probe pulse interrogates the molecular system. In order to account for all experimental effects we first measured the THz electric field in air and then performed finite difference time-domain simulations to determine the time dependence of the THz electric field experienced by the probe pulse in the complex cuvette/liquid environment. We found that the time dependence is almost identical, however with the peak electric field strength being reduced by a factor of 0.7 due to Fresnel reflections and Fabry-Perot effects. Hence, the maximum field in the sample was reduced to $(280 \pm 17)\,\mathrm{kV/cm}$. The electric field experienced by the molecules is further modified by the local field correction factor f_l, which is a measure of how the solvent cavity affects the field inside the cavity containing the molecule [36–38]. We estimated the local field correction factors for TTF-BTD and anthanthrene to 1.30 and 1.33 for conventional Stark spectroscopy and to 1.26 and 1.29 respectively for THz Stark spectroscopy (see supplemental document: Local field correction factor).

5.4 Supplemental document

5.4.1 Molecular systems

Synthesis and preparation

The two molecular systems were selected because they show either a pronounced change in dipole moment, which allows us to unambiguously observe the linear Stark effect, or a pronounced change in polarizability, which allows us to observe the quadratic Stark effect. In addition, both molecules are relevant in the field of molecular electronics and the extracted physicochemical properties are relevant in their own right.

The first molecular system is fused heterocyclic tetrathiafulvalene [39–43] – benzothiadiazole [44–46] (TTF-BTD) with Br substituted at the 4 and 8 positions of BTD [47]. This molecule is known to undergo intramolecular charge transfer [48, 49] with a correspondingly large change in dipole moment upon excitation of the HOMO-LUMO transition. The relatively

broad absorption band centered around 500 nm is a typical signature of such intramolecular charge transfer.

The second molecular system is the 4,6,10,12-tetrakis(triisopropylsilylethynyl)-anthanthrene compound [31], which bears a graphene-like aromatic skeleton and is well-known for its quantum interference effect on the single molecule conductance, [50–52] and for its versatile chromophoric properties in organic electronics [53–57]. It exhibits optically allowed transitions with significant oscillator strengths in the spectral range around 500 nm.

For all experiments, toluene was used as solvent because it has a low polarity and forms a transparent optical glass at 77 K, which is mandatory for the conventional Stark measurements. The low polarity limits effects due to varying solvent polarity at different temperatures and the potential for THz field-induced orientation of the solvent. For conventional Stark measurements, the sample concentration was 1 mM for TTF-BTD and 0.45 mM for anthanthrene. The sample concentration for the THz Stark measurements was 1 mM for TTF-BTD and 0.5 mM for anthanthrene. In the THz Stark experiment, a spectrosil quartz flow cell from Starna Scientific was used with a sample thickness of 200 μm and a wall thickness of 200 μm. Even though a flow cell is not specifically needed, it helped to suppress air bubble formation. Furthermore, any potential effects due to toluene evaporation are reduced.

While the ground state absorption spectra in conventional Stark spectroscopy were measured directly with the Stark spectroscopy apparatus (with no applied electric field at low temperature), the room temperature ground state absorption spectra were recorded separately with a spectrophotometer (Perkin-Elmer Lambda 750 Spectrometer, 1 mm thick cuvette).

Density Functional Theory calculations

We performed DFT calculations of both systems to gain further insight into the charge redistribution between the molecular orbitals involved in the observed optical transitions and the associated energies. While details on our DFT computations on TTF-BTD have already been published elsewhere [32], we here present methods and results on the second system anthanthrene.

The molecular geometries of anthanthrene were optimised at the Kohn-Sham DFT level. We used the PBE0 [58] or the B3LYP [59] functionals to approximate the exchange-correlation energy in combination with the 6-31+G(d,p) basis set [60]. The excitation energies were computed by time-dependent DFT (TD-DFT) [61]. The properties of excited states were obtained as higher-order response properties of the ground state. Specifically, the polarizability of an excited state was determined by first converging the electronic energy of the ground state and then by computing the double residue of the cubic response function as described in reference [62] and implemented in the DALTON software package [63]. Table 5.2 summarizes possible transitions originating from the ground S_0 state with corresponding wavelength, oscillator strength, major molecular orbital contributions, and transition dipole moment. Molecular orbitals and associated energies involved in the calculated transitions for the sample are illustrated in Fig. 5.5.

The DFT calculations predict one optically allowed transitions with significant oscillator strength in the our spectral observation window, which is the $S_0 \rightarrow S_1$ transition. Due to the symmetry of the molecule and the symmetry of the molecular orbital distributions associated with this transition, we do not expect a permanent dipole in any of these states and as such we also do not expect a change in dipole moment over the transition. The computed polarizability

Table 5.2: The ground state transitions of anthanthrene with wavelength, oscillator strength, and major contributing molecular orbitals calculated with TD-DFT.

Excited State	Wavelength (nm)	Oscillator strength	Major contributions (%)
S_1	**500.2**	**0.4846**	**HOMO → LUMO Pure**
S_2	419.7	0.0	HOMO-1→LUMO 36 HOMO→LUMO+1 13
S_3	402.8	0.0	HOMO-1→LUMO 13 HOMO→LUMO+1 36
S_4	395.2	0.0087	HOMO-2→LUMO 27 HOMO→LUMO+2 22
S_5	333.0	0.6133	HOMO-3→LUMO 3 HOMO-2→LUMO 20 HOMO-1→LUMO+1 2 HOMO→LUMO+2 22
S_6	315.4	0.0366	HOMO-3→LUMO 33 HOMO→LUMO+2 2 HOMO→LUMO+3 12

Table 5.3: $\Delta\alpha$ computed by TD-DFT with an aug-cc-PVDZ basis set.

State	Wavelength (PBE0)	Wavelength (B3LYP)	Tr($\Delta\alpha$) (B3LYP)
S_1	500.2 nm	518.8 nm	457 Å^3
S_5	333.0 nm	347.0 nm	333 Å^3

changes are summarized in Table 5.3. For completeness we also include the results for the $S_0 \rightarrow S_5$ transition, which has an appreciable oscillator strength but is outside of the spectral observation window of the experiment.

The average isotropic change in polarizability over the transitions was calculated using both PBE0 and B3LYP functionals. We checked convergence with the basis set (using aug-cc-PVTZ and daug-cc-PDVZ). We verified that using aug-cc-PVDZ the basis set error affects the quantitative result by less than 1%. In addition, note that the lowest energy transition $S_0 \rightarrow S_1$ splits in a well-separated vibronic progression.

5.4.2 Conventional Stark spectroscopy

To understand the limitations of conventional field Stark spectroscopy we will describe the technique in general terms here. A more detailed description of the specific Stark spectrometer used, along with technical details can be found in a previous publication [32]. Typically, a high voltage source is connected to transparent electrodes (indium tin oxide: ITO) on the inner front and back surface of the sample cell. The front and the back window are separated by a Kapton spacer with a thickness of 25 µm and the sample cavity is filled by injection with the sample solution. The sample is then mounted in a cooled Dewar at 77 K to freeze the solvent. Freezing the sample is also a common work-around to increase the breakdown voltage

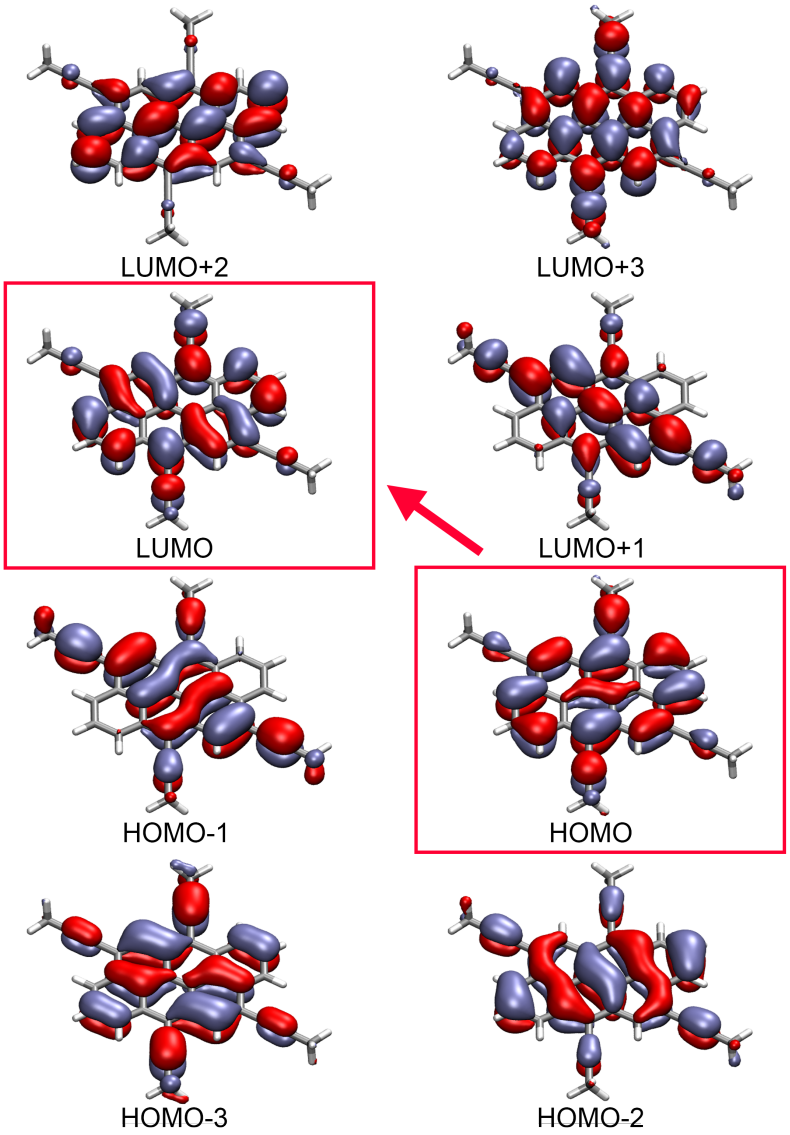

Figure 5.5: Molecular orbitals of anthanthrene. With reference to the main text, we draw the reader's attention to the HOMO→LUMO transition in particular.

and prevent unwanted redox chemistry. During the experiments, a 3.5 kHz sinusoidal signal is applied across a cell. While for TTF-BTD the applied voltage was $V_{\mathrm{rms}} = 250\,\mathrm{V}$ (with a peak field of 141 kV/cm), for anthanthrene the applied voltage was $V_{\mathrm{rms}} = 150\,\mathrm{V}$ (with a peak field of 85 kV/cm). A lamp and monochromator provide tunable probe light. The electric field-induced transmission changes are monitored at twice the AC frequency by a lock-in amplifier. The difference between the in- and out-of-phase components is plotted as a function of monochromator wavelength, resulting in a Stark spectrum. The cell can be rotated about a vertical axis within the Dewar to facilitate different relative angles between the applied field and the probe light polarization. The polarization of the probe light is set with a Glan-Taylor prism.

5.4.3 THz Stark spectroscopy

This section describes in detail all relevant steps to extract the molecular physicochemical constants. We start with a brief description of the experimental apparatus and the data recorded by it. Next, we outline how we correct for the group velocity dispersion of the probe pulses and give a detailed account of the background subtraction protocol. A further important ingredient for the analysis is the THz electric field strength in the sample and we determine it by a combination of measurements and finite difference time domain simulations. Finally, the measurements are analyzed by the Liptay formalism, which is briefly described toward the end.

Experimental setup

Figure 5.6 shows a schematic of the experimental setup. The high-field single-cycle THz waveforms were generated via tilted-pulse-front pumping in $LiNbO_3$ and the time-delayed femtosecond supercontinuum (fs-SC) probe pulses came from white-light generation in a 5-mm-thick CaF_2 crystal, which was mounted in a continuously moving mount in order to avoid photodarkening. In detail, a 1 kHz Ti:sapphire regenerative amplifier (Legend Elite Duo Femto, Coherent) delivering 90 fs pulses with an average power of 8 W at 800 nm was used to produce the single-cycle THz waveforms by optical rectification in a prism-cut $LiNbO_3$ crystal [64, 65]. The THz waveforms were imaged to the sample position by a combination of two lenses with focal lengths of 100 mm and 50 mm, resulting in a 2:1 demagnification.

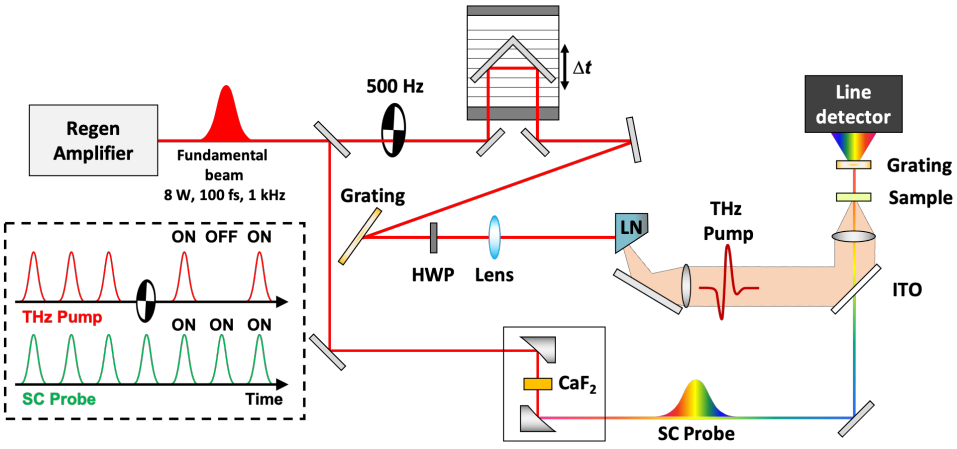

Figure 5.6: THz Stark spectroscopy. High-field single-cycle THz waveforms were generated via tilted-pulse-front pumping in $LiNbO_3$ and the fs-SC probe pulses were generated via white-light continuum in CaF_2. The probe pulses passed collinearly with the THz pulses through the sample and were analyzed by a spectrometer. A chopper running at 500 Hz alternated between THz waveform on and off.

THz waveform and fs-SC probe pulses were combined collinearly with an indium tin oxide (ITO) coated glass slide, which acts as a mirror at THz frequencies but is transparent at optical frequencies. The relative polarization between the THz waveform and the probe pulse was adjusted by an achromatic half-wave plate in the probe arm and both were subsequently focused to the sample using a TPX lens. The probe beam waist was set to $w_{SC} \approx 17\ \mu m$, which is more than one order of magnitude smaller than the THz beam waist of $w_{THz} \approx 1$ mm, and

thus probes an area of almost constant THz electric field strength at the center of the THz spot. After the sample, the probe spectrum was analyzed with a 1024-pixel CMOS array (Glaz-I, Synertronic Designs) on a pulse-to-pulse basis. A phase-locked chopper blocked every other THz waveform and from two consecutive probe spectra (with and without THz) the change in absorption, i.e. $\Delta A(\lambda) = A_{\mathrm{THz\ on}}(\lambda) - A_{\mathrm{THz\ off}}(\lambda) = -\log_{10}(T_{\mathrm{THz\ on}}(\lambda)/T_{\mathrm{THz\ off}}(\lambda))$, was calculated as a function of wavelength λ. In order to realize a sufficiently high signal-to-noise ratio we typically averaged more than 5000 pulse pairs. From a number of such measurements for different time delays τ between the THz waveform and the probe pulse, we construct two-dimensional color-coded Stark maps $\Delta A(\tau, \lambda)$ as shown in Fig. 5.7a.

Group velocity dispersion correction

The fs-SC probe pulses experience group velocity dispersion (GVD) due to a number of dispersive optical elements through which they have to propagate. As a result, each spectral component has a different effective time delay with respect to the THz waveform. Since the total GVD is independent of sample and polarization, it can be corrected for. As an example, Fig. 5.7a shows the measured and color-coded Stark signals (anthanthrene) versus time delay between probe pulse and THz waveform and wavelength of probe pulse. The black solid curve shows the 3rd order polynomial fitting, which is subsequently used for GVD correction. It is also confirmed by cross-phase modulation (XPM) of the quartz substrate at the sample position. In essence, all rows of data are shifted by a time delay that is given by the 3rd order polynomial curve and Fig. 5.7b shows the data after GVD correction. All measurements on the solid curve shown in Fig. 5.7a now have the same corrected time delay.

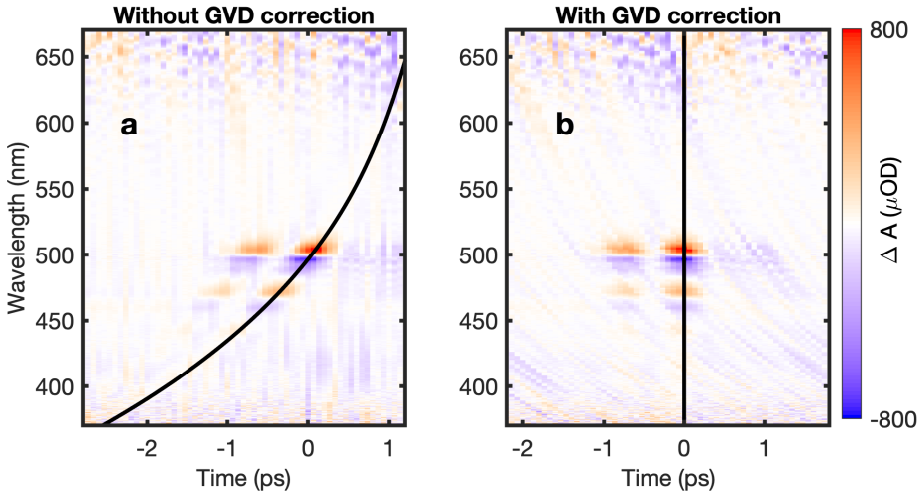

Figure 5.7: Measured color-coded Stark map for anthanthrene versus time delay and wavelength before **a** and after **b** GVD correction. The black solid curve indicates the fitted 3rd order polynomial representing the GVD, which turns into a vertical line after GVD correction.

Background measurements

To characterize the measurement background, we recorded signals for the pure solvent. Figure 5.8 shows the spectra for parallel and perpendicular orientation of THz and probe polar-

ization. For all time delays, the measurement is dominated by random noise. Note that the GVD correction introduces an apparent parabolic structure. Around time delay zero we find a positive signal for all wavelength, which is attributed to a THz Kerr effect observed in low-polar liquids [66]. In Fig. 5.8c,d the two signals integrated along the wavelength axis are shown as function of time delay. In agreement with theory, the signal for parallel orientation is larger than that for perpendicular orientation. For all measurements presented in this paper, we subtracted this background signal before plotting and analysing the data.

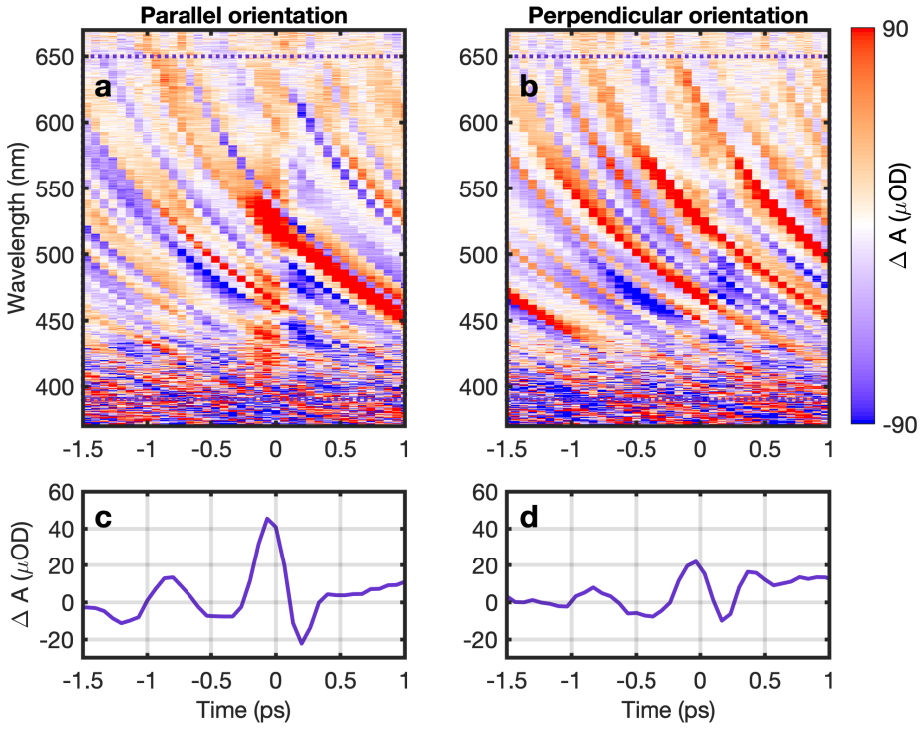

Figure 5.8: Background measurement with pure toluene for **a** parallel and **b** perpendicular orientation of THz and probe pulses. Spectral average of the change in absorption between the purple dotted lines as a function of time delay for **c** parallel and **d** perpendicular orientation.

Additional THz Stark spectroscopy results

In the main text we only show results for parallel polarization between THz waveform and probe pulse. However, the Liptay analysis requires Stark signals for two different relative polarization orientations, ideally but not necessarily parallel and perpendicular. Hence, for completeness we here show the signals for perpendicular orientation. While Fig. 5.9 shows the perpendicular orientation for TTF-BTD, Fig. 5.10 shows the corresponding results for anthanthrene.

Characterization of THz pulses

To determine the THz electric field strength in air we assume that the spatio-temporal electric field can be expressed in a product $E(x, y, t) = E_0 g_x(x) g_y(y) f(t)$, where E_0 is the peak electric

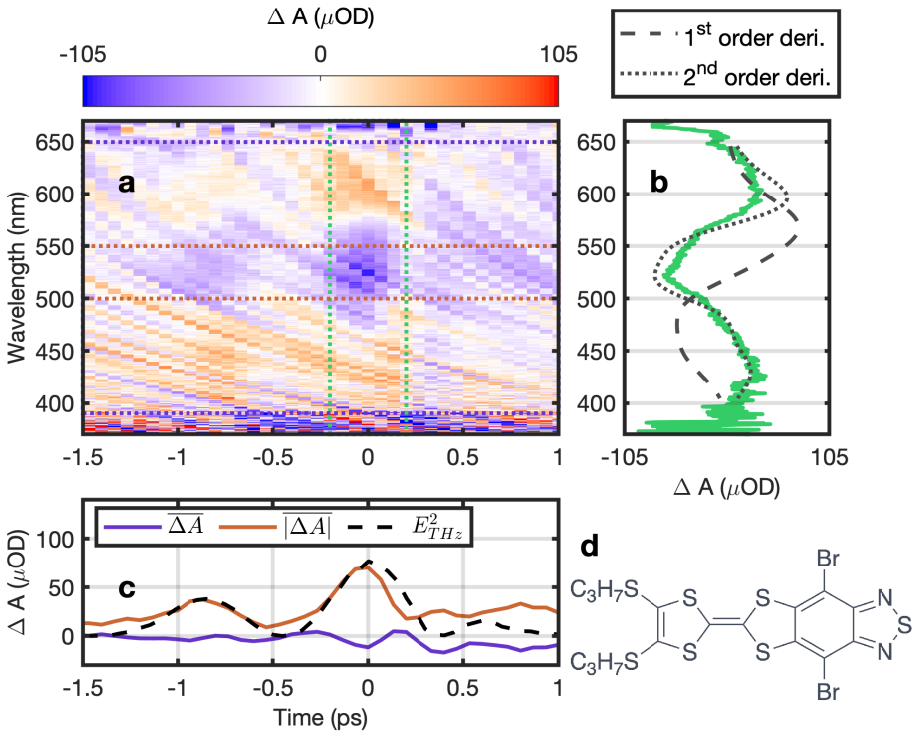

Figure 5.9: THz Stark signal of TTF-BTD with perpendicular orientation. **a** False-color plot of the measured change in absorption spectrum as a function of time delay between THz and probe pulse and wavelength. **b** Time-averaged (between the two green dotted lines) change in absorption versus wavelength (green solid curve) compared to the scaled first (black dashed curve) and second order derivative (black dotted curve) of the ground state absorption spectrum. **c** Spectral average of the change in absorption between the purple dotted (purple curve) and red dotted lines (red curve) in **a**. The red curve is compared to the scaled square of the measured THz electric field E^2_{THz} (black dashed curve). **d** Chemical structure of TTF-BTD.

field strength and $g_x(x)$, $g_y(y)$, and $f(t)$ are spatially and temporally dependent functions normalized to a peak value of one. The peak electric field strength E_0 was determined from three measurements, i.e. the average power P_{avg} at a repetition rate of f_{rep}, the spatial profiles $g_x^2(x)$ and $g_y^2(y)$, and the time dependence $f(t)$ and is calculated via

$$E_0 = \sqrt{\frac{P_{avg}}{\epsilon_0 c f_{rep} \int_{-\infty}^{\infty} g_x^2(x)dx \int_{-\infty}^{\infty} g_y^2(y)dy \int_{-\infty}^{\infty} f^2(t)dt}}, \tag{5.2}$$

where ϵ_0 is the vacuum permittivity and c is the speed of light in vacuum. The average power was recorded by a calibrated THz power meter (with a resolution of 50 µW and a relative error of ±12%), the spatial profiles were extracted from two perpendicular knife-edge measurements, and the time dependence was measured by electro-optic sampling in a 0.3-mm-thick GaP ⟨110⟩ crystal. Note that all measurements are taken at the sample position. The maximum THz power was measured to 3.6 mW at 1 kHz repetition rate, the THz spot was nearly Gaussian with a beam waist of 1 mm in x- as well as in y-direction, and the measured electro-optic signal

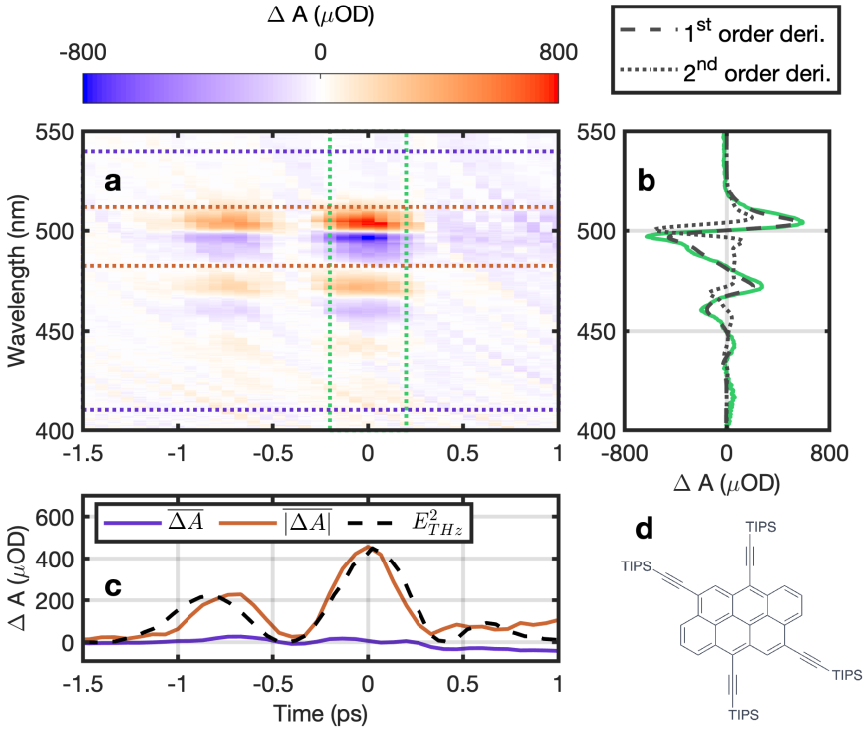

Figure 5.10: THz Stark signal of anthanthrene with perpendicular orientation. **a** False-color plot of the measured change in absorption spectrum as a function of time delay between THz and probe pulse and wavelength. **b** Time-averaged (between the two green dotted lines) change in absorption versus wavelength (green solid curve) compared to the scaled first (black dashed curve) and second order derivative (black dotted curve) of the ground state absorption spectrum. **c** Spectral average of the change in absorption between the purple dotted (purple curve) and red dotted lines (red curve) in **a**. The red curve is compared to the scaled square of the measured THz electric field E^2_{THz} (black dashed curve). **d** Chemical structure of anthanthrene.

[67–69] and the corresponding spectrum are shown in Fig. 5.11a and b. Inserting the three measurements in Eq.(5.2) results in a peak electric field of $E_0 = (400 \pm 24)\,\mathrm{kV/cm}$ for the larger of the two peaks in air.

The effective field strength, at which the probe pulse interrogates the molecular system, is typically smaller because of a number of effects. The dominating reduction factor comes from the geometry and material of the cuvette. For instance, Fresnel reflections or Fabry-Perot interferences at or within the cuvette limit the maximum electric field strength. Some solvents also have a no-negligible THz absorption coefficient and consequently reduce the electric field strength exponentially along the probe's propagation direction. Moreover, several effects lead to a smearing and averaging of the signal, such as the finite size of the probe interrogating the sample at different THz electric field strengths or the finite duration of the probe pulse and the group velocity mismatch between THz waveform and probe pulse. In order to account for all these effects we performed finite difference time-domain simulations propagating the THz waveform together with a time delayed probe pulse through the sample cuvette. We found that

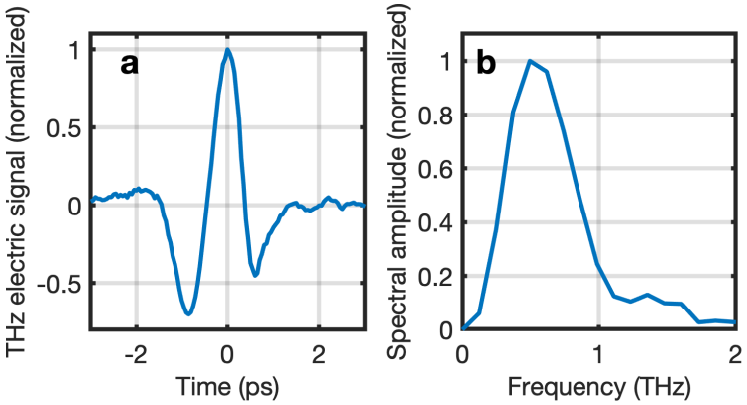

Figure 5.11: **a** Measured electro-optic signal at the sample position and **b** corresponding spectrum.

the time dependence of the THz electric field experienced by the probe pulse is almost identical to the free space THz waveform, however the peak electric field strength is reduced by a factor of 0.7 resulting in a maximum electric field of $E_0 = (280 \pm 17)\,\mathrm{kV/cm}$ for the larger of the two peaks in the sample.

Liptay analysis

The following analysis closely follows the recipe outlined in reference [5]. After having identified the Stark-active transitions, the Stark spectra are subsequently analyzed with the Liptay formalism (for details also see references [32] and [23]). The analytic expression derived by Liptay links the molar absorption $\Delta\epsilon(\bar{\nu})$ as a function of wavenumber to the square of the electric field $\mathbf{E}$ and ground state absorption spectrum $\epsilon(\bar{\nu})$

$$\Delta\epsilon(\bar{\nu}) = f_l^2 |\mathbf{E}|^2 \left\{ A_\chi \epsilon(\bar{\nu}) + \frac{B_\chi}{15hc}\bar{\nu}\frac{\mathrm{d}}{\mathrm{d}\bar{\nu}}\left(\frac{\epsilon(\bar{\nu})}{\bar{\nu}}\right) + \frac{C_\chi}{30h^2c^2}\bar{\nu}\frac{\mathrm{d}^2}{\mathrm{d}\bar{\nu}^2}\left(\frac{\epsilon(\bar{\nu})}{\bar{\nu}}\right)\right\}, \tag{5.3}$$

where h is Planck's constant and c the speed of light. The model assumes an isotropic distribution of transition dipole moments, which is provided by freezing the sample in conventional Stark spectroscopy. The measured Stark spectra are fitted with a weighted combination of the zeroth, first, and second order derivative of the ground state absorption spectrum. The coefficient A_χ is determined by the transition polarizability and/or the transition hyperpolarizability of the sample, which can usually be neglected for immobilized samples. The second and third coefficients are given by

$$B_\chi = \frac{5}{2}\mathrm{Tr}(\underline{\Delta\alpha}) + \left(3\cos^2\chi - 1\right)\left(\frac{3}{2}\mathbf{m}\underline{\Delta\alpha}\mathbf{m} - \frac{1}{2}\mathrm{Tr}(\underline{\Delta\alpha})\right) \tag{5.4}$$

$$C_\chi = |\Delta\mu|^2\left\{5 + \left(3\cos^2\chi - 1\right)\left(3\cos^2\zeta - 1\right)\right\}, \tag{5.5}$$

where $\mathrm{Tr}(\underline{\Delta\alpha})$ is the trace of the polarizability tensor, $\mathbf{m}\underline{\Delta\alpha}\mathbf{m}$ is its projection along the transition dipole moment, χ is the angle between the applied electric field and the probe polarization, $\Delta\mu$ is the change in dipole moment and ζ is the angle between the change in dipole moment and the transition dipole moment.

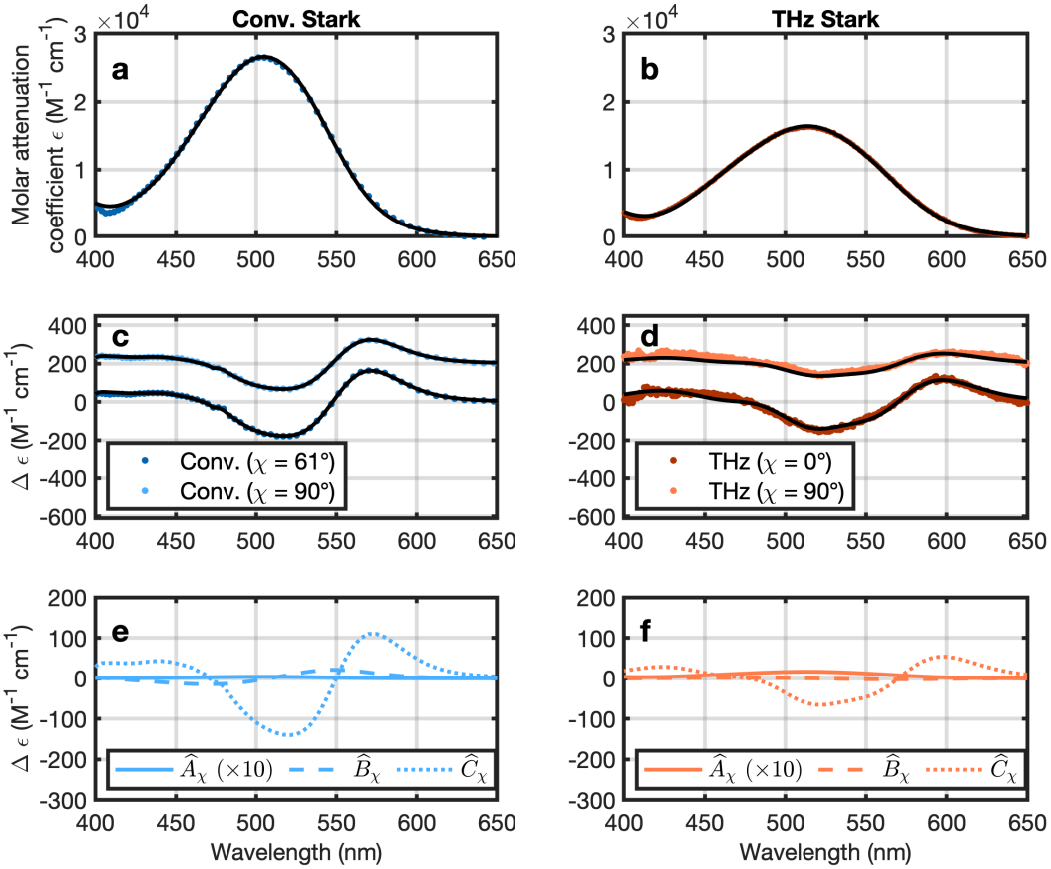

Figure 5.12: TTF-BTD conventional Stark and THz Stark spectra fitting **a, b** Ground-state absorption spectrum ϵ of TTF-BTD sample at 77 K (**a**) and at 295 K (**b**). The dots represent the data points and the black solid curves represents the fits. **c, d** Measured Stark spectra for two different incidence angles (dots) and corresponding fits (black solid curves) for the conventional Stark measurement **c** and THz Stark measurement **d**. For better visualization, the curves for $\chi = 90°$ are arbitrarily shifted along the $\Delta\epsilon$-axis. **e, f** Contribution of the zeroth (solid curve), first (dashed curve) and second (dotted curve) order derivative line form for the Stark spectra for $\chi = 90°$.

The molecular parameters are extracted by simultaneously fitting the ground-state absorption spectra and two Stark spectra for different probe polarizations. Figure 5.12 shows the measured data (dotted curves) and the corresponding fits (black solid curves) for the TTF-BTD sample. Figure 5.12a and Fig. 5.12c show the results for the conventional Stark measurement at 77 K, while Fig. 5.12b and Fig. 5.12d show the results for the THz Stark measurement at 295 K (same data as shown in Fig. 5.4 in the main text). For both experiments we find reasonable agreement between the fits and the measured data with a slightly better fit quality for the conventional Stark measurements. Figure 5.12e and Fig. 5.12f separately show the contribution of the zeroth, first and second order contribution to the fitted Stark signal for $\chi = 90°$. The contribution of the zeroth order $\widehat{A}_\chi$ is multiplied by 10 and we a find negligible contribution to

the Stark signal for both the conventional and the THz experiment, which confirms that the alignment of molecules due to the electric field is negligible.

The same fitting results are shown in Fig. 5.13 for the anthanthrene sample. Also here we find reasonable agreement between the fits and the measured data for both conventional and THz Stark spectroscopy.

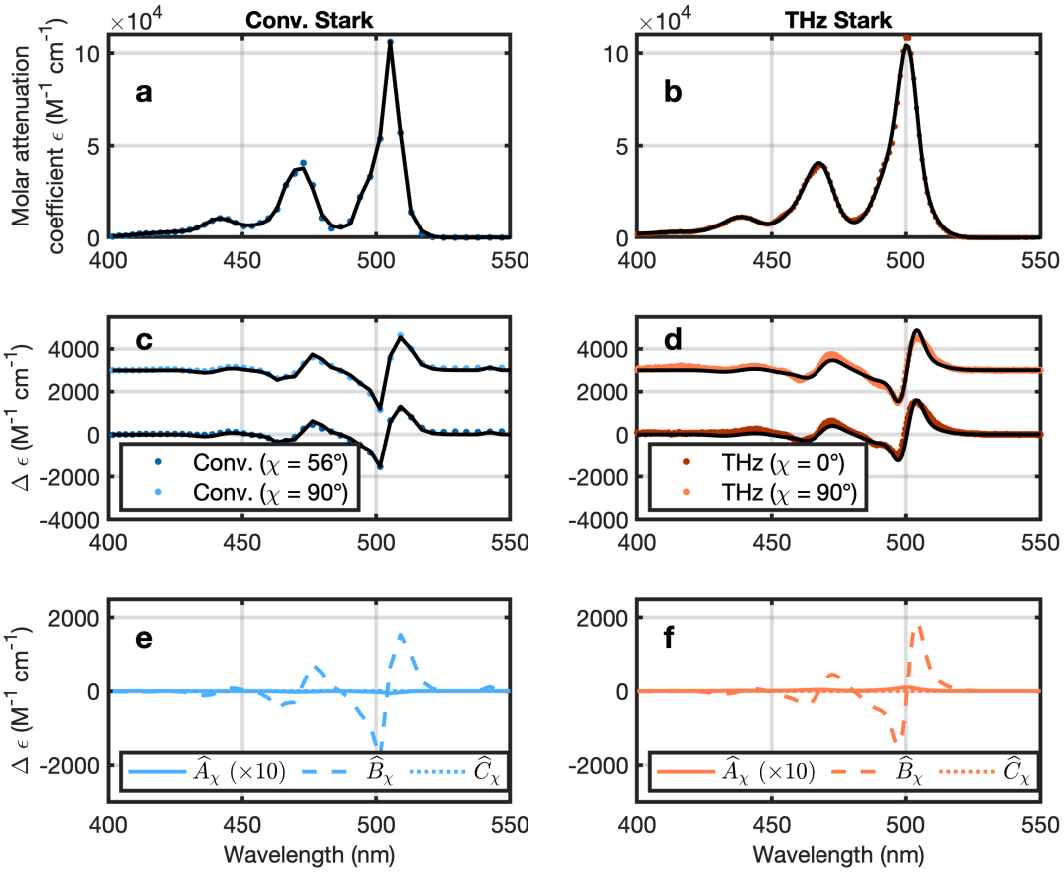

Figure 5.13: Anthanthrene conventional Stark and THz Stark spectra fitting **a, b** Ground-state absorption spectrum ϵ of anthanthrene sample at 77 K (**a**) and at 295 K (**b**). The dots represent the data points and the black solid curves represents the fits. **c, d** Measured Stark spectra for two different incidence angles (dots) and corresponding fits (black solid curves) for the conventional Stark measurement **c** and THz Stark measurement **d**. For better visualization, the curves for $\chi = 90°$ are arbitrarily shifted along the $\Delta\epsilon$-axis. **e, f** Contribution of the zeroth (solid curve), first (dashed curve) and second (dotted curve) order derivative line form for the Stark spectra for $\chi = 90°$.

Local field correction factor

The local field correction factor gives a measure of how the solvent cavity affects the field inside the cavity when an external electric field is applied. The calculations were done in analogy

to those described in literature [36–38]. We approximated the molecule as occupying a cavity with an ellipsoidal shape. For anthanthrene we estimate the ellipsoid axes to 15 Å, 15 Å, and 3 Å, while for the TTB-BTD we estimate them to 15 Å, 7 Å, and 3 Å. Note that reasonable variation of these parameters has only minor effects to the local field correction factor. Based on literature, the dielectric constant of toluene at 77 K and zero frequency is 2.52 [70], while at room temperature and 400 GHz it is 2.27 [71]. The local field correction factors f_l for TTF-BTD and anthanthrene are estimated to be 1.30 and 1.33 respectively for conventional Stark spectroscopy and to be 1.26 and 1.29 respectively for THz Stark spectroscopy. Hence, the fitted values $\mathrm{Tr}(\Delta\alpha)$ have to be divided by ${f_l}^2$ and $\Delta\mu$ by f_l before the numbers can be compared with the DFT calculation.

Bibliography

[1] B. S. Brunschwig, C. Creutz, and N. Sutin, "Electroabsorption spectroscopy of charge transfer states of transition metal complexes", Coord. Chem. Rev. **177**, 61–79 (1998), https://www.sciencedirect.com/science/article/pii/S001085459800188X.

[2] G. U. Bublitz, R. Ortiz, S. R. Marder, and S. G. Boxer, "Stark Spectroscopy of Donor/Acceptor Substituted Polyenes", J. Am. Chem. Soc. **119**, 3365–3376 (1997), https://doi.org/10.1021/ja9640814.

[3] T. Iimori, R. Ito, N. Ohta, and H. Nakano, "Stark Spectroscopy of Rubrene. I. Electroabsorption Spectroscopy and Molecular Parameters", J. Phys. Chem. A **120**, 4307–4313 (2016), https://doi.org/10.1021/acs.jpca.6b02625.

[4] L. Karki, F. W. Vance, J. T. Hupp, S. M. LeCours, and M. J. Therien, "Electronic Stark Effect Studies of a Porphyrin-Based Push-Pull Chromophore Displaying a Large First Hyperpolarizability: State-Specific Contributions to β", J. Am. Chem. Soc. **120**, 2606–2611 (1998), https://doi.org/10.1021/ja973593v.

[5] W. Liptay, "Electrochromism and Solvatochromism", Angew. Chemie Int. Ed. English **8**, 177–188 (1969), https://doi.org/10.1002/anie.196901771.

[6] S. A. Locknar and L. A. Peteanu, "Investigation of the Relationship between Dipolar Properties and Cis-Trans Configuration in Retinal Polyenes: A Comparative Study Using Stark Spectroscopy and Semiempirical Calculations", J. Phys. Chem. B **102**, 4240–4246 (1998), https://doi.org/10.1021/jp980562t.

[7] R. Mathies and L. Stryer, "Retinal has a highly dipolar vertically excited singlet state: implications for vision", eng, Proc. Natl. Acad. Sci. U. S. A. **73**, 2169–2173 (1976), https://pubmed.ncbi.nlm.nih.gov/1065867%20https://www.ncbi.nlm.nih.gov/pmc/articles/PMC430480/.

[8] R. F. Pauszek, G. Kodali, S. T. Caldwell, B. Fitzpatrick, N. Y. Zainalabdeen, G. Cooke, V. M. Rotello, and R. J. Stanley, "Excited State Charge Redistribution and Dynamics in the Donor-π-Acceptor Flavin Derivative ABFL", J. Phys. Chem. B **117**, 15684–15694 (2013), https://doi.org/10.1021/jp406420h.

[9] B. C. Pein, C. K. Lee, L. Shi, J. Shi, W. Chang, H. Y. Hwang, J. Scherer, I. Coropceanu, X. Zhao, X. Zhang, V. Bulović, M. G. Bawendi, A. P. Willard, and K. A. Nelson, "Terahertz-Driven Stark Spectroscopy of CdSe and CdSe–CdS Core–Shell Quantum Dots", Nano Lett. **19**, 8125–8131 (2019), https://doi.org/10.1021/acs.nanolett.9b03342.

[10] N. Hopkins and R. J. Stanley, "Measurement of the Electronic Properties of the Flavoprotein Old Yellow Enzyme (OYE) and the OYE:p-Cl Phenol Charge-Transfer Complex Using Stark Spectroscopy", Biochemistry **42**, 991–999 (2003), https://doi.org/10.1021/bi0268908.

[11] D. H. Oh and S. G. Boxer, "Stark effect spectra of Ru(diimine)32+ complexes", J. Am. Chem. Soc. **111**, 1130–1131 (1989), https://doi.org/10.1021/ja00185a054.

[12] J. R. Reimers and N. S. Hush, "Electronic properties of transition-metal complexes determined from electroabsorption (Stark) spectroscopy. 2. Mononuclear complexes of ruthenium (II)", J. Phys. Chem. **95**, 9773–9781 (1991), https://doi.org/10.1021/j100177a032.

[13] Y.-g. K. Shin, B. S. Brunschwig, C. Creutz, and N. Sutin, "Toward a Quantitative Understanding of Dipole-Moment Changes in Charge-Transfer Transitions: Electroabsorption Spectroscopy of Transition-Metal Complexes", J. Am. Chem. Soc. **117**, 8668–8669 (1995), https://doi.org/10.1021/ja00138a024.

[14] V. Roiati, E. Mosconi, A. Listorti, S. Colella, G. Gigli, and F. De Angelis, "Stark Effect in Perovskite/TiO2 Solar Cells: Evidence of Local Interfacial Order", Nano Lett. **14**, 2168–2174 (2014), https://doi.org/10.1021/nl500544c.

[15] M. S. Mehata, C.-S. Hsu, Y.-P. Lee, and N. Ohta, "Electroabsorption and Electrophotoluminescence of Poly(2,3-diphenyl-5-hexyl-p-phenylene vinylene)", J. Phys. Chem. C **116**, 14789–14795 (2012), https://doi.org/10.1021/jp302666f.

[16] A. Chowdhury, L. A. Peteanu, M. A. Webb, and G. R. Loppnow, "Stark spectroscopic studies of blue copper proteins: Azurin", J. Phys. Chem. B **105**, 527–534 (2001), https://doi.org/10.1021/jp0025227.

[17] G. Kodali, S. U. Siddiqui, and R. J. Stanley, "Charge Redistribution in Oxidized and Semiquinone E. coli DNA Photolyase upon Photoexcitation: Stark Spectroscopy Reveals a Rationale for the Position of Trp382", J. Am. Chem. Soc. **131**, 4795–4807 (2009), https://doi.org/10.1021/ja809214r.

[18] D. J. Lockhart and S. G. Boxer, "Stark effect spectroscopy of Rhodobacter sphaeroides and Rhodopseudomonas viridis reaction centers", Proc. Natl. Acad. Sci. **85**, 107–111 (1988), https://doi.org/10.1073/pnas.85.1.107.

[19] M. Lösche, G. Feher, and M. Y. Okamura, "The Stark effect in reaction centers from Rhodobacter sphaeroides R-26 and Rhodopseudomonas viridis.", Proc. Natl. Acad. Sci. **84**, 7537–7541 (1987), https://doi.org/10.1073/pnas.84.21.7537.

[20] L. L. Premvardhan, M. A. van der Horst, K. J. Hellingwerf, and R. van Grondelle, "Stark spectroscopy on photoactive yellow protein, E46Q, and a nonisomerizing derivative, probes photo-induced charge motion", English, Biophys. J. **84**, 3226–3239 (2003), https://doi.org/10.1016/S0006-3495(03)70047-2.

[21] O. J. G. Somsen, V. Chernyak, R. N. Frese, R. van Grondelle, and S. Mukamel, "Excitonic Interactions and Stark Spectroscopy of Light Harvesting Systems", J. Phys. Chem. B **102**, 8893–8908 (1998), https://doi.org/10.1021/jp981114o.

[22] N. Verma, Y. Tao, W. Zou, X. Chen, X. Chen, M. Freindorf, and E. Kraka, "A Critical Evaluation of Vibrational Stark Effect (VSE) Probes with the Local Vibrational Mode Theory", Sensors **20**, 2358 (2020), https://doi.org/10.3390/s20082358.

[23] G. U. Bublitz and S. G. Boxer, "STARK SPECTROSCOPY: Applications in Chemistry, Biology, and Materials Science", Annu. Rev. Phys. Chem. **48**, 213–242 (1997), https://doi.org/10.1146/annurev.physchem.48.1.213.

[24] S. Keiber, S. Sederberg, A. Schwarz, M. Trubetskov, V. Pervak, F. Krausz, and N. Karpowicz, "Electro-optic sampling of near-infrared waveforms", Nat. Photonics **10**, 159–162 (2016), https://doi.org/10.1038/nphoton.2015.269.

[25] M. Knorr, J. Raab, M. Tauer, P. Merkl, D. Peller, E. Wittmann, E. Riedle, C. Lange, and R. Huber, "Phase-locked multi-terahertz electric fields exceeding 13 MV/cm at a 190 kHz repetition rate", Opt. Lett. **42**, 4367–4370 (2017), https://opg.optica.org/ol/abstract.cfm?URI=ol-42-21-4367.

[26] H. M. Jones and E. E. Kunhardt, "Pulsed dielectric breakdown of pressurized water and salt solutions", J. Appl. Phys. **77**, 795–805 (1995), https://doi.org/10.1063/1.359002.

[27] Z. Krasucki and F. P. Bowden, "Breakdown of liquid dielectrics", Proc. R. Soc. London. Ser. A. Math. Phys. Sci. **294**, 393–404 (1966), https://doi.org/10.1098/rspa.1966.0214.

[28] D. Zhang, A. Fallahi, M. Hemmer, X. Wu, M. Fakhari, Y. Hua, H. Cankaya, A.-L. Calendron, L. E. Zapata, N. H. Matlis, and F. X. Kärtner, "Segmented terahertz electron accelerator and manipulator (STEAM)", Nat. Photonics **12**, 336–342 (2018), https://doi.org/10.1038/s41566-018-0138-z.

[29] A. Amacher, H. Luo, Z. Liu, M. Bircher, M. Cascella, J. Hauser, S. Decurtins, D. Zhang, and S.-X. Liu, "Electronic tuning effects via cyano substitution of a fused tetrathiafulvalene–benzothiadiazole dyad for ambipolar transport properties", RSC Adv. **4**, 2873–2878 (2014), http://dx.doi.org/10.1039/C3RA46784H.

[30] F. Pop, A. Amacher, N. Avarvari, J. Ding, L. M. L. Daku, A. Hauser, M. Koch, J. Hauser, S.-X. Liu, and S. Decurtins, "Tetrathiafulvalene-Benzothiadiazoles as Redox-Tunable Donor–Acceptor Systems: Synthesis and Photophysical Study", Chem. – A Eur. J. **19**, 2504–2514 (2013), https://doi.org/10.1002/chem.201202742.

[31] J.-B. Giguère, Q. Verolet, and J.-F. Morin, "4,10-Dibromoanthanthrone as a New Building Block for p-Type, n-Type, and Ambipolar π-Conjugated Materials", Chem. – A Eur. J. **19**, 372–381 (2013), https://doi.org/10.1002/chem.201202878.

[32] E. J. Rohwer, M. Akbarimoosavi, S. E. Meckel, X. Liu, Y. Geng, L. M. Lawson Daku, A. Hauser, A. Cannizzo, S. Decurtins, R. J. Stanley, S.-X. Liu, and T. Feurer, "Dipole Moment and Polarizability of Tunable Intramolecular Charge Transfer States in Heterocyclic π-Conjugated Molecular Dyads Determined by Computational and Stark Spectroscopic Study", J. Phys. Chem. C **122**, 9346–9355 (2018), https://doi.org/10.1021/acs.jpcc.8b02268.

[33] G. U. Bublitz and S. G. Boxer, "Effective Polarity of Frozen Solvent Glasses in the Vicinity of Dipolar Solutes", J. Am. Chem. Soc. **120**, 3988–3992 (1998), https://doi.org/10.1021/ja971665c.

[34] M. Akbarimoosavi, E. Rohwer, A. Rondi, J. Hankache, Y. Geng, S. Decurtins, A. Hauser, S.-X. Liu, T. Feurer, and A. Cannizzo, "Tunable Lifetimes of Intramolecular Charge-Separated States in Molecular Donor–Acceptor Dyads", J. Phys. Chem. C **123**, 8500–8511 (2019), https://doi.org/10.1021/acs.jpcc.8b11066.

[35] A. Rondi, Y. Rodriguez, T. Feurer, and A. Cannizzo, "Solvation-Driven Charge Transfer and Localization in Metal Complexes", Acc. Chem. Res. **48**, 1432–1440 (2015), https://doi.org/10.1021/ar5003939.

[36] A. Aubret, M. Orrit, and F. Kulzer, "Understanding Local-Field Correction Factors in the Framework of the Onsager-Böttcher Model", ChemPhysChem **20**, 345–355 (2019), https://doi.org/10.1002/cphc.201800923.

[37] R. J. Stanley and M. S. Siddiqui, "A Stark Spectroscopic Study of N(3)-Methyl, N(10)-Isobutyl-7,8-Dimethylisoalloxazine in Nonpolar Low-Temperature Glasses: Experiment and Comparison with Calculations", J. Phys. Chem. A **105**, 11001–11008 (2001), https://doi.org/10.1021/jp011971j.

[38] L. Premvardhan and L. Peteanu, "Electroabsorption measurements and ab initio calculations of the dipolar properties of 2-(2'-hydroxyphenyl)-benzothiazole and -benzoxazole: two photostabilizers that undergo excited-state proton transfer", Chem. Phys. Lett. **296**, 521–529 (1998), https://www.sciencedirect.com/science/article/pii/S0009261498010483.

[39] M. Bendikov, F. Wudl, and D. F. Perepichka, "Tetrathiafulvalenes, Oligoacenenes, and Their Buckminsterfullerene Derivatives: The Brick and Mortar of Organic Electronics", Chem. Rev. **104**, 4891–4946 (2004), https://doi.org/10.1021/cr030666m.

[40] N. Martín, "Tetrathiafulvalene: the advent of organic metals", Chem. Commun. **49**, 7025–7027 (2013), http://dx.doi.org/10.1039/C3CC00240C.

[41] J. Wu, N. Dupont, S.-X. Liu, A. Neels, A. Hauser, and S. Decurtins, "Imidazole-annulated tetrathiafulvalenes exhibiting pH-tuneable intramolecular charge transfer and redox properties.", eng, Chem. Asian J. **4**, 392–399 (2009), https://doi.org/10.1002/asia.200800322.

[42] J. J. Bergkamp, S. Decurtins, and S.-X. Liu, "Current advances in fused tetrathiafulvalene donor–acceptor systems", Chem. Soc. Rev. **44**, 863–874 (2015), http://dx.doi.org/10.1039/C4CS00255E.

[43] J. L. Segura and N. Martín, "New Concepts in Tetrathiafulvalene Chemistry.", eng, Angew. Chem. Int. Ed. Engl. **40**, 1372–1409 (2001), https://doi.org/10.1002/1521-3773(20010417)40:8%3C1372::aid-anie1372%3E3.0.co;2-i.

[44] K. R. Justin Thomas, J. T. Lin, M. Velusamy, Y. Tao, and C. Chuen, "Color Tuning in Benzo[1,2,5]thiadiazole-Based Small Molecules by Amino Conjugation/Deconjugation: Bright Red-Light-Emitting Diodes", Adv. Funct. Mater. **14**, 83–90 (2004), https://doi.org/10.1002/adfm.200304486.

[45] Y. Wu and W. Zhu, "Organic sensitizers from D–π–A to D–A–π–A: effect of the internal electron-withdrawing units on molecular absorption, energy levels and photovoltaic performances", Chem. Soc. Rev. **42**, 2039–2058 (2013), http://dx.doi.org/10.1039/C2CS35346F.

[46] C. R. Belton, A. L. Kanibolotsky, J. Kirkpatrick, C. Orofino, S. E. T. Elmasly, P. N. Stavrinou, P. J. Skabara, and D. D. C. Bradley, "Location, Location, Location - Strategic Positioning of 2,1,3-Benzothiadiazole Units within Trigonal Quaterfluorene-Truxene Star-Shaped Structures", Adv. Funct. Mater. **23**, 2792–2804 (2013), https://doi.org/10.1002/adfm.201202644.

[47] F. Pop, F. Riobé, S. Seifert, T. Cauchy, J. Ding, N. Dupont, A. Hauser, M. Koch, and N. Avarvari, "Tetrathiafulvalene-1,3,5-triazines as (Multi)Donor–Acceptor Systems with Tunable Charge Transfer: Structural, Photophysical, and Theoretical Investigations", Inorg. Chem. **52**, 5023–5034 (2013), https://doi.org/10.1021/ic3027336.

[48] P. Alemany, E. Canadell, Y. Geng, J. Hauser, P. Macchi, K. Krämer, S. Decurtins, and S.-X. Liu, "Exploring the Electronic Structure of an Organic Semiconductor Based on a Compactly Fused Electron Donor–Acceptor Molecule", ChemPhysChem **16**, 1361–1365 (2015), https://doi.org/10.1002/cphc.201500090.

[49] Y. Geng, R. Pfattner, A. Campos, J. Hauser, V. Laukhin, J. Puigdollers, J. Veciana, M. Mas-Torrent, C. Rovira, S. Decurtins, and S.-X. Liu, "A Compact Tetrathiafulvalene–Benzothiadiazole Dyad and Its Highly Symmetrical Charge-Transfer Salt: Ordered Donor π-Stacks Closely Bound to Their Acceptors", Chem. – A Eur. J. **20**, 7136–7143 (2014), https://doi.org/10.1002/chem.201304688.

[50] C. J. Lambert and S.-X. Liu, "A Magic Ratio Rule for Beginners: A Chemist's Guide to Quantum Interference in Molecules", Chem. – A Eur. J. **24**, 4193–4201 (2018), https://doi.org/10.1002/chem.201704488.

[51] Y. Geng, S. Sangtarash, C. Huang, H. Sadeghi, Y. Fu, W. Hong, T. Wandlowski, S. Decurtins, C. J. Lambert, and S.-X. Liu, "Magic Ratios for Connectivity-Driven Electrical Conductance of Graphene-like Molecules", J. Am. Chem. Soc. **137**, 4469–4476 (2015), https://doi.org/10.1021/jacs.5b00335.

[52] M. Famili et al., "Self-Assembled Molecular-Electronic Films Controlled by Room Temperature Quantum Interference", Chem **5**, 474–484 (2019), https://www.sciencedirect.com/science/article/pii/S2451929418305710.

[53] Y. Geng, C. Yi, M. P. Bircher, S. Decurtins, M. Cascella, M. Grätzel, and S.-X. Liu, "Anthanthrene dye-sensitized solar cells: influence of the number of anchoring groups and substitution motif", RSC Adv. **5**, 98643–98652 (2015), http://dx.doi.org/10.1039/C5RA21917E.

[54] J.-B. Giguère, N. S. Sariciftci, and J.-F. Morin, "Polycyclic anthanthrene small molecules: semiconductors for organic field-effect transistors and solar cells applications", J. Mater. Chem. C **3**, 601–606 (2015), http://dx.doi.org/10.1039/C4TC02137A.

[55] L. Zhang, B. Walker, F. Liu, N. S. Colella, S. C. B. Mannsfeld, J. J. Watkins, T.-Q. Nguyen, and A. L. Briseno, "Triisopropylsilylethynyl-functionalized dibenzo[def,mno]chrysene: a solution-processed small molecule for bulk heterojunction solar cells", J. Mater. Chem. **22**, 4266–4268 (2012), http://dx.doi.org/10.1039/C2JM14998B.

[56] B. K. Shah, D. C. Neckers, J. Shi, E. W. Forsythe, and D. Morton, "Anthanthrene Derivatives as Blue Emitting Materials for Organic Light-Emitting Diode Applications", Chem. Mater. **18**, 603–608 (2006), https://doi.org/10.1021/cm052188x.

[57] B. K. Shah, D. C. Neckers, J. Shi, E. W. Forsythe, and D. Morton, "Photophysical Properties of Anthanthrene-Based Tunable Blue Emitters", J. Phys. Chem. A **109**, 7677–7681 (2005), https://doi.org/10.1021/jp052337z.

[58] C. Adamo and V. Barone, "Toward reliable density functional methods without adjustable parameters: The PBE0 model", J. Chem. Phys. **110**, 6158–6170 (1999), https://doi.org/10.1063/1.478522.

[59] A. D. Becke, "Density-functional thermochemistry. III. The role of exact exchange", J. Chem. Phys. **98**, 5648–5652 (1993), https://doi.org/10.1063/1.464913.

[60] W. J. Hehre, R. Ditchfield, and J. A. Pople, "Self—Consistent Molecular Orbital Methods. XII. Further Extensions of Gaussian—Type Basis Sets for Use in Molecular Orbital Studies of Organic Molecules", J. Chem. Phys. **56**, 2257–2261 (1972), https://doi.org/10.1063/1.1677527.

[61] E. Runge and E. K. U. Gross, "Density-Functional Theory for Time-Dependent Systems", Phys. Rev. Lett. **52**, 997–1000 (1984), https://link.aps.org/doi/10.1103/PhysRevLett.52.997.

[62] B. Jansik, D. Jonsson, P. Sałek, and H. Ågren, "Calculations of static and dynamic polarizabilities of excited states by means of density functional theory", J. Chem. Phys. **121**, 7595–7600 (2004), https://aip.scitation.org/doi/abs/10.1063/1.1794635.

[63] K. Aidas et al., "The Dalton quantum chemistry program system", WIREs Comput. Mol. Sci. **4**, 269–284 (2014), https://doi.org/10.1002/wcms.1172.

[64] J. Hebling, G. Almási, I. Z. Kozma, and J. Kuhl, "Velocity matching by pulse front tilting for large-area THz-pulse generation", Opt. Express **10**, 1161–1166 (2002), http://opg.optica.org/oe/abstract.cfm?URI=oe-10-21-1161.

[65] J. A. Fülöp, Z. Ollmann, C. Lombosi, C. Skrobol, S. Klingebiel, L. Pálfalvi, F. Krausz, S. Karsch, and J. Hebling, "Efficient generation of THz pulses with 0.4 mJ energy", Opt. Express **22**, 20155–20163 (2014), http://www.opticsexpress.org/abstract.cfm?URI=oe-22-17-20155.

[66] M. Sajadi, M. Wolf, and T. Kampfrath, "Transient birefringence of liquids induced by terahertz electric-field torque on permanent molecular dipoles", Nat. Commun. **8**, 14963 (2017), https://doi.org/10.1038/ncomms14963.

[67] Q. Wu and X.-C. Zhang, "Free-space electro-optic sampling of terahertz beams", Appl. Phys. Lett. **67**, 3523–3525 (1995), https://doi.org/10.1063/1.114909.

[68] A. Nahata, A. S. Weling, and T. F. Heinz, "A wideband coherent terahertz spectroscopy system using optical rectification and electro-optic sampling", Appl. Phys. Lett. **69**, 2321–2323 (1996), https://doi.org/10.1063/1.117511.

[69] F. D. J. Brunner, J. A. Johnson, S. Grübel, A. Ferrer, S. L. Johnson, and T. Feurer, "Distortion-free enhancement of terahertz signals measured by electro-optic sampling. I. Theory", J. Opt. Soc. Am. B **31**, 904–910 (2014), http://opg.optica.org/josab/abstract.cfm?URI=josab-31-4-904.

[70] H. Isnardi, "Die Dielektrizitätskonstante von Flüssigkeiten in ihrer Temperaturabhängigkeit", Zeitschrift für Phys. **9**, 153–179 (1922), https://doi.org/10.1007/BF01326964.

[71] C. Ro/nne, K. Jensby, B. J. Loughnane, J. Fourkas, O. F. Nielsen, and S. R. Keiding, "Temperature dependence of the dielectric function of C6H6(l) and C6H5CH3(l) measured with THz spectroscopy", J. Chem. Phys. **113**, 3749–3756 (2000), https://doi.org/10.1063/1.1287737.

Chapter 6

Wideband dispersion-free THz waveguide platform

David Rohrbach[1], Bong Joo Kang[1], Elnaz Zyaee[1], and Thomas Feurer[1]

[1]Institute of Applied Physics, University of Bern, Sidlerstrasse 5, 3012 Bern, Switzerland

This work has been submitted.

Abstract

We present an integrated THz spectroscopy and sensing platform featuring low loss, vacuum-like dispersion, and strong field confinement in the fundamental mode. Its performance was characterized experimentally for frequencies between 0.1 THz and 1.5 THz. While linear THz spectroscopy and sensing gain mostly from low loss and an extended interaction length, nonlinear THz spectroscopy would also profit from the field enhancement associated to strong mode confinement. Moreover, the vacuum-like dispersion allows for a reshaping-free propagation of broadband single- to few-cycle pulses in gas-phase samples or velocity matching between THz pump and visible to infrared probe pulses. Our platform is based on a metallic structure and falls in the category of double ridged waveguides. We characterize essential waveguide properties, for instance, propagation and bending losses, but also demonstrate junctions and interferometers, essentially because those elements are prerequisites for integrated THz waveform synthesis, and hence, for coherently controlled linear and nonlinear interactions.

6.1 Introduction

A variety of THz applications, for instance, communication [1–4], particle acceleration [5–11], or spectroscopy [12–15] and sensing [16, 17] would benefit greatly from a versatile integrated platform. In the past, a number of different approaches have been proposed [18, 19]. Among them different dielectric waveguide geometries showing low attenuation [20–22] and potentially

strong mode confinement [23]. Interestingly, modern three-dimensional printing technologies allow for relatively simple fabrication of integrated dielectric THz waveguide structures [24, 25]. Their main drawback is the relatively high absorption loss of the dielectric material, or, if the mode is mostly guided in air, the non-negligible mode dispersion which severely hampers broadband signal transmission inasmuch as group velocity dispersion leads to strong pulse broadening. While there are various means to compensate for dispersion [26–28], none of them can be used to transport single cycle THz pulses with octave-spanning frequency bandwidth along the waveguide. Group velocity dispersion is less of an issue in metallic waveguides as the majority of the mode propagates in air. For instance, parallel metal plate waveguides show comparable little mode dispersion [29, 30], however, the mode is confined only in one dimension, which limits the achievable field enhancement. Nevertheless, efficient free space coupling [31–34] and even fundamental building units of integrated circuits, such as T-junctions [35, 36], were demonstrated. Similarly, metal wire based waveguides exhibit low attenuation and low dispersion [37, 38], but suffer from high bending losses, modest mode confinement, and generally low free space coupling efficiency. Better performance is achieved for two parallel metal wires [39–41], however, such structures are fragile and often the wires must be encapsulated with a dielectric material to mechanically stabilize the geometry, which in turn increases the mode dispersion and/or the attenuation. A very similar performance is found for slot-line waveguides [42], which are especially well suited for very compact integrated circuits [43, 44]. If no supporting substrate is present, the structure essentially becomes a metallic slit waveguide [45], which is of special interest since it combines a low group velocity dispersion with a low attenuation and a strong mode confinement [46, 47] across a wide range of frequencies. Slit waveguides consist of two parallel metal ridges separated by an air gap, with the ridge width and the air gap being of similar or smaller size than the free space wavelength. Such structures have been fabricated by milling slits in silicon wafers and by subsequent metal coating [45], or by carefully aligning two thin metal foils [11].

Here, we demonstrate a compact and robust yet flexible platform essentially using a slit waveguide as the central motif. It features low propagation and bending losses and allows for active THz pulse shaping, and hence for fully integrated, coherently controlled spectroscopy. In order to guarantee efficient coupling of free space single-cycle THz pulses, we present a judiciously designed horn antenna.

6.2 Waveguide design

Figure 6.1 (a) shows the cross-section of the proposed double-ridged waveguide. It consists of two mirror symmetric metal parts separated by a metallic spacer foil, which defines the gap between the two central ridges. In the limit of $a/s \gg 1$ and $b/g \gg 1$ the geometry resembles essentially that of a slit waveguide with the fundamental mode being confined to the gap volume. Our platform is not only robust mechanically, it also allows for integrating coupling elements, either to free space or to other waveguides, or for fabricating fully integrated functional elements, such as power splitters, filters, resonators, or interferometers.

Here, we used numerical simulations to identify a geometry that features close to zero dispersion and low propagation and bending losses combined with strong mode confinement over the frequency range of interest of 0.1 THz to 1 THz, keeping in mind that the aspect ratio b/s is limited by the CNC-machining manufacturing technique. For mode confinement, both g

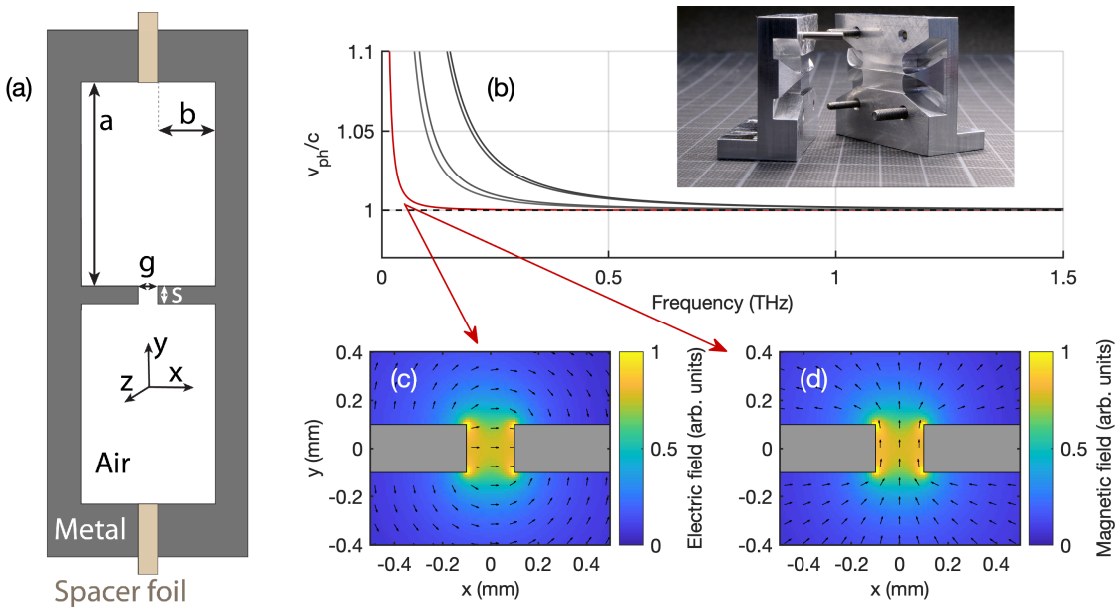

Figure 6.1: (a) Schematic cross-section of the double-ridged waveguide. (b) Waveguide dispersion of the lowest five Eigenmodes versus frequency. The inset shows a photograph (provided by Rhoda Berger) of the manufactured waveguide structure with a 20 mm long straight channel including in- and out-coupling antennas. (c) Electric and (d) magnetic field distribution of the fundamental mode in the transverse xy-plane at 0.5 THz.

and s should in general be similar or smaller than the corresponding THz free space wavelength. The optimized parameters were found to $b = 1\,\text{mm}$, $s = 0.2\,\text{mm}$, and $a = 5\,\text{mm}$. Note that the gap size g is given by the thickness of the spacer foils and was varied between $g = 30\,\mu\text{m}$ and $200\,\mu\text{m}$. The inset in Fig. 6.1(b) shows a photograph of the two mirror-symmetric parts for a 20 mm long straight waveguide. As shown, the waveguide structure also includes in- and out-coupling horn antennas at both ends of the waveguide.

The simulated waveguide dispersion relation with the first five Eigenmodes is shown in Fig. 6.1(b) for $g = 200\,\mu\text{m}$. The fundamental mode, which resembles a quasi-TEM mode with a cutoff frequency below 10 GHz, exhibits a phase velocity (red curve) coinciding with the speed of light in vacuum (dashed horizontal line) down to about 0.1 THz. The normalized transverse electric and magnetic field distribution of the fundamental mode are displayed in Figure 6.1(c) and (d), with the color-coded amplitude and the arrows indicating direction of the respective field vectors. Note that the spatial mode profile is approximately frequency independent (see supplemental document for details). While the electric field in the gap area is predominantly polarized along the x-direction, the magnetic field is mostly parallel to the y-direction.

6.3 Fundamental mode characterization

The experimental setup to characterize different waveguides is similar to the one reported in reference [34], with details given in the supplemental document. Briefly, single-cycle THz pulses are generated and detected by photo-conductive antennas, and the source is imaged to the detector via two pairs of aspherical lenses with focal lengths of 100 mm and 50 mm. The waveguides

are positioned between the two central lenses and are equipped with input and output couplers for efficient coupling. Inspired by the cylindrical tapered couplers used in combination with parallel plate waveguides [34], we designed similar structures with a cylindrical tapering with a radius of 13 mm in both transverse coordinates and a total length of 10 mm. Similar geometries were successfully used for local field enhancement [48, 49], but to the best of our knowledge never in combination with a slit waveguide structure. We simulated coupling efficiencies up to 80% for the frequency range between 0.35 THz to 1 THz (and at least 50% between 0.1 THz to 1.4 THz), which is in reasonable agreement with the experiments (see supplemental document for details). While coupling for lower frequencies is limited by reflection losses at the waveguide entrance, coupling for higher frequencies tends to be less efficient due to the smaller free space mode size.

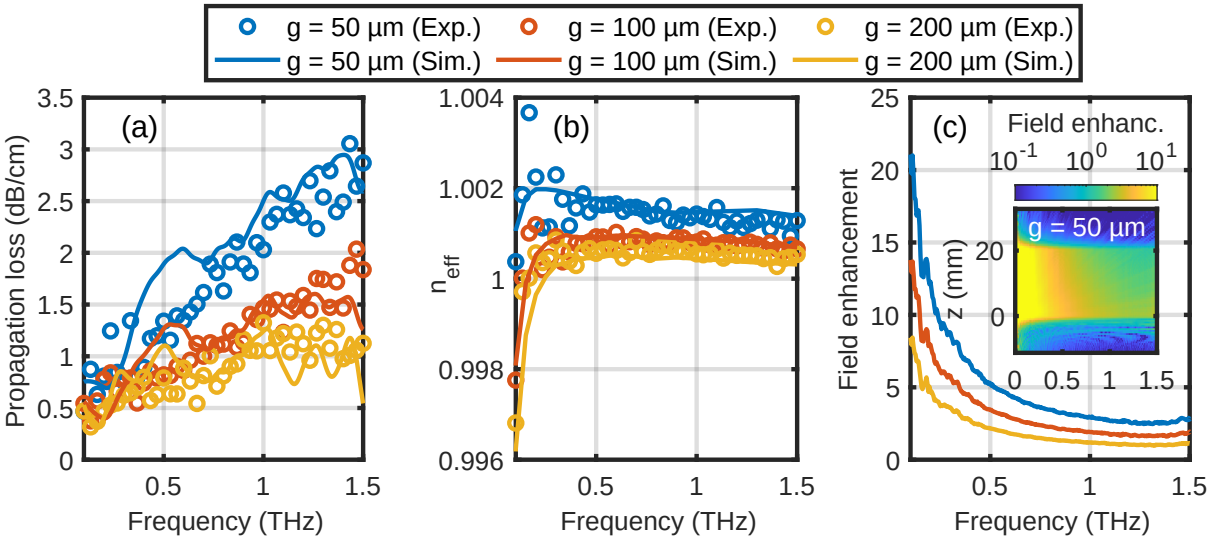

Figure 6.2: (a) Propagation loss, (b) effective refractive index, and (c) field enhancement at $z = 0$ mm as a function of frequency for three different gap sizes of 50 µm (blue), 100 µm (red), and 200 µm (yellow). Open circles corresponds to experimental data and solid curves to simulations. The inset in (c) shows the simulated color-coded field enhancement as function of frequency and position along the middle of a 20 mm long waveguide with a gap of 50 µm.

Figure 6.2 shows propagation loss, effective refractive index, as well as field enhancement of the fundamental mode as function of frequency for three different gap sizes of 50 µm (blue), 100 µm (red), and 200 µm (yellow). Generally, we find excellent agreement between measured (open circles) and simulated results (solid curves). The propagation loss increases with frequency, is larger for smaller gap sizes, and is governed mostly by Ohmic losses in the metal (aluminium). With values on the order of a few dB/cm, the propagation power loss is comparable to many other THz waveguides, for instance, microstrip lines, even though there exist exceptions where losses can be even smaller than 0.1 dB/cm in an approximately 0.1 THz wide frequency band [20]. Simulations suggest that lower attenuation can be achieved for metals with higher conductivity and should ideally vanish for superconducting materials, but in practice will be limited by scattering at waveguide imperfections. Figure 6.2(b) shows that the effective index of refraction deviates at most by about 10^{-3} from the vacuum value down to 0.1 THz. The deviation increases as the gap becomes smaller, and a similar behavior is found

for surface plasmon polaritons on metal wires [50] or in parallel plate waveguides [51]. The variations of n_{eff} between 0.2 THz to 1.5 THz are less than 0.2%. This exceptional low waveguide dispersion is of utmost relevance for THz-pump optical-probe spectroscopy of gas-phase samples ensuring not only a reshaping-free propagation of single- or few-cycle THz pulses but also a velocity matching between an optical to infrared probe and the THz pulse. The rapid decrease for frequencies below 0.2 THz is related to the mode dispersion as shown in Fig. 6.1(c) and could be shifted towards lower frequencies by increasing the distance a between the gap and the sidewalls. We also extract the group velocity dispersion and find $|\beta_2| \leq 0.1\,\mathrm{ps\,THz^{-1}\,cm^{-1}}$ for frequencies between 0.3 THz to 1.5 THz.

An appreciable electric and magnetic field enhancement - with respect to a free space focused THz pulse - is achieved because the transverse mode profile of the fundamental is smaller than a diffraction-limited free space focus for a THz pulse with the same spectral content. Here, we define the field enhancement factor shown in Fig. 6.2(c) in frequency domain as the ratio of the peak electric field amplitude in the waveguide over the peak electric field amplitude at a free space focus using a f# = 1 focusing element. Note that the field enhancement takes into account the coupling efficiency on the input side. The field enhancement can only be inferred from simulations, since we have no means to measure the electric field directly inside the gap. Similar enhancement factors are found for the magnetic field. As for most slit-based structures, lower frequencies show a higher field enhancement. This is because they have a larger mode profile when focused in free space, resulting in a larger increase in electromagnetic energy density when the mode is squeezed in the quasi-TEM mode of the waveguide. The inset in Fig. 6.2(c) shows the color-coded field enhancement as a function of frequency and along the propagation axis. Note that especially the low frequency components are already enhanced toward the end of the input coupler ($z < 0$). The field enhancement decreases along the propagation axis in essence due to propagation losses. At 0.5 THz we find a peak field enhancement of 5 and an effective field enhancement of 4.4 when averaged over a 20 mm long waveguide for $g = 50\,\mu\mathrm{m}$. Hence, a lithium niobate THz source sufficiently strong to produce an electric field strength of 400 kV/cm when focused in free space, can be enhanced to almost 2 MV/cm along the entire waveguide. Similarly, the corresponding magnetic field would increase from 130 mT to 590 mT.

6.4 Integrated circuits

The strong confinement of the fundamental THz mode is especially beneficial for waveguide bends of small radii, on the order of millimeters, leading to low bending loss. Hence, our platform is suitable for developing highly sophisticated THz integrated circuits over a small footprint, for instance, power splitters or micro-ring based filters. In order to characterize the bending loss we use structures as the one shown in Fig. 6.3(a) consisting of four 90° bends with radii of $R = 1\,\mathrm{mm}$ and $R = 5\,\mathrm{mm}$. Figure 6.3(b) shows the measured transmitted electric field (blue dashed curve) as a function of time for $R = 1\,\mathrm{mm}$ and $g = 50\,\mu\mathrm{m}$ together with the normalized reference signal (black solid curve). The green box indicates the time window in which we expect the signal guided around the four bends to appear. Compared to a straight waveguide the four bends increase the total waveguide length by 15.4 mm corresponding to a 51 ps time delay. The smaller signal contributions before and after the main guided signal are either due to scattering or leaking out of the waveguide. For example, the signal around 0 ps corresponds to a direct line-of-sight leakage through the structure. To extract only the guided signal we applied a Tukey time-window (with cosine fraction of 0.5) centered at 54.5 ps with

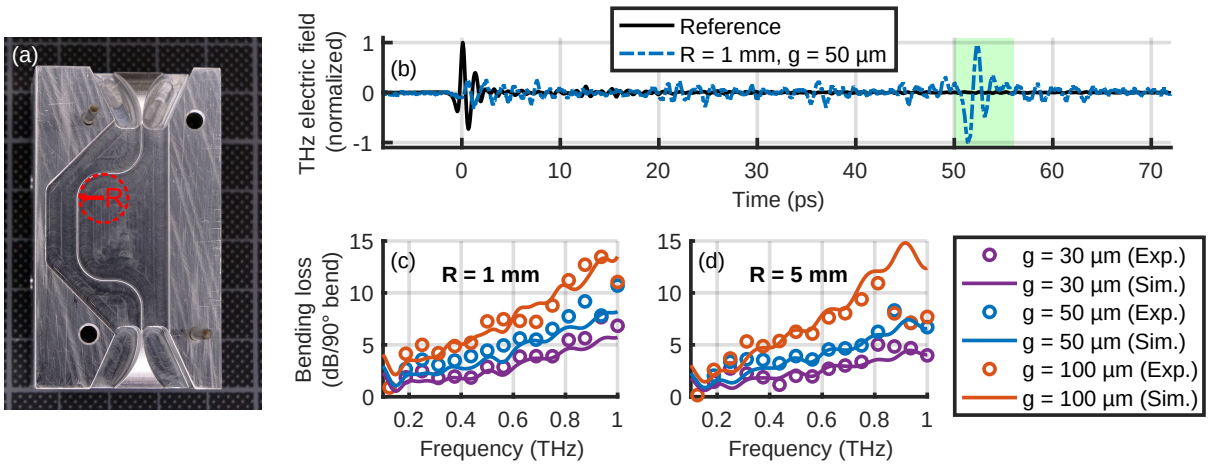

Figure 6.3: (a) Photograph (provided by Rhoda Berger) of the bending structure with four 90° bends with an inner radius $R = 5\,\text{mm}$. (b) Transmitted signal trough a structure with $R = 1\,\text{mm}$ and $g = 50\,\mu\text{m}$ together with the normalized air-reference signal (i.e., without waveguide). (c) and (d) Extracted losses per 90° bend for different gap sizes and bending radii. Circles corresponds to experimental results and solid curves to simulations.

a length of 15 ps. Note that the simulations are based on a single 90 degree bend to clearly separate the guided signal from other contributions. Figure 6.3(c) and (d) show the losses per 90° bend as a function of frequency, for different gap sizes and bending radii. Generally, we find excellent agreement between experimental (open circles) and simulated results (solid curves). There is essentially no difference in performance when decreasing the radius from 5 mm to 1 mm. Even though a bending radius of $R = 1\,\text{mm}$ is smaller than the free space wavelength for frequencies below 0.3 THz, we observe efficient guiding. Higher frequencies suffer from higher bending losses due to leakage: Based on the mode mismatch between the guided mode and the free space mode, the bending losses should be proportional to $g\nu$, which is in reasonable agreement with what we found in the experiment and the simulation. For gaps larger than 100 µm no signal guiding was observed, but for smaller gaps guiding improves irrespective of frequency. Hence, there is a trade-off between bending loss and propagation loss, which can be optimized by adjusting the gap size.

THz waveform synthesizers for coherent control of linear and nonlinear interactions with matter are often realized via spectral phase and/or amplitude shaping. Integrated versions of such devices require as fundamental building blocks power splitters and there are a number of different options ranging from a standard Y-junction to a 1×2 rib-directional coupler, a parabolic-shaped structures, or a 1×2 arrow-2D directional coupler to name but a few [52]. Here, we fabricated a Y-junction and based on that a Mach-Zehnder interferometer as a simple but fundamental waveform synthesizer. A photograph of the Y-junction is shown in Fig. 6.4(a). The branching angle is kept as low as 20° to minimize losses and the distance between the two parallel output channels is 5.2 mm. Figure 6.4(b) shows the color-coded THz electric field as a function of time and y-position measured at the edge of the Y-junction structure using a near-field detection unit. A description of the unit is given in Supplement of Ref. [53] and in Refs. [54, 55]. Indeed, we find that the THz pulse is split in two replica with similar amplitude and time dependence. Small deviations from the designed symmetric splitting ratio of 50:50

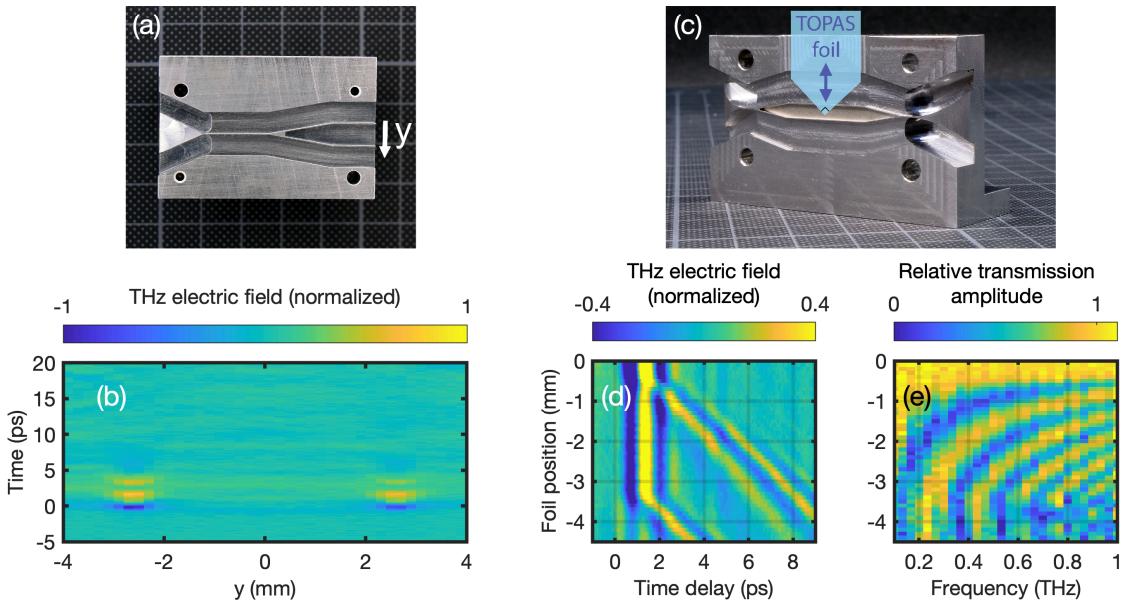

Figure 6.4: (a) Photograph of the Y-junction with in-coupler. (b) Measured electric field as a function of y-position and time. (c) Photograph of Mach-Zehnder interferometer based on two identical Y-junctions with in- and out-coupler. Position and geometry of the TOPAS foil are indicated by the blue shape. (d) THz electric field at the output of the interferometer for different foil position and (e) corresponding spectra. (Photographs are provided by Rhoda Berger)

are probably due to minor defects at the channel ends leading to different detection efficiencies. Note that the splitting ratio can be tuned by adjusting the branching angles of the two channels.

A photograph of the THz interferometer structure is shown in Fig. 6.4(c). Basically, it consists of two mirror symmetric Y-junctions with two parallel waveguide sections in between. The separation of the two parallel waveguide sections is 3 mm. In order to delay the replica in the upper interferometer arm with respect to the other, we mount a 90°-tip made of a 80 µm thick dielectric foil on a linear stage moving the foil in y-direction in and out of the 100 µm gap. The further the foil is moved in the gap, the larger the delay. The selected foil material, the cyclic olefin copolymer TOPAS, ensures low THz absorption [56]. Figure 6.4(d) shows the color-coded THz electric field after the interferometer as a function of time and foil position. The foil was moved in steps of 100 µm for a total distance of 4.5 mm. At position 0 mm the foil is ineffective and the two replica superimpose without any delay between them. For positions smaller than −0.5 mm one replica is delayed with respect to the other and we find a maximum delay of about 6 ps at −3.5 mm. For positions larger than −3.5 mm also the second waveguide section is affected by the TOPAS foil such that both replicas are delayed symmetrically. Note that a fraction of the pulse is not guided by the waveguide structure but propagates at the direct line-of-sight and is therefore mostly unaffected by the TOPAS foil. As discussed for the bending structure, this leakage signal could be reduced by further reducing the gap size. Also note that the delayed signal is slightly less intense due to Fresnel reflections and absorption. In addition, we observe an increasing dispersion as we move the TOPAS foil further in and simulations suggest this effect to be due to the air-gap between the TOPAS foil and the metal

structure [57]. Figure 6.4(d) shows the normalized color-coded THz spectra versus frequency and foil position and we observe the typical interference pattern for two time delayed THz pulses with the spectral fringes becoming more dense as the time delay increases. Well-controlled time delays between two or three phase-coherent THz pulses are essential for 2D-THz spectroscopy. Here for instance, the interferometer output can be coupled to a waveguide containing the sample and the nonlinear signal exiting the waveguide is sent to an electro-optic crystal for detection. For a three THz pulse interaction, the interferometer can be easily modified to produce an adjustable three pulse sequence.

6.5 Conclusion

We have demonstrated a versatile integrated THz waveguide platform featuring broadband performance, low bending and propagation losses of a few dB/cm, vacuum-like dispersion, efficient free space coupling, and field enhancement factors of up to 5. Above 0.1 THz its performance is essentially frequency independent such that single- or few-cycle THz pulses, like those produced by optical rectification, propagate along the waveguide without reshaping. The low losses combined with the long interaction length and the field enhancement boost any nonlinear THz light matter interaction by orders of magnitudes. Moreover, the close to one effective refractive index of the fundamental mode allows for velocity matching between a THz pump and a visible to infrared probe pulse and hence for THz-pump optical-probe spectroscopy over the entire waveguide length. In addition, we have demonstrated a power-splitter and based on that an interferometer for THz waveform synthesis. Hence, this platform can be used as a fully integrated spectroscopy system for coherently controlled linear or nonlinear spectroscopy.

6.6 Supplemental document

6.6.1 Experimental setup

A schematic of the setup is shown in Fig. 6.5. It is based on a femtosecond laser *Femto Fiber Pro* by *Toptica*, with a pulse duration of less than 100 fs, a repetition rate of 80 MHz and an average output power of 130 mW at 780 nm. At the polarizing beam splitter (BS) the beam is split in a pulse for the emitter and the detector. Approximately 10 mW are transmitted through the BS and are used for the detection. The remaining part is used for THz generation at a photoconductive antenna (PCA). It is a so-called broad area interdigital PCA *iPCA-21-05-1000-800-h* from *Batop*. As a bias voltage of the emitter PCA the 300 mV output voltage from the lock-in amplifier *HF2LI* from *Zurich Instruments* is increased to 15 V by a *Falcon Systems* amplifier. The emitter PCA is orientated such that the THz pulse is horizontally polarized. The PCA is glued on a hyperhemispherical silicon lens, which increases the escape cone of the THz pulses. The path length of the detector pulse can be adjusted by a home-built delay line which consists of a hollow roof prism mirror from *Thorlabs* mounted on a linear translation stage *Minislide MSQSD7* from *Schneeberger* driven by a linear motor *LM1483* from *Faulhaber*. The data was acquired by continuously moving the delay line with a maximum speed between 1 mm/s to 2 mm/s and averaging between 10 to 1000 scans. The encoder resolution of the delay line is 0.1 µm and the sampling distance is 0.4 µm (2.7 fs). The latter corresponds to one phase of the encoder signal and is used for triggered data acquisition. Note that the lock-in amplifier *HF2LI* allows to synchronize external signals with a frequency up to 2 MHz. The detector PCA

is a bow-tie antenna *PCA-100-05-10-800* from *Batop* including a hyperhemispherical silicon lens on top of the substrate. We detect the THz-induced current with a *HF2TA Current Amplifier* from *Zurich Instruments*. For a lock-in detection scheme, the bias voltage of the emitter PCA is modulated at 2 kHz and the lock-in integration time constant was set to 1 ms. The THz pulse is transported to the detector PCA by four aspheric THz lenses. The focal length of $L1$ and $L4$ is 100 mm while the focal length of $L2$ and $L3$ is 50 mm. We measured the beam waist at the focus using the knife-edge method and found a spot size (i.e., beam diameter at $1/e^2$) of 0.9 mm. To adjust for the different waveguide lengths, the third THz lens $L3$ was moved in $\pm z$-direction.

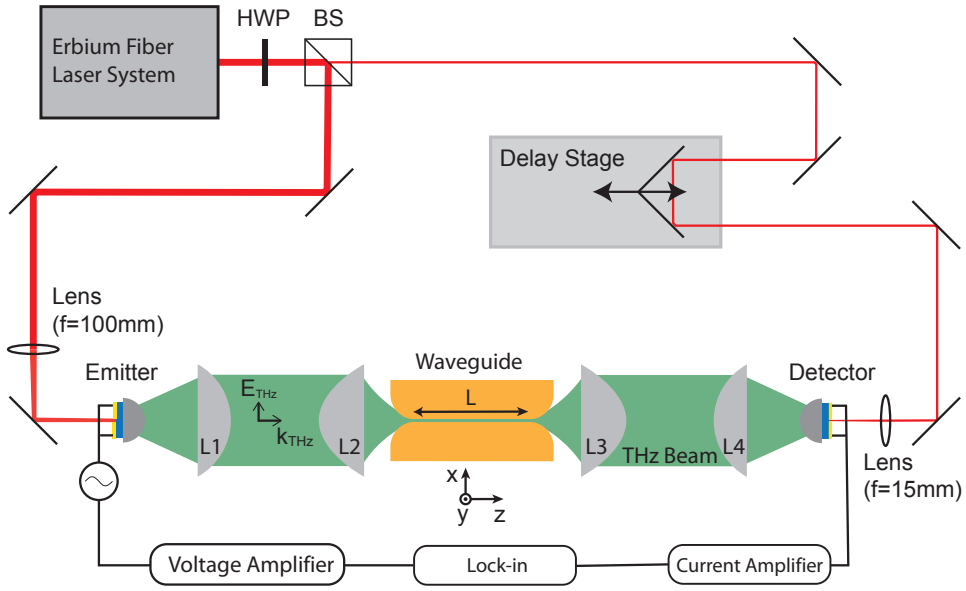

Figure 6.5: Schematic of the experimental setup: THz pulses are emitted and detected by two PCAs optically gated by a femtosecond laser pulse. The path length of the detector pulse can be adjusted by a delay stage.

6.6.2 Technical drawing of waveguide structure

Figure 6.6 shows the technical drawing of one half of the 20 mm long waveguide structure. The slit waveguide is built by assembling two mirror symmetric structures with a given gap size. Alignment holes are used for the accurate assembling of the two parts.

6.6.3 Waveguide manufacturing

All waveguide structures except for the THz interferometer were fabricated from aluminium using standard CNC-machining and subsequent lapping. For the Y-splitter, the minimum inner radius at the splitting region was set to 0.6 mm. To further improve the performance we

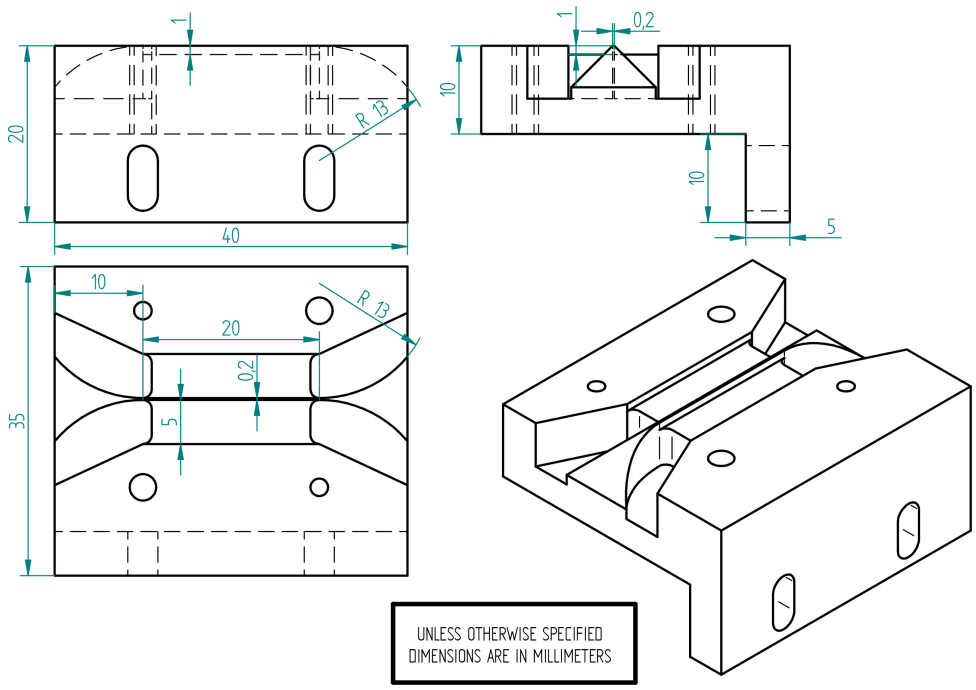

Figure 6.6: Technical drawing of one half of the 20 mm long waveguide structure with the in- and out-coupling structures. The most important dimensions are indicated in teal with units in millimeters.

use electrical discharge machining for the THz interferometer where the inner curvature radius reaches 0.2 mm. For this manufacturing technique we used *steel 1.4034* instead of aluminium.

6.6.4 Detected THz signals

Using the measured transmitted THz signals for different waveguide lengths and gap sizes, the performance of the waveguide is characterized as shown in the main text. As an example for the measured signals, Fig. 6.7(a) shows the detected signal after propagation through the different waveguide lengths all for the same gap size of $g = 200\,\mu\text{m}$. The air reference signal (i.e., without waveguide) is also shown in Fig. 6.7(a). The transmission decreases for increasing waveguide length due to propagation losses. Figure 6.7(b) shows the transmitted signal through the 80 mm long waveguide for different gap sizes. For a smaller gap size, the propagation losses increase and the phase velocity is reduced, which leads to a temporal shift of the signal towards later times as evident in Fig. 6.7(b).

6.6.5 Data evaluation

We consider the transmitted THz field through straight waveguides with different lengths L of 20 mm, 40 mm and 80 mm. Similar as in [29] we assume single-mode propagation such that the detected output electric field E_{out} and the reference electric field E_{ref} (i.e., without the waveguide structure) is given by

$$E_{out}(\omega) = E_{ref}(\omega)\, T(\omega)\, C(\omega)^2 \exp\left(-\mathrm{i}[k_z - k_0]L\right) \exp\left(-\alpha L\right), \tag{6.1}$$

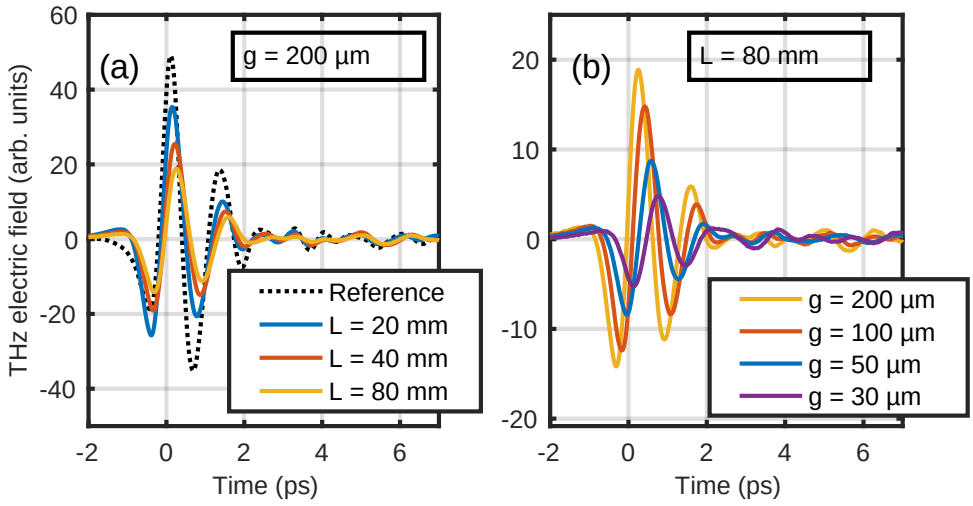

Figure 6.7: Measured transmitted THz signals for different waveguide lengths L (a) and different gap sizes g (b).

where $\omega/(2\pi)$ is the frequency, $T(\omega)$ is the total transmission coefficient taking into account reflections, $C(\omega)$ is the amplitude coefficient which is assumed to be the same at the entrance and the exit, α is the amplitude attenuation coefficient, k_z is the z-component of the wavevector and $k_0 := \omega/c$. By measuring the transmission through two waveguides of different lengths we can extract the propagation coefficient α and the wavevector k_z.

6.6.6 Mode pattern at different frequencies

Figure 6.8 shows the simulated spatial mode profile of the electric (a), (b) and the magnetic field (c), (d) at 0.25 THz (a), (c) and at 1 THz (b), (d). We find that the mode profile is approximately frequency independent. We believe that this is due to the metal being an almost perfect electric conductor (PEC) at THz frequencies and the evanescent fields inside the metal decaying rapidly, transporting only a small fraction of the total energy.

6.6.7 Coupling and misalignment effects

Figure 6.9 shows the extracted overall coupling coefficient TC^2 for a gap size of 200 µm. Here, we compare the experimental data from the time-domain spectroscopy (TDS), direct power measurements in a high power THz setup (with center frequency at 0.5 THz and a power FWHM of 0.4 THz) and numerical simulations. The experimental data from the TDS and the simulations show that the optimal coupling is obtained for frequencies between 0.35 THz to 1 THz. The coupling of lower frequencies is limited by reflection losses at the waveguide entrance due to the larger modal size, while at higher frequencies the coupling to the TEM mode of the waveguide seems to be less efficient due to the reduced mode confinement. The best coupling efficiency based on the simulation is 80 % and we even find somewhat larger values for the TDS experimental data, which we attribute to imperfect imaging of the reference signal [34]. This is confirmed by the direct THz power transmission measurements in a high power THz setup where we find an averaged coupling coefficient TC^2 around 80 % for the considered THz frequency spectrum. The shaded area indicates the estimated uncertainty based on measurement of three

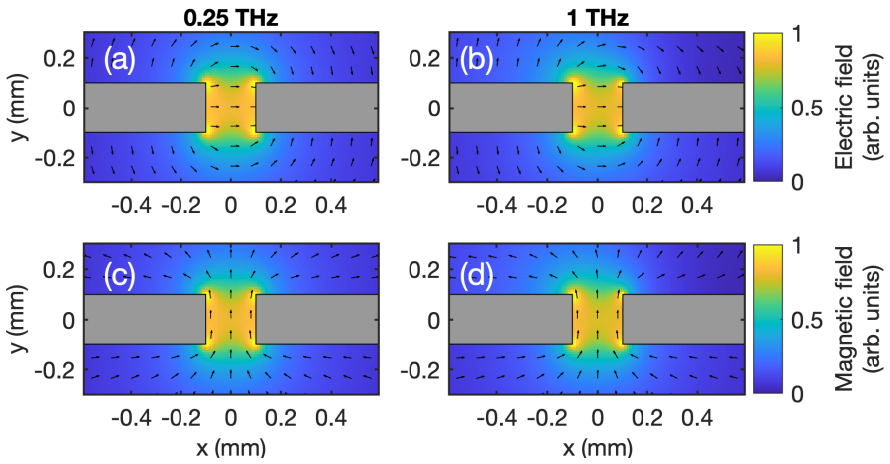

Figure 6.8: Simulated electric (a),(b) and magnetic field (c),(d) of the waveguide mode at 0.25 THz (a),(c) and 1 THz (b),(d).

different waveguide lengths. In order to reduce noise in the TDS-data, we apply a moving average along 0.2 THz.

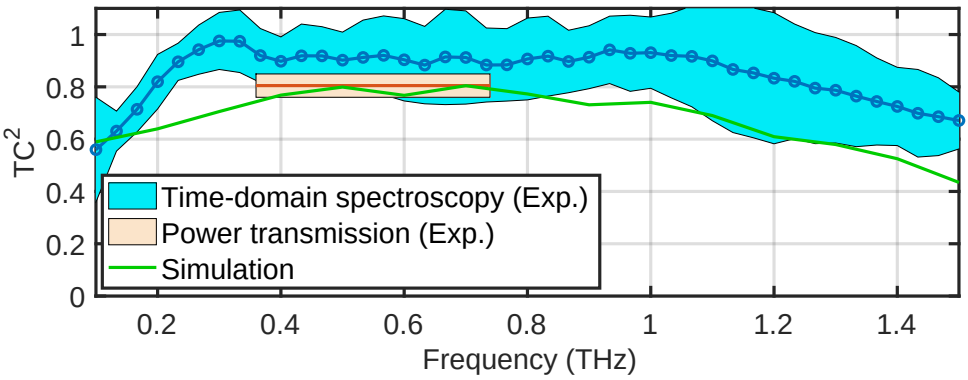

Figure 6.9: Total coupling coefficient TC^2 for the optimal alignment based on time-domain spectroscopy measurements, direct transmission power measurements and numerical simulations.

We measured the influence of slightly misalignment to the coupling efficiency using a 80 mm long waveguide with a fixed gap size of 200 µm. Figure 6.10(a) shows the transmitted spectrum for different z-positions of the waveguide in steps of 1 mm. Note that here we adjusted also the position of the third THz lens $L3$ such that the distance from both lenses to the waveguide remained the same. The transmission spectrum is normalized to the peak transmission for a given frequency. The z-position at 0 mm corresponds to a waveguide alignment such that the THz focus plane is located at the transition between the coupling structure and the straight waveguide. Interestingly, the highest coupling coefficient is found for $z = 2\,\text{mm}$, which corresponds to the focal plane located inside the coupler, in 2 mm distance to the waveguide beginning. In order to verify this finding, we performed numerical simulations and calculate the coupling coefficient based on the mode overlap integral of the electric fields at the waveguide

output. The corresponding results are shown in Fig. 6.10(b) where we again find an optimal coupling for $z = 2\,\mathrm{mm}$.

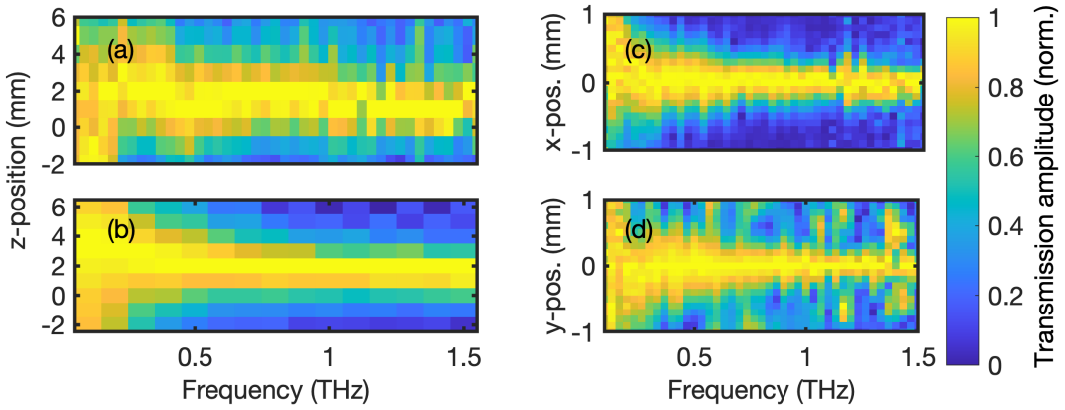

Figure 6.10: Measured normalized transmitted spectra for a 80 mm long waveguide with a 200 µm gap for different misalignment in z- (a), x- (c) and y-direction (d). In (b) the corresponding results from numerical simulations are shown for different z-alignments.

Furthermore, we consider misalignment of the waveguide in x- and y-direction in steps of 100 µm by a total of $\pm 1\,\mathrm{mm}$, as shown in Fig 6.10(c) and Fig 6.10(d) respectively. The coupling of lower frequencies seems to be less affected by misalignment than the higher frequency parts, where the waveguide must be aligned with 100 µm precision in both lateral dimensions for optimal performance. Any asymmetry of the coupling efficiency with respect to $x = 0\,\mathrm{mm}$ or $y = 0\,\mathrm{mm}$ is attribution mainly to asymmetries in the THz setup. For the largest misalignment in y-direction, the THz pulse is also partially guided in the air region parallel to the waveguide channel, which explains the weaker decrease in the coupling efficiency for misalignment in y-direction compared to the x-direction.

6.6.8 Numerical simulation

Two types of three-dimensional simulations of the waveguide geometries were performed in CST Microwave Studio. First, we used an Eigenmode solver for the waveguide structure to determine the modes together with their dispersive and absorptive properties. For this mode calculation as shown in Fig. 1(b), (c) and (d) we calculate the port modes in the waveguide cross-section without applying any symmetry constrains. Second, the full geometry, including the incident focused THz beam and the coupling structure at the input and the exit of the waveguide, was simulated via the finite difference time domain (FDTD) method. An example of the simulation geometry is shown in Fig. 6.11(a). The waveguide structure is based on metal surrounded by a perfect electrical conductor (PEC). For the metal (aluminium) we assumed a conductivity of $12\,\mathrm{MS\,m^{-1}}$ based on fitting to the experimental results. The focused linearly polarized THz pulse was modelled with a transverse Maxwell-Gaussian beam profile [58, 59] acting as a so-called 'near-field source'. To account for the diffraction limited THz focusing, the beam waist was scaled inversely proportional with frequency and we set the beam waist to 0.5 mm at 0.6 THz. The simulation effort was reduced by applying symmetry conditions for the xz- and yz-plane (PMC and PEC respectively) as indicated in Fig. 6.11(b). Open boundary

conditions were applied to eliminate artificial reflections. In the simulation of the bending losses, we considered one single 90 degree bend and did not apply a PMC symmetry condition.

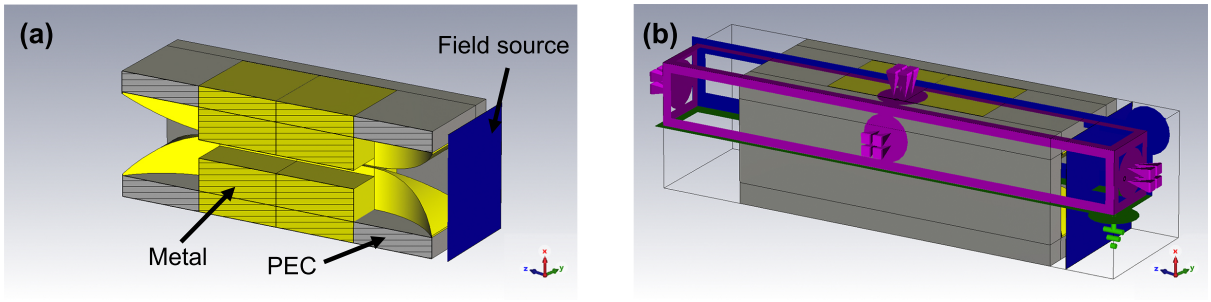

Figure 6.11: (a) Simulation geometry for a 20 mm long waveguide including the in- and out-coupling horn antennas. The focused linearly polarized THz pulse is launched by a near-field source. (b) Applied symmetry and boundary conditions, with perfect electrical conductor (PEC) in green, perfect magnetic conductor (PMC) in blue and open boundary conditions in magenta.

Bibliography

[1] R. Piesiewicz, M. Jacob, M. Koch, J. Schoebel, and T. Kurner, "Performance Analysis of Future Multigigabit Wireless Communication Systems at THz Frequencies With Highly Directive Antennas in Realistic Indoor Environments", IEEE J. Sel. Top. Quantum Electron. **14**, 421–430 (2008), https://doi.org/10.1109/JSTQE.2007.910984.

[2] J. Federici and L. Moeller, "Review of terahertz and subterahertz wireless communications", J. Appl. Phys. **107**, 111101 (2010), https://doi.org/10.1063/1.3386413.

[3] T. Kleine-Ostmann and T. Nagatsuma, "A review on terahertz communications research", J. Infrared, Millimeter, Terahertz Waves **32**, 143–171 (2011), https://doi.org/10.1007/s10762-010-9758-1.

[4] Z. Chen, X. Ma, B. Zhang, Y. Zhang, Z. Niu, N. Kuang, W. Chen, L. Li, and S. Li, "A survey on terahertz communications", China Commun. **16**, 1–35 (2019), https://ieeexplore.ieee.org/document/8663550.

[5] J. Fabiańska, G. Kassier, and T. Feurer, "Split ring resonator based THz-driven electron streak camera featuring femtosecond resolution", Sci. Rep. **4**, 5645 (2014), https://doi.org/10.1038/srep05645.

[6] E. A. Nanni, W. R. Huang, K. H. Hong, K. Ravi, A. Fallahi, G. Moriena, R. J. D. Miller, and F. X. Kärtner, "Terahertz-driven linear electron acceleration", Nat. Commun. **6**, 8486 (2015), https://doi.org/10.1038/ncomms9486.

[7] D. Zhang, A. Fallahi, M. Hemmer, X. Wu, M. Fakhari, Y. Hua, H. Cankaya, A.-L. Calendron, L. E. Zapata, N. H. Matlis, and F. X. Kärtner, "Segmented terahertz electron accelerator and manipulator (STEAM)", Nat. Photonics **12**, 336–342 (2018), https://doi.org/10.1038/s41566-018-0138-z.

[8] M. A. K. Othman, M. C. Hoffmann, M. E. Kozina, X. J. Wang, R. K. Li, and E. A. Nanni, "Parallel-plate waveguides for terahertz-driven MeV electron bunch compression", Opt. Express **27**, 23791–23800 (2019), http://opg.optica.org/oe/abstract.cfm?URI=oe-27-17-23791.

[9] E. C. Snively, M. A. K. Othman, M. Kozina, B. K. Ofori-Okai, S. P. Weathersby, S. Park, X. Shen, X. J. Wang, M. C. Hoffmann, R. K. Li, and E. A. Nanni, "Femtosecond Compression Dynamics and Timing Jitter Suppression in a THz-driven Electron Bunch Compressor", Phys. Rev. Lett. **124**, 54801 (2020), https://link.aps.org/doi/10.1103/PhysRevLett.124.054801.

[10] D. Rohrbach, Z. Ollmann, M. Hayati, C. B. Schroeder, W. P. Leemans, and T. Feurer, "THz-driven split ring resonator undulator", Phys. Rev. Accel. Beams **24**, 010703 (2021), https://doi.org/10.1103/PhysRevAccelBeams.24.010703.

[11] I. H. Baek, H. W. Kim, H. S. Bark, K.-H. Jang, S. Park, J. Shin, Y. C. Kim, M. Kim, K. Y. Oang, K. Lee, F. Rotermund, N. A. Vinokurov, and Y. U. Jeong, "Real-time ultrafast oscilloscope with a relativistic electron bunch train", Nat. Commun. **12**, 6851 (2021), https://doi.org/10.1038/s41467-021-27256-x.

[12] S. Fleischer, Y. Zhou, R. W. Field, and K. A. Nelson, "Molecular orientation and alignment by intense single-cycle THz pulses", Phys. Rev. Lett. **107**, 1–5 (2011), https://doi.org/10.1103/PhysRevLett.107.163603.

[13] S. Fleischer, R. W. Field, and K. A. Nelson, "Commensurate Two-Quantum Coherences Induced by Time-Delayed THz Fields", Phys. Rev. Lett. **109**, 123603 (2012), https://link.aps.org/doi/10.1103/PhysRevLett.109.123603.

[14] H. Y. Hwang, S. Fleischer, N. C. Brandt, B. G. P. Jr., M. Liu, K. Fan, A. Sternbach, X. Zhang, R. D. Averitt, and K. A. Nelson, "A review of non-linear terahertz spectroscopy with ultrashort tabletop-laser pulses", J. Mod. Opt. **62**, 1447–1479 (2015), https://doi.org/10.1080/09500340.2014.918200.

[15] J. Lu, Y. Zhang, H. Y. Hwang, B. K. Ofori-Okai, S. Fleischer, and K. A. Nelson, "Nonlinear two-dimensional terahertz photon echo and rotational spectroscopy in the gas phase", Proc. Natl. Acad. Sci. U. S. A. **113**, 11800–11805 (2016), https://doi.org/10.1073/pnas.1609558113.

[16] A. Ren, A. Zahid, D. Fan, X. Yang, M. A. Imran, A. Alomainy, and Q. H. Abbasi, "State-of-the-art in terahertz sensing for food and water security – A comprehensive review", Trends Food Sci. Technol. **85**, 241–251 (2019), https://www.sciencedirect.com/science/article/pii/S0924224418308768.

[17] N. Akter, M. M. Hasan, and N. Pala, "A Review of THz Technologies for Rapid Sensing and Detection of Viruses including SARS-CoV-2", Biosensors **11**, 10.3390/bios11100349 (2021), https://doi.org/10.3390/bios11100349.

[18] O. Mitrofanov, R. James, F. A. Fernandez, T. K. Mavrogordatos, and J. A. Harrington, "Reducing Transmission Losses in Hollow THz Waveguides", IEEE Trans. Terahertz Sci. Technol. **1**, 124–132 (2011), https://doi.org/10.1109/TTHZ.2011.2159547.

[19] S. Atakaramians, S. A. V., T. M. Monro, and D. Abbott, "Terahertz dielectric waveguides", Adv. Opt. Photon. **5**, 169–215 (2013), http://opg.optica.org/aop/abstract.cfm?URI=aop-5-2-169.

[20] K. Nielsen, H. K. Rasmussen, A. J. L. Adam, P. C. M. Planken, O. Bang, and P. U. Jepsen, "Bendable, low-loss Topas fibers for the terahertz frequency range", Opt. Express **17**, 8592–8601 (2009), http://opg.optica.org/oe/abstract.cfm?URI=oe-17-10-8592.

[21] C.-H. Lai, Y.-C. Hsueh, H.-W. Chen, Y.-j. Huang, H.-c. Chang, and C.-K. Sun, "Low-index terahertz pipe waveguides", Opt. Lett. **34**, 3457–3459 (2009), http://opg.optica.org/ol/abstract.cfm?URI=ol-34-21-3457.

[22] H. Bao, K. Nielsen, O. Bang, and P. U. Jepsen, "Dielectric tube waveguides with absorptive cladding for broadband, low-dispersion and low loss THz guiding", Sci. Rep. **5**, 7620 (2015), https://doi.org/10.1038/srep07620.

[23] M. Nagel, A. Marchewka, and H. Kurz, "Low-index discontinuity terahertz waveguides", Opt. Express **14**, 9944–9954 (2006), http://opg.optica.org/oe/abstract.cfm?URI=oe-14-21-9944.

[24] M. Weidenbach, D. Jahn, A. Rehn, S. F. Busch, F. Beltrán-Mejía, J. C. Balzer, and M. Koch, "3D printed dielectric rectangular waveguides, splitters and couplers for 120 GHz", Opt. Express **24**, 28968–28976 (2016), https://doi.org/10.1364/oe.24.028968.

[25] E. Mavrona, J. Graf, E. Hack, and P. Zolliker, "Optimized 3D printing of THz waveguides with cyclic olefin copolymer", Opt. Mater. Express **11**, 2495–2504 (2021), http://opg.optica.org/ome/abstract.cfm?URI=ome-11-8-2495.

[26] T. Fobbe, S. Markmann, F. Fobbe, N. Hekmat, H. Nong, S. Pal, P. Balzerwoski, J. Savolainen, M. Havenith, A. D. Wieck, and N. Jukam, "Broadband terahertz dispersion control in hybrid waveguides", Opt. Express **24**, 22319–22333 (2016), https://opg.optica.org/oe/abstract.cfm?URI=oe-24-19-22319.

[27] F. Wang et al., "Short Terahertz Pulse Generation from a Dispersion Compensated Modelocked Semiconductor Laser", Laser Photon. Rev. **11**, 1700013 (2017), https://doi.org/10.1002/lpor.201700013.

[28] K. Strecker, S. Ekin, and J. F. O'Hara, "Compensating Atmospheric Channel Dispersion for Terahertz Wireless Communication", Sci. Rep. **10**, 5816 (2020), https://doi.org/10.1038/s41598-020-62692-7.

[29] R. Mendis and D. Grischkowsky, "Undistorted guided-wave propagation of subpicosecond terahertz pulses", Opt. Lett. **26**, 846–848 (2001), http://opg.optica.org/ol/abstract.cfm?URI=ol-26-11-846.

[30] R. Mendis and D. Grischkowsky, "THz interconnect with low-loss and low-group velocity dispersion", IEEE Microw. Wirel. Components Lett. **11**, 444–446 (2001), https://doi.org/10.1109/7260.966036.

[31] S.-H. Kim, E. S. Lee, Y. B. Ji, and T.-I. Jeon, "Improvement of THz coupling using a tapered parallel-plate waveguide", Opt. Express **18**, 1289–1295 (2010), http://opg.optica.org/oe/abstract.cfm?URI=oe-18-2-1289.

[32] M. Theuer, A. J. Shutler, S. S. Harsha, R. Beigang, and D. Grischkowsky, "Terahertz two-cylinder waveguide coupler for transverse-magnetic and transverse-electric mode operation", Appl. Phys. Lett. **98**, 71108 (2011), https://doi.org/10.1063/1.3554761.

[33] A. J. Shutler and D. Grischkowsky, "Gap independent coupling into parallel plate terahertz waveguides using cylindrical horn antennas", J. Appl. Phys. **112**, 73102 (2012), https://doi.org/10.1063/1.4754846.

[34] M. Gerhard, M. Theuer, and R. Beigang, "Coupling into tapered metal parallel plate waveguides using a focused terahertz beam", Appl. Phys. Lett. **101**, 41109 (2012), https://doi.org/10.1063/1.4738982.

[35] S. Pandey, G. Kumar, and A. Nahata, "Slot waveguide-based splitters for broadband terahertz radiation", Opt. Express **18**, 23466–23471 (2010), http://opg.optica.org/oe/abstract.cfm?URI=oe-18-22-23466.

[36] K. S. Reichel, R. Mendis, and D. M. Mittleman, "A Broadband Terahertz Waveguide T-Junction Variable Power Splitter", Sci. Rep. **6**, 28925 (2016), https://doi.org/10.1038/srep28925.

[37] K. Wang and D. M. Mittleman, "Metal wires for terahertz wave guiding", Nature **432**, 376–379 (2004), https://doi.org/10.1038/nature03040.

[38] V. Astley, J. Scheiman, R. Mendis, and D. M. Mittleman, "Bending and coupling losses in terahertz wire waveguides", Opt. Lett. **35**, 553–555 (2010), http://opg.optica.org/ol/abstract.cfm?URI=ol-35-4-553.

[39] M. K. Mridha, A. Mazhorova, M. Clerici, I. Al-Naib, M. Daneau, X. Ropagnol, M. Peccianti, C. Reimer, M. Ferrera, L. Razzari, F. Vidal, and R. Morandotti, "Active terahertz two-wire waveguides", Opt. Express **22**, 22340–22348 (2014), http://opg.optica.org/oe/abstract.cfm?URI=oe-22-19-22340.

[40] A. Markov, H. Guerboukha, and M. Skorobogatiy, "Hybrid metal wire-dielectric terahertz waveguides: challenges and opportunities", J. Opt. Soc. Am. B **31**, 2587–2600 (2014), http://opg.optica.org/josab/abstract.cfm?URI=josab-31-11-2587.

[41] J. Dong, A. Tomasino, G. Balistreri, P. You, A. Vorobiov, É. Charette, B. Le Drogoff, M. Chaker, A. Yurtsever, S. Stivala, M. A. Vincenti, C. De Angelis, D. Kip, J. Azaña, and R. Morandotti, "Versatile metal-wire waveguides for broadband terahertz signal processing and multiplexing", Nat. Commun. **13**, 741 (2022), https://doi.org/10.1038/s41467-022-27993-7.

[42] H. Pahlevaninezhad, B. Heshmat, and T. E. Darcie, "Efficient terahertz slot-line waveguides", Opt. Express **19**, B47–B55 (2011), http://opg.optica.org/oe/abstract.cfm?URI=oe-19-26-B47.

[43] K. Sengupta, T. Nagatsuma, and D. M. Mittleman, "Terahertz integrated electronic and hybrid electronic–photonic systems", Nat. Electron. **1**, 622–635 (2018), https://doi.org/10.1038/s41928-018-0173-2.

[44] L. Smith, W. Gomma, H. Esmaeilsabzali, and T. Darcie, "Tapered transmission lines for terahertz systems", Opt. Express **29**, 17295–17303 (2021), http://opg.optica.org/oe/abstract.cfm?URI=oe-29-11-17295.

[45] M. Wächter, M. Nagel, and H. Kurz, "Metallic slit waveguide for dispersion-free low-loss terahertz signal transmission", Appl. Phys. Lett. **90**, 61111 (2007), https://doi.org/10.1063/1.2472544.

[46] L. Smith, F. Ahmed, A. Jooshesh, J. Zhang, M. Jun, and T. Darcie, "THz Field Enhancement by Antenna Coupling to a Tapered Thick Slot Waveguide", J. Light. Technol. **32**, 3676–3682 (2014), https://doi.org/10.1109/JLT.2014.2321992.

[47] R. Peretti, F. Braud, E. Peytavit, E. Dubois, and J.-F. Lampin, "Broadband Terahertz Light–Matter Interaction Enhancement for Precise Spectroscopy of Thin Films and Micro-Samples", Photonics **5**, 10.3390/photonics5020011 (2018), https://www.mdpi.com/2304-6732/5/2/11.

[48] H. Zhan, R. Mendis, and D. M. Mittleman, "Characterization of the terahertz near-field output of parallel-plate waveguides", J. Opt. Soc. Am. B **28**, 558–566 (2011), http://opg.optica.org/josab/abstract.cfm?URI=josab-28-3-558.

[49] K. Iwaszczuk, A. Andryieuski, A. Lavrinenko, X.-C. Zhang, and P. U. Jepsen, "Terahertz field enhancement to the MV/cm regime in a tapered parallel plate waveguide", Opt. Express **20**, 8344–8355 (2012), http://opg.optica.org/oe/abstract.cfm?URI=oe-20-8-8344.

[50] K. Wang and D. M. Mittleman, "Dispersion of Surface Plasmon Polaritons on Metal Wires in the Terahertz Frequency Range", Phys. Rev. Lett. **96**, 157401 (2006), https://link.aps.org/doi/10.1103/PhysRevLett.96.157401.

[51] D. Takeshima, T. Sakon, S. Tsuzuki, F. Matsui, Y. Kusuda, T. Furuya, S. Nishizawa, K. Kurihara, F. Kuwashima, E. Estacio, K. Yamamoto, and M. Tani, "Influence of metal surface roughness on the phase velocity of terahertz waves propagating in parallel plate waveguides", in 38th int. conf. infrared, millimeter, terahertz waves (2013), pp. 1–2, https://doi.org/10.1109/IRMMW-THz.2013.6665758.

[52] A. Llobera, "Integrated Optics Technology on Silicon: Optical Transducers", PhD thesis (Universitat Autònoma de Barcelona, 2002), pp. 150–154, http://hdl.handle.net/10803/3342.

[53] D. Rohrbach, B. J. Kang, and T. Feurer, "3D-printed THz wave- and phaseplates", Opt. Express **29**, 27160–27170 (2021), https://doi.org/10.1364/OE.433881.

[54] A. Bitzer, H. Merbold, A. Thoman, T. Feurer, H. Helm, and M. Walther, "Terahertz near-field imaging of electric and magnetic resonances of a planar metamaterial", Opt. Express **17**, 3826–3834 (2009), http://www.opticsexpress.org/abstract.cfm?URI=oe-17-5-3826.

[55] S. Bagiante, F. Enderli, J. Fabiańska, H. Sigg, and T. Feurer, "Giant electric field enhancement in split ring resonators featuring nanometer-sized gaps", Sci. Rep. **5**, 8051 (2015), https://doi.org/10.1038/srep08051.

[56] E. Castro-Camus, M. Koch, and A. I. Hernandez-Serrano, "Additive manufacture of photonic components for the terahertz band", J. Appl. Phys. **127**, 210901 (2020), https://doi.org/10.1063/1.5140270.

[57] R. Mendis, "Nature of subpicosecond terahertz pulse propagation in practical dielectric-filled parallel-plate waveguides", Opt. Lett. **31**, 2643–2645 (2006), http://opg.optica.org/ol/abstract.cfm?URI=ol-31-17-2643.

[58] L. W. Davis, "Theory of electromagnetic beams", Phys. Rev. A **19**, 1177–1179 (1979), https://link.aps.org/doi/10.1103/PhysRevA.19.1177.

[59] J. P. Barton and D. R. Alexander, "Fifth-order corrected electromagnetic field components for a fundamental Gaussian beam", J. Appl. Phys. **66**, 2800–2802 (1989), https://doi.org/10.1063/1.344207.

Chapter 7

THz-induced gas alignment in field enhancing waveguides

David Rohrbach[1], Hans-Martin Frey[1], Bong Joo Kang[1], Elnaz Zyaee[1], and Thomas Feurer[1]

[1]Institute of Applied Physics, University of Bern, Sidlerstrasse 5, 3012 Bern, Switzerland

This work is in preparation for submission.

Abstract

We demonstrate an integrated platform for THz-induced orientation and alignment of gas molecules that boosts the detected transient birefringence signal by more than an order of magnitude compared to standard THz free space focusing. This increase in the optical probing signal results from a longer interaction length of several centimeters, and a locally enhanced electric field strength by up to a factor of five. We demonstrate this new approach for nonlinear THz spectroscopy using two molecular systems and compare the results to the theory. Furthermore, we present integrated THz pulse modulation for coherently controlled nonlinear interactions.

7.1 Introduction

Spectroscopic signatures in gases and liquids are usually averaged over all spatial orientation of the molecules due to their isotropic angular distribution. Most light-matter processes depend on the projection of the field polarization on the permanent, or induced, dipole moment. Therefore, preparing the sample with well defined angular distribution potentially leads to higher efficiency, selectivity and resolution. For instance, it can boost photoinduced strong field ionization [1, 2], surface scattering phenomena [3–6], high harmonic generation [7–11], and many others.

In recent decades, this motivated the development of "laser-induced molecular alignment", in which ultrashort laser pulses rotationally excite gas-phase molecules. In particular, this excitation leads to alignment in a field-free environment, which is essential for molecular studies

[12–14]. Other approaches to modify the molecular angular distribution are based on direct current (dc) fields, which interact with the permanent dipole moment of the molecule [15], mixed dc and optical excitation [16, 17], or two-color optical excitation [18]. In the last decade, a novel approach based on intense THz pulses was demonstrated, where the rotational degrees of freedom are excited resonantly by a THz electric fields [19–21]. In a classical picture, the electric field $\mathbf{E}$ thereby exerts a torque $\mu \times \mathbf{E}$ on the molecules, where μ is the permanent molecular dipole moment. Quantum mechanically, rotational states with $\Delta J = \pm 1$ are coupled by the resonant THz electric field, leading to population transfer and induced coherences [19]. This interaction initiates coherent rotational motion and leads to field-free orientation and alignment of gas molecules with a revival period $T_{rev} = 1/(2Bc)$, where B is the molecular rotation constant (in cm^{-1}) and c the speed of light in vacuum. The net *orientation* is described by the ensemble average $\langle \cos\theta \rangle$, where θ is the angle between the dipole vectors and a specific lab-frame axis. The molecular *alignment* is usually characterized by the ensemble average $\langle \cos^2\theta \rangle$ which is found to be 1/3 for an isotropic angular distribution in three dimensions [19, 22].

THz-induced molecular orientation and alignment is currently limited by the available electric field strength in state-of-the-art THz sources. To date, these intense fields have been generated by focusing THz pulses in free space, with the spot size ultimately limited by diffraction, and the interaction length limited by the Rayleigh length. Here, we show that these limitations can be overcome using a THz waveguide. A schematic of the experimental realization is shown in Fig. 7.1. Intense THz pulses are efficiently coupled to a metallic slit waveguide installed in a gas cell. The considered THz waveguide platform was first presented in Ref. [23], where it was characterized in detail both experimentally and by simulations. There, it was found that both the electric and magnetic fields are enhanced in the sub-wavelength gap region. Since the waveguide shows negligible dispersion and low losses, the THz pulse propagates reshaping-free along the whole waveguide length at the speed of light. This allows for velocity matching with an optical pulse probing the THz-induced transient birefringence as a measure of the molecular alignment. The transient birefringence reveals characteristics of the sample such as the molecular rotation constant or the sign of the polarizability. The detected signal is proportional to the interaction length and the square of the electric field. Therefore, the THz waveguide increases the detected signal twofold: It enhances the THz electric field and increases the interaction length.

We considered two different molecular gaseous samples, namely acetonitrile (CH_3CN) and fluoroform (CHF_3), which are both polar ($\mu_0 = 3.9$ D and 1.6 D, respectively) but show different signs of the polarizability anisotropies ($\Delta\alpha = 2.15\,\text{Å}^3$ and $-0.18\,\text{Å}^3$, respectively) [24]. The rotation constant B is $0.307\,\mathrm{cm}^{-1}$ and $0.345\,\mathrm{cm}^{-1}$ [25], with a corresponding revival time $T_{rev} = 1/(2Bc)$ of 54 ps and 48 ps, respectively. In the experiments, we used the vapor pressure of acetonitrile at room temperature (100 mbar), while the pressure of fluoroform was set to 500 mbar.

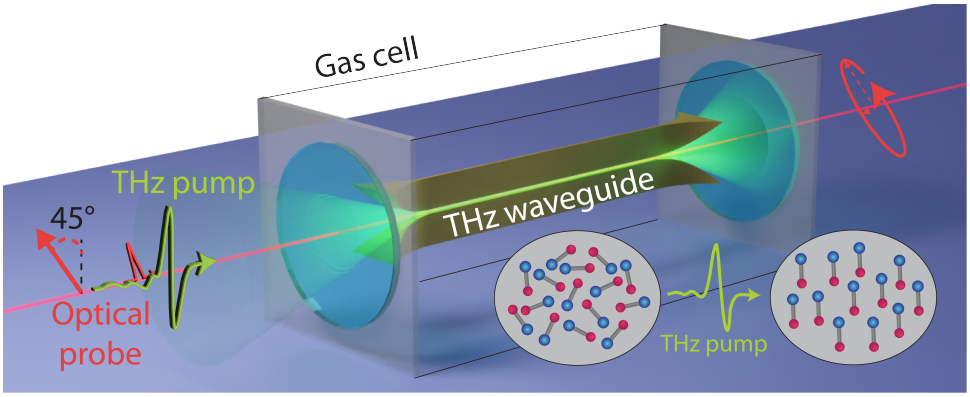

Figure 7.1: Experimental concept. An intense THz pulse is focused in a waveguide structure installed in a gas cell. The THz electric field modifies the alignment and orientation of the gas molecules. The molecular alignment is measured by the polarization change of a time-delayed optical probe pulse.

7.2 Results and discussion

7.2.1 Effect of the waveguide

First, we characterize the enhancement of the transient birefringence signal due to the waveguide compared to standard free space THz focusing. The blue curve in Fig. 7.2a shows the signal when no waveguide was used, while the other three signals were measured with a 20 mm long waveguide and different gap sizes g of 200 µm, 100 µm and 50 µm. In all measurements we find a step-like increase of the birefringence when the THz interacts at times 0 ps. This signal reaches its maximum at the end of the THz pulse and is attributed to a non-thermal rotational state distribution due to transferred population [19, 22]. This signal continuously decays back to its thermal value and is therefore referred to as background signal level. In addition to this signal, at half of the revival time (i.e., about 27 ps) we expect so-called revival signals due to coherences, which we can observe only clearly when using the waveguide structure.

In order to quantify the effect of the waveguide, we calculate the signal-to-noise ratio (S/N) for the different experimental configurations. This is shown in Fig. 7.2b, where we define the 'signal' as the change of the background signal at times 0 ps, and the 'noise' as the mean absolute deviation of the detected signal before the time zero. We scaled all data points with respect to the S/N obtained without waveguide, so that the presented values directly show the S/N improvement due to the waveguide. We find an increase in S/N of at least one order of magnitude for all considered gap sizes, resulting from a longer interaction length of approximately 20 mm, and locally enhanced electric field compared to free space THz focusing. The higher values of the S/N for smaller gap sizes reflect the stronger local field enhancement. From simulations we know that the field is enhanced by up to a factor of five in the 50 µm gap [23]. Note that the minimum gap size is ultimately limited by the transport of the probe beam through the waveguide structure. For the 200 µm gap, we find that only a small fraction (4 %) of the probe is blocked by the structure, but the losses increase to 70 % for the 50 µm gap, which limits the maximum effective field enhancement affecting the transmitted probe beam.

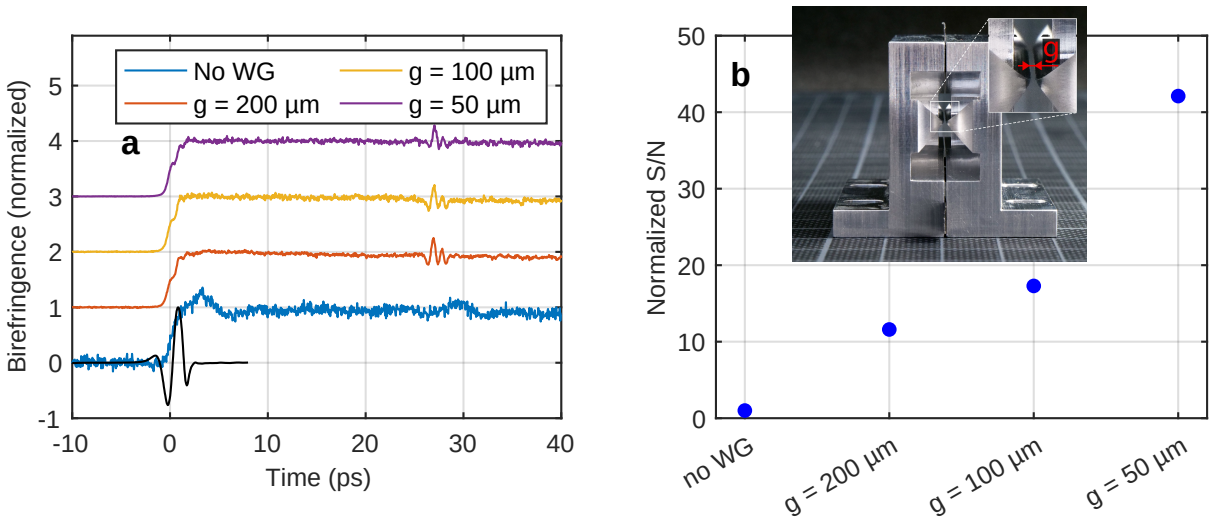

Figure 7.2: **a** Measured THz-induced birefringence in acetonitrile without (blue curve) and with waveguide (WG) for three different gap sizes g. All curves are normalized to the maximum signal and arbitrarily shifted along the y-axis. The solid black curve shows the measured THz electric field. **b** Signal-to-noise ration (S/N) for different gap sizes normalized to the S/N without waveguide. The inset shows a photograph (provided by Rhoda Berger) of the THz waveguide structure together with a zoom to the gap region indicating the gap size g.

7.2.2 Details of the Kerr signals

Next, we discuss the birefringence signals shown in Fig 7.3a from the two different molecular samples in more detail. Note that fluoroform shows approximately 20 times smaller signal than acetonitril and therefore it could not have been measured with reasonable S/N using standard free space focusing. As already reported in Ref. [24], we found a different sign of the polarizability anisotropy for acetonitrile and fluoroform. Furthermore, we see up to three revival signals at the expected time delays (indicated by dotted lines). The revival signal between $1/2\ T_{rev}$ and $1\ T_{rev}$ is most likely due to a coherent excitation from the main THz pulse and an echo with 30 ps delay generated inside the waveguide structure resulting from unguided pulse parts which are reflected at the waveguide's side walls. The black curve in Fig. 7.3a shows the measured signal for an empty (0 mbar) gas cell. As expected, the signal fluctuates around zero within the noise floor of the measurement. Only at times 0 ps we observe some minor feature which we attribute to a Kerr signal from the gas cell windows. [26].

In order to estimate the degree of molecular alignment, we measured the relative intensity change $\Delta I/I$ due to the probe polarization modulation, which we found to be 2.8 % for acetonitrile at the maximum of the background signal. Using the relation $\Delta I/I = \sin\left(\frac{2\pi\Delta n L}{\lambda}\right)$, we find $\Delta n = 1.8 \times 10^{-7} = \frac{3N\Delta\alpha}{4\epsilon_0}\Delta\langle\cos^2\theta\rangle$ [19] for $\lambda = 800\,\text{nm}$ and $L = 20\,\text{mm}$. The maximum degree of alignment is calculated to be $\langle\cos^2\theta\rangle = 0.034$, which is three orders of magnitude larger than what was reported in Ref. [19] for an OCS sample.

Figure 7.3b and Fig. 7.3c show a zoom to the first and second revival signals for acetonitril and fluoroform. As expected, we find that successive revival signal profiles are inverted, which is a clear feature of two-quantum rotational coherences [19, 27].

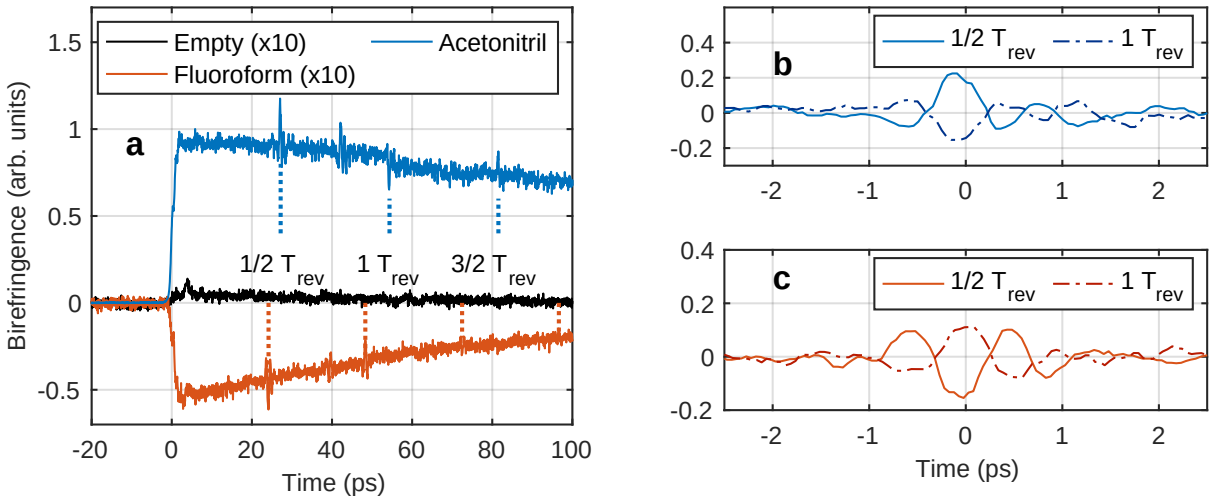

Figure 7.3: **a** Measured THz-induced birefringence in an empty gas cell, in fluoroform and in acetonitril gas sample. All measurement were performed with a 20 mm long waveguide and a 50 µm gap size. The signals for the empty gas cell and for fluoroform are scaled by a factor of 10 as indicated in the legend. **b** and **c** Zoom to the revival signals at 1/2 T_{rev} and 1 T_{rev} for acetonitril and fluoroform. The signals are shifted by -1/2 T_{rev} and -1 T_{rev} respectively and we subtract the exponential decay of the background signal for better comparison.

7.2.3 Coherent control

As we have demonstrated in Ref. [23], the THz waveguide platform also allows for integrated signal manipulation. Since the revival signals originate from two field-dipole-interactions, two THz pulses with a controlled inter-pulse delay allow for coherently controlled nonlinear interactions. THz pulse pairs with variable inter-pulse delay are generated using a waveguide interferometer structure, which has a dielectric material in one of the interferometer arms (see Ref. [23] for details). The dielectric material is cyclic olefin copolymer TOPAS foil with 140 µm thickness. Different foil widths up to 15 mm were considered to adjust the inter-pulse delay. The setup for this integrated THz signal manipulation consists of two additional aspherical THz lenses for coupling in and out of the interferometer structure, which is placed prior to the gas cell (see supplemental document for details about the setup). The THz pulse pairs are then coupled to the 20 mm long waveguide with 50 µm gap inside the gas cell filled with acetonitrile, similar as in previous experiments.

Figure 7.4a shows the measured birefringence as function of time delay and Fig. 7.4b shows the corresponding electric field of the THz waveform when placing a 6 mm long foil in one interferometer arm. The inter-pulse delay $\Delta\tau$, indicated by dashed black lines, is approximately 9 ps, corresponding to an effective refractive index of 1.45 for the material in the interferometer arm. We find an increase of the background birefringence signal for both THz pulses at times 0 ps and 9 ps respectively. The observed revival signal at times 32 ps is in agreement with the expected time delay for commensurate two-THz revivals at times $(T_{rev} + \Delta\tau)/2$ indicated by a green line in Fig. 7.4a [20]. The time delays for the revival signals arising from the individual THz pulses are indicated by blue lines, which could not explain the observed revival signal. Figure 7.4c shows the transient birefringence for various TOPAS foil widths. For all THz pulse pairs we find the expected time delays of the revival signals as indicated by the dashed

black lines. Note that, as expected, the subsequent second revival signals are inverted with respect to the first revival signal. The additionally observed revival features are discussed in the supplemental document.

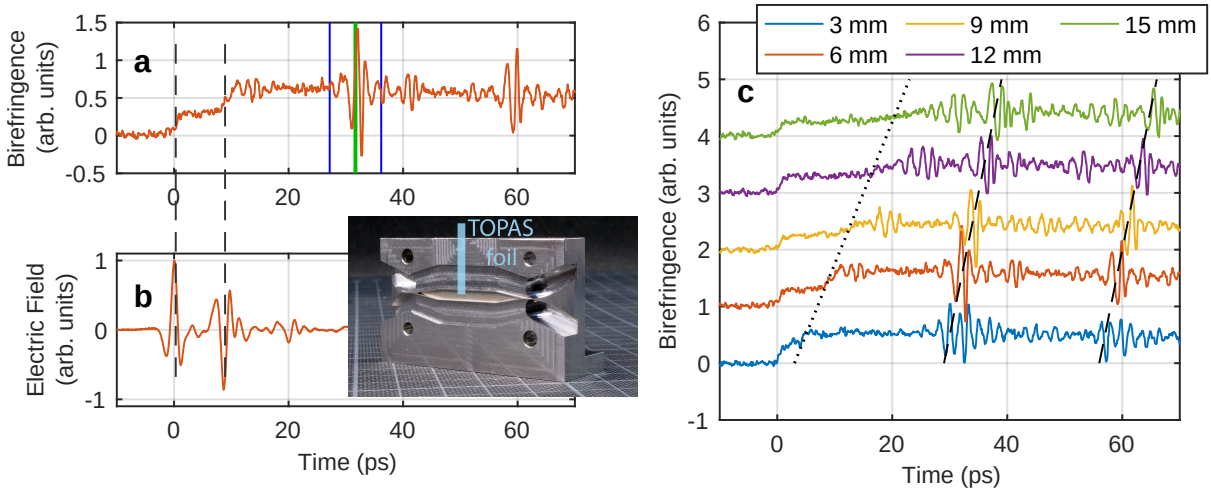

Figure 7.4: **a** Measured THz-induced birefringence in acetonitrile produced by a manipulated THz waveform. **b** THz electric field of the corresponding waveform as function of time delay. The inset shows a photograph (provided by Rhoda Berger) of the THz interferometer structure, where the position of the TOPAS foil is indicated by the blue shape. **c** Measured birefringence for various TOPAS foil widths as indicated in the legend. The curves are arbitrarily shifted in y-direction. The dotted black line indicates the time delay of the second THz pulses and the dashed black lines show the expected time delays for commensurate two-THz revivals.

7.3 Conclusion

We have demonstrated that the birefringence signal in THz-induced gas alignment is increased by more than one order of magnitude due to a judiciously designed THz waveguide platform, compared to standard THz free space focusing. Increasing the S/N by more than an order of magnitude allows to detect nonlinear signals which could otherwise only be observed by averaging over 100 to 1000 times more laser shots, which would significantly increase the total measurement time from a few tens of minutes to more than a day. For both considered sample molecules (acetonitrile and fluoroform) we find the expected revival periods, sign of the polarizability anisotropy, and inversion of successive revival signal profiles. All these features could have not be studied in our setup using standard free space focusing of the THz pump pulses. Furthermore, integrated THz pulse modulation techniques are applied for coherently controlled interactions. This platform can also be used to increase the signal in a variety of other nonlinear THz spectroscopy applications for gas, liquid or solid samples in combination with various probing techniques such as x-ray, optical or THz probing.

7.4 Supplemental document

7.4.1 Experimental setup

Figure 7.5 shows a schematic of the experimental setup. The laser system is a 1 kHz Ti:sapphire regenerative amplifier (Legend Elite Duo Femto, Coherent) delivering 100 fs pulses with an average power of 6 W at 800 nm. Single-cycle THz waveforms with 3.1 mW average power are generated by optical rectification in a prism-cut $LiNbO_3$ crystal via tilted-pulse-front pumping [28, 29] (see Ref. [30] for more detail about the THz generation setup). The focal length of the aspheric lens $L1$ is 100 mm while the focal length of $L2$ and $L3$ is 50 mm. THz pulses are coupled to the waveguide structure with a parabolic mirror with 50 mm focal length. The material of the gas cell windows is TPX (front window) and z-cut quartz (back window). The whole THz beam path was under dry air purging to reduce absorption losses and free induction decay signals arising from water vapor. A chopper is used to subtract background noise, while we have averaged over 2×250 laser shots at each time delay for all measurements presented here.

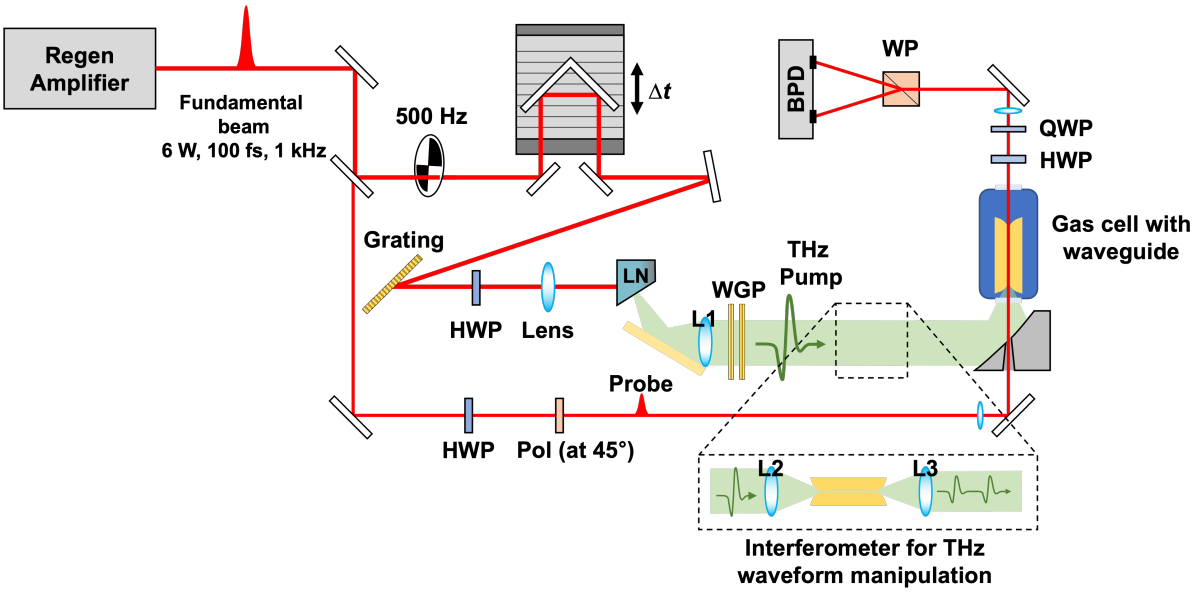

Figure 7.5: Intense single-cycle THz pulses were generated in $LiNbO_3$ via tilted-pulse-front pumping, and coupled to the THz waveguide installed in a gas cell. The probe pulses propagate collinear with the THz pulses through the waveguide and are analyzed by balanced detection. A chopper running at 500 Hz alternated between THz pulse on and off for background noise subtraction. A THz interferometer waveguide structure can be installed for THz waveform manipulation as indicated in the dashed box. **LN**, lithium niobate; **HWP**, half-waveplate; **QWP**, quarter-waveplate; **WGP**, wire grid polarizers; **Pol**, polarizer; **WP**, Wollaston prism; **BPD**, balanced photodiodes.

7.4.2 Field strength dependent coherent excitation

In order to study the coherently controlled birefringence signals as shown in Fig. 7.4 in more detail, we applied a different approach for the THz waveform manipulation. Here, we installed a 8 mm thick high-density polyethylen slab in half of the collimated THz beam path. The generated waveform is a THz pulse pair with approximately 14 ps inter-pulse delay as shown by the black curve in Fig. 7.6a. By using this approach, we reach higher THz field strength than with the interferometer structure which suffers from additional coupling and propagation losses. To study the scaling as a function of THz field strength, we used a pair of wire grid polarizers in the collimated THz beam path.

Figure 7.6a shows the birefringence signal in acetonitrile at different electric field strengths relative to the maximum E_0. Step-like increases of the background signal are observed at times 0 ps and 14 ps similar as discussed in Sec. 7.2.3. Interestingly, the commensurate two-THz revivals at times 35 ps are reduced for increasing field strength. Note that such behaviour was not observed in experiments without THz waveform manipulation (as shown for example Fig. 7.2). Furthermore, additional revivals at times 20 ps are observed, which are also reduced at high field strength. Note that the observed signal at low field strength is similar as the signal shown in Fig. 7.4c for a 9 mm long TOPAS foil. To study the field strength dependency in more detail, we show the peak-to-peak value for some characteristic features as function of relative field strength E_{THz}/E_0 in Fig. 7.6b. Both the first and second step-like increases at times 0 ps and 14 ps scale with the square of the electric field. A similar scaling would naively be expected for the revival signals. However, we find that they saturate at intermediate field strength and are even reduced. The origin of this behavior, as well as the revival signal around 20 ps, is not yet fully understood. But we believe that we will gain more insight through numerical simulations that will be performed in the near future, but after the submission of this thesis.

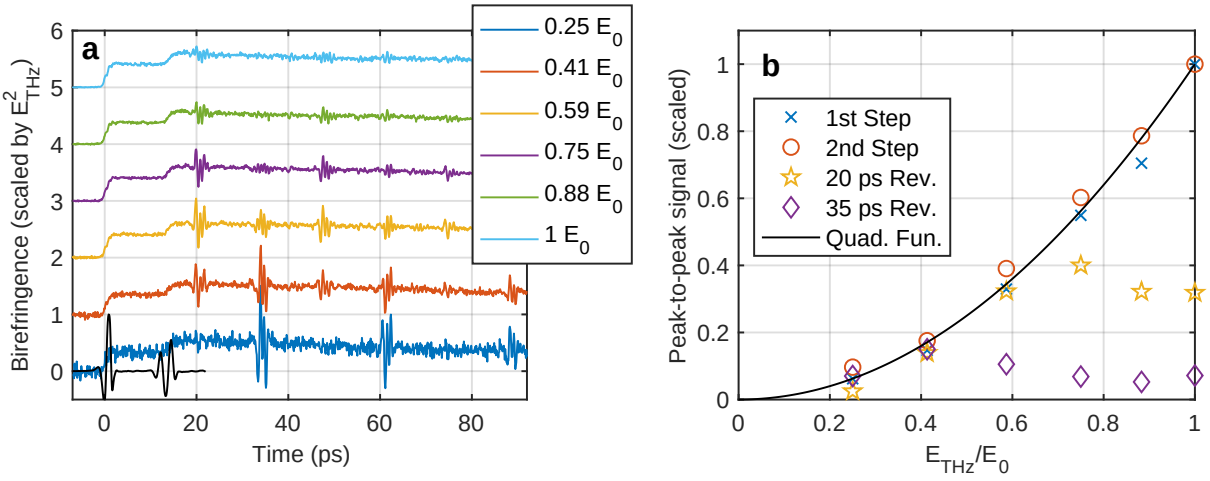

Figure 7.6: **a** Measured THz-induced birefringence in acetonitrile produced by a manipulated THz waveform for different relative THz electric field strength E_{THz}/E_0 indicated in the legend. All curves are scaled by E^2_{THz} and arbitrarily shifted in y-direction. The black curve shows the THz electric field as function of time delay. **b** Extracted peak-to-peak signals at different relative field strengths at times 0 ps (1st step), 14 ps (2nd step), 20 ps and 35 ps. The black curve shows a quadratic function as guide to the eyes.

Bibliography

[1] I. V. Litvinyuk, K. F. Lee, P. W. Dooley, D. M. Rayner, D. M. Villeneuve, and P. B. Corkum, "Alignment-Dependent Strong Field Ionization of Molecules", Phys. Rev. Lett. **90**, 233003 (2003), https://link.aps.org/doi/10.1103/PhysRevLett.90.233003.

[2] J. L. Hansen, L. Holmegaard, J. H. Nielsen, H. Stapelfeldt, D. Dimitrovski, and L. B. Madsen, "Orientation-dependent ionization yields from strong-field ionization of fixed-in-space linear and asymmetric top molecules", J. Phys. B At. Mol. Opt. Phys. **45**, 15101 (2012), https://dx.doi.org/10.1088/0953-4075/45/1/015101.

[3] T. Seideman, "Molecular optics in an intense laser field: A route to nanoscale material design", Phys. Rev. A **56**, R17–R20 (1997), https://link.aps.org/doi/10.1103/PhysRevA.56.R17.

[4] Y. Khodorkovsky, I. S. Averbukh, and E. Pollak, "Classical theory of rotational rainbow scattering from uncorrugated surfaces", J. Phys. Condens. Matter **22**, 304004 (2010), https://dx.doi.org/10.1088/0953-8984/22/30/304004.

[5] G. M. McClelland, G. D. Kubiak, H. G. Rennagel, and R. N. Zare, "Determination of Internal-State Distributions of Surface Scattered Molecules: Incomplete Rotational Accommodation of NO on Ag(111)", Phys. Rev. Lett. **46**, 831–834 (1981), https://link.aps.org/doi/10.1103/PhysRevLett.46.831.

[6] B. G. Perkins and D. J. Nesbitt, "Quantum-State-Resolved CO2 Scattering Dynamics at the Gas-Liquid Interface: Dependence on Incident Angle", J. Phys. Chem. A **111**, 7420–7430 (2007), https://doi.org/10.1021/jp0709048.

[7] R. Velotta, N. Hay, M. B. Mason, M. Castillejo, and J. P. Marangos, "High-Order Harmonic Generation in Aligned Molecules", Phys. Rev. Lett. **87**, 183901 (2001), https://link.aps.org/doi/10.1103/PhysRevLett.87.183901.

[8] J. Itatani, J. Levesque, D. Zeidler, H. Niikura, H. Pépin, J. C. Kieffer, P. B. Corkum, and D. M. Villeneuve, "Tomographic imaging of molecular orbitals", Nature **432**, 867–871 (2004), https://doi.org/10.1038/nature03183.

[9] B. K. McFarland, J. P. Farrell, P. H. Bucksbaum, and M. Gühr, "High Harmonic Generation from Multiple Orbitals in N2", Science (80-.). **322**, 1232–1235 (2008), https://doi.org/10.1126/science.1162780.

[10] H. Soifer, P. Botheron, D. Shafir, A. Diner, O. Raz, B. D. Bruner, Y. Mairesse, B. Pons, and N. Dudovich, "Near-Threshold High-Order Harmonic Spectroscopy with Aligned Molecules", Phys. Rev. Lett. **105**, 143904 (2010), https://link.aps.org/doi/10.1103/PhysRevLett.105.143904.

[11] C. Zhang, J. Yao, F. A. Umran, J. Ni, B. Zeng, G. Li, and D. Lin, "Enhanced narrow-bandwidth emission during high-order harmonic generation from aligned molecules", Opt. Express **21**, 3259–3264 (2013), https://opg.optica.org/oe/abstract.cfm?URI=oe-21-3-3259.

[12] H. Stapelfeldt and T. Seideman, "Colloquium: Aligning molecules with strong laser pulses", Rev. Mod. Phys. **75**, 543–557 (2003), https://link.aps.org/doi/10.1103/RevModPhys.75.543.

[13] S. Fleischer, Y. Khodorkovsky, E. Gershnabel, Y. Prior, and I. S. Averbukh, "Molecular Alignment Induced by Ultrashort Laser Pulses and Its Impact on Molecular Motion", Isr. J. Chem. **52**, 414–437 (2012), https://doi.org/10.1002/ijch.201100161.

[14] M. Lemeshko, R. V. Krems, J. M. Doyle, and S. Kais, "Manipulation of molecules with electromagnetic fields", Mol. Phys. **111**, 1648–1682 (2013), https://doi.org/10.1080/00268976.2013.813595.

[15] B. Friedrich and D. R. Herschbach, "Spatial orientation of molecules in strong electric fields and evidence for pendular states", Nature **353**, 412–414 (1991), https://doi.org/10.1038/353412a0.

[16] A. Goban, S. Minemoto, and H. Sakai, "Laser-Field-Free Molecular Orientation", Phys. Rev. Lett. **101**, 13001 (2008), https://link.aps.org/doi/10.1103/PhysRevLett.101.013001.

[17] O. Ghafur, A. Rouzée, A. Gijsbertsen, W. K. Siu, S. Stolte, and M. J. J. Vrakking, "Impulsive orientation and alignment of quantum-state-selected NO molecules", Nat. Phys. **5**, 289–293 (2009), https://doi.org/10.1038/nphys1225.

[18] S. De, I. Znakovskaya, D. Ray, F. Anis, N. G. Johnson, I. A. Bocharova, M. Magrakvelidze, B. D. Esry, C. L. Cocke, I. V. Litvinyuk, and M. F. Kling, "Field-Free Orientation of CO Molecules by Femtosecond Two-Color Laser Fields", Phys. Rev. Lett. **103**, 153002 (2009), https://link.aps.org/doi/10.1103/PhysRevLett.103.153002.

[19] S. Fleischer, Y. Zhou, R. W. Field, and K. A. Nelson, "Molecular orientation and alignment by intense single-cycle THz pulses", Phys. Rev. Lett. **107**, 1–5 (2011), https://doi.org/10.1103/PhysRevLett.107.163603.

[20] S. Fleischer, R. W. Field, and K. A. Nelson, "Commensurate Two-Quantum Coherences Induced by Time-Delayed THz Fields", Phys. Rev. Lett. **109**, 123603 (2012), https://link.aps.org/doi/10.1103/PhysRevLett.109.123603.

[21] A. Beer, R. Damari, Y. Chen, and S. Fleischer, "Molecular Orientation-Induced Second-Harmonic Generation: Deciphering Different Contributions Apart", J. Phys. Chem. A **126**, 3732–3738 (2022), https://doi.org/10.1021/acs.jpca.2c03237.

[22] S. Ramakrishna and T. Seideman, "Intense laser alignment in dissipative media as a route to solvent dynamics", Phys. Rev. Lett. **95**, 1–4 (2005), https://doi.org/10.1103/PhysRevLett.95.113001.

[23] D. Rohrbach, B. J. Kang, E. Zyaee, and T. Feurer, "Wideband dispersion-free THz waveguide platform", arXiv (2022), http://arxiv.org/abs/2208.00678.

[24] T. Kampfrath, M. Wolf, and M. Sajadi, "The sign of the polarizability anisotropy of polar molecules is obtained from the terahertz Kerr effect", Chem. Phys. Lett. **692**, 319–323 (2018), https://doi.org/10.1016/j.cplett.2017.12.061.

[25] *Computational Chemistry Comparison and Benchmark DataBase*, (2023) https://cccbdb.nist.gov/exp1x.asp (visited on 01/31/2023).

[26] M. Sajadi, M. Wolf, and T. Kampfrath, "Terahertz-field-induced optical birefringence in common window and substrate materials", Opt. Express **23**, 28985–28992 (2015), https://opg.optica.org/oe/abstract.cfm?URI=oe-23-22-28985.

[27] S. Fleischer, I. S. Averbukh, and Y. Prior, "Selective Alignment of Molecular Spin Isomers", Phys. Rev. Lett. **99**, 93002 (2007), https://link.aps.org/doi/10.1103/PhysRevLett.99.093002.

[28] J. Hebling, G. Almási, I. Z. Kozma, and J. Kuhl, "Velocity matching by pulse front tilting for large-area THz-pulse generation", Opt. Express **10**, 1161–1166 (2002), http://opg.optica.org/oe/abstract.cfm?URI=oe-10-21-1161.

[29] J. A. Fülöp, Z. Ollmann, C. Lombosi, C. Skrobol, S. Klingebiel, L. Pálfalvi, F. Krausz, S. Karsch, and J. Hebling, "Efficient generation of THz pulses with 0.4 mJ energy", Opt. Express **22**, 20155–20163 (2014), http://www.opticsexpress.org/abstract.cfm?URI=oe-22-17-20155.

[30] B. J. Kang, E. J. Rohwer, D. Rohrbach, M. Akbarimoosavi, Z. Ollmann, E. Zyaee, R. F. Pauszek, G. Sorohhov, A. Borgoo, M. Cascella, A. Cannizzo, S. Decurtins, R. J. Stanley, S.-X. Liu, and T. Feurer, "Time-resolved THz Stark spectroscopy", arXiv, https://doi.org/10.48550/arXiv.2212.10333 (2022).

Chapter 8

Conclusions

In this thesis, we have developed and tested technologies for various strong THz field applications, such as free electron bunch manipulation, ultrafast carrier generation in semiconductors, Stark spectroscopy of molecular samples, and field-free alignment of gas molecules.

In many applications of intense THz pulses, control over the THz polarization state and the wavefront is crucial. In this context, we have shown that various wave- and phase-plates can be manufactured by 3D-printing based on fused deposition modeling (chapter 2). By using a broadband THz source with a useful spectral range from 0.08 THz to 1.5 THz we demonstrated that 3D-printed waveplates are not limited to a frequency range < 0.2 THz, as indicated by previous publications, but perform as expected up to about 0.6 THz. We have experimentally evaluated 3D-printed quarter-waveplates, half-waveplates, q-plate, and spiral phaseplates in detail by spatial characterization of all three electric field components, and compared the results with finite element simulations. We have also demonstrated a route to achieve broadband performance so that 3D-printed waveplates can be used in combination with few-cycle THz pulses, as typically encountered in applications with strong THz fields. This work is of general interest to the THz community due to the cost-efficient and time-saving manufacturing technique for optical components with similar performance as commercial products.

One application of intense THz pulses is the manipulation of free electron bunches. In collaboration with the Korea Atomic Energy Research Institute (South Korea), we have demonstrated in a previous work an electron streak camera based on the local field enhancement in a THz-driven split-ring resonator. In chapter 3, we have further developed this concept of THz-induced electron deflection to construct short-period undulator structures that can be used as compact novel x-ray sources. Undulator periods around 1 mm with a deflection electric field strength of 1 GV/m are experimentally achievable, with a corresponding undulator parameter K of approximately 0.3. We have presented a simulation study to compare the performance of different geometric configurations, and we have shown that a 100 MeV electron bunch with 5 pC charge emits 83 eV photons with a peak brightness of 10^{19} photons/(s mrad^2 mm^2 0.1% BW) when propagating through a 100 mm long undulator structure. At a higher bunch energy of 1 GeV, the photon energy increases to 8.2 keV with a peak brightness of 10^{21} photons/(s mrad^2 mm^2 0.1% BW). Therefore, a THz-driven split ring resonator undulator is a promising candidate for a low cost and compact radiation source producing directional, linearly polarized, and narrow band radiation pulses in the UV to x-ray range, with applications in radiotherapy, ultrafast x-ray diffraction experiments, or time-resolved x-ray spectroscopy.

Another application of intense THz pulses is ultrafast mode switching in metamaterials (chapter 4). Here, the electric field of the THz pulses is locally enhanced in nanometer-sized gaps of split-ring resonators and triggers nonlinear carrier generation in the semiconductor substrate. These additional carriers in turn alter the resonance mode of the split-ring resonators. To gain better insight into the observed nonlinear response, we developed coupled three-dimensional time-domain simulations for the electromagnetic fields and the carrier generation processes in the semiconductor substrate. We found that impact ionization dominates in germanium and silicon, while Zener tunneling is the main source of carrier generation in gallium arsenide. Furthermore, we found that mode switching can occur within a few hundred femtoseconds, paving the way for ultrafast modulators with THz bandwidth.

In chapter 5, we have shown that intense THz pulses induce a Stark shift in molecular samples and can therefore be used for ultrafast time-resolved Stark spectroscopy in liquids. Using two judiciously selected molecular systems, we have demonstrated that THz Stark spectroscopy reveals the same physicochemical molecular properties as conventional Stark spectroscopy. However, THz Stark spectroscopy has several advantages, the most important of which is that the sample does not need to be immobilized by freezing the solvent. Therefore, molecular properties can be studied over a broader range of temperatures and solvents, i.e., directly under the environmental conditions most relevant to applications in chemistry and biology. In addition, the intrinsic temporal resolution of about 100 fs allows the observation of transient or non-equilibrium electronic properties of molecules. This facilitates, for example, the study of the time-dependent physicochemical properties of a molecule during its photo-cycle and, in particular, enables time-resolved Stark spectroscopy of excited states.

To achieve higher field strengths in such nonlinear THz spectroscopy, we have developed a broadband dispersion-free THz waveguide platform featuring field-enhancement (chapter 6). We have demonstrated low bending and propagation losses of a few dB/cm, vacuum-like dispersion, efficient free space coupling, and field enhancement of up to a factor of five. The structure is based on a double-ridged metal waveguide which simultaneously enhances both the electric and the magnetic field components of a THz pulse with excellent spatial homogeneity in a few tens of microns gap. It is optimized for frequencies between 0.1 THz and 1 THz and is therefore particularly suitable for THz sources based on lithium niobate. A key feature is the relatively large volume in which the field is enhanced, allowing access to small bulk samples. In addition, we have demonstrated a compact power-splitter and based on that a THz-interferometer for waveform synthesis. Hence, this platform can be used as a fully integrated spectroscopy system for coherently controlled linear or nonlinear spectroscopy.

We have successfully tested this waveguide platform through measurements of transient birefringence induced in molecular gases by intense THz pulses (chapter 7). Compared to standard THz free space focusing, the integrated THz platform boosts the detected optical birefringence signal by more than an order of magnitude, which results from a longer interaction length of several centimeters and a locally enhanced electric field strength. Therefore, samples can be examined at unprecedented field strengths and features can be detected that could not otherwise be measured. This versatile platform can also be used for a variety of other nonlinear THz spectroscopy applications for gaseous, liquid or solid samples in combination with different probing techniques such as x-ray, optical or THz probing.

Acknowledgment

After all the happy years as part of the laser group, it is now time to look back and thank all the people who have supported me during this time:

- Thomas, thank you for supervising this work, for all your support and your always helpful ideas every time I am stuck on a problem. Thank you also for giving me the opportunity to attend conferences and collaborate with other scientists from all over the world – something I have enjoyed very much during these years. You once said that life is like a sushi restaurant where you have to recognize and choose the "golden tablets" on the conveyor belt – my time in the laser group was certainly one of them.

- Thanks to Bong Joo, Zoltan and Hansi, for your support in the lab and the many useful tricks I could learn from you. Thanks also for fixing our laser whenever it was broken again.

- A special thanks to all members of the laser group, especially Anuradha, Maryam, Roxana, Mozhgan, Christoph, Tobias, Aaron, Elnaz, Andrea, Flavio, Korinna, Jan, Alex, Dunia, Benoît and Pascal, who supported me not only in the lab but also with the after-work drinks.

- I thank our collaborators at LBNL in the U.S., Wim and Carl, for taking time during my visit as an unsuspecting undergraduate student and giving me a first impression of international and state-of-the-art science. I still remember Carl's saying when we discussed about writing a paper: "Science is like a game where your publications determine your wealth."

- Many thanks also to our collaborators at ETRI in South Korea, Dr. Shin and Won Bae, who not only helped Elnaz and me in the lab (I still have fond memories of how we could wish the desired laser power: "You want 300 mJ? Here you have 300 mJ."), but also for showing us this beautiful country and introducing us to the exquisite Korean cuisine.

- Thanks also to Adrian Cavalieri and Keith A. Nelson for supporting this thesis as second supervisor and external reviewer, respectively.

- I am also grateful to our secretarial team – Beatrice, Simone and Franziska – for their help with administrative matters and when I got a form mixed up again.

- Thanks to Andres and Nik in the electronics workshop, who were always willing to fix my problem right away, whether it was just replacing a plug or, worse, fixing a burnt motor control.

- Many thanks to Adrian from the mechanical workshop for pushing his machines to their limits for the waveguide structures (and apparently still having fun with all my special requests), but also for simply drilling holes in a metal plate (something I also learned to do at home on the balcony during Covid, but I still prefer your method).

- Thanks to all my friends, especially you Sebi for your support as a roommate during the enforced Covid home office and our regular coffee breaks, to my "theoretical" colleagues, Patrick, Nicolas and Samuel, who reminded me that there are many other problems than just experimental noise, and to Rhoda who was always on hand when I needed good photographs. My thanks also go to my colleagues in the running club, especially Henä, who made sure I didn't became slow myself while doing ultrafast science.

- Thanks also to my family for their support and for providing me with an environment where I could be curious about nature and always invent and discover new things.

- And finally, thanks to you, Bettina, for all the beautiful and happy moments outside the lab, when THz radiation was present only in the form of heat radiation from a fireplace or in the seemingly never-ending sunlight in Jokkmokk. Thank you for your ever watchful eye for the funny things in life, as well as in proofreading this thesis. I am looking forward to our future.

- Last but not least, one should always keep in mind that such projects can only be realized in countries that support science, both financially and politically. So my thanks also go to the Swiss taxpayers and supporters of Swiss researchers. I hope that I can continue to contribute to consolidating Switzerland's leading role in science in the future.

Declaration of consent

on the basis of Article 18 of the PromR Phil.-nat. 19

Name/First Name: Rohrbach David

Registration Number: 13-109-293

Study program:

Bachelor ☐ Master ☐ Dissertation ☑

Title of the thesis: Enabling Technology and Proof-of-Principle Experiments for Strong Field Terahertz Spectroscopy

Supervisor: Prof. Dr. Thomas Feurer

I declare herewith that this thesis is my own work and that I have not used any sources other than those stated. I have indicated the adoption of quotations as well as thoughts taken from other authors as such in the thesis. I am aware that the Senate pursuant to Article 36 paragraph 1 litera r of the University Act of September 5th, 1996 and Article 69 of the University Statute of June 7th, 2011 is authorized to revoke the doctoral degree awarded on the basis of this thesis.
For the purposes of evaluation and verification of compliance with the declaration of originality and the regulations governing plagiarism, I hereby grant the University of Bern the right to process my personal data and to perform the acts of use this requires, in particular, to reproduce the written thesis and to store it permanently in a database, and to use said database, or to make said database available, to enable comparison with theses submitted by others.

Place/Date

Signature

Research output list

All of the listed publications result from my PhD time at the University of Bern. For clarity, my name and the publication year are highlighted in bold font. If applicable, a direct internet link is given for the publication.

Publications in peer-reviewed scientific journals

- K. Töpfer, A. Pasti, A. Das, S. M. Salehi, L. I. Vazquez-Salazar, **D. Rohrbach**, T. Feurer, P. Hamm, and M. Meuwly, *Structure, Organization and Heterogeneity of Water-Containing Deep Eutectic Solvents* in J. Am. Chem. Soc., (**2022**), DOI: `https://doi.org/10.1021/jacs.2c04169`.

- B. J. Kang, **D. Rohrbach**, F. D. J. Brunner, S. Bagiante, H. Sigg, and T. Feurer, *Ultrafast and Low-Threshold THz Mode Switching of Two-Dimensional Nonlinear Metamaterials* in Nano Letters, **22**, 2016-2022, (**2022**), DOI: `https://doi.org/10.1021/acs.nanolett.1c04776`.

- **D. Rohrbach**, B. J. Kang, and T. Feurer, *3D-printed THz wave- and phaseplates*, in Optics Express **29** (17), 27160-27170 (**2021**), DOI: `https://doi.org/10.1364/OE.433881` (**Editors' Pick**).

- **D. Rohrbach**, Z. Ollmann, M. Hayati, C.B. Schroeder, W. P. Leemans, and T. Feurer, *THz-driven split ring resonator undulator* in Phys. Rev. Accel. Beams **24**, 010703 (**2021**), DOI: `https://doi.org/10.1103/PhysRevAccelBeams.24.010703`.

- **D. Rohrbach**, C. B. Schroeder, A. Pizzi, R. Tarkeshian, M. Hayati, W. P. Leemans, and T. Feurer, *THz-driven surface plasmon undulator as a compact highly directional narrow band incoherent x-ray source* in PRAB **22**, 090702 (**2019**), DOI: `https://doi.org/10.1103/PhysRevAccelBeams.22.090702`.

Peer-reviewed conference proceedings

- **D. Rohrbach**, Z. Ollmann, M. Hayati, C. B. Schroeder, H. W. Kim, I. H. Baek, K. Y. Oang, M. H. Kim, Y. C. Kim, K.-H. Jang, Y. U. Jeong, W. P. Leemans, and T. Feurer, *THz-driven Electron Deflection for Streaking and Undulators*, in IEEE Xplore, **2021** Conference on Lasers and Electro-Optics Europe & European Quantum Electronics Conference (CLEO/Europe-EQEC), pp. 1-1, 21-25 June 2021, DOI: `https://doi.org/10.1109/CLEO/Europe-EQEC52157.2021.9542026`.

- B. J. Kang, **D. Rohrbach**, F. Brunner, S. Bagiante, H. Sigg, and T. Feurer, *Ultrafast Mode Switching of Metamaterials Driven by Intense THz Field-Induced Impact Ionization* in IEEE Xplore, **2021** Conference on Lasers and Electro-Optics Europe & European Quantum Electronics Conference (CLEO/Europe-EQEC), pp. 1-1, 21-25 June 2021, DOI: `https://doi.org/10.1109/CLEO/Europe-EQEC52157.2021.9541999`.

Contributions to conferences

- **D. Rohrbach**, B. J. Kang, F. D. J. Brunner, S. Bagiante, H. Sigg, and T. Feurer *Ultrafast and Low-Threshold THz Mode Switching of Two-Dimensional Nonlinear Metamaterials* in Physics School "As thin as it gets: Physics of 2D Materials and Heterostructures" (Bad Honnef, Germany, 24-29 July **2022**) as poster presentation, `https://www.dpg-physik.de/veranstaltungen/2022/as-thin-as-it-gets-physics-of-2d-materials-and-heterostructures`.

- **D. Rohrbach**, B. J. Kang, A. Jenk, and T. Feurer, *A broadband dispersion-free THz waveguide platform featuring field-enhancement* in OTST 2022 (Budapest, Hungary, 19-24 June **2022**) as oral presentation, `https://otst2022.hu/ProgrammeBook.pdf`.

- **D. Rohrbach**, B. J. Kang, T. Feurer, *3D-printed THz wave- and phaseplates* in OTST 2022 (Budapest, Hungary, 19-24 June **2022**) as poster presentation, `https://otst2022.hu/ProgrammeBook.pdf`.

- **D. Rohrbach**, B. J. Kang, E. J. Rohwer, M. Akbarimoosavi, Z. Ollmann, E. Zyaee, A. Cannizzo, T. Feurer, S. E. Meckel, R. J. Stanley, R. F. Pauszek III, G. Sorohhov, S. Decurtins, S.-X. Liu, A. Borgoo, and M. Cascella, *Time-resolved THz Stark spectroscopy of molecules in solution and solid matrices* in MUST2022 (Grindelwald, Switzerland, 7-10 June **2022**) as oral presentation, `https://must2022.ch/wp-content/uploads/2022/05/Rohrbach.pdf`.

- E. Zyaee, **D. Rohrbach**, B. J. Kang, A. Jenk, and T. Feurer, *Broadband integrated THz platform for time-resolved spectroscopy* in MUST2022 (Grindelwald, Switzerland, 7-10 June **2022**) as poster presentation (presented by E. Zyaee), `https://must2022.ch/wp-content/uploads/2022/05/Zyaee.pdf`.

- K. Töpfer, A. Pasti, A. Das, S. M. Salehi, L. I. Vazquez-Salazar, **D. Rohrbach**, T. Feurer, P. Hamm, and M. Meuwly, *Structural Motifs and Dynamics of a Deep Eutectic Mixture: Experimental THz and 2D IR Spectra Combined with Atomistic Simulations* in MUST2022 (Grindelwald, Switzerland, 7-10 June **2022**) as poster presentation (presented by K. Töpfer).

- B. J. Kang, **D. Rohrbach**, F. D. J. Brunner, S. Bagiante, H. Sigg, and T. Feurer, *Intense THz Field-Induced Ultrafast Mode Switching of THz Nano-Structures* in MUST Annual Meeting 2021 (Grindelwald, Switzerland, 13-15 Sept **2021**) as oral presentation (presented by B. J. Kang).

- B. J. Kang, **D. Rohrbach**, F. Brunner, S. Bagiante, H. Sigg, and T. Feurer, *Ultrafast Mode Switching of Metamaterials Driven by Intense THz Field-Induced Impact Ionization* in CLEO/ Europe EQEC 2021 (Virtual conference, 21-25 June **2021**) as oral presentation (presented by B. J. Kang) `https://doi.org/10.1109/CLEO/Europe-EQEC52157.2021.9541999`.

- **D. Rohrbach**, Z. Ollmann, M. Hayati, C. B. Schroeder, H. W. Kim, I. H. Baek, K. Y. Oang, M. H. Kim, Y. C. Kim, K.-H. Jang, Y. U. Jeong, W. P. Leemans, and T. Feurer, *THz-driven Electron Deflection for Streaking and Undulators* in CLEO/Europe EQEC 2021 (Virtual conference, 21-25 June **2021**) as oral presentation, `https://doi.org/10.1109/CLEO/Europe-EQEC52157.2021.9542026`.

- **D. Rohrbach**, Z. Ollmann, C. B. Schroeder, M. Hayati, R. Tarkeshian, W. P. Leemans, and T. Feurer *THz-driven short period undulators* in EAAC 2019 (Elba, Italy, 15-21 Sep **2019**) as poster presentation, `https://agenda.infn.it/event/17304/contributions/98825/`.

- T. Feurer, **D. Rohrbach**, H. W. Kim, I. H. Baek, K. Y. Oang, K.-H. Jang, M. H. Kim, M. Hayati, R. Tarkeshian, Y. C. Kim, Y. U. Jeong, and Z. Ollmann, *THz streaking of ultrashort electron bunches* in EAAC 2019 (Elba, Italy, 15-21 Sep **2019**) as oral presentation (presented by T. Feurer), `https://agenda.infn.it/event/17304/contributions/98987/`.

- Z. Ollmann, **D. Rohrbach**, M. Hayati, R. Tarkeshian, and T. Feurer, *THz metamaterials meet accelerators* in OTST 2019 (Santa Fe, USA, 10-15 Mar **2019**) as oral presentation (presented by Z. Ollmann).

- **D. Rohrbach**, M. Hayati, Z. Ollmann, R. Tarkeshian, and T. Feurer, *THz driven surface plasmon undulator* in ICFDT5-conference (Frascati, Italy, 3-5 Oct **2018**) as poster presentation, `https://agenda.infn.it/event/15217/contributions/28887/`.

- Z. Ollmann, **D. Rohrbach**, M. Hayati, R. Tarkeshian, and T. Feurer, *THz metamaterials meet accelerators* in ICFDT5-conference (Frascati, Italy, 3-5 Oct **2018**) as oral presentation (presented by Z. Ollmann), `https://agenda.infn.it/event/15217/contributions/28909/`.

Outreach activities

- Assistance at the Night of Research, *In search of time*, University of Bern (09/2022)

- Assistance at the Bachelor information days in Mathematics, Physics and Astronomy for high-school students, University of Bern (2015, 2016, 2017, 2018)

- Various public seminar talks at the University of Bern (*3D-printed THz waveplates*, *THz-driven surface plasmon polariton undulator* and *THz-driven graphene plasmon-based undulator*)

Submitted but not yet accepted/published publications

- **D. Rohrbach**, B. J. Kang, E. Zyaee, and T. Feurer, *Wideband dispersion-free THz waveguide platform*, preprint available on arXiv (**2022**): `http://arxiv.org/abs/2208.00678`.
- B. J. Kang, E. J. Rohwer, **D. Rohrbach**, M. Akbarimoosavi, Z. Ollmann, E. Zyaee, A. Cannizzo, T. Feurer, S. E. Meckel, R. J. Stanley, R. F. Pauszek III, G. Sorohhov, S. Decurtins, S.-X. Liu, A. Borgoo, and M. Cascella, *Time-resolved THz Stark spectroscopy of molecules in solution*, preprint available on arXiv (**2022**): `https://arxiv.org/abs/2212.10333`.

Unpublished work

- Z. Ollmann, **D. Rohrbach**, B. J. Kang, M. Hayati, R. Tarkeshian, T. Feurer, H. W. Kim, I. H. Baek, K. Y. Oang, M. H. Kim, Y. C. Kim, K.-H. Jang, and Y. U. Jeong, *THz streaking of relativistic electron bunches.*
- B. J. Kang, M. A. Stucki, **D. Rohrbach**, H. Park, S. J. Hong, Y.-M. Bahk, and T. Feurer *Optical-induced nonlinear dynamics of complementary THz meta-surfaces on long-carrier lifetime semiconductor.*
- **D. Rohrbach**, H.-M. Frey, B. J. Kang, E. Zyaee, and T. Feurer, *THz-induced gas alignment in field enhancing waveguides.*